

N° d'ordre: 41177

UNIVERSITE LILLE 1 - SCIENCES ET TECHNOLOGIES
ECOLE DOCTORALE DES SCIENCES POUR L'INGENIEUR

THESE

présentée en vue d'obtenir le grade de

DOCTEUR

en

Génie Electrique

par

Carlos Enrique CUELLAR QUISPE

DOCTORAT DELIVRE PAR L'UNIVERSITE LILLE 1 - SCIENCES ET TECHNOLOGIES

HF characterization and modeling of magnetic materials for
the passive components used in EMI filters

Caractérisation et modélisation HF des matériaux
magnétiques pour la conception des composants passifs des
filtres CEM

Soutenue le 07 octobre 2013 devant le jury d'examen

Président	François COSTA, <i>Professeur des universités,</i> <i>SATIE - Université Paris 12.</i>
Rapporteur	Marie Ange RAULET, <i>Maître de Conférences HDR.</i> <i>Laboratoire Ampère – Université de Lyon 1</i>
Rapporteur	Flavio CANAVERO, <i>Professeur des universités,</i> <i>Politecnico di Torino, Italie</i>
Directeur de thèse	Nadir IDIR, <i>Professeur des universités,</i> <i>L2EP – Université de Lille 1</i>
Co-encadrant de thèse	Abdelkader BENABOU, <i>Maître de Conférences,</i> <i>L2EP – Université de Lille 1</i>
Co-encadrant de thèse	Xavier MARGUERON, <i>Maître de Conférences,</i> <i>L2EP – Ecole Centrale de Lille</i>
Invité	Houmam MOUSSA, <i>Dr. Ingénieur,</i> <i>Hispano-Suiza - SAFRAN</i>

Thèse préparée au Laboratoire d'Electrotechnique et d'Electronique de Puissance (L2EP)

Ecole Doctorale SPI 072

PRES – Université Lille Nord-de-France

Abstract

The switching semiconductor devices in static converters are the main source of electromagnetic interference (EMI). Reduction of these emissions can be achieved by different techniques including the use of EMI filters which design requires the use of magnetic cores. These must have adequate physical properties allowing the EMI filter to fulfill its task within a specified frequency range whatever the operating conditions (saturation, temperature...). Therefore, in the present work, some methodologies and models are developed in order to be able to design the EMI filter within its real operating conditions.

First, the magnetic core is considered in small-signal conditions and a method is proposed to measure the complex magnetic permeability in high frequency (HF). Two models, analytical and lumped-circuit network, are developed to account for the HF characteristics. In a second step, the material is considered saturable as the EMI filter can be subjected to more important currents, leading to the modification of its main characteristics. Then, a non-linear modeling approach, with and without hysteresis effect, including a material capacitance is considered for modeling the magnetic core. Additionally, a technique is proposed to characterize in HF the magnetic hysteresis loop from a single turn flat coil configuration.

Finally, an improved current injection method, with new designed current probes, is used to characterize the input impedance of a converter. The impedance, combined with the developed small-signal and high-signal material models, is used to predict the insertion loss of an EMI filter. Simulation results are validated by the experiment.

Keywords: EMI filter, Inductive Components, Magnetic materials, Measuring, Modeling, Equivalent circuit, Current probes, Power Electronics.

Résumé

Les commutations des interrupteurs dans les convertisseurs statiques sont à l'origine des principales perturbations faisant l'objet de la compatibilité électromagnétique (CEM). La réduction de ces perturbations se fait, entre autre, à l'aide de filtres CEM qui nécessitent l'utilisation de noyaux magnétiques. Ces matériaux doivent posséder des propriétés physiques adaptées pour assurer le bon fonctionnement du filtre CEM dans la gamme de fréquences souhaitée, et ce, quel que soit les contraintes d'utilisation (saturation, température ...). Ainsi, dans ce travail, des méthodologies et des modèles sont développés afin de dimensionner le filtre CEM dans les conditions réelles de fonctionnement.

Tout d'abord, le noyau magnétique est étudié pour de faibles signaux d'excitation en proposant une méthode de caractérisation de la perméabilité magnétique complexe en hautes fréquences (HF). Deux modèles, l'un analytique et l'autre en circuit équivalent, sont développés pour prendre en compte ce comportement HF. Dans un second temps, le matériau est considéré saturable. En effet, le filtre CEM peut être soumis à des courants plus importants, conduisant alors à la modification de ses caractéristiques principales. C'est pourquoi, une approche non-linéaire est développée pour représenter le matériau, avec et sans hystérésis, tout en y incluant le comportement capacitif du matériau en HF. De plus, une méthode expérimentale, basée sur l'utilisation d'une spire plate, est proposée pour caractériser l'hystérésis magnétique en HF.

Enfin, une amélioration de la méthode d'injection de courant est proposée, notamment par l'utilisation de nouvelles sondes, pour caractériser l'impédance d'entrée d'un convertisseur. Cette impédance, combinée avec les modèles précédents de matériaux sous faibles et fortes excitations, est utilisée pour déterminer la perte d'insertion d'un filtre CEM. Les résultats de simulations sont validés par la mesure expérimentale.

Mots-clés: Filtre CEM, Composant Inductive, Composant, Matériaux magnétiques, Modélisation analytique, Circuit équivalent, Sondes de courant, Électronique de puissance



Table of content

GENERAL INTRODUCTION	19
CHAPTER 1. STATE OF ART	25
1.1 EMI in Power electronics	27
1.1.1 Radiated emissions	28
1.1.2 Conducted emissions	28
1.2 Techniques to mitigate the EMI.....	31
1.2.1 At the source.....	31
1.2.2 At the coupling paths.....	31
1.3 Passive EMI filters	32
1.3.1 Overview	32
1.3.2 Insertion loss	34
1.3.3 Parasitic elements of EMI filter	35
1.4 Ring core inductors	37
1.4.1 Overview	37
1.4.2 Theoretical modeling methods.....	38
1.4.3 Experimental modeling methods	39
1.4.4 Winding	40
1.4.5 Magnetic Core.....	43
1.5 Characteristics of magnetic material	44
1.5.1 Magnetic permeability.....	46
1.5.2 Hysteresis loop	48
1.6 Conclusion.....	50
CHAPTER 2. SMALL-SIGNAL CHARACTERIZATION AND MODELING OF THE MAGNETIC CORE	51
2.1 Overview of the magnetic permeability.....	53
2.2 Measurement of complex magnetic permeability	57
2.2.1 Magnetic material test fixture.....	57
2.2.2 Proposed method.....	60
2.2.3 Influence of the number of turns	61
2.2.4 Method of CMP measurement compensation in HF	65
2.2.5 Magnetic material variation	67
2.2.6 Influence of the voltage level.....	70
2.2.7 Summarize.....	72
2.3 Modeling of complex magnetic permeability	73
2.3.1 State of the art.....	73
2.3.2 RFCMP model	76

2.3.3	Validation of the RFCMP model	79
2.4	Electrical equivalent circuit of the ring cores inductors.....	82
2.4.1	State of art.....	82
2.4.2	New RCI model.....	84
2.4.3	Parasitic capacitance	85
2.4.4	Skin effect in the magnetic material.....	90
2.4.5	High frequency parasitic elements	91
2.4.6	Validation of the new RCI model.....	92
2.5	Conclusion.....	95
CHAPTER 3. HIGH-SIGNAL CHARACTERIZATION AND MODELING OF THE MAGNETIC CORE		97
3.1	Introduction	99
3.2	Experimental setup	101
3.2.1	Overview	101
3.2.1	Improvement of the experimental setup.....	103
3.2.2	Connector characterization.....	105
3.2.3	Experimental setup	106
3.2.4	Mismatch impedance of RF amplifier.....	106
3.2.5	Characteristics of the measurement instruments.....	107
3.3	Magnetic material models	108
3.3.1	Overview	108
3.3.2	Average BH-curve model.....	110
3.3.3	Jiles-Atherton model	112
3.3.4	Stray capacitance due to the magnetic material.....	113
3.3.5	Numerical resolution of the Jiles-Atherton model	113
3.4	Experimental identification of model parameters	114
3.4.1	Specification of the magnetic material.....	114
3.4.2	Average BH-curve parameters identification.....	116
3.4.3	Jiles-Atherton parameters identification	121
3.4.4	Robustness of the hysteresis model	123
3.4.5	Core loss and copper losses.....	128
3.5	Application: EMI filter for power converter	130
3.5.1	Differential mode filter	130
3.5.2	Common mode filter.....	133
3.6	Temperature influence in the magnetic material	135
3.6.1	Overview	135
3.6.2	Test bench.....	136
3.6.3	Evolution of the J-A parameters with the temperature.....	139
3.7	Conclusion.....	141

CHAPTER 4. EMI FILTER DESIGN	143
4.1 Introduction	145
4.2 Equipment under test – buck converter	145
4.3 Conducted emissions measurement	147
4.3.1 Overview	147
4.3.2 Measurement with LISN	147
4.3.3 Measurement with current probe	148
4.4 Conducted emissions of the buck converter.....	149
4.5 EMI source impedance measurement	150
4.5.1 Overview	150
4.5.2 Measurement in off-state.....	151
4.5.3 Current injection method	152
4.5.4 Measurement of passive components.....	154
4.5.5 Measurement of static converter impedances	156
4.6 Current probes	162
4.6.1 Transfer impedance of the current probe	163
4.6.2 New current probes	165
4.6.3 Measurement of the common mode source impedance	168
4.7 EMI filter design	172
4.7.1 Common mode filter.....	176
4.7.2 Differential mode filter	179
4.7.3 Realization of the EMI Filter	181
4.8 Insertion loss with S-parameters	182
4.8.1 Introduction	183
4.8.2 Insertion loss with arbitrary input and output impedances.....	184
4.9 Conclusion.....	189
GENERAL CONCLUSION	191
FUTURE WORK.....	197
BIBLIOGRAPHY	201

List of figures

Figure 1-1 (a) General EMC elements and (b) EMI induced by the buck converter	28
Figure 1-2 (a) CM noise current path and (b) DM noise current path.....	28
Figure 1-3 (a) Equivalent circuit of LISN (b) Typical impedance of the LISN to EUT side..	29
Figure 1-4 Currents in power line: I_{L1} , I_{L2} and I_G . Voltage drop in the LISN: V_{L1} and V_{L2} ...	30
Figure 1-5 Conducted emissions limits defined by C.I.S.P.R. 11 standard	30
Figure 1-6 Different techniques for mitigate EMI in power energy conversion [9]	31
Figure 1-7 Classical EMI power line filter topology	33
Figure 1-8 Thevenin Equivalent Circuit (a) without and (b) with EMI filter	34
Figure 1-9 (a) EMI filter with its parasitic elements. (b) CM insertion loss considering parasitic elements (c) DM insertion loss considering parasitic elements	35
Figure 1-10 Magnetic cores shapes (a) RM (b) PM (c) EP (d) P (e) E (f) ELP (g) EQ (h) ETD (i) UI (j) Toroid or Ring.....	37
Figure 1-11 (a) Differential mode inductance (b) Common mode inductance.....	38
Figure 1-12 Models of inductor	40
Figure 1-13 Winding strategies in ring cores.....	41
Figure 1-14 Magnetic dipole and the magnetization process	44
Figure 1-15 Soft magnetic materials used in power electronics [54]	45
Figure 1-16 CMP of (a) Ferrite EPCOS®-N30 and (b) Nanocrystalline Metglas® FT-1KM	47
Figure 1-17 General hysteresis loop of ferrimagnetic material.....	49
Figure 2-1 Description of magnetic test fixture (MMTF) and procedure for CMP measurement	57
Figure 2-2 Typical relative permeability measurement accuracy of MMTF	58
Figure 2-3 Comparison of CMP by MMTF measurement and the datasheet	59
Figure 2-4 Ring core magnetic material with N turns.....	60
Figure 2-5 Influence of N in the impedance measurement.....	62
Figure 2-6 Equivalent circuit of measurement.....	63
Figure 2-7 (a) Wire resistance R_{par} frequency evolution (b) Leakage inductance L_{par}	64
Figure 2-8 Configuration of wire surface variation test	66
Figure 2-9 Impedance comparison when wire surface varies (a) module (b) phase	66
Figure 2-10 Leakage inductance of one-turn winding surface	66
Figure 2-11 (a) Module and (b) phase of the impedance measured with MMTF and the proposed method	67
Figure 2-12 (a) CMP of four N30 ring cores of type C1 and (b) relative variation for N30 (c) CMP of four N6E3 ring cores of type C5 and (d) relative variation for N6E3.....	69
Figure 2-13 (a) CMP of three N30 ring cores (C2, C3, C4) and (b) relative variation for N30 (c) CMP of three N6E3 ring cores (C6, C7, C8) and (d) relative variation for N6E3..	70
Figure 2-14 (a) Real part of CMP (μ') for the ring core type C1 (Table 2-4) when the voltage level varies (b) Small-signal B_m - H_m relation.....	71
Figure 2-15 (a) Imaginary part of CMP for the ring core type C5 when the voltage level varies (b) Small-signal average B_m - H_m relation.....	72
Figure 2-16 CMP flow diagram for small-signal characterization	72

Figure 2-17 Measurement and simulation of N30 ferrite CMP with 2 nd grade rational function	74
Figure 2-18 The negative value of the CMP real part. N30 ferrite	76
Figure 2-19 Flow diagram of the Householder algorithm that leads to the coefficients of (53)	79
Figure 2-20 Validation of the RFCMP (4 th grade) model for (a) N30 MnZn ferrite (b) N6E3 nanocrystalline and (c) M43 NiZn ferrite	80
Figure 2-21 Different models for ring core inductors in HF (a) Measurement with scattering parameter [75] (b) Gytrators [76] (c) RLC lumped circuit [77] (d) PEEC-BIM [78] (e) Transmission line [79] (f) Cauer-Foster [35]	84
Figure 2-22 Block diagram of the equivalent circuit model of RCI	85
Figure 2-23 Impedance of three ferrite materials with the same number of turns and the same core size	86
Figure 2-24 Inductor's impedance with ferrite N87: Influence of turns (a) $N \geq 58$ (b) $N \leq 23$	87
Figure 2-25 Stray capacitance	87
Figure 2-26 Circuit model for the <i>material capacitance</i>	88
Figure 2-27 Geometric definitions for the winding capacitance calculation	89
Figure 2-28 Skin depth of the materials (a) ferrite MnZn N30 and (b) N6E3 nanocrystalline	91
Figure 2-29 Circuit model of skin effect in the material	91
Figure 2-30 Transmission line (a) lumped circuit (b) TLOSSY element	92
Figure 2-31 Equivalent circuit for the ferrite RCI	93
Figure 2-32 (a) Equivalent circuit and simulation (b) N=1 (c) N=10 and (d) N=30	93
Figure 2-33 Equivalent circuit for the nanocrystalline RCI	94
Figure 2-34 (a) Equivalent circuit and simulation (b) N=1 (c) N=10 and (d) N=30	94
Figure 3-1 Two-coil measurement prototype (a) first and (b) second prototype	102
Figure 3-2 N30 ferrite hysteresis loop measured with the second prototype (a) 50kHz and 100kHz (b) above 5MHz (c) CMP (small-signal) (d) equivalent impedance of CMP	102
Figure 3-3 Experimental setup used to characterize the magnetic material using a single turn of flat copper ribbon	103
Figure 3-4 (a) Impedance (b) Resistance and (c) Inductance of the one-turn wire and STFC	104
Figure 3-5 Electric potential and magnetic flux density in the proposed connector	104
Figure 3-6 Equivalent circuit of the setup configuration	105
Figure 3-7 Electric potential on the N-connector	106
Figure 3-8 Equivalent circuit of RF amplifier	107
Figure 3-9 Current sensors (a) shunt LEM 20m Ω (b) hall sensor TCP 202	108
Figure 3-10 Representation of the hysteresis loop with the Langevin curve	110
Figure 3-11 Calculation procedure of average BH-curve	112
Figure 3-12 The impedance magnitude of the STC: The resonance of the N30 ferrite material occurs near 1MHz	113
Figure 3-13 Calculation procedure of B(t) from H(t)	114
Figure 3-14 Evolution of parameter <i>a</i> : (a) N30 ferrite (b) M43 ferrite (c) N6E3 nanocrystalline	117
Figure 3-15 The average BH-curve model (f=20kHz) (a) N30 ferrite (b) M43 ferrite and (c) N6E3 nanocrystalline	119

Figure 3-16 Measurement (X) and Steinmetz model result of power loss density for (a) N30 (MnZn) (b) M43 (NiZn) and (c) N6E3 Nanophy (Nanocrystalline) materials	120
Figure 3-17 Measured and simulation results of the hysteresis loops for (a) N30 MnZn (b) M43 NiZn (c) N6E3 Nanocrystalline with J-A model.....	122
Figure 3-18 Hysteresis loop of N30 ferrite for frequencies of 200kHz, 500kHz and 1MHz	123
Figure 3-19 Complex magnetic permeability (CMP) for ferrite core N30 calculated with hysteresis loop (markers ‘o’ and ‘*’)	124
Figure 3-20 Square signal; Current and Voltage in self-inductor of N30 (MnZn) at 500kHz	126
Figure 3-21 Saw-tooth signal; Current and Voltage in self-inductor of N30 (MnZn) at 500kHz	126
Figure 3-22 Arbitrary waveform with DC-bias: Current and Voltage in self-inductor of N30 (MnZn) at 100kHz (simulation with HCM)	127
Figure 3-23 (a) Relative permeability of N30 ferrite with DC-bias magnetic field.....	128
Figure 3-24 Extrapolation of the volumetric loss for ferrite core N30 ($B_{max}=50mT$)	129
Figure 3-25 Core loss of N30 ferrite and copper loss in the STFC.....	129
Figure 3-26 Equivalent circuit of the (a) DM filter and (b) CM filter	130
Figure 3-27 Buck converter and DM equivalent circuit (b) without coupled inductor (c) with coupled inductor (separer, DC-DC)	132
Figure 3-28 Measured DM noise attenuation with load resistor (a) 15Ω (b) 30Ω and (c) 60Ω	133
Figure 3-29 Simulated DM noise attenuation with load resistor (a) 15Ω (b) 30Ω and (c) 60Ω	133
Figure 3-30 Simulation of CM filter (a) equivalent circuit (b) insertion loss for different input voltage (V_{in})	134
Figure 3-31 Test bench for temperature influence.....	137
Figure 3-32 Temperature sensor distribution	137
Figure 3-33 Frequency-dependent impedance (a) N30 ferrite and (b) N6E3 nanocrystalline	138
Figure 3-34 Temperature test configuration.....	139
Figure 3-35 Hysteresis loop variation with temperature (N30 ferrite at 100 kHz)	140
Figure 3-36 Jiles-Atherton parameters: N30 ferrite (a) parameter “ a ” (b) “ Ms ”; and N6E3 nanocrystalline (c) “ a ” (d) “ Ms ”	141
Figure 4-1 Schematic of IGBT Buck converter	146
Figure 4-2 Buck converter (a) drive and power PCB and (b) global view of the system	146
Figure 4-3 Equivalent circuit of mono-phase LISN (EMCO 3810/2)	147
Figure 4-4 (a) Conducted emissions over the spreading paths (b) DM current and (c) CM current measurement setup.....	149
Figure 4-5 Conducted emissions measurement setup.....	149
Figure 4-6 Conducted emissions (QP) of the buck converter with LISN (a) V_{L1} and (b) V_{L2}	150
Figure 4-7 Conducted emissions of the buck converter (a) V_{DM} and (b) V_{CM}	150
Figure 4-8 Measurement configurations of the converter impedance in off-state	151
Figure 4-9 Impedances of the buck converter measured with impedance analyzer in off-state	152
Figure 4-10 CIM to measure the unknown impedance Z_X (a) connection (b) equivalent circuit	153

Figure 4-11 Frequency evolution (a) parameter K and (b) Z_{setup}	154
Figure 4-12 Impedance of precision resistors measured with CIM	155
Figure 4-13 Impedance measurement of (a) a capacitor and (b) an inductor	155
Figure 4-14 Impedance measurement of SiC buck converter in operating conditions by CIM	156
Figure 4-15 Measurement of the DM impedance of the buck converter and load	156
Figure 4-16 DM configuration test to determine K and Z_{setup} (a) $Z_X = 0\Omega$ (b) $Z_X = 50\Omega$...	157
Figure 4-17 Frequency evolution of (a) K and (b) Z_{setup} in the DM configuration.....	157
Figure 4-18 Impedance measurement of the LISN (a) DM configuration setup and (b) Comparison of measurement results.....	158
Figure 4-19 Evolution of Z_{SDM}	159
Figure 4-20 Measurement of the CM impedance of the buck converter and load	160
Figure 4-21 CM configuration test to determine K and Z_{setup} (a) $Z_X = 0\Omega$ (b) $Z_X = 50\Omega$...	160
Figure 4-22 Frequency evolution of (a) K and (b) Z_{setup} in the CM configuration.....	161
Figure 4-23 Impedance measurement of the LISN (a) CM configuration setup and (b) Comparison of measurement results.....	161
Figure 4-24 Evolution of the buck converter impedance Z_{SCM}	162
Figure 4-25 Commercial and proposed current probes	163
Figure 4-26 (a) Structure to measure the transfer impedance of the current probe (b) The equivalent circuit of the structure.....	164
Figure 4-27 Transfer impedance of: (a) F-52A current probe and (b) F-120-3 current injection probe	165
Figure 4-28 Magnetic permeability of the nanocrystalline material (097-12-1-E2 from Aperam®)	166
Figure 4-29 The new current probe transfer impedance with nanocrystalline material.....	167
Figure 4-30 Measurement of the SiC buck converter impedance with new current probes ..	168
Figure 4-31 Common mode impedance of buck converter in off-state measured with (a) commercial current probes and (b) with new current probes	168
Figure 4-32 Different test configurations to measure the common mode impedance of a SiC buck converter + load	169
Figure 4-33 CM impedance with configurations (a) and (b).....	171
Figure 4-34 CM impedance with configurations (c) and (d) with converter in off-state and on-state.....	171
Figure 4-35 CM impedance with configurations (e) and (f) in off and on-operating conditions	172
Figure 4-36 (a) Thévenin equivalent circuit of the converter (b) T-network of the EMI filter	172
Figure 4-37 Steps in EMI filter design	173
Figure 4-38 Required level of conducted emission attenuation in DM and CM	174
Figure 4-39 Buck converter impedances (a) Z_{SDM} impedance (b) Z_{SDM} equivalent circuit (c) Z_{SCM} impedance and (d) Z_{SCM} equivalent circuit.....	175
Figure 4-40 LISN impedance (a) measured and simulation results (b) equivalent circuit	175
Figure 4-41 Common mode filter structures.....	176
Figure 4-42 Simulation results of the insertion loss of the three CM filter topologies (a) LC filter, (b) CL filter and (c) LCL filter	177

Figure 4-43 Insertion losses of CM filter with ferrite N87 and N6E3 nanocrystalline material	178
Figure 4-44 Differential model filter structures	179
Figure 4-45 Insertion loss of three DM EMI filter topologies	180
Figure 4-46 EMI filter schematic connected to the LISN and to the static converter + load	181
Figure 4-47 EMI filter prototype with ferrite N87.....	181
Figure 4-48 Reduction of conducted emissions using the designed EMI filter in (a) DM emission (b) CM emission.....	182
Figure 4-49 (a) CM and DM filters (a) equivalent circuits (b) black box models	184
Figure 4-50 Insertion loss of the black-box and spectrum analyzer (under $50\Omega/50\Omega$).....	185
Figure 4-51 Characterization setup with additional impedance (a) parallel output (b) series output (c) parallel input (d) series input	186
Figure 4-52 Measured CM impedance of the buck converter.....	187
Figure 4-53 Validation of the additional impedance (a) for parallel output IL_{po} (b) series output IL_{so} (c) parallel input IL_{pi} (d) and series input IL_{si}	188
Figure 4-54 (a) Measurement of the insertion loss with buck converter input impedance in series with the EMI filter, and (b) insertion loss measured and simulated	188

List of tables

Table 1-1 Different magnetic material	45
Table 1-2 Permeability measurement methods.....	48
Table 2-1 Different MUT sizes.....	58
Table 2-2 Magnetic materials under test.....	59
Table 2-3 Parameters for R_{par} and L_{par} calculation (PVC ring core)	64
Table 2-4 List of N30 ferrite ring cores	68
Table 2-5 List of N6E3 nanocrystalline ring cores.....	68
Table 2-6 Rational Function model coefficients for N30.....	81
Table 2-7 Rational Function model coefficients for N3E6	81
Table 2-8 Rational Function model Coefficients for M43.....	82
Table 2-9 Equivalent RLC circuit of the first resonance (48 turns winding)	86
Table 3-1 Mismatch impedance evaluation	107
Table 3-2 Magnetic materials under test.....	115
Table 3-3 N30 MnZn material: amplitude of the voltage values	115
Table 3-4 M43 NiZn material: amplitude of the voltage values.....	116
Table 3-5 N6E3 nanocrystalline material: amplitude of the voltage values	116
Table 3-6 Coefficients of the exponential expression of parameter a	117
Table 3-7 Coefficients of the Langevin function	117
Table 3-8 Steinmetz coefficients for power losses model.....	118
Table 3-9 Jiles-Atherton model parameters	121
Table 3-10 Values of equivalent circuit elements	125
Table 3-11 Elements of DC DC buck converter	132
Table 3-12 Coefficients of the models.....	140
Table 4-1 Characteristics of the buck converter	146
Table 4-2 Characteristics of the three CM filters	176
Table 4-3 Characteristics of the three calculated DM filters	179

Glossary

AVG	: Average detector
CIM	: Current injection method
CIP	: Current injection probe
CISPR	: Comité International Spécial des Perturbations Radioélectriques
CM	: Common mode
CMP	: Complex magnetic permeability
CP	: Current measurement probe
CPUT	: Current probe under test
DM	: Differential mode
EMC	: Electromagnetic compatibility
EMI	: Electromagnetic interferences
EPC	: Inductor's equivalent parallel capacitance
EPR	: Inductor's equivalent parallel resistance
ESL	: Capacitor's equivalent series inductance
ESR	: Capacitor's equivalent series resistance
ETR	: EMI test receiver
EUT	: Equipment under test
FEA	: Finite Element Analysis
FFT	: Fast Fourier Transform
HF	: High frequency
HCM	: Hysteretic and capacitive material behavior model
IA	: Impedance analyzer
IL	: Insertion loss
IRFA	: Iterative ration function approximation
J-A	: Jiles-Atherton model
LISN	: Line impedance stabilization network
MDUT	: Magnetic material under test
MMTF	: Magnetic material test fixture
MnZn	: Manganese-Zinc
MRF	: Material resonance frequency
MUT	: Material under test

NCP	:	New current probes
NiZn	:	Nickel-Zinc
PEEC	:	Partial Element Equivalent Circuit
PEEC-BIM	:	PEEC and the Boundary Integral method
QP	:	Quasi-peak detector
RCI	:	Ring core inductor
RF	:	Radio frequency
RFA	:	Rational function approach
RFCMP	:	Rational function of CMP
SA	:	Spectrum analyzer
SiC	:	Silicon Carbide
STFC	:	Single turn of flat copper ribbon
VNA	:	Vector network analyzer
VSWR	:	Voltage standing wave ratio

General introduction

The present PhD was carried out from September 2010 to June 2013 under the PhD program of ERASMUS-University of Lille 1 and financed by Erasmus Mundus External Window. This work was completed at the Laboratoire d'Electrotechnique et d'Electronique de Puissance (L2EP) of the University Lille 1.

Scope of the work

Nowadays, a large research effort is being devoted in the power electronic industry to design high-frequency and high-density static converters. The developments of wide band gap semiconductors (e.g. SiC and GaN) allow the increase of converter operating frequencies. However, the electromagnetic interferences generated from these switching devices also become more important in a wide frequency band. Many solutions can be applied in order to reduce and limit these emissions by acting on: the EMI sources, on the victim or on the coupling paths. This last solution is commonly employed through the use of EMI filters. The latter will be the central topic of the present PhD work.

In order to build EMI filters that are reliable regarding the expected behavior at the design stage, and thus prevent multiple prototyping, it is necessary to develop accurate high frequency (HF) behavior models for each passive component of the filter: coupled inductor, self-inductor and capacitors. In that context, a key point in the EMI filter performance is related to the physical and geometrical properties of the magnetic core. Furthermore, the EMI filter, when inserted in the targeted device, lead to an insertion loss that depends on the input and output impedances. Usually, these impedances can be identified from the experiment and should to be taken into account right from the design step of the filter. All these aspects cover a large research spectrum from the study of magnetic materials, characterization and modeling process, conception of filters up to the determination of the insertion losses in real operating conditions.

In this PhD work, the main objective is to characterize and model the behavior of magnetic materials used in EMI filters. In particular, three aspects have been dealt in details: the first one is related to the characterization of the magnetic material with small signal (complex magnetic permeability), the second one deals with the characterization of the magnetic material with high signal (magnetic hysteresis) and finally, the last one is linked to the EMI filter design.

Organization of the dissertation

The organization of this dissertation is detailed as follows.

In chapter 1, the state of art is briefly described in order to provide the context necessary to understand the problematic of this research topic.

In chapter 2, the small-signal characterization of magnetic materials is widely discussed. This is realized in terms of the complex magnetic permeability (CMP) that represents the frequency evolution of the magnetic material. However, due to the limited information in datasheets, experimental characterizations are carried out in order to extend the identification of the CMP to higher frequencies. Thus, an experimental approach is developed to measure the CMP of different magnetic materials cores. This approach overcomes the sample size limitation of the commercial measurement equipment (only available for small size cores) and allows measuring the CMP of bigger size cores in a wide frequency band up to 100MHz. Furthermore, the CMP representation is intrinsically limited as it only takes account for the inductive and loss behaviors of the material. It is reflected by the negative value of the real part of the CMP in HF. This behavior is linked to a capacitive phenomenon that is introduced in this work through the notion of “material capacitance”. The corresponding measured CMP is then modeled by two approaches: the first one is based on a mathematical model using the rational functions and the second one is based on the utilization of an electrical equivalent circuit. These two models allow modeling the evolution of the CMP up to 100MHz.

Chapter 3 deals with the high-signal characterization of the magnetic material. The CMP measurement method developed in Chapter 2 is only meaningful when the magnetization level of the material is low. However, in operating conditions of the static converter, the EMI filter and the inductive components can be subject to higher current levels, changing the behavior of the material. In these conditions, the magnetic non-linearity of the material must be considered. The development and identification of the magnetic material model require experimental data. Moreover, as such measurements can be tricky in the MHz range; a method is proposed to characterize the magnetic hysteresis loop of the material. The approach is based on a single turn flat coil that allows avoiding and/or reducing the HF parasitic elements that exist in the two winding configuration. From these experimental data, two modeling approaches are identified for the HF behavior of the magnetic core: the average BH-curve and the magnetic hysteresis loop based on the Jiles-Atherton model. Both approaches are associated to the previously mentioned “material

capacitance” and compared with the experimental results. Additionally, an introduction to the study of the temperature influence on the CMP and the hysteresis loop is carried out with an automatic testing bench.

To illustrate and validate the developed experimental techniques and models, the design of an EMI filter associated to its power converter is detailed in Chapter 4. First, the impedance measurement of the power converter is described. To that purpose, the current injection method is considered and improved by the use of two proposed current probes. Their transfer impedances are identified from a specific characterization technique. Second, the insertion loss of the filter is obtained through simulations by using the magnetic material models, that were previously developed, and the measured input/output impedances. The attenuation results are then validated by comparisons with the experimental data. Moreover, insertion loss measurements based on scattering parameters are discussed when the input/output impedances are different from 50Ω .

Chapter 1. State of art

Nowadays, the power electronics becomes necessary in the electrical energy application domain. They are replacing more and more mechanic, hydraulic and pneumatic systems. The static converters play an important role for this electrification. However, the fast commutations of the modern semiconductor devices, is the main source of the electromagnetic interference conducted and radiated emissions. When these emissions are extended in the system, electric malfunctioning can occur. There are many solutions to reduce the conducted emissions among them the EMI filter. In this chapter the state of the art related to EMI filters and its components are presented. Basic concepts, methods and previous related works are referenced.

1.1 EMI in Power electronics

In power electronics, the application of fast power semiconductors devices in static converters improves the efficiency and electrical energy quality [1]. The miniaturizing trend of the power conversion systems leads to the increase of switching frequencies from kHz to MHz. This process of energy conversion generates high frequency (HF) electromagnetic noises, mainly brought about by the sharp edges of the voltage (dv/dt) and current (di/dt) during the power conversion process [2]. These EMI or disturbances can interrupt, obstruct or degrade the effective performances of electrical and electronic devices. Hence, the electromagnetic compatibility (EMC) standards are essential to protect the electronic devices [3]:

- a. Does not cause interference to other systems.
- b. Does not cause interference to itself.
- c. Is not susceptible to interference from other systems.

The EMC aspect, illustrated in Figure 1-1(a), consists of an emitter that generates the EMI; then it is transmitted to a *victim* (receiver) via a transmission coupling paths. This energy transfer can be divided into [4]:

- *Radiated emissions* which are undesired electromagnetic energy in the form of electric and magnetic fields that propagate through space.
- *Conducted emissions* which are an undesired electromagnetic energy that is propagated along the coupling paths.

The equivalence with a buck converter is shown in Figure 1-1(b), where the power lines are the principal coupling paths for conducted emissions.

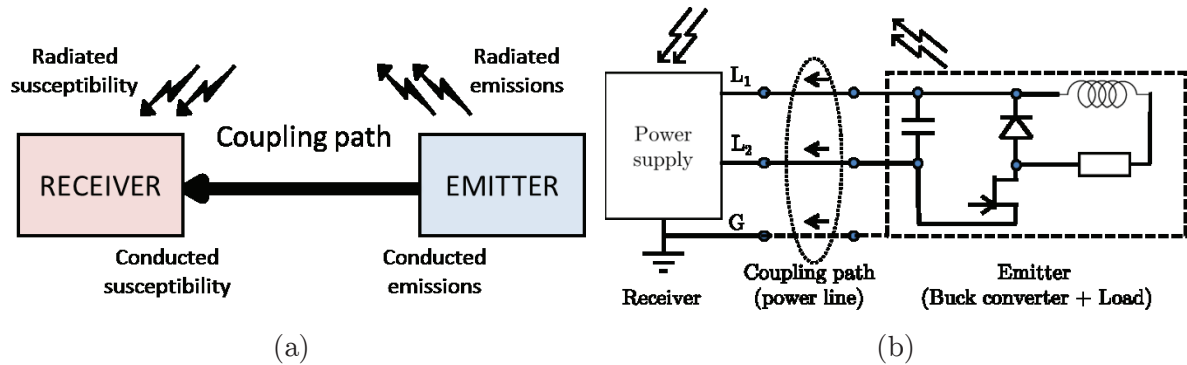


Figure 1-1 (a) General EMC elements and (b) EMI induced by the buck converter

1.1.1 Radiated emissions

The EMC standard defines the radiated emissions in the range of 30 MHz to 1GHz. The measurement of these emissions can be achieved in an open space or in anechoic chambers using antenna configurations. Many of these procedures are well established and standardized, as for example, in avionics [5], trains or automotive vehicles. These radiated emissions are out of the scope of this work.

1.1.2 Conducted emissions

The conducted emissions are composed from currents which spread from the electrical or electronic device through the power line (coupling paths) to another electrical device. There are two modes of conducted emissions: the common mode (CM) and differential mode (DM) as shown in Figure 1-2.

- The common mode current (I_{CM}) flows in the same direction in all wires and return by ground wire through capacitive coupling (symmetrical)
- The differential mode current (I_{DM}) flows between the supply wires (asymmetrical).

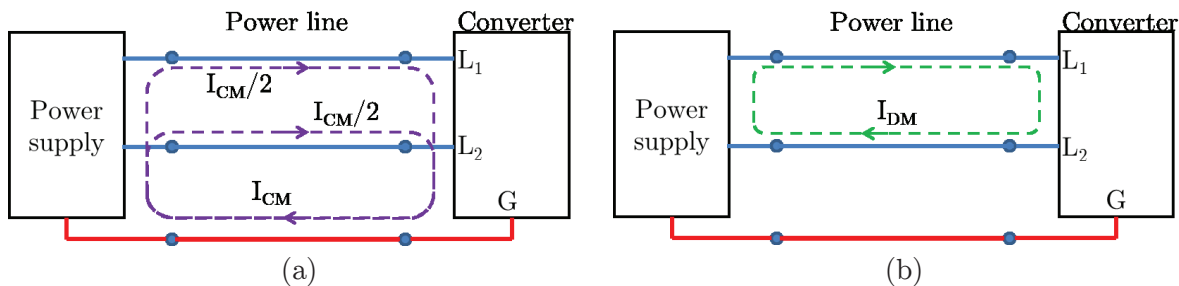


Figure 1-2 (a) CM noise current path and (b) DM noise current path

The measurement of conducted emission are carried out with an Artificial Main Network, or Line Impedance Stabilization Network (LISN), connected between the power supply (Input) and the equipment under test (EUT) (Output) as shown in Figure 1-3(a). This device prevents from external noise interferences and provides some *constant* impedance. The typical LISN output impedance (Z_{LISN}) is 50Ω by phase. As illustrated in Figure 1-3(b), the CM impedance ($Z_{LISN-CM}$) is half of the Z_{LISN} and the DM impedance ($Z_{LISN-DM}$) is the double of Z_{LISN} .

In the Figure 1-4, three currents are defined: I_{L1} , I_{L2} and I_G . These are composed of the I_{CM} and I_{DM} currents. The drop voltages over the LISN output impedances, V_{L1} and V_{L2} , induced by I_{L1} and I_{L2} currents, are then used to measure the corresponding noises. There are two techniques to perform the conducted emissions measurements:

- Applying a software noise-separation technique [6].
- Using a hardware noise-separator [7]

The conducted emissions generated by the EUT have to be evaluated using EMC standards setup depending on its final application. The EMC standards have been introduced and continuously reinforced to define the maximum limits of conducted emissions, the levels of immunity and the methods and tools for verifying the immunity and emissions levels. The *Comité International Spécial des Perturbations Radioélectriques* (CISPR) have published the CISPR-11 standard for Information Technology Equipment, radio disturbance characteristics and limits [8], which is adopted in this work.

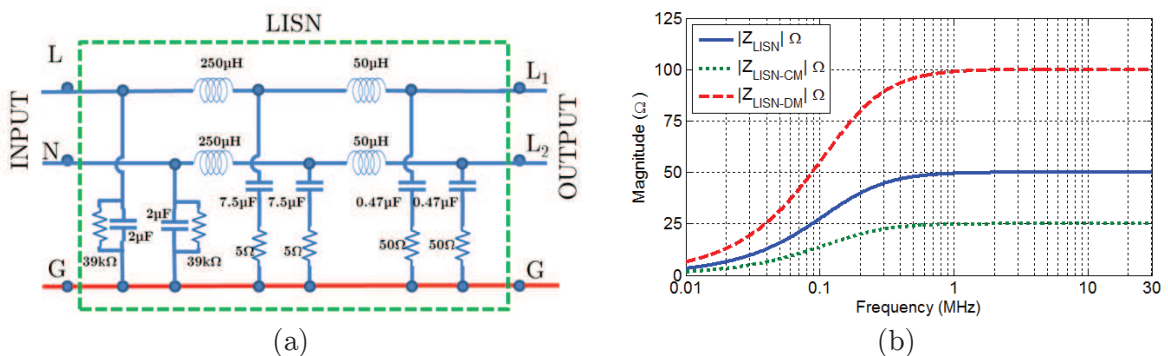


Figure 1-3 (a) Equivalent circuit of LISN (b) Typical impedance of the LISN to EUT side

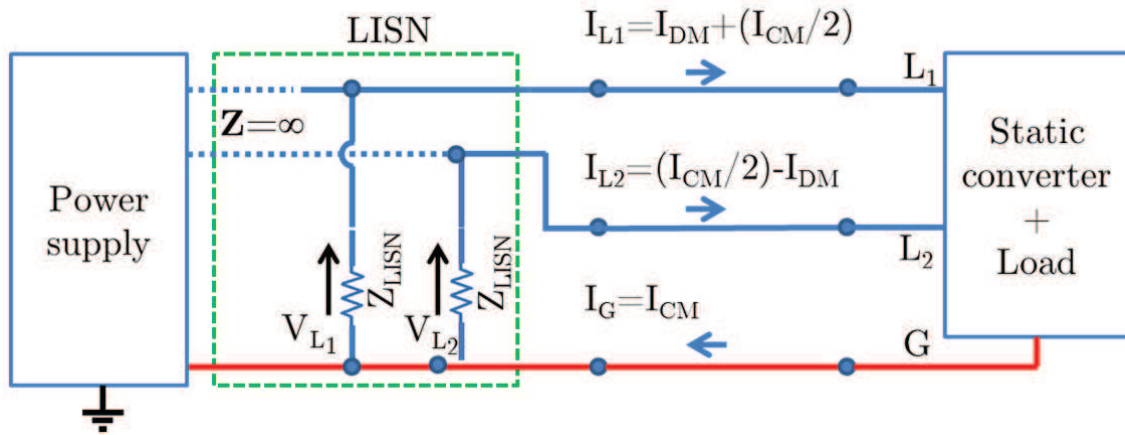


Figure 1-4 Currents in power line: I_{L1} , I_{L2} and I_G . Voltage drop in the LISN: V_{L1} and V_{L2}

The frequency range of the conducted emissions given in the EMC standard varies from 150 kHz to 30 MHz. The Class A is applied for industrial or commercial equipment, while Class B is for residential use. The EMC standard defines two types of detectors: the quasi-peak (QP) and the average (AVG) detectors, as shown in Figure 1-5. The QP detector weighs the signals according to their repetition rate and the AVG detector averages the HF components takes from the peak signal that passes through a filter whose bandwidth is much less than the resolution bandwidth.

In most of the cases, the level of the conducted noise exceeds the limit established by the EMC standards. Then, some solutions to reduce the EMI in power converters are often applied, as described in the following section.

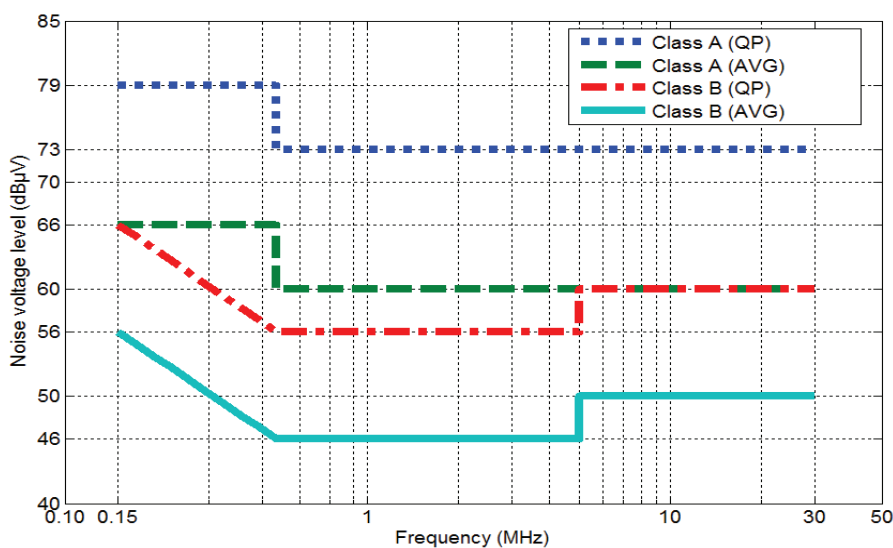


Figure 1-5 Conducted emissions limits defined by C.I.S.P.R. 11 standard

1.2 Techniques to mitigate the EMI

When the equipment under test does not meet the EMC standards, the EMI have to be mitigated. Different techniques can be applied by acting on the emitter (the source of EMI) or on the coupling paths. These different methods are listed in Figure 1-6.

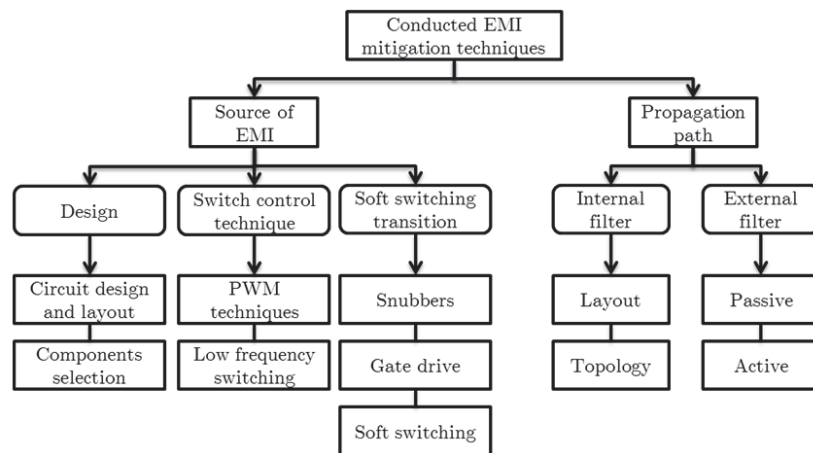


Figure 1-6 Different techniques for mitigate EMI in power energy conversion [9]

1.2.1 At the source

To reduce the EMI at the source, various techniques are used. The soft switching techniques have been applied to accomplish significant reduction in conducted EMI in HF [10]. The switch control technique linked to the switching frequency was reported in [11], where the “spread-spectrum technique” is applied. Another technique is based on the selection of the layout and circuit design. The position of static converter components and the strategy of ground line connection can also be intended to reduce the EMI of the whole system [12]. The balancing technique, which looks for equivalent impedances in the phase lines of the converter, reports an achievement in EMI reduction [13]. Even if these techniques are applied, often the EMC is not fully guaranteed. As a consequence, techniques linked on the coupling path (power line) need to be considered.

1.2.2 At the coupling paths

The conducted emissions pass through the coupling paths to reach other components of the system. Spreading paths between the source and the victim can be

modified by EMI filters. The EMI filter over the power line still provides a typical (and sometimes the unique) solution to meet with the EMC standards even if a mitigation technique at the source has been early implemented. Three different types of filters can be distinguished:

- Passive filters, with only passive elements like inductors, capacitors and resistors
- Active filters with active elements such as operational amplifiers
- Hybrid filters, with a combination of both of the previous techniques.

The active filter usually reduces the volume of the filter. However, their weakness is mainly due to their low range frequency applications [14]. These filters can present better performances in HF when they are combined with some passive ones [15]. Nevertheless, in many HF power applications, the passive EMI filters are the unique solution.

1.3 Passive EMI filters

1.3.1 Overview

As introduced in Figure 1-4, the noise currents pass through the LISN output impedance, which generates a voltage drop (V_{L1} and V_{L2}). The latter are measured by EMI receiver apparatus to determine the noise level of the EUT when EMC standard is verified. When this condition is not met, a passive EMI filter has to be placed at the input of the static converter.

Many topologies of passive filter are presented and discussed in [16]. The main criteria to choose a filter's topology are the attenuation required and the input/output impedances connected to the filter. Four basic schemas are proposed in [17], where only capacitor-inductor elements are used. The different topologies as LC, CL, CLC or LCL, are selected according to the static converter impedance and power network impedance. In the case where the input/output impedances are unknown, the configuration $50\Omega/50\Omega$ can be applied.

A topology known as *one-stage* filter is illustrated in Figure 1-7. The main objective of this filter is to reduce the currents which flow through the LISN output impedance. In this way, the current paths for the conducted emissions are modified in the frequency range established by the EMC standard.

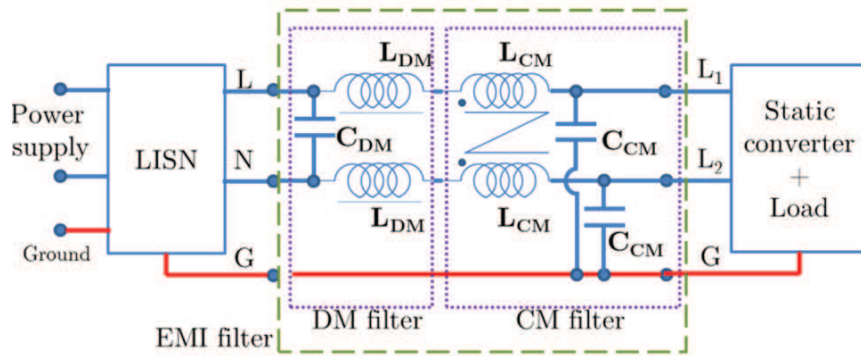


Figure 1-7 Classical EMI power line filter topology

Two inductor-capacitor (LC) low pass filters can be differentiated. The first pair conforms to the DM inductor L_{DM} and the DM capacitor C_{DM} , while the second one corresponds to the CM inductor L_{CM} and the CM capacitor C_{CM} . The coupled inductor L_{CM} , known as *choke inductor*, captures the magnetic flux created by the CM current while rejecting the flux generated by the DM current. Sometimes, the leakage flux of the choke inductor can be employed as L_{DM} . The symmetry of the EMI filter topology allows the division of the filter into CM and DM filters [18]. However, the *mixed-mode* noise that has been reported in [19] implies the asymmetry of the filter, which is a product of the relationship between CM and DM mode. This mixed-mode noise is out of scope in the present work and only general equivalent circuit, like Thevenin source-circuit, is employed supposing the CM and DM filters as independent and symmetric components.

It is well known that the static converters are the EMI source in the energy conversion system. However the noise source is represented by the Thevenin source-circuit (V_s and Z_s), as shown in Figure 1-8. Different techniques were developed to measure, calculate and model these two circuit elements. In [20] a measurement technique, in off-state of the converter, is proposed to determine Z_s and V_s . With this approach the noise spectrum can be reproduced up to 10MHz. Another technique, described in [21], discusses the possibility of representing the noise spectrum up to 100MHz based on a three-terminal model. This model is composed of two current sources and three impedances, when the converter is assumed linear and time invariant.

On the other hand, predicting technique such as [22], based on time-domain function convolution, presents good results up to 50MHz. The objective of these methods is to correctly simulate the complete power conversion system with the aid of some circuit simulator software like Pspice® or Saber®.

By using these methods, the noises induced by the power converter can be simulated and as a consequence, the drop voltages at LISN output impedance with

(V_{Lwo}) and without EMI filter (V_{Lw}). The rapport of these drop voltages are known as EMI filter's *insertion loss*.

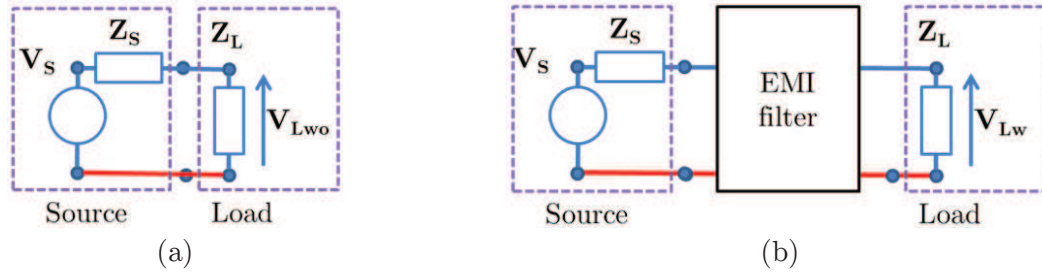


Figure 1-8 Thevenin Equivalent Circuit (a) without and (b) with EMI filter

1.3.2 Insertion loss

The term insertion loss (IL) of the filter designates the loss power of the noise signal when the filter is introduced. The expression (1) is the ratio between the noise spectrum voltages (V_{Lwo}) in the load impedance (Z_L) before introducing the filter (Figure 1-8(a)); divided by the noise spectrum voltage (V_{Lw}) across the load impedance after the filter has been introduced (Figure 1-8(b)).

$$IL_{dB} = -20 \log \left| \frac{V_{Lwo}}{V_{Lw}} \right| \quad (1)$$

The IL can be directly measured by specific apparatus such as spectrum analyzer (SA), vector network analyzer (VNA) or EMI test receiver (ETR). All of these instruments have the 50Ω internal impedance, that means (Figure 1-8) $Z_S = Z_L = 50\Omega$. Other tests, recommended in [23] for example, use *baluns* to evaluate the performances of the filter for 0.1Ω - 100Ω and 100Ω - 0.1Ω configurations. Another procedure, proposed in [23] which is based on the current injection method to measure the attenuation over the frequency range 100 kHz-30 MHz under known or 50Ω impedance.

It should be noted that, the IL do not only depend on the input and output impedances connected to the EMI filter, but also on the parasitic elements of the filter's passive components (Figure 1-9(a)). Traditionally, these parasitic elements are noted as following:

- ESL = Capacitor's equivalent series inductance
- ESR = Capacitor's equivalent series resistance
- EPC = Inductor's equivalent parallel capacitance
- EPR = Inductor's equivalent parallel resistance

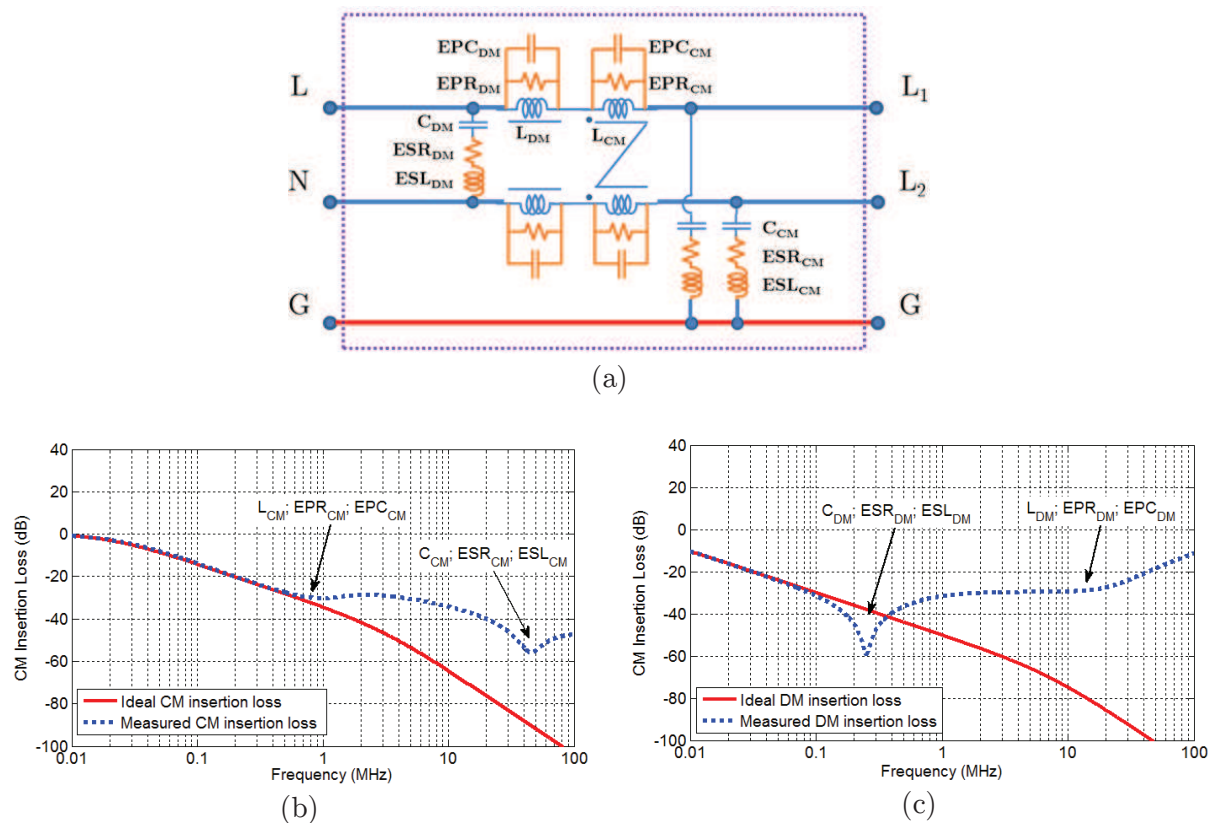


Figure 1-9 (a) EMI filter with its parasitic elements. (b) CM insertion loss considering parasitic elements (c) DM insertion loss considering parasitic elements

These parameters impact strongly the HF response of the filter and deteriorate its performance. In the example of Figure 1-9(b), the CM insertion loss is affected, above few kHz, by these parasitic elements (ESR_{CM} , ESL_{CM} , EPC_{CM} and EPR_{CM}). The same effect is observed for the DM insertion loss in Figure 1-9(c), where the parasitic elements (ESR_{DM} , ESL_{DM} , EPC_{DM} and EPR_{DM}) modify the response of the filter. In order to evaluate the impact due to capacitors and inductors parasitic elements, characterization and modeling processes become essential and constitute one of the subjects of this work.

1.3.3 Parasitic elements of EMI filter

As previously observed in Figure 1-9, the LC components in the EMI filter are composed of parasitic elements that have a large impact in effectiveness of the filter.

Capacitor

In frequency domain, the capacitor's impedance (Z_C) can be described using expression (2), accounting for the ESR and the ESL of the component. These two elements conventionally model the parasitic effects inside the capacitor.

$$Z_c = ESR + j\omega ESL + \frac{1}{j\omega C} \quad (2)$$

The capacitance C in equation (2) is already standardized for EMI applications because of safety conditions, such as EN 60384-14. These capacitors are divided into X (line-to-line connection) and Y (line-to-ground) type capacitors for DM and CM filters respectively. The values of the X capacitors are limited by the level of the peak voltage. The limitation of the Y capacitor value is determined by the maximum current value. Moreover, the capacitors are also nonlinear elements. For example, the value of the capacitance is temperature-dependent and can reach 50% of variation at 200°C as reported in [24]. However, this aspect and other physical variations such as non-linear dielectric behavior are out of the scope of the present work.

New technologies and better design process are developed to increase the bandwidth application of EMI capacitors, e.g. shifting the resonance frequencies to higher frequencies by reducing the ESR and the ESL. The feed-through capacitors are a good example but still are limited by their maximum voltage values [25]. Another technique, developed in [26], compensates the resonance of the EMI filter at HF by ESL parasitic cancellation with additional components. Another cancellation is introduced in [27], where extra wires are strategically added to compensate the magnetic field created by capacitors. Finally, near-field and position in PCB are studied in order to avoid coupling effects and to reduce the ESL value [28]. All of these techniques help in the amelioration of HF capacitor behavior, and in consequence, the IL of the EMI filters. In our case, the capacitor is going to be represented with RLC series circuit.

Inductor

The inductor is one of the most challenging components, notably when it is involved in the EMI filter design. Numerous technologies and types of inductors force designers to use databases in order to well select/design the appropriate component and sometimes they do not exist in the market and must be fabricated [29].

There are two mains aspects that enter in this inductor's design: the winding and the core. Regarding the winding technique, planar inductors are becoming a trending issue in the field of power electronics [30]. The advantages of this technology are: the small size, low fabrication costs, repeatability and high power density. On the other hand, wound inductors are still widely employed for high power

transformers and choke inductors. The advantages of this type of component are linked to the ease of prototyping and the high effective inductance value. Indeed, the inductance value (L), given by (3), is directly related to the number of turns (N) squared. The inductance factor (A_L) is usually a constant number found in datasheets for low frequency range.

$$L = A_L N^2 \quad (3)$$

The commercial core of inductors can have different shapes and geometries [31] (RM, PM, EP, P, E, ELP, EQ, ETD, UI, Toroid) due to the diversity of applications in power electronic, as shown in Figure 1-10. In addition, a hybrid core was also designed using EQ and toroid core looking for better performances in HF [29]. In the present work, only the toroidal cores or ring cores will be studied.

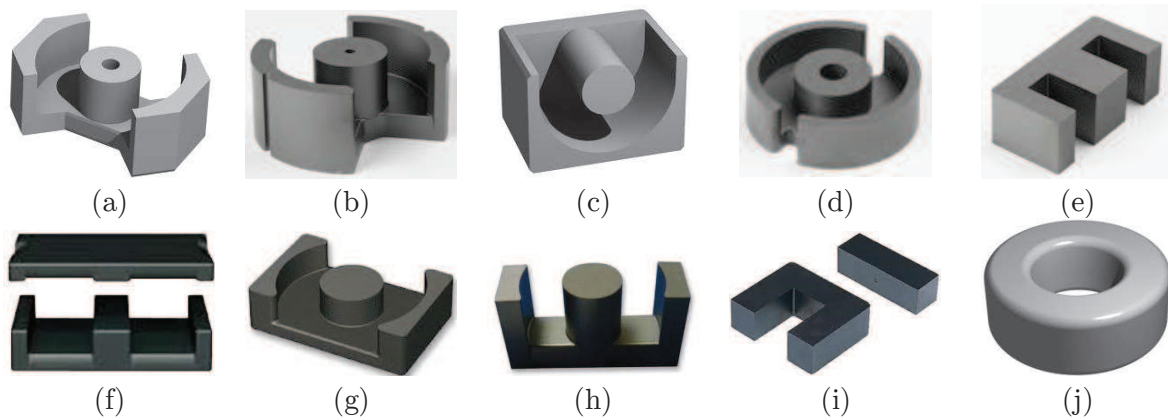


Figure 1-10 Magnetic cores shapes (a) RM (b) PM (c) EP (d) P (e) E (f) ELP (g) EQ (h) ETD (i) UI (j) Toroid or Ring

1.4 Ring core inductors

1.4.1 Overview

The ring core shown in Figure 1-10(j) is one of the simplest structures for designing inductors. They are also really useful in order to characterize the magnetic material properties due to the continuity in the magnetic circuit (core without gaps).

For EMI filter application, these ring core inductors can be divided into a single inductor and coupled inductor. The single inductor (one winding) is often applied in DM EMI filters. More windings can be added, following the same winding

direction as shown in Figure 1-11(a). Ideally, this configuration catches the magnetic flux, created by DM current, inside the core while the CM magnetic flux is cancelled. In the case of CM magnetic flux, the configuration of Figure 1-11(b) is used. The ring core catches the CM magnetic flux while cancelling the DM flux. However, this is not the case when the application bandwidth reaches the HF range where the parasitic elements appear and the leakage flux (in DM and CM) is not zero. Indeed, it seems evident that the inductor is not independent of the winding (i.e. direction) nor the magnetic material. There are parasitic elements that describe the HF inductor response.

Different methods to model the ring core inductor have been proposed in the literature. Theoretical and experimental methods were used to characterize and model the ring core inductor. Some of these methods are briefly reviewed in the next paragraphs.

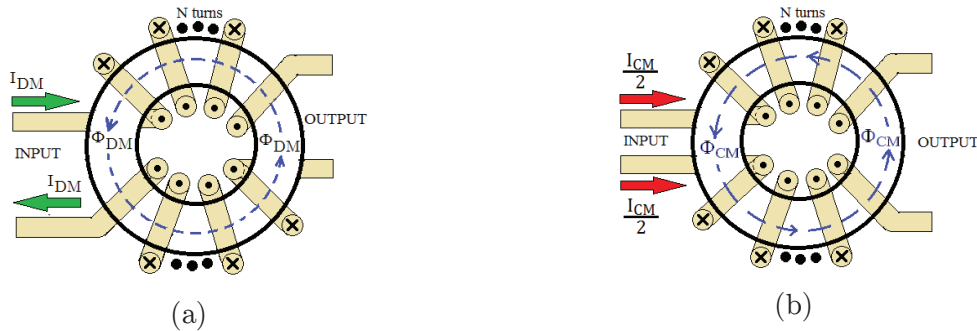


Figure 1-11 (a) Differential mode inductance (b) Common mode inductance

1.4.2 Theoretical modeling methods

Numerical model

The theoretical method based on Maxwell equations can be resolved applying Finite Element Analysis (FEA). The ring core inductor is a device where multi-physic simulations have to be performed. Electromagnetic, radio frequency (RF) and thermal domains are some of the basic fields that can be involved with this method. The finite elements have the advantage of precision for complex systems. However, the penalty is the simulation time and also the consumed memory resource that become one of the main drawbacks of this method. In [32], FEA is applied to understand the saturation of the magnetic material due to the DM current in a CM filter. In this approach, the ring core inductor is approximated using two solid blocks for windings, the distance between the core and the winding was neglected. Moreover, only magnetostatic investigations were discussed.

On the other hand, the Partial Element Equivalent Circuit (PEEC) method is becoming effective to model the toroid inductor. This method is based on low frequency formula to extract the electrical parameters (resistance, self and mutual inductance) from geometries [33]. However, the nonlinear behavior of the core magnetic material, the permeability and permittivity becomes one of the limitations for its representation. In [34], the toroid inductor 3D modeling is discussed. The Partial Element Equivalent Circuit and the Boundary Integral method (PEEC-BIM) enable modeling of magnetic core by magnetic current loops in the simulation. The results show that the insertion loss of the filter made with toroid inductor is valid up to 10MHz.

The third analytical method can be attributed to the hysteretic models. The magnetic material of the core is modeled using mathematical representations and then it is included for the inductor calculation. This issue will be treated in the present work.

1.4.3 Experimental modeling methods

Some models based on experimental data are summarized in Figure 1-12. In [35] a fitting process is applied on the measured impedances using rational function approximation (RFA). The magnetic material is then represented by a lumped circuit where a negative component can be obtained. Another experimental approach is presented in [36], where the impedances measured with a two-port network are represented by mutual and crossed impedances. The obtained model is applied to design the EMI filter by simulations. The automatic identification of the equivalent circuit of the inductor is reported in [37], where the measured impedance is approached using parallel-RLC circuits. This model can have a large number of parallel-RLC circuits to obtain better accuracy. A similar approach, using concatenated RLC circuits, is developed in [38], where the number of turns increases the number of elements to be simulated. These models reported a good representation of the inductor's impedance up to 100MHz. However, none of the previous works have defined the magnetic material in the impedance model. Consequently, if the material of the inductor is changed, these models have to be adjusted from new experimental data. In the following section, the winding and the material core influence on the ring core inductor will be described.

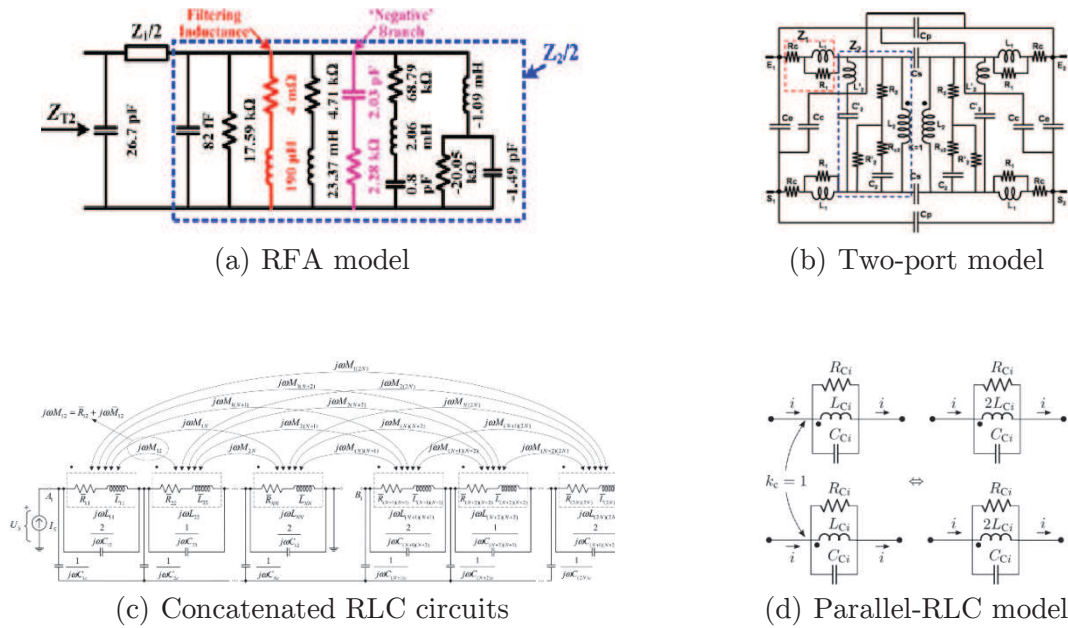


Figure 1-12 Models of inductor

1.4.4 Winding

The winding has a critical role in the design of the ring core inductors. Four aspects are described here: the winding strategy, the winding resistance, the parasitic capacitance and the leakage inductance.

Winding strategies

The objectives of the winding strategy are:

- the good magnetization of the material
- the reduction of the leakage flux/inductance
- the limitation of the parasitic capacitance
- the reduction of the joules loss
- the decrease of external coupling effects
- the smart-use of the available space

Of course, it is not possible to obtain all the benefits at the same time. The optimal strategy/criteria will be fixed depending on the inductor's application.

In [39], different winding arrangements are studied in the case of a toroidal current sensor. A single winding is wound around the toroid core, as shown in Figure 1-13(a). The magnetic loop created by the core and the winding is reduced applying the half winding return path in order to reduce the leakage inductance. Indeed, the effective surface of the leakage (represented by the surface created by the wire) is reduced. However, with this method, the stray capacitance increases greatly because of the proximity of the wires.

Another winding arrangement was studied in [40] to quantify its influence in the case of material characterization as illustrated in Figure 1-13(b). The winding's turns are homogeneous spaced in order to well magnetize the material, reducing the stray capacitance but increasing the leakage inductance.

In [41], the distribution of the winding around the ring core was studied. The leakage inductance and the resistance are compared for three investigated structures (Figure 1-13(c)). In addition, the number of layers was also addressed. The inductance value is well augmented with the number of turns. However, the number of layers increases the parasitic capacitance of the windings. This phenomenon limits the application bandwidth in HF due to the resonance frequency that has been shifted to lower frequencies.

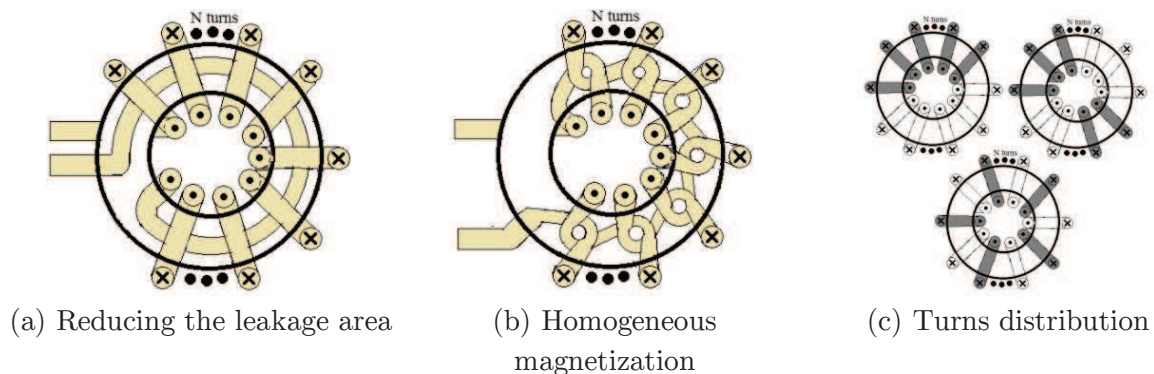


Figure 1-13 Winding strategies in ring cores

The EMI filter application needs good performances of the passive component in the frequency range from 150 kHz to 30MHz, as previously stated. Then, the HF parasitic elements have to be taken into account. It can be seen that the winding strategy directly affects the parasitic elements of the inductor. In the aim to reduce the impact of these parasitic elements, the single layer winding will always be preferred. If the inductance value, given by (3), requires more turns, then the size of the ring core is increased. When two or more windings are applied, the single layer is still preferred with side-to-side winding technique (not interlaced).

Winding Resistance

The winding resistance is a subject that has been largely studied [42, 43] and will be briefly described here. The skin effect in the wire (4) increases the effective resistance when frequency increases. Different solutions have been developed to reduce its effects, such as Litz wires [42], where the number of strengths are optimized, or the flat copper wire [43]. In both cases, the surface of the conductor is reduced in order to mitigate the impact of the skin effect.

$$\delta = \frac{1}{\sqrt{f\pi\mu\sigma}} \quad (4)$$

When numerous wires are wound, the proximity effect becomes predominant. This phenomena has been studied in [44] in the case of some toroidal air-core inductor applications. Skin and proximity effects significantly reduce the effective cross section of the wire, which leads to the increase of the equivalent resistance value.

In EMI filter applications, wire resistance has an important impact in the design procedure. High value of resistance means high joules loss in the filter, which implies increasing the consuming power and reducing the efficiency of the converter [45]. This is inconvenient for self-inductors where the joules losses are critical. However, this can be used in the CM inductors, where the increase of resistance in HF considerably decreased the noise level.

Parasitic capacitance

The parasitic capacitance of the windings limits the magnetic behavior of the inductor in HF (Figure 1-9(b)). It is partially related to the inter-winding capacitances and the winding-core capacitance which are highly associated to the winding strategy. The inter-winding capacitances can be extracted by empirical formula [46], analytical approach [47], measurement method [48] or numerical calculation [49].

Because the parasitic capacitance degrades the HF behavior of the inductor, many techniques can be applied to reduce its value. For example, the stray capacitance can be compensated [50] or reduced adding extra elements [27]. The optimization of the winding topology, like extending the distance between turns [40], can also reduce its value. Due to HF application of the EMI filter, the parasitic capacitances are always a barrier/limit for the inductive component behavior and the

efficiency of the EMI filters in HF. The control of this parameter is a guarantee of performance of the filter, and, consequently, the inductor performance.

Leakage inductance

The leakage inductance is produced by the magnetic flux coupled in the air *instead of* inside the magnetic core. It can be extracted by empirical formula [51], analytical calculation [38], measurement method [36] or numerical computation [32]. The leakage inductance value also varies with the winding strategy, and depends on the inductor final application, where lower or higher values can be expected.

In EMI filters, low leakage inductance in DM inductors will reduce the coupling effect of the inductive components of a near system, and hence the HF behavior would be ameliorated. However, high values leakage inductance of choke inductor (CM inductor) are well appreciated because it can be used as a DM filter inductor. Thus, if high value is attempted, lowering of the DM inductor and DM capacitor are needed. Nevertheless, the coupling effects are still present.

1.4.5 Magnetic Core

The second element of the inductor is the magnetic core. The requirements of the magnetic core used in HF inductors are:

- High saturation magnetization = constant characteristics with current level.
- High resistivity = low core losses.
- High Curie temperature = unchanged characteristics with temperature.
- High ferromagnetic resonance = constant characteristics with frequency.
- High mechanical robustness = constant characteristics with mechanical forces.

However, the air-core could be the only *material* that can satisfy all these requirements. This is the principal reason why, in the RF domain, the air-core inductors are still preferred [43]. Unfortunately, the inductive value of these components only reaches some micro-henries in the frequency bandwidth of the conducted EMI. Moreover, the wire losses become one of the major limitation criteria.

Nowadays, a large variety of magnetic material, regarding the final application

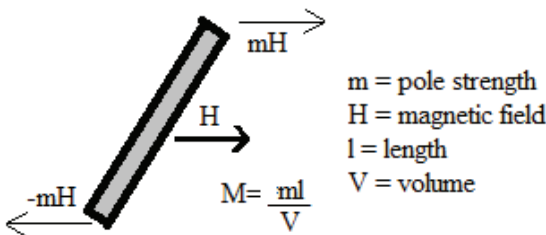
of the inductors, has been proposed to overcome these drawbacks. Nevertheless, new constraints appear about material characteristics regarding the requirements previously listed. In the next section, some of these characteristics will be described.

1.5 Characteristics of magnetic material

Magnetic materials have been developed to ameliorate characteristics of the inductors depending upon their final application. A first classification can be made following the ratio between the volumetric magnetization M ($A\cdot m^2/m^3$) and the applied magnetic field H (A/m), as shown in Figure 1-14. Their ratio (5), is known as volumetric susceptibility χ_v , and can be used to classify the magnetic materials into:

- paramagnetic-antiferromagnetic ($\chi > 1$)
- diamagnetic ($\chi < 1$)
- ferromagnetic-ferrimagnetic ($\chi \gg 1$) materials.

Antiferromagnetic (paramagnetic in high temperatures) and ferrimagnetic (uncompensated antiferromagnetic) materials are both based on oxides. Although the antiferromagnetic do not have much commercial interest, that helps to explain the ferrimagnetic materials widely used in power electronic applications [52].

$$\chi_v = \frac{M}{H} \quad (5)$$


m = pole strength
 H = magnetic field
 l = length
 V = volume

Figure 1-14 Magnetic dipole and the magnetization process

The ferromagnetic and ferrimagnetic materials have been developed to overcome the drawback of air-core inductors in low/medium/high frequencies applications [53]. A typical classification could be made regarding the “ease” of magnetization in the material. *Hard* materials, known as permanent magnets, have the main characteristic to store magnetostatic energy due to the high coercive force (H_c) and high residual induction (B_r). It means that the material requires a more

intense magnetic field to be demagnetized. In contrast, the *soft* material has the characteristic of high inductance values with low losses, which can be interpreted as low coercive force and low residual induction. Therefore, they are better candidates for inductors in power electronic applications, such as EMI filters [54]. Figure 1-15 summarizes graphically some of these materials regarding their relative initial permeability and saturation magnetization characteristics. More particularly, the characteristics of four soft material examples are listed in Table 1-1.

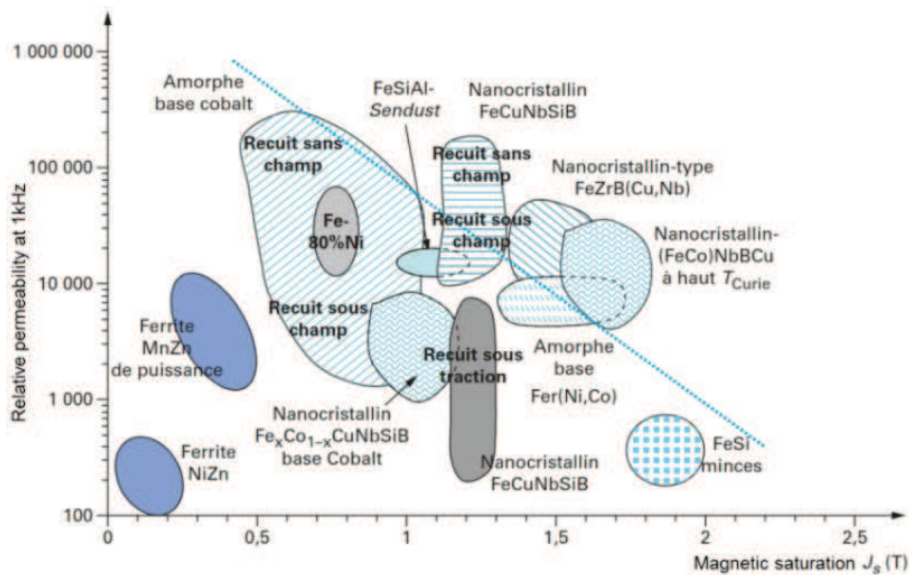


Figure 1-15 Soft magnetic materials used in power electronics [54]

Table 1-1 Different magnetic material

Materials	Ferrites MnZn	Ferrite NiZn	Nanocrystalline	Iron powder
Model	EPCOS: N30	FAIR-RITE: 61	MITTAL: Nanophy	CURIE:75-TAF200
Relative initial permeability	4300 (at 10kHz)	125 (at 10 kHz)	90000 (at 10kHz)	75 (at 10kHz)
Maximum magnetic flux saturation	380mT	235mT	1.2T	1.3T
Resistivity	0.5 Ωm	$1 \times 10^6 \Omega\text{m}$	$0.6 \times 10^{-6} \Omega\text{m}$	$1.2 \times 10^{-6} \Omega\text{m}$
Density	4900 kg/m ³	-----	735 kg/m ³	-----
Curie temperature	>130°C	>300°C	600°C	500°C
Frequency range	< 1MHz	< 250MHz	<1MHz	<250MHz
Applications	Broadband transformers	EMI suppression of noise	Common mode chokes. Filters	PFC chokes. Filter inductors

These soft materials can be divided into high (MnZn and Nanocrystalline) and low (NiZn and iron powder) magnetic permeability materials. These two types of ferrites, the MnZn and NiZn, are classical ones used at medium and high frequency for power electronic applications. However, the nanocrystalline and iron powder are becoming more suitable due to higher levels of saturation. Nevertheless, because of costs, shapes and wide type of applications, the ferrites are still used.

Two parameters are well taken into account for their classification: *permeability* and the *magnetic saturation*. However, there are other parameters that define some particular characteristics such as *electric conductivity* and *dielectric permittivity*. Thus, considering that the principal application of these materials is EMI filter inductors, magnetic permeability and magnetization are going to be studied.

1.5.1 Magnetic permeability

The permeability (μ) is the relationship between the flux density (B) and the magnetic field strength (H) of a magnetized material. This permeability can be described with free space permeability ($\mu_0 = 4\pi \times 10^{-7} A/m$) and relative permeability (μ_r), as given in (6). The relative permeability has a relationship (7) with the susceptibility previously described (5). However, the expression (6) is more often used in physical analysis.

$$B = \mu H = \mu_0 \mu_r H \quad (6)$$

$$\mu_r = \chi_v + 1 \quad (7)$$

The relative permeability μ_r is a common parameter in the material datasheets. However, it is given as a constant value in low frequency or as a curve evolution with frequency (relative initial permeability). This parameter is very practical because it presents in direct relation two parameters (B and H) but the provided information of the material does not represent the behavior of the permeability. The permeability is a nonlinear parameter because it depends on the operating condition. For example, in Table 1-1, the values provided for the permeability represent only one operating point of work where the magnetic field is small, while the temperature and the frequency are kept as constants. Some information regarding temperature can show the material's evolution up to the Curie

temperature, after the materials become paramagnetic [55].

In HF applications, the complex magnetic permeability (CMP) is preferred. The expression (8) is the CMP series representation of the magnetic energy (μ' = real part) and the loss (μ'' = imaginary part). Both of them, usually found in datasheets, are frequency-dependent parameters, as illustrated in Figure 1-16 for ferrite material Epcos®-N30 and nanocrystalline Metglas® FT-1KM.

$$\bar{\mu} = \mu' - j\mu'' \quad (8)$$

The permeabilities μ' and μ'' for the N30 ferrite material (Figure 1-16(a)) are shown up to 4MHz, above this frequency no information is provided. On the other hand, the permeability curves for the nanocrystalline material are given up to 10MHz. In the case of EMI filter application in the frequency range from 150 kHz to 30MHz, the behavior of these materials will be unknown in HF. To overcome this, the CMP parameter can be measured by different methods as summarized in Table 1-2. This CMP parameter will be better detailed in chapter 2.

As previously stated, the CMP represents the behavior of the material in wide frequency range. However, the representation of the material for different operating points and the nonlinear behavior cannot be taken into account with the expression (8). The approach based on the magnetic hysteresis loop, briefly described in the next section and detailed in chapter 3, is preferred. Hereinafter, the term *small-signal representation* will be linked to the CMP representation, and the term *high-signal representation* to magnetic hysteresis loop representation.

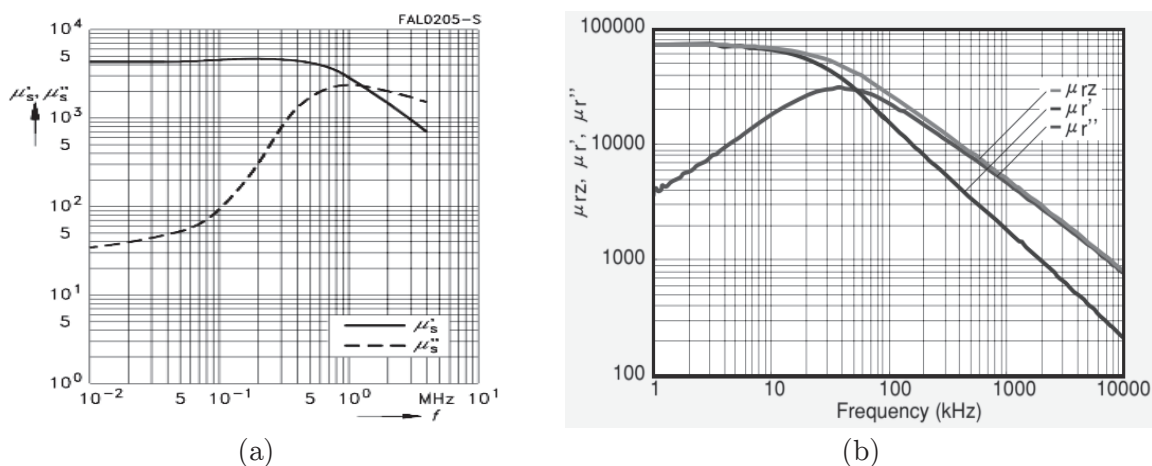


Figure 1-16 CMP of (a) Ferrite EPCOS®-N30 and (b) Nanocrystalline Metglas® FT-1KM

Table 1-2 Permeability measurement methods

Method	Advantages	Disadvantages
Transmission Line Permeability measurement using Network analyzer: uses a sample of the material into the closed transmission line space [56]	Broadband analysis. Rectangular and ring core material.	Homogeneous flat material. Fill out cross section. Software conversion S-parameters to permeability and permittivity.
Free space Microwave energy passes through the material [57]	Non-contacting, non-destructive Useful in HF	Large, flat, parallel-faced samples Calibration of network analysis
Resonant cavity A piece of sample material affects the center frequency and quality factor of the cavity [58]	High impedance environment Measurement at any frequency	Small piece of material Larger samples Measurement at only one frequency
Magnetic material test fixture Closed metal container with a FMM ring core, emulating one turn coil [59]	Direct measurement Avoid leakage inductance	Specific ring core size Limited in frequency

1.5.2 Hysteresis loop

In the macroscopic description of the ferrimagnetic materials, the magnetization mechanism follows the crystallographic direction in which the magnetization is easiest (“ease” direction) when an external magnetic field is applied, and stays null when no field is present. The magnetic materials create small magnetic domains (regions with the same direction of magnetization), which can be very complex to study because of grain boundaries, impurities, and others. These domain walls separate the small magnetic domains which have opposite directions of magnetization. The magnetic polarization, intrinsic flux density or intensity of magnetization J , presented in (9), contain the influence of these effects in the magnetization process M .

$$B(H) = \mu_0(H + M(H)) = \mu_0H + J(H) \quad (9)$$

The depicted magnetization curve in Figure 1-17, using the expression (9), can be usually found in the material datasheets. The ferromagnetic and ferrimagnetic materials hysteresis loop can be illustrated using $B(H)$ or $J(H)$. Because the magnetic permeability in these materials has high values, both curves are basically superposed. Here, the $B(H)$ function is adopted. The principal points, shown in Figure 1-17, are:

- The saturation flux density B_s : The maximum magnetic flux density, where the material behaves like an air core.
- The remanence or remanent magnetization flux density B_r : It is the magnetic energy stored in the core when no magnetic field is present.
- The coercivity H_c : It represents the magnetic energy that can be stored in the core. (Usually low in soft materials and high in hard materials)
- The primary magnetization curve: It is the first curve that represents the magnetization process when the material hasn't been magnetized before.
- The BH surface: It represents the total magnetic energy per period that the core dissipates.

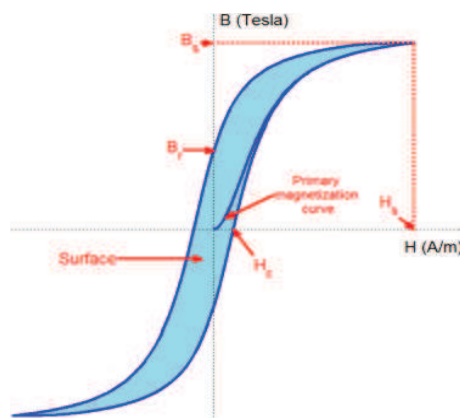


Figure 1-17 General hysteresis loop of ferrimagnetic material

A hysteresis loop is a typical phenomenon in the magnetic material domain. Measurement techniques and the modeling methods have been widely treated in literature. In [60], different measurement techniques using ring cores has been described. The transformer configuration (two windings) is a classic approach to measure the hysteresis loop; it is known as the volt-amperometric method. Also, there are configurations that apply pulses or sinusoidal signals to obtain minor hysteresis loops.

The hysteresis loop depends on current level, frequency, temperature and mechanical factors [53]. The hysteresis with sinusoidal, direct and arbitrary current waveforms has been discussed in different papers [61, 62], as well as the influence of the frequency and temperature [63].

The hysteresis loop is modeled using static or dynamic models. Different approaches are found in literature to reproduce the hysteresis loop using mathematical expressions and functions. Two of the most extended models that

represent the hysteresis loop are the Preisach model [64] and Jiles-Atherton [65] model.

The Preisach model is a behavioral one, that describes the hysteresis loop based on magnetic relays called *hysterons* [64]. These relays have a bi-stable (positive/negative) response in presence of any external magnetization field and the Preisach triangle permits representation of its state. However, this model is disconnected to physical meanings of the hysteresis. In our approach, the Jiles-Atherton model [65] will be preferred. It is based on the *Bloch* wall movement that supposes the friction strength in the material during the magnetization process.

1.6 Conclusion

In this chapter, the general notions of the electromagnetic interferences for power converters were described. The conducted emissions generated by static converters can be mitigated using passive EMI filters to meet the EMC standard. It was stated that the insertion loss depends on the input and output impedance connected to the EMI filter, as well as the HF parasitic elements of its components. The EMI filter is composed of the capacitors that have values already standardized, and the inductors which become cumbersome to design due to the multiple parameters and constraints that need to be taken into account.

The magnetic material is the main objective of the present work. The soft magnetic materials were described as the actual solution for inductor design. The characterization and modeling of magnetic materials become a fundamental piece in the design of inductive components due to its influence on the effectiveness of the filter response. The existing models are quite limited related to magnetic materials used in EMI filter. Among these characteristics, the magnetic permeability and magnetization were identified as principal due to the EMI filter application and will be treated in the following chapters. The EMI filter design procedure will be presented taking into account the magnetic material model.

Chapter 2. Small-signal characterization and modeling of the magnetic core

Magnetic materials for power electronic inductive components have been the subject of many researches. The typical nonlinear behavior of a magnetic core depends on frequency, temperature, and also on mechanical strength. In a first approach, its behavior can be studied as a linear one, using small-signal characterization. In this chapter, the small-signal is considered as low levels of current and voltage excitations. This is performed when using measurement instruments such as the impedance analyzer (IA), vector network analyzer (VNA) and spectrum analyzer (SP).

2.1 Overview of the magnetic permeability

The general relationship, between the magnetic flux density B and the magnetic field strength H , can be written as (10) for ferromagnetic or ferrimagnetic materials. The vacuum permeability μ_0 ($4\pi \times 10^{-7} \frac{V \cdot s}{A \cdot m}$) is constant while the relative permeability μ_r represents the nonlinear relationship between B and H .

$$B(H) = [\mu_0 \mu_r(H)] H \quad (10)$$

For this type of material, the relative permeability μ_r is higher than one and defined for different small-signal measurement conditions as described in the following [52, 53, 60].

Initial permeability (μ_i)

The initial permeability is defined for very low excitation levels. It is measured using closed magnetic circuits such as ring cores. This parameter, expressed in relation (11), correspond to the slope between ΔB_i and ΔH_i in low magnetization level when ΔH_i approaches zero.

$$\mu_i = \frac{1}{\mu_0} \frac{\Delta B_i}{\Delta H_i} \quad (\Delta H_i \rightarrow 0) \quad (11)$$

Effective permeability (μ_e)

When magnetic cores do not have closed magnetic path and some air gap is present, the effective permeability μ_e is thus defined. The core and its gap are taken into account in the form factor term $\Sigma \frac{l}{A}$ (12), where l is the effective length and A is

the effective cross-section area of the magnetic core and air gap, L is the inductance value (in the linear zone at low frequency) and N is the number of turns.

$$\mu_e = \frac{1}{\mu_0} \frac{L}{N^2} \sum \frac{l}{A} \quad (12)$$

Apparent permeability (μ_{app})

The apparent permeability μ_{app} is applicable for non-ring cores, *i.e.* cylindrical and threaded ones. This parameter is not usually found in datasheets but an approximation is obtained calculating the ratio of the inductance value with (L_{with}) and without the magnetic core ($L_{without}$), as given in (13).

$$\mu_{app} = \frac{L_{with}}{L_{without}} \quad (13)$$

Reversible permeability (μ_{rev})

The reversible permeability (14) is obtained by DC analysis in small-signal. The magnetic field is imposed as a constant (H_{DC}) while an alternating field is added. Thus, the relative permeability in the nonlinear region of the material is obtained.

$$\mu_{rev} = \frac{1}{\mu_0} \lim_{\Delta H \rightarrow 0} \left(\frac{\Delta B}{\Delta H} \right)_{H_{DC}} \quad (14)$$

Pulse permeability (μ_{π})

The amplitude of the relative permeability is evaluated when the rate of change in the magnetic induction (B_{π}) is held substantially constant over a period of time during a cycle (15). The frequency and duration of the stated period of time must be established. The magnetic flux variation ΔB_{π} is the change in induction during the stated time interval.

$$\mu_{\pi} = \frac{1}{\mu_0} \frac{\Delta B_{\pi}}{\Delta H_{\pi}} \quad (15)$$

Differential permeability (μ_{dif})

This parameter corresponds to the rate of change of the differential magnetic induction dB when a small change in field strength dH is produced (16).

$$\mu_{dif} = \frac{1}{\mu_0} \frac{dB}{dH} \quad (16)$$

Impedance permeability (μ_z)

The magnetic induction B_i is the maximum intrinsic flux density while the magnetic field is calculated by $H_z = \sqrt{2}NI/l_e$. This expression (17) is widely used in design process when $B_i = B_{max}$ to estimate the maximum current before saturation of the material.

$$\mu_z = \frac{B_i}{H_z \mu_0} \quad (17)$$

Instead of the impedance permeability, the peak permeability μ_{pk} is defined as the maximum magnetic strength field ($N\hat{I}/l_e$) applied to estimate the magnetic flux density of the material and calculated by (18).

$$\mu_{pk} = \frac{B_i l_e}{N\hat{I} \mu_0} \quad (18)$$

All the previous expressions represent the material's magnetic permeability in some specific measurement conditions, which are defined by the final application of the power inductive component. The estimation of the final inductive value is valid only if the material behavior is calculated in a region where the used expression of the permeability is defined.

However, another expression to represent the magnetic permeability is the complex magnetic permeability (CMP). The interest of the CMP is the ability to represent the frequency evolution of the magnetic material permeability in a large frequency bandwidth. The CMP is defined as following.

Complex permeability ($\bar{\mu}$)

The representation of the CMP enables a better comparison of magnetic materials and their frequency characteristics at HF for weak magnetic fields. This representation takes into consideration the phase displacement between voltage and current signals, which can be modeled in series representation (19) or in parallel one (20). The series CMP will be adopted herein for convenience.

$$\bar{\mu} = \mu'_s - j\mu''_s \quad (19)$$

$$\frac{1}{\bar{\mu}} = \frac{1}{\mu'_p} - j \frac{1}{\mu''_p} \quad (20)$$

The main advantage of a complex representation is the direct transition from the magnetic circuit to the electrical equivalent circuit. The real part of the CMP is related to the magnetic energy in the materials, while the imaginary part is related to core loss. This parameter is applied to define two factors: the dissipation factor and the quality factor.

Dissipation factor: It is defined as the ratio of the imaginary and the real part of the series CMP, where δ_n is the loss angle (21).

$$\tan \delta_n = \frac{\mu_s''}{\mu_s'} = \frac{\mu_p'}{\mu_p''} \quad (21)$$

Quality factor: For inductive components, the quality factor (22) is defined as the inverse of the dissipation factor. This parameter describes how *inductive* is the component with regard to the losses.

$$Q = \frac{1}{\tan \delta_n} \quad (22)$$

Then, the CMP is better adapted to represent the nonlinearity of the material versus the frequency. The core loss and magnetic energy are naturally included in this representation. Usually, the CMP is given by manufacturers in order to characterize and classify the materials depending on the final application and associated frequency range. However, some materials are not always fully described, especially in the frequency range of interest. For example, the MnZn ferrites are usually presented with the limit of application at 1 MHz. Above this frequency there is no information regarding the properties of the material while they are traditionally employed in EMI filters for a frequency range up to 30 MHz.

Moreover, the CMP of these materials is guaranteed within a $\pm 25\%$ dispersion interval in the datasheets. This disparity is basically due to inhomogeneity issues that occur during the fabrication process. Nevertheless, the accurate characterization of the magnetic materials remains a mandatory step if more specific and detailed information of the magnetic permeability is required.

In the next section, in order to better characterize the material, an existing measurement method is applied to ring core samples. Additionally, a new measurement method will be developed and detailed due to the drawbacks of the existing one.

2.2 Measurement of complex magnetic permeability

2.2.1 Magnetic material test fixture

In chapter one, the Table 1.1 summarizes different methods to measure the magnetic permeability where specific test instruments, combined with processing softwares, allow measuring the permeability and permittivity of the magnetic materials. The material samples can have different shapes but ring cores are usually preferred because of the closed magnetic path in the core. For example, the magnetic material test fixture (MMTF) from Agilent (16454A), coupled together with the impedance analyzer (4294A), is a technique that measures directly the CMP of ring cores. The flow diagram of the measurement procedure is illustrated in Figure 2-1. The MMTF can be defined as a one-turn coil without leakage flux.

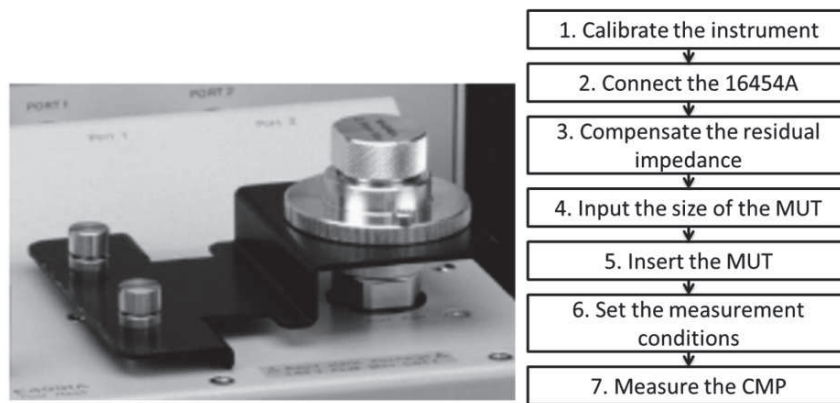


Figure 2-1 Description of magnetic test fixture (MMTF) and procedure for CMP measurement

To measure the CMP with such MMTF, the *residual impedance* - impedance caused by the additional connection, must be first compensated by open and short-circuit tests with the connection terminals. Then, geometric constants and measurements conditions are set inside the software. Finally, the material under test (MUT), introduced in the container, is characterized using a pre-compiled IBASIC program in the Impedance Analyzer and post processed with a MATLAB® script.

The measurement frequency range, with such apparatus, is within the interval 1kHz to 110MHz. Nevertheless, the maximum DC Bias current is limited to 500mA, which does not allow saturating most of the commonly used materials. Besides, the geometrical aspect of the ring core size is the principal restricting parameter. Indeed, the typical size of a MUT for this MMTF is limited to some millimeters. More

detailed information about the holders (accessories of the MMTF to keep the ring cores centered into the fixture) is listed in Table 2-1. Smaller ring cores (external diameter < 8mm) can be measured with holders A and B, while larger ring cores (external diameter < 20 mm) with C and D. The height is limited to 8.5 mm and the internal diameter needs to be greater than 5 mm.

The measurement error is given by the MMTF datasheet and reproduced in Figure 2-2. It indicates a maximum of 10% for the relative permeability μ' (real part of the CMP) in the frequency band from 10 kHz to 100 MHz.

Table 2-1 Different MUT sizes

Holder	Maximum external diameter	Minimum internal diameter	Maximum height
A	8 mm	3.1 mm	3 mm
B	6 mm	3.1 mm	3 mm
C	20 mm	6 mm	8.5 mm
D	20 mm	5 mm	8.5 mm

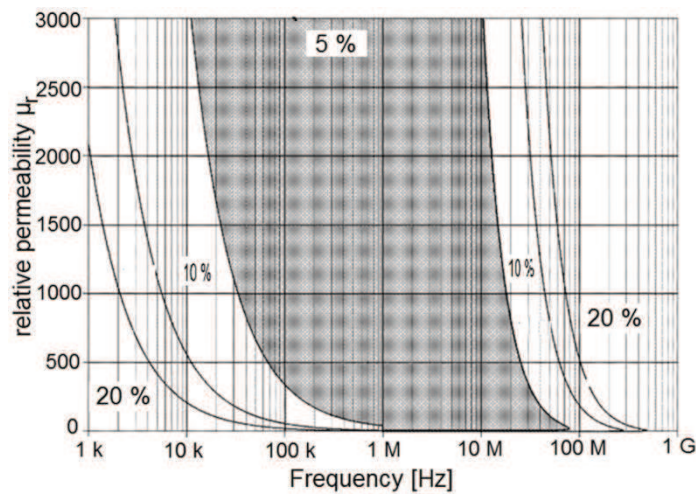
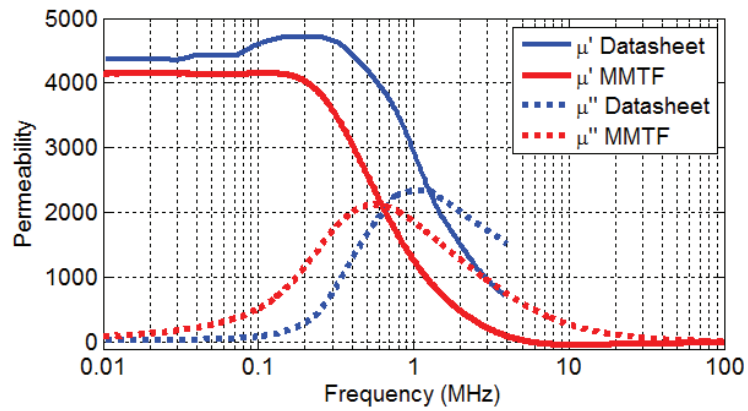


Figure 2-2 Typical relative permeability measurement accuracy of MMTF

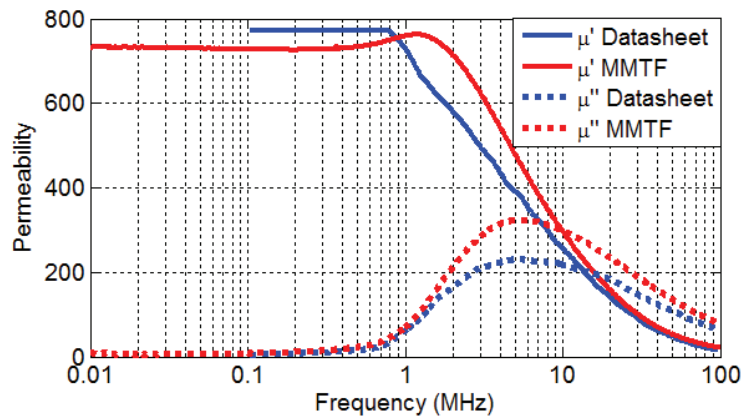
Three ring cores, with different magnetic materials and appropriate dimensions, are tested with the MMTF. Their geometrical characteristics are summarized in Table 2-2. The corresponding permeabilities are plotted from datasheets and compared with those measured with the MMTF from 10kHz to 100MHz (Figure 2-3). In the case of ferrites (N30 and M43) the CMP from the datasheets are easily obtained whereas the imaginary part of the CMP for nanocrystalline cores is rarely given.

Table 2-2 Magnetic materials under test

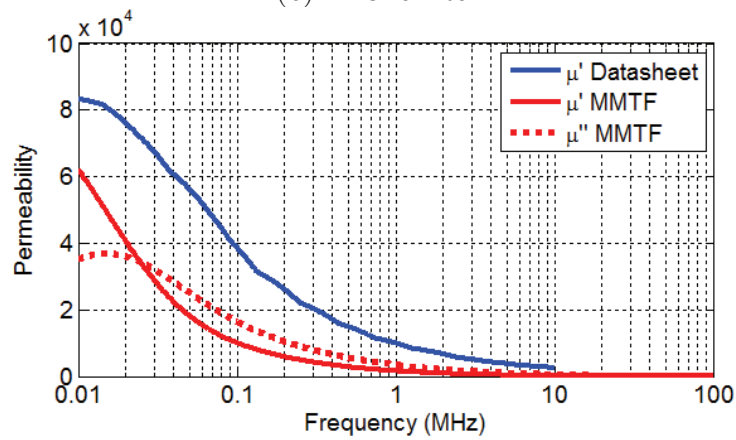
Material	Manufacturer	External diameter	Internal diameter	Height	Form factor $F = h_e \ln(d_e/d_i)$
N30 (MnZn)	Epcos®	16.2 mm	9.2 mm	6.7 mm	3.8 mm
M43 (NiZn)	Fair-rite®	14 mm	6.4 mm	5 mm	3.5 mm
N6E3 (Nanocr.)	Aperam®	16.2 mm	9.4 mm	6.4 mm	3.7 mm



(a) N30 ferrite



(b) M43 ferrite



(c) N6E3 nanocrystalline

Figure 2-3 Comparison of CMP by MMTF measurement and the datasheet

The differences between datasheets and measured values are clearly emphasized in Figure 2-3. Considering the accuracy of the MMTF acceptable (Figure 2-2), the measured CMP has an average 5% of accuracy error from 100 kHz to 10 MHz. Then, the datasheets values can reach the error of 50% for some frequencies. Therefore, designs based on these results lead to over- or under-estimation of the final inductance values. The ideal procedure, based on a first ring core characterization prior to utilization, requires time and resources. In one hand, the process design optimization needs this detailed characterization. On the other hand, this disparities can be taken into account while designing magnetic components in the frame of a worst case scenario based on the datasheet that gives a dispersion of $\pm 25\%$ for the initial permeability (μ_i). The other aspect is related to the limit on the ring core size that can be used in the container of the test fixture. Therefore, a new CMP measurement method is proposed in the following.

2.2.2 Proposed method

The objective of this method is to measure the CMP of ring core magnetic materials, with dimensions that overload the test fixture 16454A. A typical ring core with a N-turn winding and its main parameters is presented in Figure 2-4.

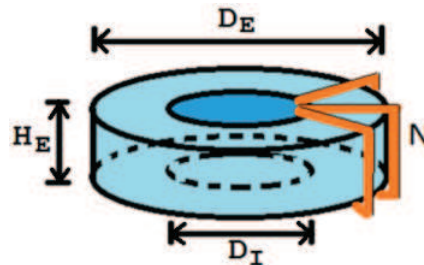


Figure 2-4 Ring core magnetic material with N turns

The measurement conditions and winding additional parameters have to be initially identified in order to measure correctly the CMP of the cores. In fact, parasitic effects may also have a strong impact, especially in HF. These effects are firstly identified with the measured impedance of the inductor performed with the impedance analyzer. This impedance Z_{mea} (23) is considered as the *ideal* inductive response Z_L (24) where the permeability is equal to $\bar{\mu}$ (19). By identifying both expressions, the CMP value can finally be calculated with (25) and (26).

The measurement frequency range starts at 10 kHz and stops at 100 MHz.

This bandwidth covers largely the EMI filter frequency range (150 kHz to 30 MHz). Additional tests are discussed in the following paragraphs to understand the advantages and drawbacks of this technique. Aspects related to the number of turns, the position of the winding and the material dispersion has also been considered.

$$Z_{mea} = R_{mea} + jX_{mea} \quad (23)$$

$$Z_L = j\omega \left[\frac{\bar{\mu} \mu_o}{2\pi} N^2 H_E \ln \left(\frac{D_E}{D_I} \right) \right] \quad (24)$$

$$\mu' = \frac{2\pi}{\omega \mu_o H_E \ln \left(\frac{D_E}{D_I} \right)} \left(\frac{X_{mea}}{N^2} \right) \quad (25)$$

$$\mu'' = \frac{2\pi}{\omega \mu_o H_E \ln \left(\frac{D_E}{D_I} \right)} \left(\frac{R_{mea}}{N^2} \right) \quad (26)$$

2.2.3 Influence of the number of turns

The first parameter analyzed is the number of turns (N). The standard of test procedures [60] recommends a number of turns equals to 25 when the initial permeability (μ_i) is 400 or below, and only 5 turns for upper values when characterizing the ring cores. However, there are no specific recommendations when the frequency varies. Instead, the expression *low number of turns* is usually given to estimate the appropriate number of turns. With no clear standard value, the influence of the number of turn has been investigated.

In order to valid the proposed method, the CMP obtained from the MMTF is taken as reference and compared with the measured permeability of the ring cores listed in Table 2-2 when N increases. Indeed, the test performed for N=1, 5, 10 and 15 turns are normalized to N=1 (impedance divided by N^2) to show the impact on the measurement in high frequency. In Figure 2-5, it is observed that above 1 MHz the normalized measured impedance of N30 ferrite ($\mu_i \approx 4300$) implies the presence of an extra component, clearly linked to the number of turns that affects the HF measurement. Similar effects are also observed for the both other materials; the N6E3 nanocrystalline ($\mu_i \approx 90000$) and the M43 ferrite ($\mu_i \approx 800$), as illustrated in Figure 2-5.

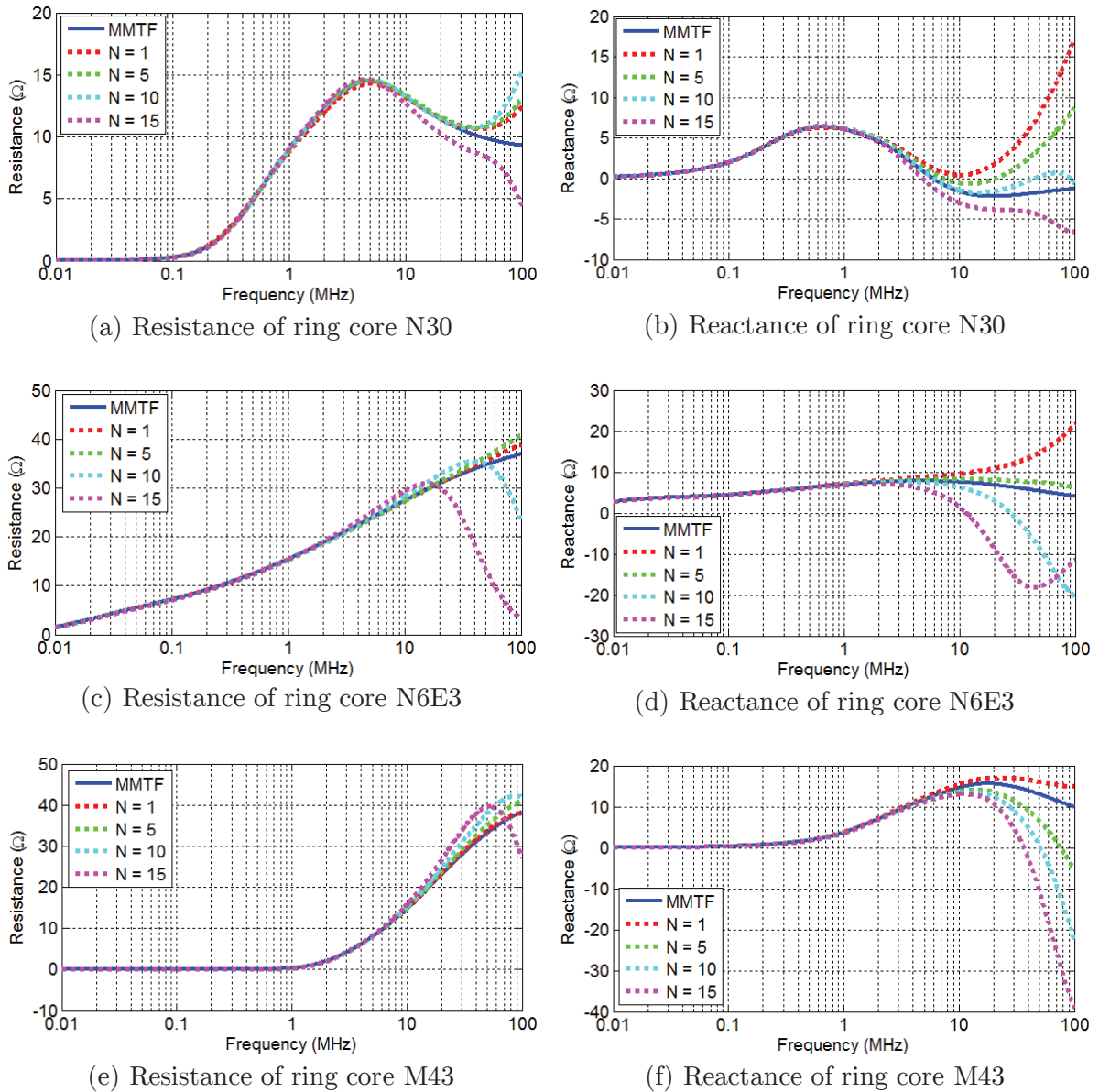


Figure 2-5 Influence of N in the impedance measurement

This behavior can be explained by the wire resistance (due to skin and proximity effects), the leakage inductance and the winding capacitances that become more and more preponderant at HF. In particular, the winding parasitic capacitances can be observed in the reactance figures at HF where the reactance value decreases while the number of turns increases (Figure 2-5). This figure suggests, as well, that the number of turns could be limited to 5 turns without introducing large impact on the measured impedances compared with the MMTF ones. However, in the present work, the configuration N=1 is chosen to limit the wire resistance and parasitic inter-turn capacitances. Nevertheless, some measurement compensation is still necessary in HF. This aspect will be detailed herein after.

An equivalent circuit (Figure 2-6) is used to represent the HF effects of the winding. The measured impedance Z_{mea} is composed of the material impedance Z_{mat} in series with the parasitic impedance Z_{par} . The CMP (μ' and μ'') is included in the impedance Z_{mat} . The impedance Z_{par} is composed by the resistance R_{par} (modeling the winding losses: skin and proximity effect) and the reactance X_{par} (representing the leakage inductance). The winding parasitic capacitance is neglected in this method because the reactance curves in Figure 2-5 show that the influence of the parasitic capacitances in HF for N=1 is above 100 MHz.

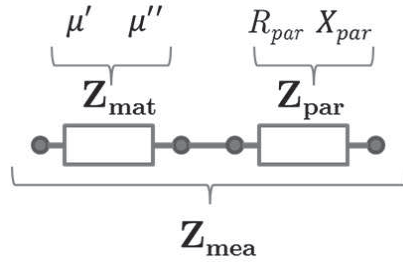


Figure 2-6 Equivalent circuit of measurement

First, the resistance of the wire R_{par} can be expressed by (27), which takes into account the variation with frequency. This expression is detailed in [66] where N_i is the number of layers. The DC resistance R_{DC} can be calculated with (28), where the resistivity per meter of the winding material is ρ , the number of turns is N, the wire length is l_w , and d_w is the round wire diameter. The variable A is given by (29), where δ is the skin depth and l_t is the distance between the turns.

In order to evaluate the resistance of the winding R_{par} , a ring core replica in PVC material is used. The parameters listed in Table 2-3 are replaced in (27)- (29) and the calculated results are depicted in Figure 2-7(a).

$$R_{par} = R_{DC}A \left[\frac{e^{2A} - e^{-2A} + 2 \sin(2A)}{e^{2A} + e^{-2A} - 2 \cos(2A)} + 2 \left(\frac{N_i^2 - 1}{3} \right) \frac{e^A - e^{-A} + 2 \sin(A)}{e^A + e^{-A} - 2 \cos(A)} \right] \quad (27)$$

$$R_{DC} = \frac{4\rho N l_w}{\pi d_w^2} \quad (28)$$

$$A = \frac{(\pi/4)^{3/4} d_w^{3/2}}{\delta \sqrt{l_t}} \quad (29)$$

Table 2-3 Parameters for R_{par} and L_{par} calculation (PVC ring core)

N	ρ (Ωm)	l_w (mm)	d_w (mm)	l_t (mm)	N_i	L_0 (nH)
1	17.24×10^{-9}	20.4	0.5	1.5	1	14.8

From these results, it can be observed that the model R_{par} follows the resistance evolution with frequency and a good agreement is obtained below 10 MHz. Above this frequency, the expression (27) cannot represent correctly the fast increase of resistance. An additional term has to be added to improve the compensation impedance Z_{par} , which can be linked to the proximity effects. However, as previously stated, using only one-turn winding, this resistance value can be reduced and less difference is obtained in HF.

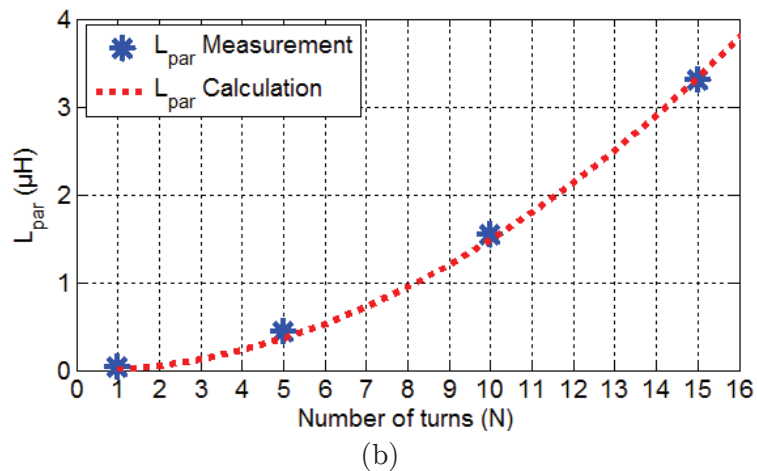
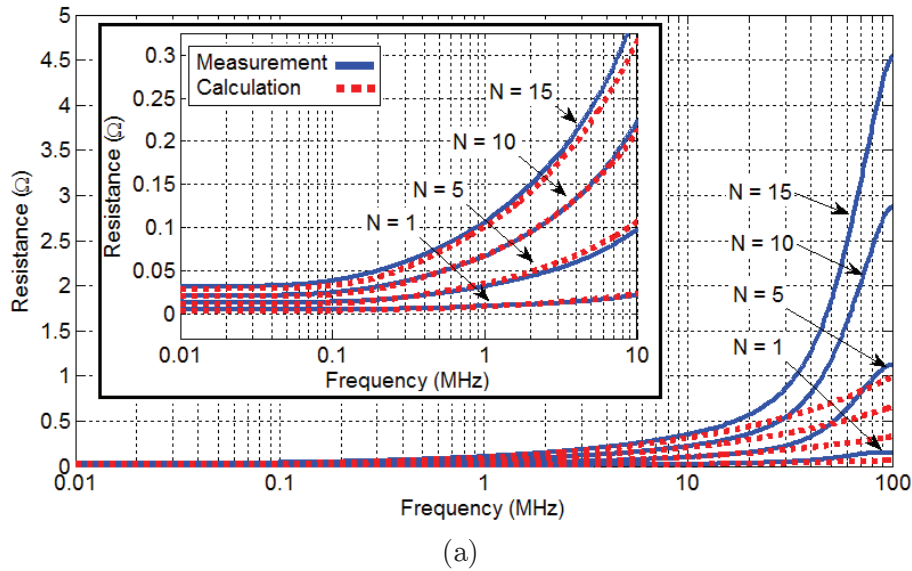


Figure 2-7 (a) Wire resistance R_{par} frequency evolution (b) Leakage inductance L_{par}

On the other side, the leakage inductance can be represented by the expression (30) deducted from measurements. The evolution of L_{par} is equal to N^2 multiplied by the equivalent one-turn inductance L_0 , which can be obtained from analytical, numerical computation or direct measurement. The measured and calculated L_{par} are compared in Figure 2-7(b) with a good agreement.

$$L_{par} = \frac{X_{par}}{j\omega} = N^2 L_0 \quad (30)$$

In sum up, the small-signal measurement results observed in Figure 2-5 show that the CMP can be obtained using one-turn coil around the ring core when the HF variation is taken into account. Moreover, it was observed that the one-turn winding allows measuring the CMP with low Z_{par} .

2.2.4 Method of CMP measurement compensation in HF

Previously, the one-turn winding has been chosen to characterize the CMP of a ring core material due to better response at HF. In the aim to reduce more and more these HF parasitic effects, a study has been carried out on the one-turn configuration with a variable wound surface. One flat copper wire is then wound around the ring core, first, to cover the entire core and then reducing its surface to characterize the leakage inductance variation (Figure 2-8). For this experiment a ring core sample of ferrite N87 with dimensions 20mm/9.6mm/7.4mm ($D_E/D_I/H_E$) was used.

The impedance measured with MMTF is taken as reference. For different angle covered by flat wire (30° , 180° and 360°), the impedance is measured by the proposed method. The obtained results are presented in Figure 2-9. The impedance's module increases in HF when the wound surface decreases. The phase information (Figure 2-9(b)) shows an inductive behavior in HF that can be modeled as inductive impedance. The evolution of this leakage inductance, extracted from the measured impedance, is illustrated in the Figure 2-10 as function of the wound-surface percentage. Then, the expression (31) is fitted to model this leakage inductance as a function of the winding surface (S in percent) and two parameters (a and b). In the particular case of ferrite N87, the parameters values are: $a = 76.36nH$ and $b = 5.87nH$. Finally, the impedance measurement is compensated by applying the leakage model. Its parasitic impedance is subtracted from the original measurement. The results are presented in Figure 2-11.

$$L_{leak} = \frac{a}{\sqrt{S\%}} + b \quad (31)$$

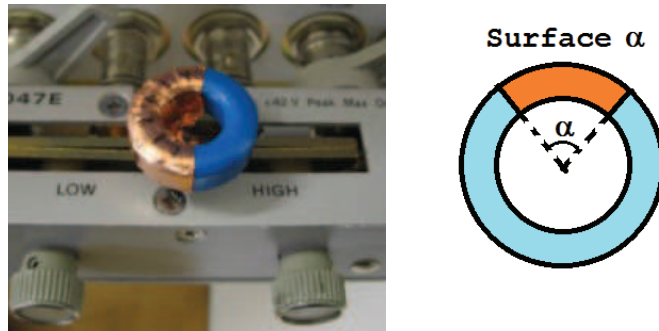


Figure 2-8 Configuration of wire surface variation test

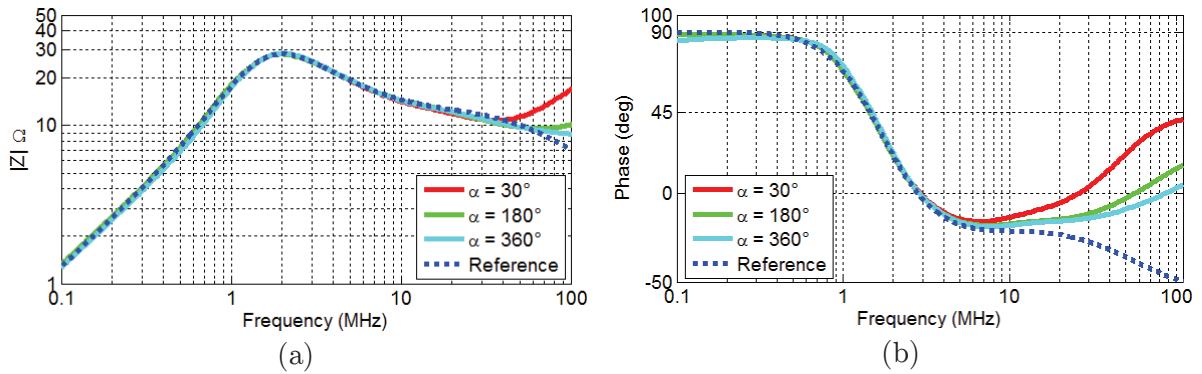


Figure 2-9 Impedance comparison when wire surface varies (a) module (b) phase

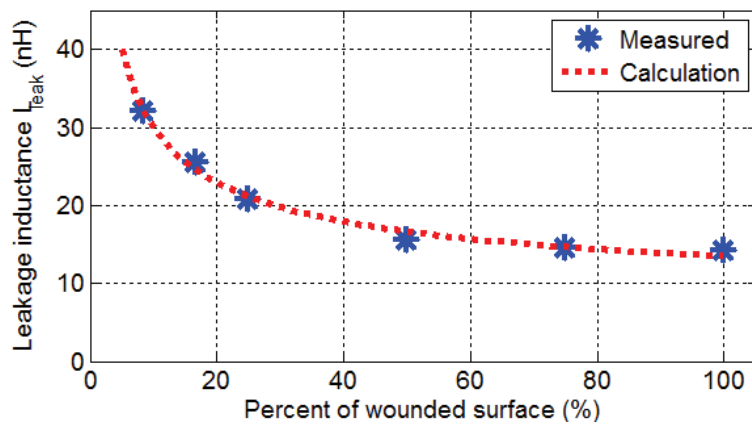


Figure 2-10 Leakage inductance of one-turn winding surface

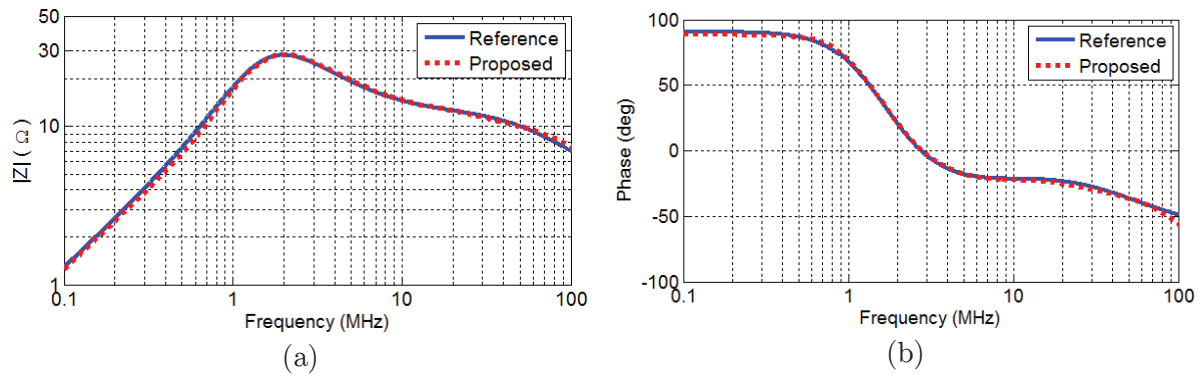


Figure 2-11 (a) Module and (b) phase of the impedance measured with MMTF and the proposed method

There is one key point to remember: the more number of turns are increased, the more parasitic effects are generated in HF. The one-turn winding seems enough to characterize the magnetic material, whether the effect of the wire resistance and leakage inductance are well compensated. Moreover, the leakage inductance decreases when the surface of the one-turn winding increases.

2.2.5 Magnetic material variation

The characterization of the magnetic material is subjected to the intrinsic variation of the material composition. Non-homogeneities due to the fabrication process produces ring cores with different properties even if the *same material* is produced. The composition of the material can alter its final response in frequency and its material resonance frequency (MRF), which is a property of the magnetic materials that limits the effective magnetization [67]. In the aim to study the variation of the material, two tests are carried out:

- First, the CMP of ring cores is measured for a same material with the same core dimensions
- Secondly, the CMP of the ring cores is still measured for a same material but with different core dimensions.

The proposed method of measurement, explained in the previous section, is applied to measure the CMP of N30 ferrite and N6E3 nanocrystalline. The ring cores tested are listed in Table 2-4 and Table 2-5.

Table 2-4 List of N30 ferrite ring cores

Core	Material	D_E (mm)	D_I (mm)	H_E (mm)
C1	N30 ferrite	16	9.6	6.3
C2	N30 ferrite	20	9.6	7.4
C3	N30 ferrite	25.6	14.6	10.9
C4	N30 ferrite	58.7	40.8	18.5

Table 2-5 List of N6E3 nanocrystalline ring cores

Core	Material	D_E (mm)	D_I (mm)	H_E (mm)
C5	Nanocr. N6E3	16	9.5	6.4
C6	Nanocr. N6E3	20	12	8.5
C7	Nanocr. N6E3	25	15.7	10.6
C8	Nanocr. N6E3	40	23.8	15.7

Same material with same dimensions

In these first tests, the core C1 (N30 ferrite) and C5 (N6E3 nanocrystalline) are characterized. Four different samples and three other samples are tested for C1 and C5 respectively. The results for N30 ferrite CMP are plotted in Figure 2-12(a). The average CMP ($\bar{\mu}'$ and $\bar{\mu}''$) is also illustrated on this graph. The relative variation between the measured CMP and the average CMP value for each frequency point is calculated by (32). The Figure 2-12(b) shows 20% difference in the frequency range from 10 kHz to 400 kHz. One can note that this frequency range is the one recommended in the datasheet. From 400 kHz up to 10 MHz, the CMP presents a 30% of maximum variation, basically linked to MRF. The CMP above 10 MHz still presents a maximum variation of 10% approximately.

$$relative\ variation(\%) = \max \left(\sqrt{\frac{(\bar{\mu}' - \mu'_i)^2 + (\bar{\mu}'' - \mu''_i)^2}{\bar{\mu}'^2 + \bar{\mu}''^2}} \right) * 100\% \quad (32)$$

With the same experimental approach, the nanocrystalline material N6E3 was also tested. The CMP is plotted in Figure 2-12(c), and the relative variation in Figure 2-12(d). It is observed, in the frequency range from 10 kHz to 100 MHz, that the relative variation is still lower than 10%. The material seems to have a more stable response and less disparity between the samples.

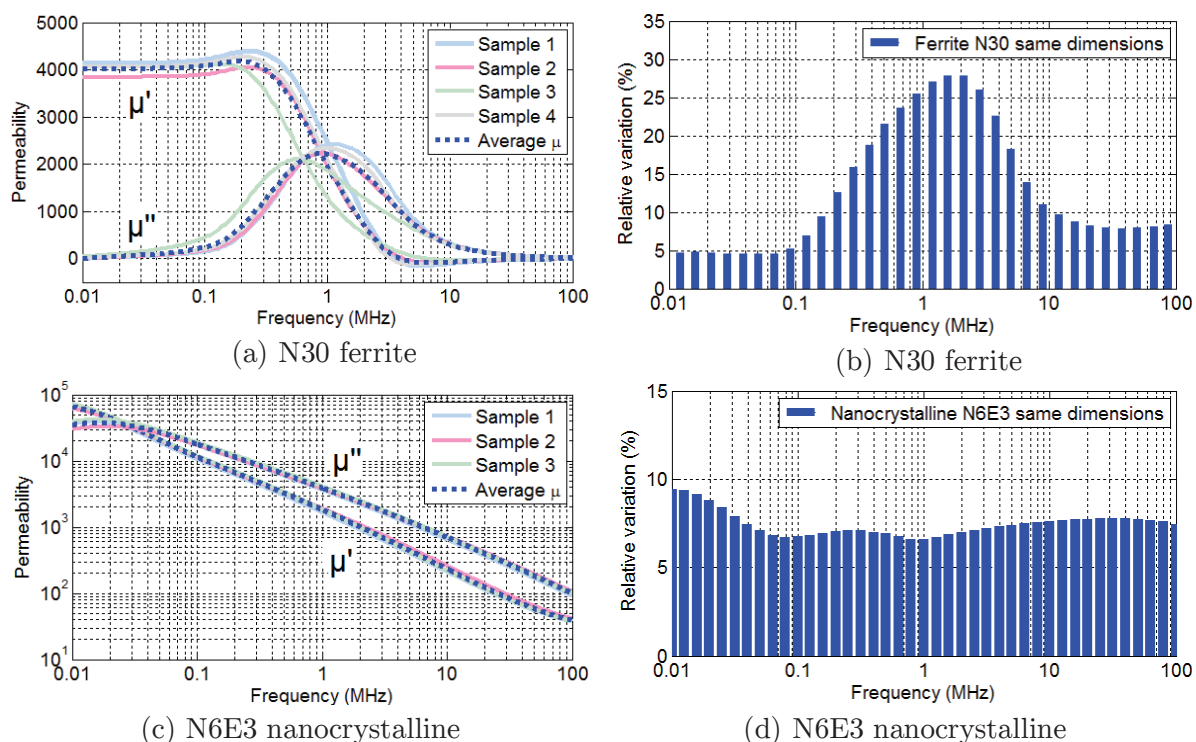


Figure 2-12 (a) CMP of four N30 ring cores of type C1 and (b) relative variation for N30
(c) CMP of four N6E3 ring cores of type C5 and (d) relative variation for N6E3

Same material with different dimensions

In this second analysis with different dimensions for the same magnetic material, the cores C2, C3, C4 for the N30 ferrite, and cores C6, C7 and C8 for the N6E3 nanocrystalline are studied. Results are illustrated in Figure 2-13(a) and Figure 2-13(c) for the ferrite and nanocrystalline samples respectively.

For the ferrite samples, the differences can present more relative variation in all frequency range, as shown in Figure 2-13(b). Below 400 kHz, the relative variation is under 35%. However, higher values appear in the range above 400 kHz, to reach more than 40% at 1 MHz. In contrast, the relative variation for the nanocrystalline material (Figure 2-13(d)) presents a more stable tendency below 10 MHz and is limited to 10%.

To sum up, these two conclusions can be highlighted:

- The highest dispersion in the CMP measurement is located near to the MFR (up to 45% for ferrites).
- The CMP of the nanocrystalline, in the frequency range of measurement, presents more stable values (variation in the order of 10%).

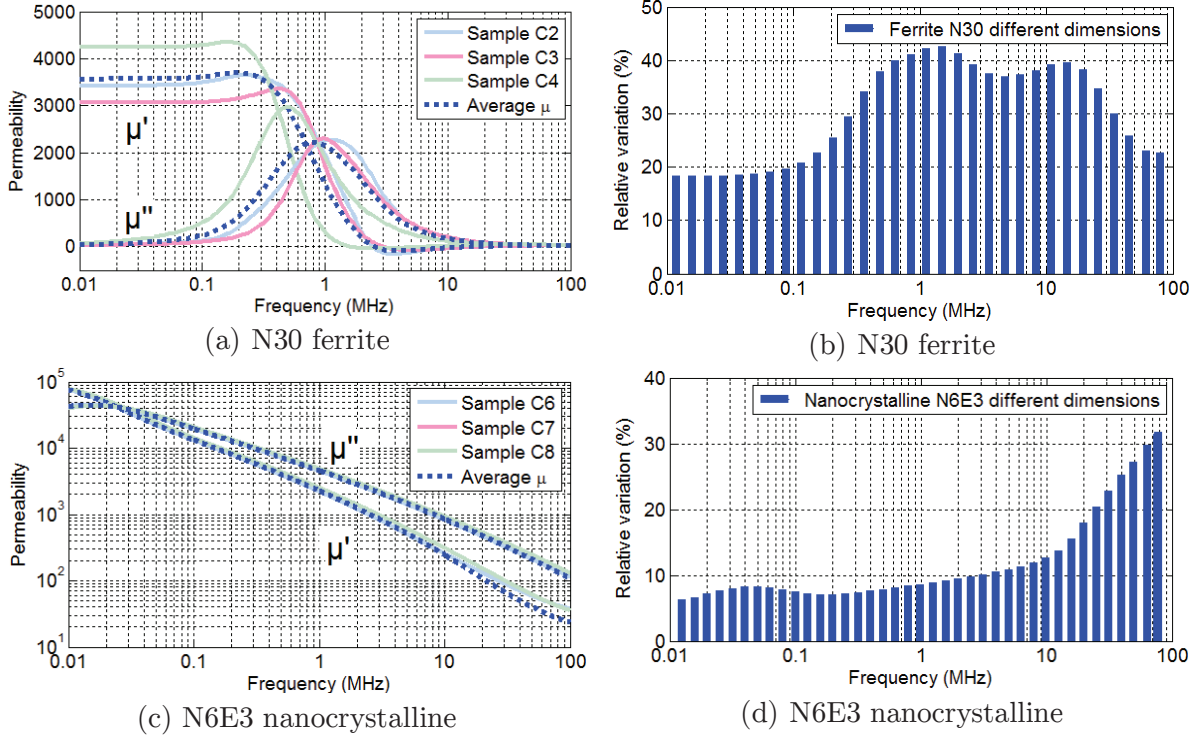


Figure 2-13 (a) CMP of three N30 ring cores (C2, C3, C4) and (b) relative variation for N30
 (c) CMP of three N6E3 ring cores (C6, C7, C8) and (d) relative variation for N6E3

2.2.6 Influence of the voltage level

The last aspect in CMP measurement is the voltage level in the characterization process. To evaluate the influence of this parameter, some tests with variable voltage excitation were performed. The voltage level was set from 5mV to 500mV in the impedance analyzer. These tests were made only under alternative signals voltage with no bias.

This variation of the CMP with the voltage level can be expressed by the average slope in the $B_m - H_m$ curve where the maximum magnetic flux density (B_m) and the corresponding magnetic field strength (H_m) are given by the expressions (33) and (34) respectively. The phase displacement δ_n is linked to the ratio between the imaginary and the real part of the CMP (35).

$$B_m = \frac{V}{NA_e \omega} \quad (33)$$

$$H_m = \frac{B_m \sin \delta_n}{\mu_0 \mu''} \quad (34)$$

$$\delta_n = \arctan\left(\frac{\mu''}{\mu'}\right) \quad (35)$$

On the one hand, the real part of CMP (μ') for N30 ferrite is depicted in Figure 2-14(a). The imaginary part of CMP (μ'') is not illustrated because the voltage variation does not influence as much as in the real part. The major variations in the measurement are observed at low frequencies (below 400 kHz). For the N30 ferrite the $B_m - H_m$ average relation is obtained with the small-signal of the impedance analyzer. As shown in Figure 2-14(b), the slope of the curves stays close the same for all the voltage levels.

For each $B_m - H_m$ curve (obtained at each voltage level), the point on the curve corresponds to one point in frequency. The highest value of the pair B_m and H_m on the curve is given for the frequency equals 10 kHz. Moreover, because the voltage level is in the order of the millivolts, the magnetic flux density B_m and the magnetic strength field H_m can reach 40mT and 8A/m respectively. Thus, the characterization can be considered to lie within the Rayleigh zone, i.e. in the initial permeability region.

On the other hand, the imaginary part of the CMP (μ'') for the N6E3 nanocrystalline is depicted in Figure 2-15(a). In contrast to ferrites, the nanocrystalline material shows more variation in the imaginary part of the CMP (μ'') than in μ' . In consequence, only the imaginary part is illustrated. The $B_m - H_m$ average relation is illustrated in Figure 2-15(b). The slope of the curve changes depending of the voltage level used. Indeed, the material characteristics are not in the same for this region of magnetization. The maximum magnetic inductance flux measured $B_m = 240mT$ is below of the saturation level $B_{sat} = 1.2T$ of the nanocrystalline. However, the magnetic field strength $H_m = 2.1A/m$ exceeds the coercive value $H_c = 1A/m$.

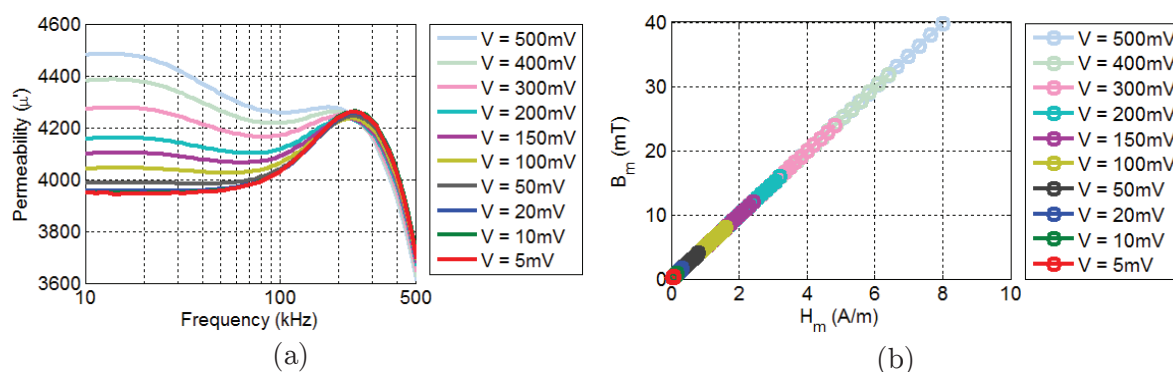


Figure 2-14 (a) Real part of CMP (μ') for the ring core type C1 (Table 2-4) when the voltage level varies (b) Small-signal $B_m - H_m$ relation

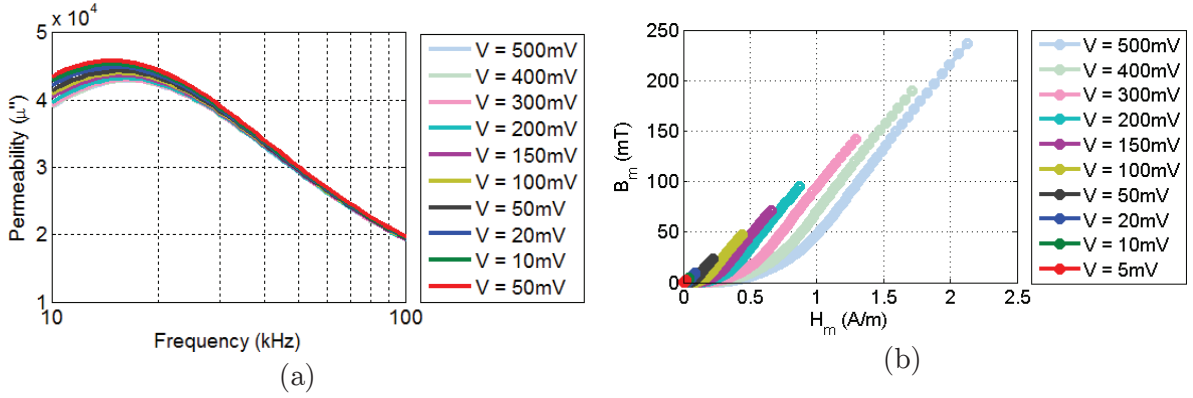


Figure 2-15 (a) Imaginary part of CMP for the ring core type C5 when the voltage level varies (b) Small-signal average B_m - H_m relation

2.2.7 Summarize

To sum up, the procedure for measuring the CMP using one turn winding starts with the impedance measurement in frequency of a ring core inductor. This measurement takes into account the leakage inductance, the losses and the number of turns. This method is summarized in the flow diagram illustrated in Figure 2-16. These CMP identified values can then be inserted into simulation softwares, such as look-up-tables, to describe the magnetic behavior of the material.

The next step is the development of a mathematical model for CMP that could be more adapted to the optimization. Thus, the next section describes the different analytical models that can represent the complex permeability variation in frequency.

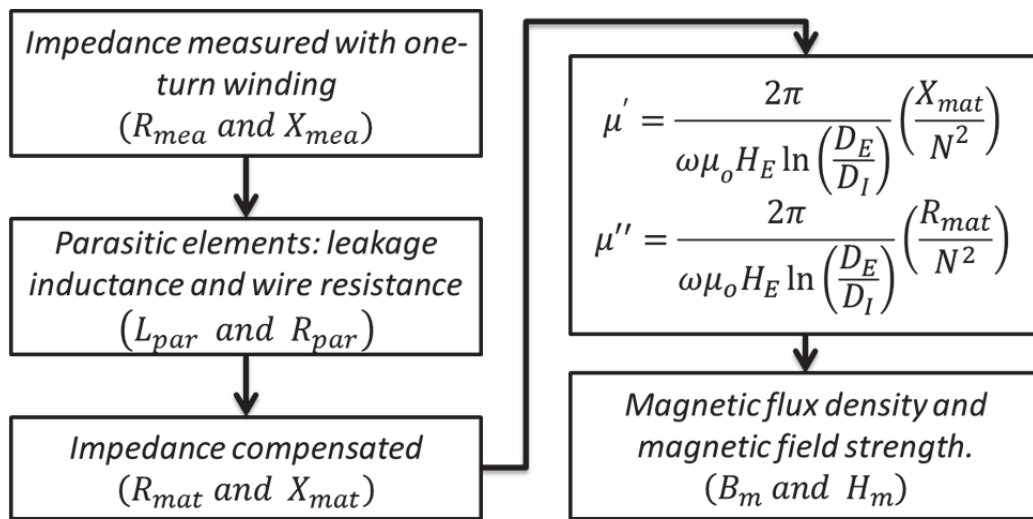


Figure 2-16 CMP flow diagram for small-signal characterization

2.3 Modeling of complex magnetic permeability

The CMP describes the behavior of magnetic materials in large frequency band. When inductive components are designed, the CMP plays an important role to represent the intrinsic parasitic effects of the material. Indeed, the inductive components are not purely inductive for all the frequency range. These parasitic effects are the result of a nonlinear material composition and internal magnetization effects such as the skin effect, domain wall and rotational movement [68]. The domain walls are interfaces between regions with spontaneous magnetizations into the magnetic material. The response of these domains to an applied field is called the domain wall movement. And the rotational movement is the rotation of the magnetic vector of each domain until it is parallel with the applied field. Moreover, the permittivity of the material can become an important parameter in the high frequency range. All of these aspects have been modeled by different approaches as following described.

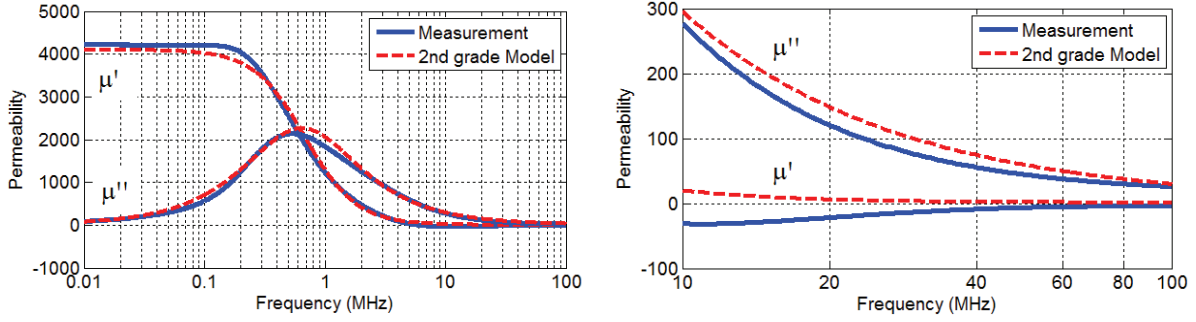
2.3.1 State of the art

The first studied model [39] is a second grade rational function (36) that can represent the two MRF due to the domain wall and rotational magnetic losses. In the CMP expression (36), χ_1 is the low frequency susceptibility of the domain wall movement while χ_2 is the low frequency susceptibility of the rotational magnetic losses; τ_1 and τ_2 are time constants which depend on material properties.

$$\bar{\mu} = 1 + \frac{\chi_1}{1 + j\omega\chi_1\tau_1} + \frac{\chi_2}{1 + j\omega\chi_2\tau_2} \quad (36)$$

However, the drawback of this model appears mainly at HF for magnetic materials especially for MnZn ferrites. Indeed, it can be observed that the permeability becomes negative in the region above 1 MHz which is linked to the dielectric behavior of the material. This issue will be treated with more details in the stray capacitance study in the following section.

As shown in Figure 2-17, the model (36) can follow the fundamental form of the curve, but does not represent the CMP in all the frequency range with sufficient accuracy.


 Figure 2-17 Measurement and simulation of N30 ferrite CMP with 2nd grade rational function

The second model [69], add two more factors α , β in the aim of damping the resonance of the material. The expression (37) becomes a 3rd grade rational function which can be reduced to a 2nd grade one when $\alpha \rightarrow \infty$. The other parameters in the expression (37) are:

- The resonance frequency for domain-wall (ω_d) and for gyromagnetic spin component (ω_s)
- The static magnetic susceptibility for domain-wall motion (χ_{d0}) and for gyromagnetic spin motion (χ_{s0}).

$$\mu_r(j\omega) = 1 + \frac{\omega_d^2 \chi_{d0}}{\omega_d^2 + \omega + j\omega\beta} + \frac{(\omega_s + j\omega\alpha)\omega_s \chi_{s0}}{(\omega_s + j\omega\alpha)^2 - \omega^2} \quad (37)$$

The third method is the gyromagnetic model introduced in [70]. This model represents the CMP with a permeance of the material. The main objective of this method is to couple the electrical and magnetic models into only one simulation.

The variation of the magnetic flux φ (V*s/turn) linked to magnetomotive force ψ (A-turns) is replaced by an equivalent *capacitance* that represents the magnetic energy stored in terms of permeance (H/turns²) (38). From an adequate mathematical transformation detailed in [70], this time-domain expression is formulated in frequency-domain by an equivalent impedance \bar{Z} (39). This equation is the ratio of the magnetic flux (Φ) and the magnetomotive force (Ψ) in frequency domain. However, this impedance \bar{Z} can be represented by generic circuit and increase the complexity of the network.

$$C_m = \frac{d\varphi}{d\psi} \quad (38)$$

$$\bar{Z} = \frac{\Psi(j\omega)}{j\omega \Phi(j\omega)} \quad (39)$$

The fourth model is presented in [56]. This model is based on the transmission line theory applied to the inductive components for power electronic converters. This method requires two measurements (Z_{short} , Z_{open} = open and short circuit impedance), to determine the four parameters:

- The resistance R_w of the inductor (40)
- The reactance X_w of the inductor (40)
- Two coefficients α and β of the propagation constant $\gamma = \alpha + j\beta$ (41), where l is the length of the transmission line sample.

$$Z_w = \sqrt{Z_{short}Z_{open}} = R_w + jX_w \quad (40)$$

$$\tanh[(\alpha + j\beta)l] = \sqrt{\frac{Z_{short}}{Z_{open}}} \quad (41)$$

Then the CMP is approximated by the expression (42) where Z_0 is the line characteristic impedance. The results are obtained in time-domain, representing the transmission and reflection phenomena over different converter topologies. The material parasitic effects are not covered in this model because the inductive component is considered as a constant in low frequency.

$$\bar{\mu} = \frac{c}{\omega Z_0} [R_w\beta + X_w\alpha - j(R_w\alpha - X_w\beta)] \quad (42)$$

The last model was described in [71]. The CMP is linked to the material permittivity by the energetic model of the ring core inductor. Both electric (S_E) and magnetic (S_H) energy are involved in the resolution of the permittivity and permeability of the material; only the permeability expression is represented here. In this model, the resistance of the connections and the parasitic capacitance are neglected. The CMP of the inductor is given by (43), where H_E , D_E and D_I are dimension of the ring core. Its characterization process, based on Newton-Raphson algorithm, solves the corresponding μ_r and ϵ_r for each frequency point using the measured impedance of the wound ring core inductor.

$$\bar{\mu} = -\frac{j2\pi(S_E + S_H)}{\omega|I|^2N^2H_E \ln\left(\frac{D_E}{D_I}\right)} \quad (43)$$

Having described the previous models of CMP traditionally used, they are not able enough to represent the HF behavior. In fact, another mathematical model, based on rational function, is developed in this work to describe the CMP evolution over a wide frequency range. This rational function of CMP (RFCMP) and its parameters are extracted from fitting procedures. In the following section, the RFCMP model is detailed.

2.3.2 RFCMP model

Some of the previous models can be represented by second and third grade rational functions [39, 69]. In this work, the fourth grade rational function is proposed in order to take into account the influence of other parameters like the dielectric behavior of the magnetic materials and losses in HF. Indeed, as observed in the Figure 2-18, the real part of the CMP of some materials presents a negative value in the HF. For example, the MnZn ferrites (N30 in the Figure 2-18), reaches negative permeability values above 2 MHz, that cannot be related to the winding parasitic capacitance because of the one-turn winding measurement process. The high values of the material's permittivity mask the measurement in HF when permeability achieve low values [72]. This negative part values in μ' (Figure 2-18) is linked to the *material capacitance* as will be discussed in the next section. In order to take into account this effect, the RFCMP model uses an extra grade on the rational function (fourth grade rational function).

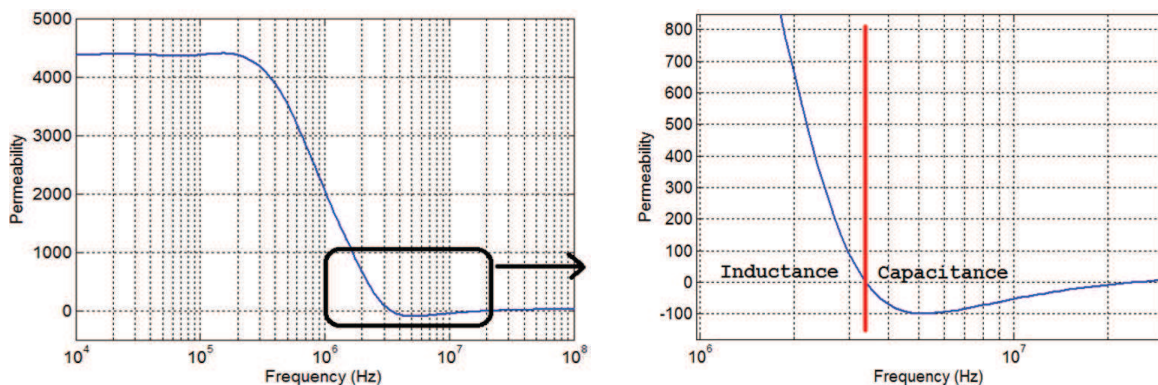


Figure 2-18 The negative value of the CMP real part. N30 ferrite

The Rational Function Approach (RFA) was introduced in [73] to represent the impedance measurement with a rational function (44), where the grade of the numerator and denominator are defined as $|m - n| \leq 1$ and $s = j\omega$.

$$Z(s) = \frac{N(s)}{D(s)} = \frac{b_m s^m + b_{m-1} s^{m-1} + \dots + b_1 s + b_0}{a_n s^n + a_{n-1} s^{n-1} + \dots + a_1 s + a_0} \quad (44)$$

Due to fitting problems in the low frequency range, the previous technique was not able to correctly identify the parameters for the impedance behavior. This is reason why an improved parameter identification method for the expression (44) was introduced in [35]. The algorithm was also enhanced based in the application of weight factors. As a result, the Iterative Ration Function Approximation (IRFA) method enables to fit the measured impedance Z_{mea} with a real good accuracy.

This method is based on two expressions (45) and (46), that are solved iteratively in order to identify the $a_n \dots a_0$ and $b_m \dots b_0$ coefficients (44). The real and imaginary parts of the formulation are given by (45) and (46) respectively. The weight factors, $P_{Re}^{[t]}(s_k)$ and $P_{Im}^{[t]}(s_k)$, are functions of the complex parameter s_k ; the superscript $[t]$ is the present value of iteration, and the subscript k is the index of the frequency vector. The corresponding real and imaginary expressions of these factor weighting are given by (47) and (48) respectively. Both expressions depend on the previous iteration values $[t - 1]$.

The link with the CMP measurement comes from equations (25) and (26). The measured Z_{mea} can be expressed with (49) and the CMP equivalent rational function or RFCMP is given by (50).

$$\text{Re} \left\{ P_{Re}^{[t]}(s_k) N^{[t]}(s_k) \right\} - \text{Re} \left\{ P_{Re}^{[t]}(s_k) Z_{mea}(s_k) D^{[t]}(s_k) \right\} = 0 \quad (45)$$

$$\text{Im} \left\{ P_{Im}^{[t]}(s_k) N^{[t]}(s_k) \right\} - \text{Im} \left\{ P_{Im}^{[t]}(s_k) Z_{mea}(s_k) D^{[t]}(s_k) \right\} = 0 \quad (46)$$

$$P_{Re}^{[t]}(s_k) = \frac{D^{[t-1]}(s_k)^*}{\text{Re}\{D^{[t-1]}(s_k)\}\text{Re}\{N^{[t-1]}(s_k)\} + \text{Im}\{D^{[t-1]}(s_k)\}\text{Im}\{N^{[t-1]}(s_k)\}} \quad (47)$$

$$P_{Im}^{[t]}(s_k) = \frac{D^{[t-1]}(s_k)^*}{\text{Re}\{D^{[t-1]}(s_k)\}\text{Im}\{N^{[t-1]}(s_k)\} - \text{Im}\{D^{[t-1]}(s_k)\}\text{Re}\{N^{[t-1]}(s_k)\}} \quad (48)$$

$$Z_{mea}(s) = \frac{N^2 \omega \mu_o H_E \ln\left(\frac{D_E}{D_I}\right)}{2\pi} [\mu'(s) - j\mu''(s)] \quad (49)$$

$$\bar{\mu} = \mu'(s) - j\mu''(s) = \frac{s^4 + b_3 s^3 + b_2 s^2 + b_1 s + b_0}{s^4 + a_3 s^3 + a_2 s^2 + a_1 s + a_0} \quad (50)$$

Notice that the coefficient of the higher element in the numerator and denominator are equal to one (50). That assumption is done because the relative CMP has not got any units. In addition, the CMP can be represented by a general equation (51), where $f(s)$ is an arbitrary unitless rational function.

$$\bar{\mu} = 1 + f(s) \quad (51)$$

A linear matrix equation $AX=B$ is written for both real and imaginary part of (50). Replacing the complex parameter $s = j\omega$ the corresponding matrix equations are obtained (52) - (54).

$$A = \begin{bmatrix} -\omega_k^3 & 0 & \omega_k & 0 & \mu'_k \omega_k^3 & -\mu''_k \omega_k^2 & -\mu'_k \omega_k & \mu''_k \\ \vdots & 0 & \vdots & 0 & \vdots & \vdots & \vdots & \vdots \\ 0 & -\omega_k^2 & 0 & 1 & \mu''_k \omega_k^3 & \mu'_k \omega_k^2 & -\mu''_k \omega_k & -\mu'_k \\ 0 & \vdots & 0 & 1 & \vdots & \vdots & \vdots & \vdots \end{bmatrix} \quad (52)$$

$$X = [b_3 \ b_2 \ b_1 \ b_0 \ a_3 \ a_2 \ a_1 \ a_0]^T \quad (53)$$

$$B = \begin{bmatrix} -\omega_k^4 \mu''_k \\ \vdots \\ \omega_k^4 (\mu'_k - 1) \\ \vdots \end{bmatrix} \quad (54)$$

In the matrix representation of A and B, the ellipsis (\vdots) indicates that there are the rows as points in the frequency vector. The consequence of this representation is that our matrix equation is over determined; it means that the number of equations is bigger than the unknown variables. To overcome this issue, the Householder transformation, combined with the factorization QR is applied [74]. The complete flow diagram illustrated in Figure 2-19. The rational function coefficients are solved in the vector X.

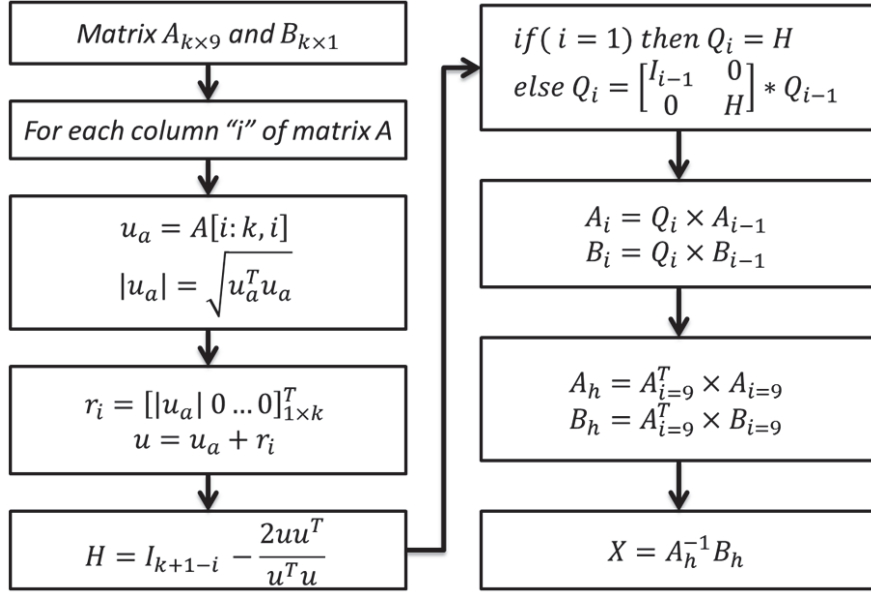


Figure 2-19 Flow diagram of the Householder algorithm that leads to the coefficients of (53)

2.3.3 Validation of the RFCMP model

The procedure of RFCMP coefficient identification was applied on the three materials listed in Table 2-2. As stated previously, the rational function degree is set to 4th. However, the algorithm was also tested for lower degrees (2nd and 3rd) in order to compare the improvements brought by RFCMP.

The measurements and models results for ferrite MnZn (N30) are plotted from 10 kHz to 100 MHz in the Figure 2-20(a). In order to observe their representations at high frequencies, a zoom from 10MHz is realized in Figure 2-20(b). Obtained improvements are more evident for the negative values in the real part of the CMP. In addition, the RFCMP model has a good agreement with measured values in all the frequency range of measurement (where the EMI filter frequency bandwidth is included).

Following the same logic, the coefficients identification for the nanocrystalline material was also performed (Figure 2-20(c)). Two particular characteristics for these materials can be highlighted:

- First, the material resonance is located at low frequencies (below 100 kHz). This is the reason why the only part observed of the CMP curve is still decreasing.
- Second, the measured permeability does not become negative in the frequency range under study.

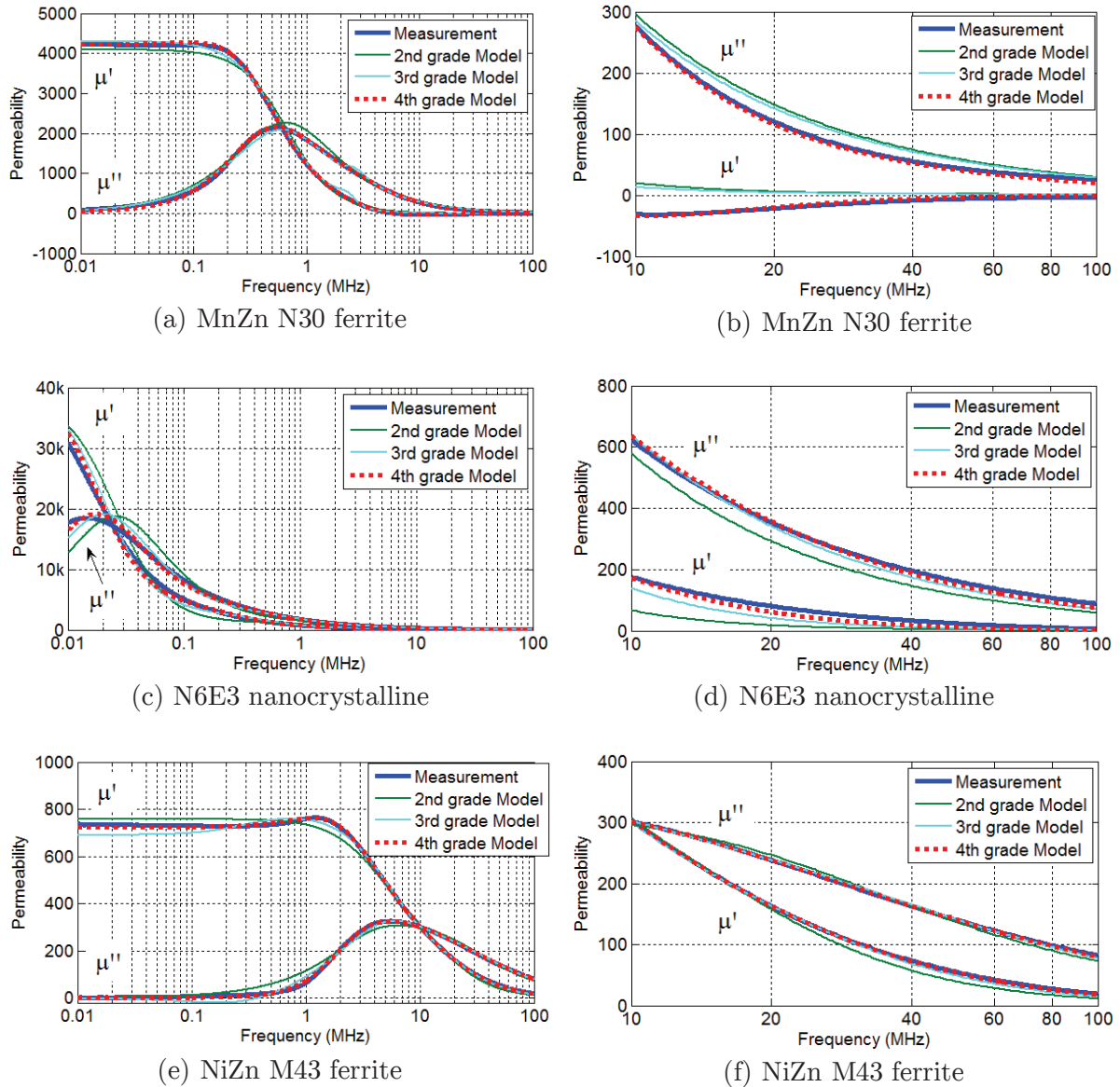


Figure 2-20 Validation of the RFCMP (4th grade) model for (a) N30 MnZn ferrite (b) N6E3 nanocrystalline and (c) M43 NiZn ferrite

As it can be seen in Figure 2-20(d), the RFCMP model for the nanocrystalline material fits better up to 100 MHz in comparison with the two other models. The CMP for the ferrite NiZn (M43) has also be modeled with RFCMP. This material is mainly used in radio frequency applications because its behavior stays inductive up to 200 MHz. As a consequence, no CMP negative values have appeared in the measurement. However, as observed in Figure 2-20(e), the representation of the CMP in low frequency has been improved, even close to the MRF (~ 5 MHz). The three models are compared at HF (Figure 2-20(f)) and better representation is still observed.

The obtained coefficients for the previous models (Figure 2-20) are listed in the Table 2-6 to Table 2-8 for the materials N30, N6E3 and M43 respectively. An additional column on these tables presents the coefficients of the RFCMP model when the CMP has 40% of variation (value estimated in the section of material dispersion). It is observed that the coefficients of the numerator (coefficients b_n) change linearly to the variation. It means that the variation in CMP can be taken into account when the simulation of the material is carried on, multiplying the numerator coefficients by the respective variation in percentage, while the denominator coefficients stays the same.

Table 2-6 Rational Function model coefficients for N30

Material N30	2 nd degree Rational F.	3 rd degree Rational F.	4 th degree Rational F.	4 th degree Rat.F+40%
b_3	--	--	1.270×10^{10}	1.782×10^{10}
b_2	--	1.788×10^{10}	1.536×10^{18}	2.143×10^{18}
b_1	1.868×10^{10}	1.725×10^{17}	1.434×10^{25}	2.001×10^{25}
b_0	-3.628×10^{16}	4.228×10^{24}	1.066×10^{31}	1.485×10^{31}
a_3	--	--	8.439×10^7	8.409×10^7
a_2	--	1.234×10^7	1.243×10^{15}	1.239×10^{15}
a_1	2.079×10^6	2.882×10^{14}	3.814×10^{21}	3.800×10^{21}
a_0	-8.863×10^{12}	9.822×10^{20}	2.526×10^{27}	2.512×10^{27}

Table 2-7 Rational Function model coefficients for N3E6

Material N6E3	2 nd degree Rational F.	3 rd degree Rational F.	4 th degree Rational F.	4 th degree Rat.F+40%
b_3	--	--	4.822×10^{10}	5.305×10^{10}
b_2	--	4.420×10^{10}	2.287×10^{18}	2.517×10^{18}
b_1	3.706×10^{10}	9.024×10^{17}	1.442×10^{25}	1.588×10^{25}
b_0	1.326×10^{16}	1.082×10^{24}	8.982×10^{30}	9.891×10^{30}
a_3	--	--	7.118×10^7	7.122×10^7
a_2	--	3.576×10^7	7.427×10^{14}	7.434×10^{14}
a_1	1.078×10^6	1.082×10^{14}	1.059×10^{21}	1.060×10^{21}
a_0	1.717×10^{12}	0.320×10^{20}	1.071×10^{26}	1.072×10^{26}

Table 2-8 Rational Function model Coefficients for M43

Material M43	2 nd degree Rational F.	3 rd degree Rational F.	4 th degree Rational F.	4 th degree Rat.F+40%
b_3	--	--	5.428×10^{10}	7.615×10^{10}
b_2	--	5.113×10^{10}	1.244×10^{19}	1.767×10^{19}
b_1	4.690×10^{10}	3.977×10^{18}	4.896×10^{26}	6.991×10^{26}
b_0	2.313×10^{18}	6.428×10^{24}	2.693×10^{33}	3.841×10^{33}
a_3	--	--	3.680×10^8	3.721×10^8
a_2	--	1.895×10^8	3.160×10^{16}	3.215×10^{16}
a_1	1.390×10^8	5.344×10^{15}	6.934×10^{23}	7.072×10^{23}
a_0	3.052×10^{15}	9.309×10^{21}	3.719×10^{30}	3.788×10^{30}

Until now, the measurement techniques were described and the modeling procedures to describe the magnetic material in small-signal levels were developed. Moreover, the proposed mathematical model based on the 4th rational function can be used in simulation softwares (mathematical or finite elements simulators). Even though, the most of the electrical simulator softwares are based on lumped circuit schematics. Thus, an electrical equivalent circuit for the ring cores inductors is presented as following.

2.4 Electrical equivalent circuit of the ring cores inductors

2.4.1 State of art

Ring core inductor (RCI) models have been a topic treated in the academic literature since many years. This kind of circuits is very useful and specific aspects have been developed because of RCI's wide fields of application. Some models were conceived to simulate such component with circuit simulator softwares. The difficulties regarding the inductive component simulation are linked to the representation of the material nonlinear behavior, and more precisely, their frequency-dependent CMP.

The model introduced in [36] is an equivalent circuit of the inductor (in this case a choke inductor), whose elements values were calculated from direct

measurements. The circuit model gets to represent the choke inductance up to 100MHz. However it cannot be easily applied to others components because it is not based on physical approach. By the same approach, but with some different technique, the model detailed in [75] has RLC parallel and series circuits with magnetic coupling coefficients (Figure 2-21(a)). The scattering parameters were used to identify all the EMI filter elements and the corresponding inductive components. This characterization technique can represent the inductor up to 30MHz, and the material properties are intrinsically involved in the final equivalent circuit. Nevertheless, the obtained model is specific to the filter's inductor and not suitable for others inductors. When different inductors are involved, new characterization have to be made.

Other approaches for ring core inductors are based on lumped elements. In [70] the gyrator element represents the link between the electrical and magnetic field in the circuit model. Each of the turns (or group of turns) in the winding is modeled by a gyrator-block. Then the HF behavior of the inductance is modeled using capacitors and resistors. The same technique was applied in [76], where the gyrators are modeled with dependent voltage sources considering neither the winding parasitic capacitance nor the winding-core capacitance (Figure 2-21(b)).

The RCI model in [38] is composed by a RLC lumped circuit. Each turn in the winding is modeled independently taking into account the capacitance between the core and the winding, and the magnetic coupling between turns. Because each of the turns in the winding is modeled, the number of elements increases with the number of turns. Similar approach is proposed in [37, 77]. They employ the distribute RLC parallel circuit to represent the impedance of the RCI. However, the number of elements increases with the number of resonances in the frequency-dependent impedance measurement (Figure 2-21(c)).

Recently, the Partial Element Equivalent Circuit and the Boundary Integral method (PEEC-BIM) detailed in [78] uses basically equivalent lumped circuits to represent the surface current coils of the magnetic core (Figure 2-21(d)). In order to build these surface coils, the CMP information has to be provided. Another approach is based on the transmission line method as detailed in [79]. The transmission line model replaces the inductors in RF domain. However, this model only considers the inductor as a linear component (Figure 2-21(e)).

Finally, the models presented in [35, 80-82] take into account the nonlinear frequency-behavior of the nanocrystalline materials by models based on Cauer or Fosters expressions. Particularly, the model in [35] introduces the HF effects of the

material in the inductor model. The equivalent circuit is fitted with the iterative rational function approximation (IRFA) method. Nevertheless, the final equivalent circuit has some negative elements' value that is not easy to reduce.

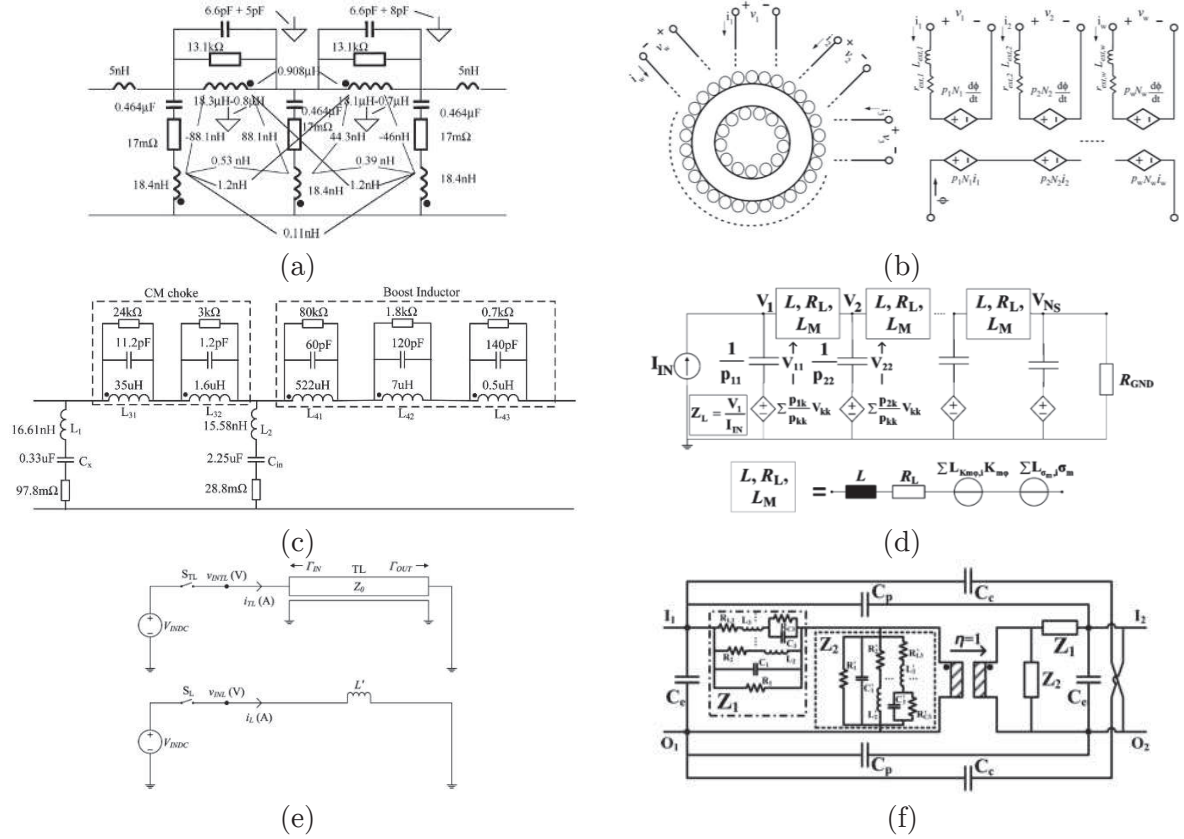


Figure 2-21 Different models for ring core inductors in HF (a) Measurement with scattering parameter [75] (b) Gyration [76] (c) RLC lumped circuit [77] (d) PEEC-BIM [78] (e) Transmission line [79] (f) Cauer-Foster [35]

2.4.2 New RCI model

All of the previous approaches have limits to model the magnetic materials. They consider inductor like a black-box. Instead of that, the new RCI model of the ring core in this work is based on the magnetic material characteristics, and complementary elements to build the final RCI model. The block diagram show in Figure 2-22 identifies all the elements of the new RCI model. The magnetic block, together with the dielectric and losses blocks are linked to the CMP of the material, which depends on the number of turns. The coil-capacitance block represents the parasitic capacitance of the winding. The wire block is the resistance of the wire, which has been detailed previously and modeled with the equation (27). The HF elements block, where the leakage inductance and the transmission line effects are considered.

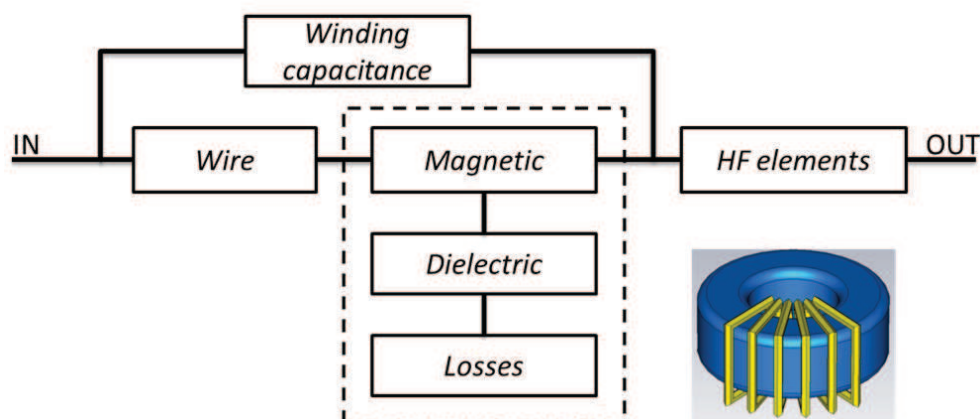


Figure 2-22 Block diagram of the equivalent circuit model of RCI

2.4.3 Parasitic capacitance

The term of *parasitic capacitance*, also known as stray capacitance, is one of the most difficult parameters to estimate. In this work, the parasitic capacitance of the new RCI model is subdivided into two components:

- The *material capacitance* (C_m)
- The *winding capacitance* (C_b)

Firstly, the winding capacitance is evaluated in this section. A testis performed for three ferrite materials with the same number of turns (N) and the same ring core size. In order to have a high value of the stray capacitance, N is chosen arbitrarily *high*. The ferrite N87, N30 and T35 from Epcos®[®], with dimensions $D_E = 20\text{mm}$, $D_I = 10\text{mm}$ and $H_E = 7\text{mm}$, were wound with 48 turns. This number of turns is the maximum single-layer winding that were wound around the ring core with a 5mm diameter round wire. The initial magnetic permeabilities of these materials, given in datasheets, are 2200, 4300 and 6000 respectively. The module and phase of the measured impedances are illustrated in Figure 2-23. It is observed that the first resonance frequency of the impedance is different for the three materials because of their inductance value at low frequency. Indeed, the inductive value makes a resonance with the parasitic capacitance introduced by the winding, which can be considered the same for these three inductors. From the Figure 2-23, a simple parallel RLC circuit approach for the first resonance leads to the values listed in Table 2-9. There is a quite evident inductance variation due to the material, while the parasitic capacitance can be considered as a constant for the three cases. Moreover, the high frequency impedance (above 10 MHz) follows the same tendency for the three inductors.

Table 2-9 Equivalent RLC circuit of the first resonance (48 turns winding)

Material	R (kΩ)	L (mH)	C (pF)
N87	163.8	4.60	4.6
N30	63.7	9.63	4.9
T35	61.8	11.48	5.1

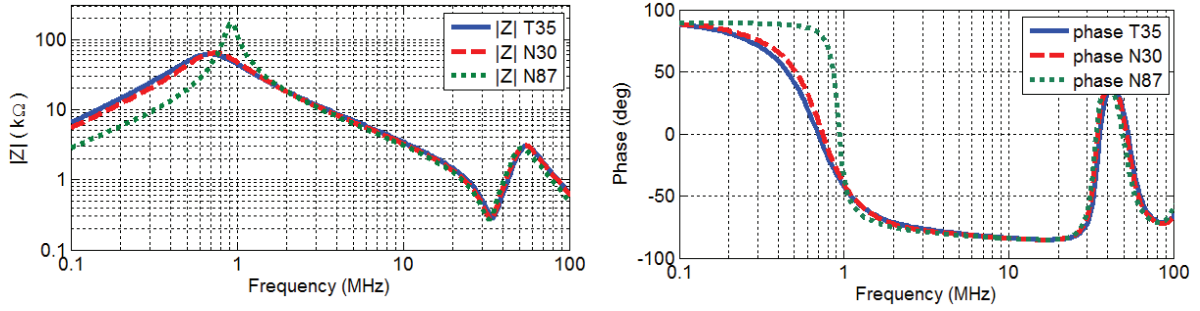


Figure 2-23 Impedance of three ferrite materials with the same number of turns and the same core size

As a consequence, the core material of the inductor and the winding can be modeled independently. The parasitic capacitance is observed when the number of turns is increased (here only the ferrite N87 is presented). As shown in Figure 2-24(a), the first resonance of the inductor is shifted to lower frequencies and the corresponding capacitance follows a linear increasing trend with regard on the number of turns. However, when N is low, below 25 turns for example, as shown in Figure 2-24(b), the capacitance is inversely proportional to N^2 . The explanation for this phenomenon is illustrated in the same figure; the resonance frequency stays invariable even if the number of turns increases. And it puts in evidence the capacitance produced by the magnetic material or the *material capacitance*.

In the Figure 2-25, the stray capacitance of the inductor can be modeled by two equations: the *material capacitance* with $C_m(1/N^2)$ and the winding capacitance with $C_b(N)$. Both of them contribute to the first resonance frequency of the ring core inductor impedance. The capacitance C_m can be calculated using the proposed expression given by (55), where f_m is the material frequency resonance, μ_i is the initial permeability, $\mu_0 = 4\pi \times 10^{-7} H/m$ and H_E, D_E, D_I are geometric constants of the ring core.

$$C_m(N) = \frac{1}{2\pi f_m^2 \mu_i \mu_o H_E \ln\left(\frac{D_E}{D_I}\right) N^2} \quad (55)$$

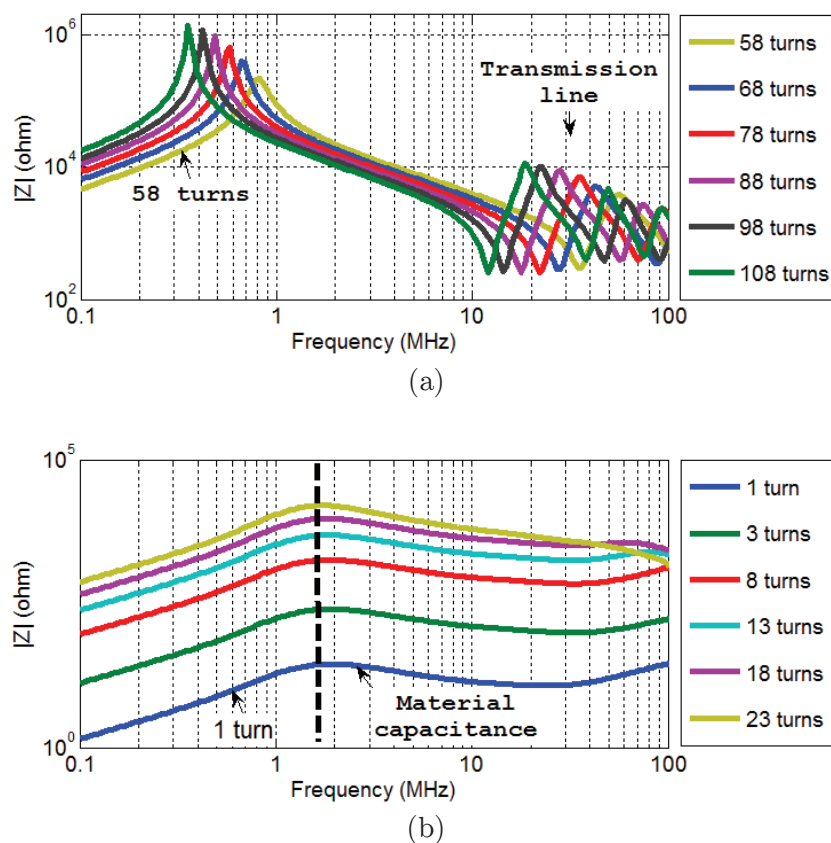


Figure 2-24 Inductor's impedance with ferrite N87: Influence of turns (a) $N \geq 58$ (b) $N \leq 23$

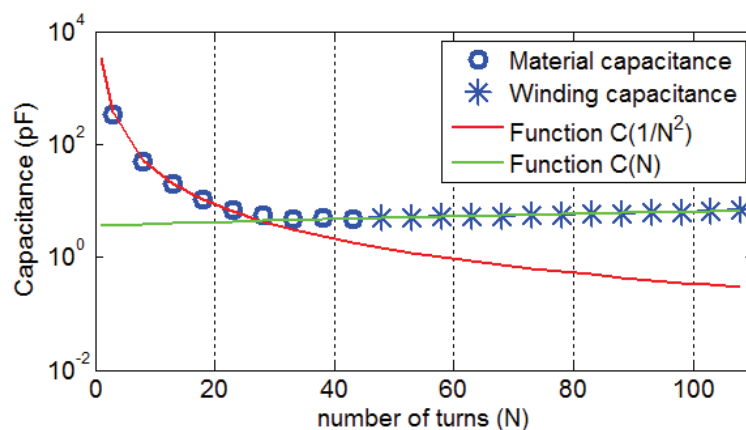


Figure 2-25 Stray capacitance

However, the expression (55) is only a *reference value* of the *material capacitance*. That means, C_m is a constant value in the frequency f_m which it is not the case for all frequencies above the MRF. To overcome this point, a more adapted circuit model is proposed based on R-C ladder network, as shown in the Figure 2-26. The resistance elements will represent the losses in the material and the capacitive elements the dielectric behavior of the material. As previously stated, the capacitance

elements will be adjusted by $1/N^2$ if the number of turns changes. In addition, the losses of the material represented by the resistance elements will increase by N^2 because they are linked to the CMP.

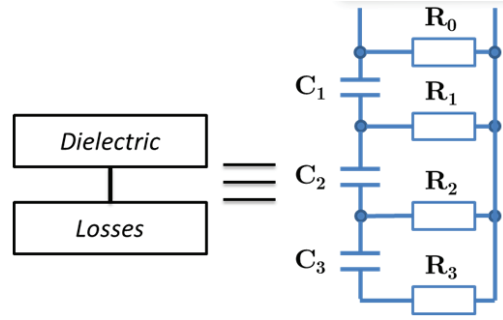


Figure 2-26 Circuit model for the *material capacitance*

The presence of the RC circuit in the model is basically due to the MnZn ferrite material. The *material capacitance* will play an important role in future characterizations because it modifies the magnetic behavior. This part is going to be detailed in the next chapter. Whether other materials intended to be characterized may or may not include these elements in the final model. For example, the nanocrystalline material, such as N6E3, will not present this effect because the real part of the CMP remains positive in the frequency bandwidth up to 100 MHz. It is the same for the NiZn ferrite. Otherwise, the winding capacitance C_b is present for all the ring core inductors.

In [83], the winding capacitance C_b is calculated with the expression (56) where the coefficient k is adjusted, p is the pitch of the spire, r is the radius of wire, the diameter of winding is represented with $D = p/2\pi$. The model was applied for solenoid inductors with air core. Nevertheless, in our case, the correction factor k can be adjusted for each material, the form of the core can be considered as solenoid due to the linear evolution of the winding capacitance with the number of turns. For example, the ring core ferrite N87 with $N=20$ turns and $D_E = 20\text{mm}$, $D_I = 10\text{mm}$ and $H_E = 7\text{mm}$, the wire diameter equals 1mm and the average distance between the wire and the magnetic material equals 0.5mm, is fitted with this equation and the factor k results equal to 0.15. The winding capacitance is approximately 4pF, which is close to the measured 4.12pF.

$$C_b = k \sum_{i=0}^N \left[\frac{\epsilon_o \pi^2 \left(\frac{p}{2\pi} \right) (N-1)}{\log \left(i \frac{p}{2r} \right) i} \right] \quad (56)$$

Another approach is proposed here using the geometric characteristics of the inductor. The surface of the wire is considered as a constant one and approximated with (57). The round wire is considered as a ribbon where the diameter of the wire is equals to the width of the ribbon. As shown in Figure 2-27, the diameter of the wire (dc), the distance between the winding and core (bf), the external distance between two turns (me), together with the geometric values of the ring core are employed to calculate the angle between two spires (58). The winding capacitance can then be approximated with the expression (59).

$$A_w = dc * (2H_E + D_E - D_I + 8bf + 4dc) \quad (57)$$

$$\theta = 2 \sin^{-1} \left(\frac{dc + me}{D_E + dc + 2bf} \right) \quad (58)$$

$$C_b = 8.85 \times 10^{-12} \frac{A_w}{(D_E/2 + D_I/2) * \sin(\theta/2)} N \quad (59)$$

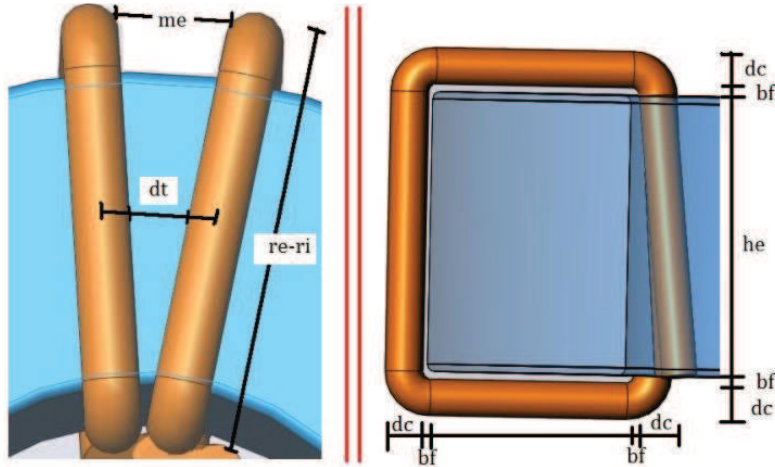


Figure 2-27 Geometric definitions for the winding capacitance calculation

These expressions are susceptible to change due to the small values of some parameters in contrast with the ring core dimension. Nevertheless, a correction factor could be added in the expression (59) to adjust the linear variation of the winding capacitance with the number of turns.

The new RCI model subdivides the stray capacitance into the material capacitance and the coil capacitance. The first is modeled with R-C network ladder and the second with analytical expressions.

2.4.4 Skin effect in the magnetic material

The skin effect in the ring core has influence in the frequency-dependent impedance of the inductor. Two kinds of materials have been studied: ferrite and nanocrystalline. Both have different characteristics that will affect the skin depth value. The ferrite materials are made of granules compressed in small crystals with an average dimension of 10 to 20 μm . The electrical resistivity is higher for the NiZn ferrites in the order of $M\Omega \cdot m$, while for the MnZn ferrite this value is in the order of $\Omega \cdot m$. On the other hand, the nanocrystalline material is composed by 10nm crystals, which forms a ribbon with a thick of 20 μm after a *rapid solidification* process. The electrical resistivity of the nanocrystalline is very small, usually in the order of the $\mu\Omega \cdot m$.

The skin effect given by the expression (60) shows the relation between the absolute permeability of the material and the resistivity. Two materials are compared: the N30 ferrite ($\rho = 0.5 \Omega m / \mu_i = 4300$), and the N6E3 nanocrystalline ($\rho = 1.15 \mu\Omega \cdot m / \mu_i = 90000$). In the Figure 2-28(a) the skin depth in the ferrite is illustrated when the permeability value is constant ($\mu = 4300$) and when the permeability is modeled with new RIC from the Table 2-6. It is observed that both curves are superposed up to 300-400 kHz. After that frequency, more precisely, below a 10 μm skin depth value, the two curves start to diverge. The change in the curve indicates that the material cannot be considered as a homogeneous one if low values of the skin depth are attempted. In the case of MnZn ferrite, it was attributed to the *material capacitance*, which has been previously modeled with RC elements.

However, the nanocrystalline material presents a different behavior. As shown in Figure 2-28(b), the skin depth curve for the constant permeability ($\mu = 90000$) and the new RCI model in Table 2-7 are superposed up to 9 kHz. Above that frequency, or below the 20nm of skin depth, the curves become different. Unlike the case of MnZn ferrite, the nanocrystalline material does not present negative values in the real part of its CMP. Therefore, this skin depth has to be modeled separately with RL elements. In this work the topology shown in Figure 2-29 is adopted. The number of RL elements will increase if more accurate representation is needed.

In conclusion, the skin effect for the MnZn ferrites is not as higher as the dielectric effects, and then the RC circuit is used to model de material above the skin effect at 10 μm . Otherwise, in nanocrystalline material the skin effect is more evident and the RL circuit is used to model the material above the skin effect at 20nm.

$$\delta = \sqrt{2\rho/\omega\mu} \quad (60)$$

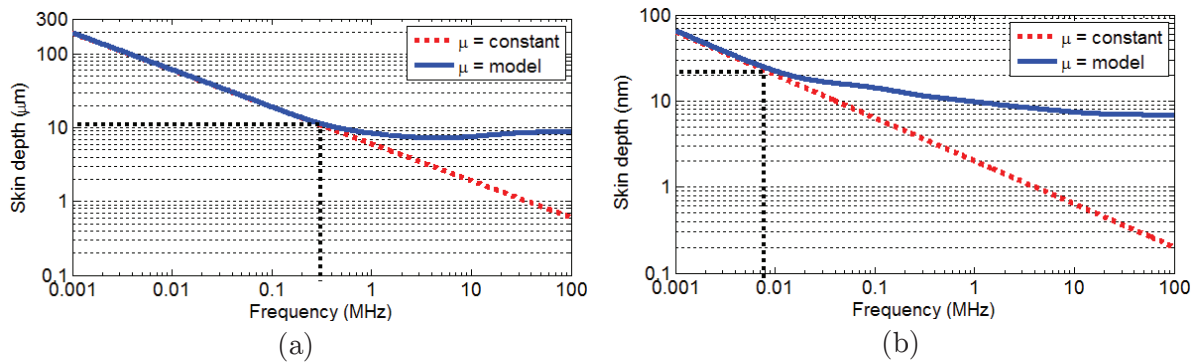


Figure 2-28 Skin depth of the materials (a) ferrite MnZn N30 and (b) N6E3 nanocrystalline

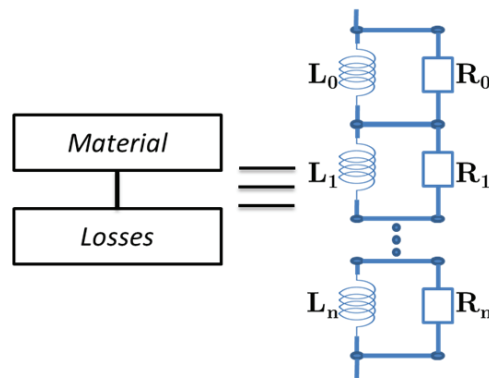


Figure 2-29 Circuit model of skin effect in the material

2.4.5 High frequency parasitic elements

In the CMP measuring section, the term of leakage inductance described the HF effects or parasitic elements that have been compensated from the impedance measurement in order to extract the CMP information. To remind, the number of turns was limited to no more than 5 turns and the parasitic capacitance was neglected. However, the ring core inductor could have more number of turns and then the leakage and parasitic capacitance cannot be neglected anymore.

In [51], the leakage inductance (L_{leak}) was modeled with the expression (61). This expression links the angle of the surface (θ) with the leakage inductance. However, this approach is correct only if the second resonance frequency in the impedance measurement is attempted to be modeled. In [38], the analytical investigation of the leakage inductance was performed. The geometrical-based model of the leakage inductance was then used to simulate the ring core impedance with a nanocrystalline material. However, the high frequency resonances were not well represented by the model, moreover the details about the other resonances were not pointed out.

$$L_{leak} = \mu_{eff} \frac{0.4\pi N^2 A_e}{l_e \sqrt{[(\theta/360) + (\sin(\theta/2)/\pi)]}} \quad (61)$$

In this work, the leakage inductance is included into the high frequency parasitic elements. The additional HF resonance frequencies when N increases (long copper wire length) can be modeled by the transmission line theory. The advantage of the transmission line is the option to model the resonances with RLCG lumped circuits or with the element TLOSSY of PSPICE, as shown in Figure 2-30. Then the accuracy of the model in high frequency will depend on the correct modeling of the transmission line. Nonetheless, the analytical expression for a toroid winding is not detailed here and could be considered for a future research. Otherwise, the existing model of the transmission line can be fitted to the measured impedance in order to determine the corresponding RLCG elements.



Figure 2-30 Transmission line (a) lumped circuit (b) TLOSSY element

2.4.6 Validation of the new RCI model

Two materials were tested to evaluate the new RCI model: the ferrite N87 and the N6E3 nanocrystalline. First, the CMP of ferrite N87 was measured and then modeled with the equivalent circuit illustrated in Figure 2-31. The simulation was performed with Orcad-Cadence® and the comparison between the measurement and the model simulation is depicted in Figure 2-32.

As shown in Figure 2-32(a), all the elements for the impedance when $N=1$ were identified and linked to the number of turns. The parasitic capacitance ($C1$) varies linearly with N , such as the DC resistance ($R1$). The inductance ($L1$) and resistances ($R2$ to $R5$) increase by factor N^2 . The *material capacitance* is represented with the capacitances ($C2$ to $C4$), which are updated by the factor $1/N^2$ as previously stated. The transmission line parameters have been identified by fitting process with one meter cable wound around the ring core. The length is then updated by N . Notice that the losses in the wire (parameter R) depends on frequency and the expression can be configured as more convenient possible in order to represent with more accuracy the amplitude in HF resonance frequencies. The simulation and

measured impedances for $N=1$ are compared in Figure 2-32(b). Indeed, the impedance curve represents also the CMP of the material, which has a good agreement up to 100 MHz. The result of simulation for $N=10$ (Figure 2-32(c)), has a little difference above 40 MHz that is result of the variation in the TLOSSY parameters. In the case of $N=30$ (Figure 2-32(d)), the representation of the impedance has a good agreement up to 70 MHz.

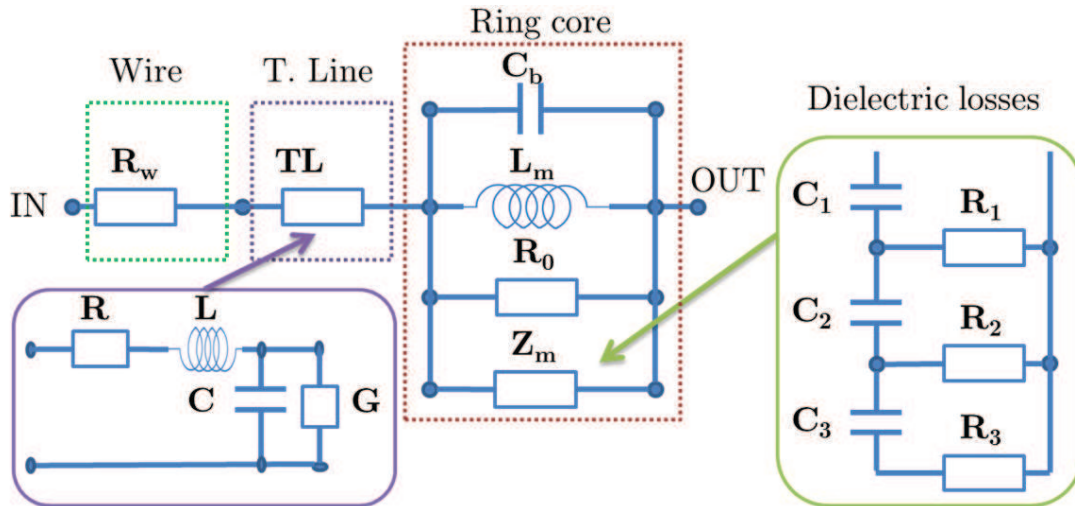


Figure 2-31 Equivalent circuit for the ferrite RCI

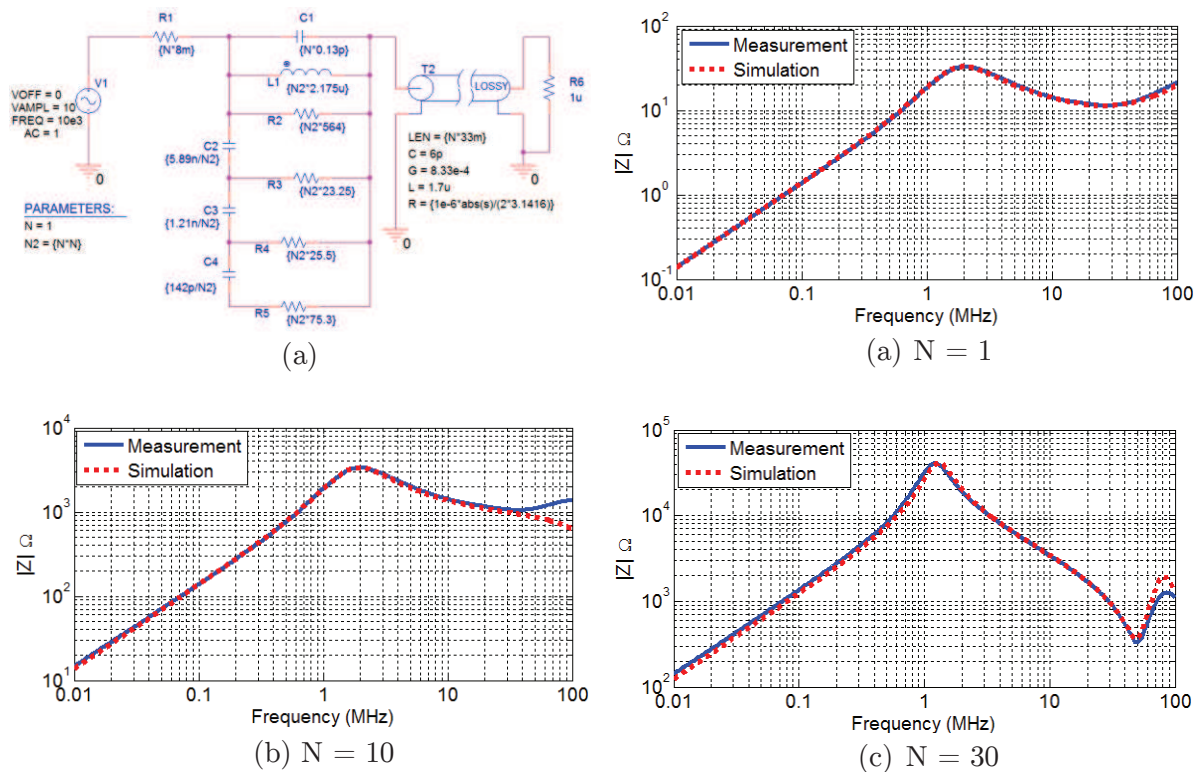


Figure 2-32 (a) Equivalent circuit and simulation (b) $N=1$ (c) $N=10$ and (d) $N=30$

The same technique is used to model the nanocrystalline material N6E3. In this case, the *material capacitance* (dielectric losses) is neglected and the skin effect is preponderant. The equivalent circuit of the material is presented in Figure 2-33.

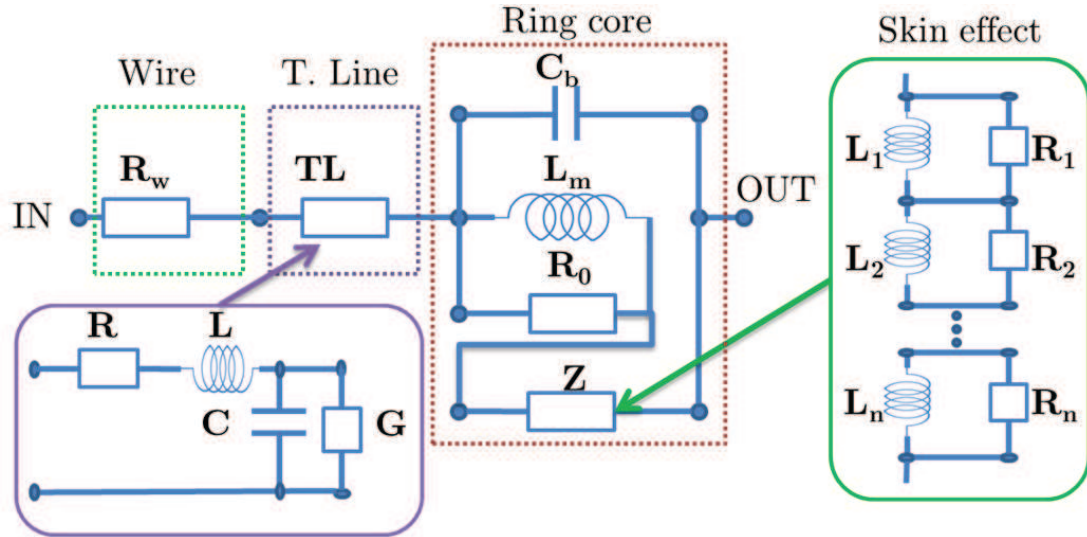


Figure 2-33 Equivalent circuit for the nanocrystalline RCI

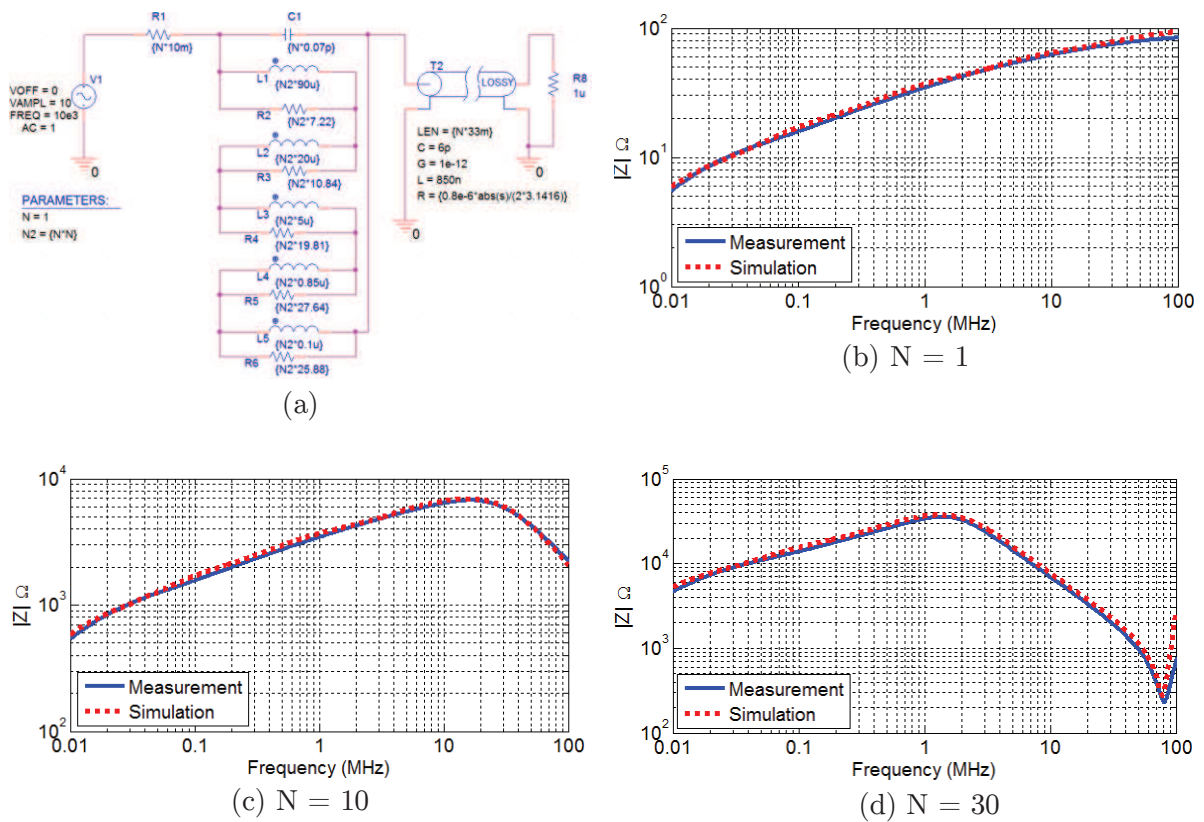


Figure 2-34 (a) Equivalent circuit and simulation (b) $N=1$ (c) $N=10$ and (d) $N=30$

The ring core is modeled with the parasitic capacitance, the low frequency inductance, the skin elements, the dc resistance and a transmission line. As shown in Figure 2-34(a), these element were identified with a fitting procedure and the simulation and measurement results are illustrated in Figure 2-34(b) for $N=1$. The simulation and measurement result for the cases of $N=10$ and $N=30$ are also illustrated showing a good agreement in the range of frequency up to 80MHz. These results validate the new RCI (impedance when $N=1$) and the corresponding simulations when N increases.

2.5 Conclusion

In this chapter the complex magnetic permeability (CMP) has been addressed. The CMP is the first approach to characterize the nonlinear behavior of the magnetic materials with a small-signal. In order to measure the CMP, the typical magnetic material test fixture was employed. However, due to the limitation linked to the size of the samples, this method was improved. This proposed method takes into account the leakage inductance, the losses and the number of turns. Moreover, the identification of two capacitances was detailed. Indeed, the notion of *material capacitance* was introduced to represent the negative values of the CMP in HF. Meanwhile, the dispersion in the CMP and the influence of the low level voltage were also studied in different scenarios.

Once the experimental data has been obtained, the modeling of the CMP was developed. First, the frequency evolution of the CMP was modeled with the proposed rational function of CMP. This model was validated by comparing with other existing models and showing that a better representation of the material behavior in HF is obtained up to 100MHz.

Second, the CMP has been modeled with an equivalent circuit. Many other models have introduced an equivalent circuit to model the ring core inductor. However, the link with the magnetic material was not often addressed. Then, the proposed new RCI model was developed to overcome this. Two magnetic materials were modeled (ferrite and nanocrystalline materials), and the simulation results shown a good agreement with the experimental ones.

Finally, the CMP can be enough, in certain cases, to model the magnetic material. However, different operating conditions like the current level or the temperature can also change the behavior of the material. For that reason, a high-signal characterization is investigated in the next chapter.

Chapter 3. High-signal characterization and modeling of the magnetic core

The magnetic material characterization is usually realized at low power levels (low current and low voltage). When the inductor is subjected to larger currents through its windings, the principal characteristics of the filter (inductance evolution with current and frequency) vary. Non-linear models of inductors become necessary to include these variations, basically for the estimation of inductance and losses. In this chapter the magnetic hysteresis loop will be characterized and a non-linear hysteretic model is studied.

3.1 Introduction

The design of an EMI filter by simulation needs to use an accurate model of the passive components. This is essential when reducing the uncertainty on the behavior of the filters under specific operating conditions. The inductive components are in part responsible for the HF behavior of the EMI filter, which are made from magnetic materials that can be subjected to different magnetization levels.

Usually, the datasheets of these magnetic materials provide information about the CMP curves which allow the calculation of the inductance (real part of CMP) and the losses – damping effect (imaginary part), for example in [84]. However, two limitations can be observed:

- First some ferrites (such as MnZn ferrites) are applied for self-inductance or choke inductance in EMI filters at very high frequencies (above some MHz), even if the CMP information is not specified for these frequencies. In that case, direct measurements can be performed, as developed in chapter 2.
- Second, this CMP information is obtained from a small-signal measurement process (usually with an impedance analyzer) where the applied current to magnetize the material reaches milliamps as maximum. Then, the measurement is typically in the Rayleigh zone, which does not always correspond to the real operating conditions of the material.

Therefore, most of the inductor models are based on small-signal levels [36, 38] and consequently, the nonlinear effects of the material are not taken into account.

The complexity of the nonlinearity in the material model is linked to various parameters such as the applied current, frequency, temperature and intrinsic material properties. In the literature, hysteresis models are widely used for laminated electrical steels such as in [85]. For HF applications, some authors use static models with additional parameters to consider the frequency effect, as described in [86] where the inrush current of a ferrite-core inductor is studied. In [87], the hysteresis loops are modeled with the Basso-Bertotti static model with two additional parameters to represent the influence of the frequency on the hysteresis loop.

In the present work, the first point concerns the magnetic behavior law of the material that is approached with a quasi-static magnetic hysteresis model (Jiles-Atherton model) together with an additional parameter linked to the *material capacitance*. In chapter 2, the notion of material capacitance (C_m) was introduced to represent the negative values of the real permeability component in HF ferrites. The effect of this parasitic capacitance is emphasized in [88] by the hysteresis loop measurement. The proposed hysteretic and capacitive material behavior model is called hereafter HCM. Moreover, this hysteretic model is compared with an average BH-curve model in order to highlight the advantages when considering the hysteresis information.

The second point of this work deals with the experimental characterization of the material behavior law. Measurements of hysteresis loops in HF ranges (up to 100 kHz) are described in [89], where a two-coil method (transformer configuration) is applied in the measurement setup. In [87] an automatic test system with two coils, as in the previous case, was presented to characterize the hysteresis loop of MnZn ferrites. A different procedure is presented in [62], where a pulsed excitation is applied to a two-coil configuration to characterize the hysteresis loop, including minor loops that reach some kHz. In all these references, the two winding configuration is basically proposed since the primary side requires a significant number of turns to saturate the core (which usually has low permeability). And the voltage of the secondary, i.e. the electromotive force, allows deducing the magnetic flux density. Another technique, that obtains the hysteresis loop and core losses, consists in a pulsed excitation with one coil as reported in [60]. However, the HF effects in the measurements setup are not usually addressed. Hence, a characterization method of the hysteresis (up to 1MHz) using a single turn of flat copper ribbon (STFC) is proposed. The advantages of this structure are: no magnetic coupling with another winding, no inter-turns capacitances and no proximity effect. Nevertheless, the calculation of the magnetic flux density is made from the primary voltage that also includes the resistive component.

Finally, the following steps will be adopted in this chapter:

- The characterization of the material using a single turn of flat copper ribbon (STFC)
- The magnetic behavior law including material capacitive effect
- Validation of the inductor model used in two EMI filter applications (differential and common modes)

The chapter is organized as follows. First, the proposed measurement setup is detailed. Second, the parameters of the average BH-curve and HCM are identified from the experiment. Third, the measuring setup is described and the robustness of the obtained model is discussed using square and saw-tooth signals to finally be compared with measurements. Fourth, the hysteresis model is applied for a differential mode inductor (current with DC bias) and a common mode coupled inductor.

3.2 Experimental setup

3.2.1 Overview

Two prototypes were designed in order to characterize the hysteresis loop for ring core magnetic materials. In both cases, two windings have been wound around the core. In the first prototype shown in Figure 3-1(a), the primary is supplied by a sinusoidal voltage from the RF amplifier (AR 75A250A) while the current is measured with a hall current probe (TCP 202). The electromotive force is measured in the secondary, as recommended in [60]. However, the parasitic elements such as wire losses, inductive and capacitive couplings between windings became preponderant when the signal frequency increases. These elements are difficult to discriminate and quantify. Therefore, to reduce the parasitic elements, a second prototype has been built. The configuration, shown in Figure 3-1(b), reduces the contact resistance of the connection and the coupling effects are minimized. The Faraday cage around the device under test was included to shield the measurement from external RF sources. Nevertheless, the measurement showed that the cage becomes an optional element in the frequency range considered. The measured hysteresis loop by the second prototype is shown in in Figure 3-2.

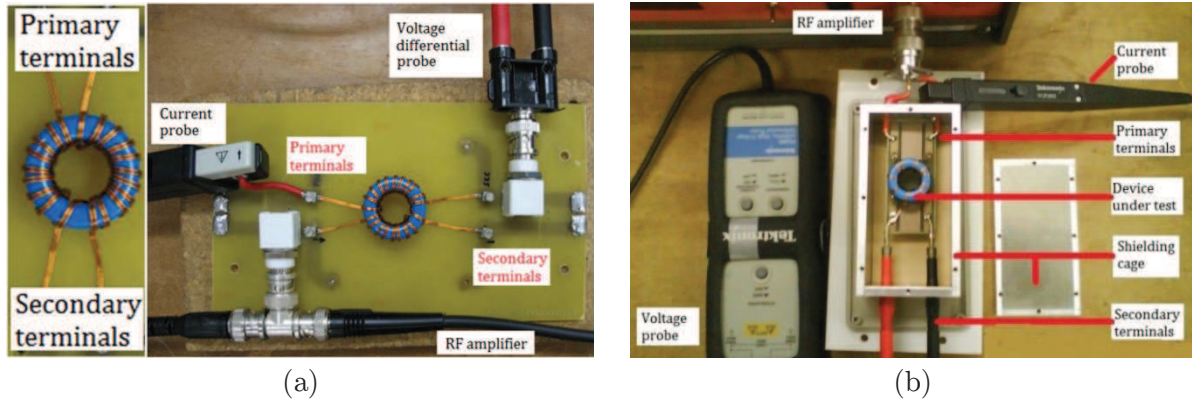


Figure 3-1 Two-coil measurement prototype (a) first and (b) second prototype

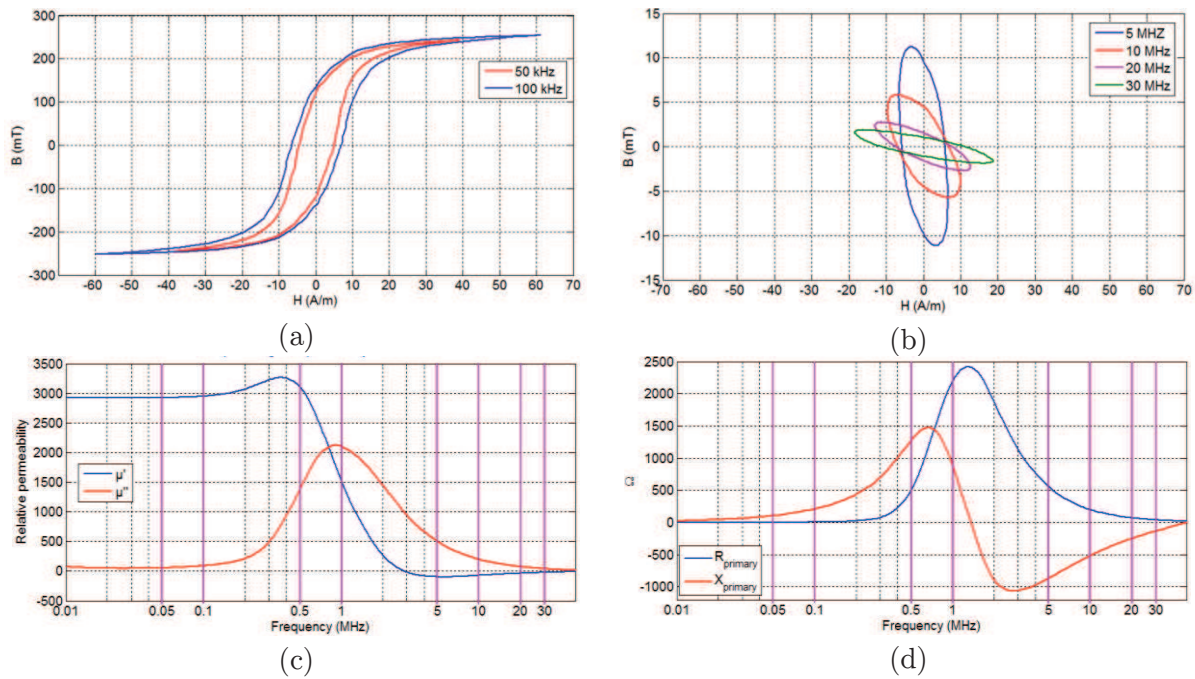


Figure 3-2 N30 ferrite hysteresis loop measured with the second prototype (a) 50kHz and 100kHz (b) above 5MHz (c) CMP (small-signal) (d) equivalent impedance of CMP

The typical hysteretic behavior of a N30 ferrite is observed in Figure 3-2(a) and evaluated in the frequencies 50 kHz and 100 kHz. However, when the frequency is increased, the *hysteresis loops* show the phase displacement between B and H. The hysteresis loop is no longer in the first and third quadrant of the BH, which means a negative slope or *negative permeability* of the material (Figure 3-2(b)). Indeed, the complex magnetic permeability (in Figure 3-2(c)) and its equivalent impedance (in Figure 3-2(d)), also represent this change in the frequency range above 1MHz. The second prototype measures the hysteresis loop and this phase displacement indicates the HF parasitic effects. Although, this parasitic effects need to be identified in order to do an adequate characterization of the hysteresis loop. The dynamic effect in the material can also be the explanation of this behavior in HF [90]. However as

mentioned before, the *material capacitance* will include all these effects. In fact, to reduce more the influence of other parasitic effects and improve the hysteresis measurement setup, a third prototype using STFC is proposed and detailed as follows.

3.2.1 Improvement of the experimental setup

In high frequency, the winding is one of the most important elements for the hysteresis loop characterization. Even if one or more coils are used, the method to extract the hysteresis information from HF measurements needs to avoid the extra parasitic capacitance which becomes relevant when frequency increases. For all that, the STFC is proposed and illustrated in Figure 3-3.

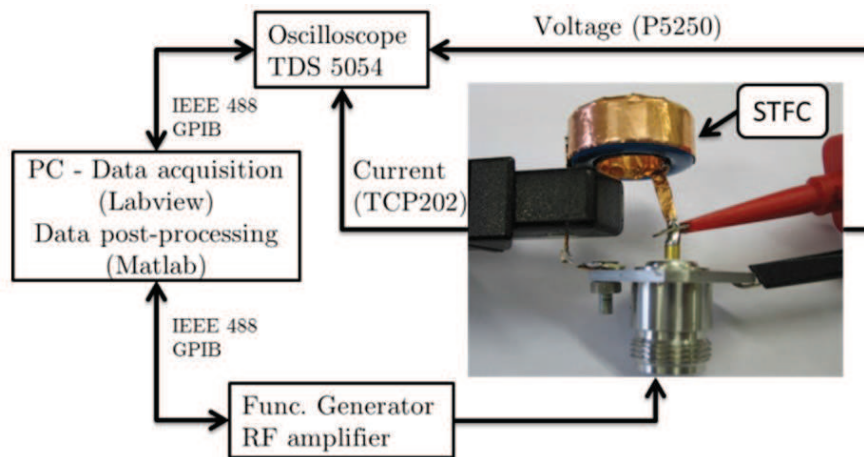


Figure 3-3 Experimental setup used to characterize the magnetic material using a single turn of flat copper ribbon

In this STFC configuration, the magnetic coupling with another winding, the inter-turns capacitances and the proximity effects between the turns are avoided. To emphasize this point, the measured impedances without the core of both configurations (the STFC and one-turn wire) are compared in Figure 3-4. For these measurements, the current and voltage probes are connected and powered (Figure 3-3). The impedance introduced by the STFC at HF is observed to be lower than the one-turn wire.

The utilization of a coil with multiple turns increases the core perimeter this improves the magnetization homogeneity of the core but also lead to a higher inductance and inter-turns capacitance. The proposed approach using STFC aims to reduce the winding stray capacitances to identify the parasitic capacitance due to the

magnetic material. Considering all these aspects, the proposed characterization method has an advantage in comparison with classical one.

To make the STFC, the thickness of the copper foil used in this test is $40\mu\text{m}$ so that the skin effect in the copper can be neglected in the considered frequency range. Also, the length of the wire (between the N-connector and winding) must be as short as possible to minimize the resistance plus enough space to insert the current probe. To illustrate the electromagnetic behavior of the proposed STFC, a simulation with the COMSOL multiphysics® software was carried out as shown in Figure 3-5. The electric potential and the magnetic flux density are also illustrated.

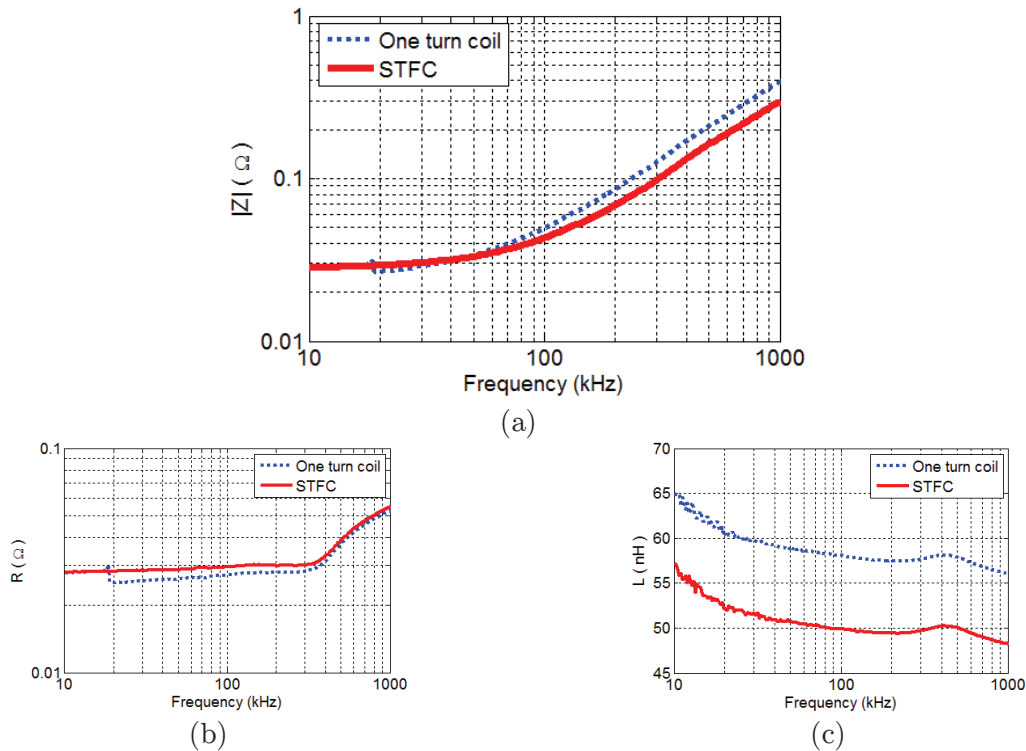


Figure 3-4 (a) Impedance (b) Resistance and (c) Inductance of the one-turn wire and STFC

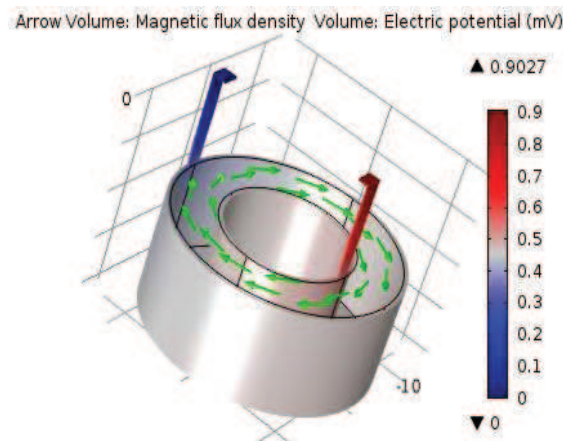


Figure 3-5 Electric potential and magnetic flux density in the proposed connector

The simulation result confirms the observed effect of less leakage with the STFC configuration (Figure 3-4). From this simulation without the ring core, the inductance and resistance of the copper foil are found to be, respectively, 20nH and 0.57m Ω . An additional measurement of the STFC (without magnetic core and the two probes connected) results in 49nH and 30m Ω for the inductance and resistance respectively. The difference in results can be linked to the impedance introduced by the probes and the contact resistance of the measurement connector.

3.2.2 Connector characterization

The measurement of HF hysteresis is cumbersome due to parasitic elements. Even if the proposed configuration reduces these parasitic elements, some of them still need to be identified for a better representation of the configuration setup. The equivalent circuit of the measuring configuration is shown in Figure 3-6. The power source, which applies a variable voltage, is represented with a voltage source V_{in} and a series impedance Z_{in} . Then, the N-connector is represented by a capacitance C_{cn} with a R_w wire resistance.

The magnetic material under test (MDUT) is represented with L_m and R_m connected in series, whose values are calculated from the nonlinear inductive and nonlinear losses behavior. As explained in the introduction section, an additional element is added in parallel and corresponds to the *material capacitance* C_m (dielectric effect). The importance of taking into account this element is to represent the phase displacement in the hysteresis loop measurement in the HF range.

The voltage-differential probe is represented by the capacitance (C_{inst}) and the resistance (R_{inst}). The impedance coupling effect of the current probe is considered in the STFC (Figure 3-4). In practice, two measurements are carried out, the voltage over the MDUT (V_{mea}) in parallel to parasitic elements and the current in the input (I_{mea}).

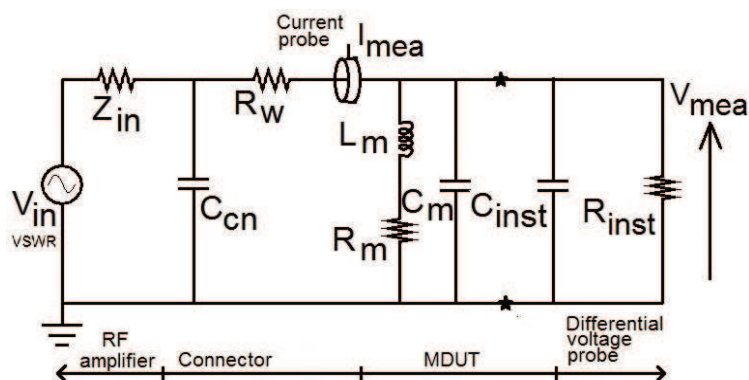


Figure 3-6 Equivalent circuit of the setup configuration

To determine the parasitic capacitance value of the N-connector connected to the STFC, an electrostatic study using the COMSOL multiphysics® software has been carried out. This simulation shows a low capacitance C_{cn} , as observed in Figure 3-7 where a capacitance value of 1.46pF is obtained and confirmed by the measurement (1.5pF). This result shows that there will be no significant influence of the parasitic capacitance (within the connector) on the considered frequency range.

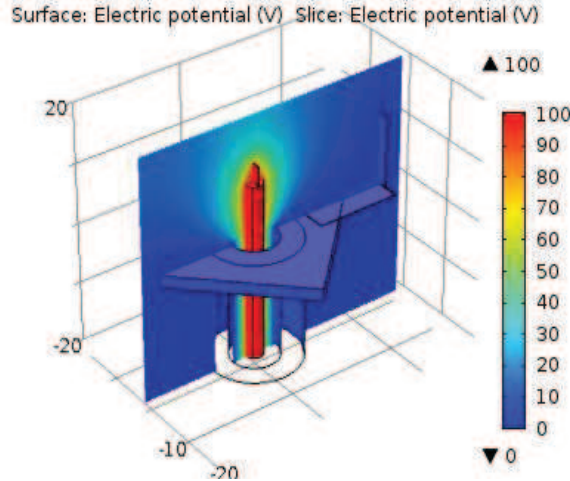


Figure 3-7 Electric potential on the N-connector

3.2.3 Experimental setup

To perform an automatic hysteresis loop characterization the experimental setup shown in Figure 3-3 was implemented. The reference signal is generated by an Agilent 33250A Arbitrary Waveform Generator, with a power output of 0dBm and 0V DC offset. This reference signal is amplified with the AR 75A250A RF amplifier of 75W maximum output power and with variable gain. The output voltage is applied to the MDUT. The voltage is measured with a P5250 differential voltage probe and the current with a TCP 202 current probe. Both probes are connected to a TDS 5054 Tektronix oscilloscope. The delay time introduced by the probes in the measurement setup is corrected in the post-processing stage. Finally, the magnetic flux density B (obtained from the voltage measurement) and the magnetic field strength H (obtained from the current measurement) are post-processed on a personal computer.

3.2.4 Mismatch impedance of RF amplifier

The RF amplifier has been designed with a nominal output impedance of 50Ω , and ideally supplies full power when is applied to 50Ω load. That is not the case of the MDUT because the impedance varies with frequency, so then the condition of mismatch impedance appears. The manufacturer datasheet includes the Voltage

Standing Wave Ratio (VSWR) parameter which represents the ratio between source output impedance and the load impedance.

The equivalent circuit of the RF amplifier is shown in Figure 3-8 and the expression of the output voltage is given by (62). The mismatch impedance of the amplifier was evaluated for two resistive loads (25Ω and 50Ω), as summarized in Table 3-1. The voltage of the amplifier in open circuit conditions (V_{in}) is 20V. Then it can be observed that the ratio between the measured voltage V_o and the open voltage V_{in} decreases when the MDUT impedance is close to 50Ω . In other cases, this ratio V_o/V_{in} decreases with a factor of 1.5 or 2. Therefore, the characterization of the hysteresis by using the STFC enables us to get the voltage information from V_o and not from V_{in} . However, the limits of the voltage level are reduced. Then, the measurements have been performed for voltage levels within the limitation of the specified VSWR values.

$$A_v = \frac{V_o}{V_i} = \left(\frac{R_{in}}{R_i + R_{in}} \right) K \left(\frac{R_{load}}{R_{out} + R_{load}} \right) \quad (62)$$

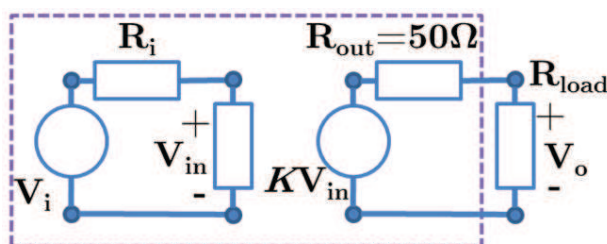


Figure 3-8 Equivalent circuit of RF amplifier

Table 3-1 Mismatch impedance evaluation

	50Ω		25Ω	
Frequency = 100 kHz to 1MHz	13.6V	280mA	10.4V	440mA

3.2.5 Characteristics of the measurement instruments

Voltage measurement

The parasitic elements related to measurement instruments in the equivalent circuit (Figure 3-6) are discussed here. The differential voltage probe presents a resistance R_{inst} equals to $8M\Omega$. But, to quantify the value of the capacitance C_{inst} , two tests have been carried out: first, direct measurement with the impedance

analyzer (4pF) and second, with the open-circuit voltage of the RF amplifier. The open-circuit measurement was obtained from the differential voltage probe connected in parallel to the amplifier output, and the current probe clamped on one phase of the voltage probe. The voltage and current signals are measured and the impedance of the open-circuit measurement gives the value of 6pF. As this value also includes the 1.5pF capacitance of the N-connector, then the C_{inst} can be considered as 4.5pF.

Current measurement

Different measurements are used to measure the current. In some cases [61, 91], the measurement configuration includes a shunt as the current sensor (Figure 3-9(a)). This is mainly made in order to avoid the saturation effects in the current probes (when high level of current passes through the MDUT). In this work, the 20m Ω shunt (LEM) has been tested and compared with measurements performed with current probe (TCP 202) as shown in Figure 3-9(b). It has been observed, in the shunt configuration, that a coupling capacitance appears between the shunt and the MDUT that impacts the measurement close to 1MHz. Moreover, the shunt voltage measurement requires an extra voltage probe, increasing the parasitic elements in the circuit. In contrast, the current probe has the available bandwidth of 50 MHz; the supported current is up to 15A-DC and 50A in peak pulse that is well adapted for the developed test bench.

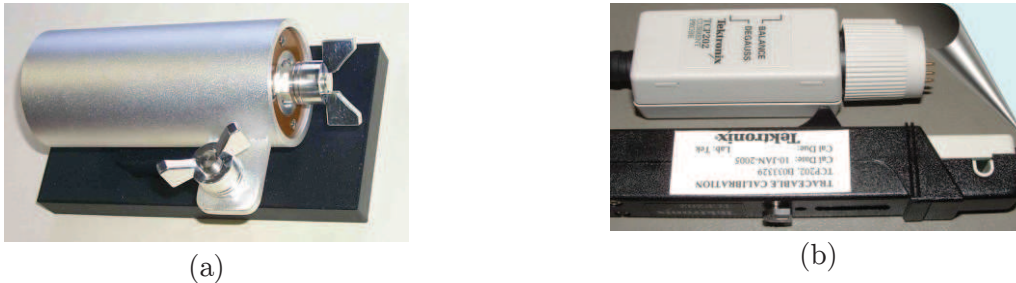


Figure 3-9 Current sensors (a) shunt LEM 20m Ω (b) hall sensor TCP 202

3.3 Magnetic material models

3.3.1 Overview

Two types of magnetic material models are frequently distinguished: the static and dynamic models. Static models, like Rayleigh, Fractional or Frölich are examples of the multiple variants and approximations. The static and dynamic hysteresis models of ferrimagnetic materials can be derived from the ones of ferromagnetic materials.

The classic Rayleigh model given by (63) represents the magnetic behavior of the material in the low field region where the hysteresis loop describes an ellipsoidal form. The parameters to be identified are the initial permeability μ_{in} , the hysteresis coefficient η , the residual magnetic flux B_r , the maximum magnetic field H_{max} and the maximum magnetic flux density B_{max} .

$$B = (\mu_{in} + \eta H_{max})H \pm \frac{\eta}{2} \left(H^2 - \frac{2B_r}{\eta} \right) \quad (63)$$

Another approach is the Fractional model given by (64). The parameters to be identified are: the saturation magnetization M_s , the residual magnetization M_r , the coercive field H_c , and two hysteresis coefficients H_k and H_n .

$$B = \mu_0 M_s \left(1 - \frac{a}{H + H_n \pm H_c} - \frac{b}{H^2 - H_k^2} \right) + \mu_0 H \quad (64)$$

The Fröhlich model can be employed to model the hysteresis loop by solving the equation (65) when $B(H \rightarrow 0) = B_r$ and $B(H \rightarrow \infty) = B_s$. Where α and β are coefficients to be determined.

$$B = \frac{H \pm H_c}{|\alpha + \beta|H \pm H_c|} \quad (65)$$

These previous models can be useful for a simple approach when the required conditions of their use are fulfilled. Besides, they can be well modeled and their parameters well identified. However, in our case, the saturation effect and hysteresis loop area has been taken into account. Therefore, two approaches, based on the Langevin equation (66), are considered in the follows:

- The average BH-curve model
- The quasi-static Jiles-Atherton hysteresis model with capacitance due to material (HCM)

$$Y = Y_0 \left(\coth\left(\frac{X}{\alpha}\right) - \frac{\alpha}{X} \right) \quad (66)$$

The independent value is X and the constants α and Y_0 are found by fitting process. The Jiles-Atherton model [65] is quite well adapted to represent ferromagnetic as well as ferrimagnetic materials. Moreover, its parameters are linked to physical characteristics. In order to show the improvement that a hysteresis model can offer in the context of this work, the average BH-curve model approach will also

be considered in the following. Finally, the average BH-curve model and the HCM will be studied in parallel in order to emphasize the advantage of the HCM in the application section.

3.3.2 Average BH-curve model

In this first approach, the magnetic behavior law (BH-curve) is obtained from the average of the major hysteresis loops. It means that the Langevin curve will represent the magnetization of the material. And the associated hysteresis losses are obtained from an analytical loss model (Steinmetz equation) that is identified from the hysteresis loop surface area (Figure 3-10).

In the expression given by (67), the magnetic flux saturation B_s and the parameter a are fitted with the experimental data. The parameter a adjusts the slope of the BH-curve and the parameter B_s modifies the amplitude of the hysteresis loop.

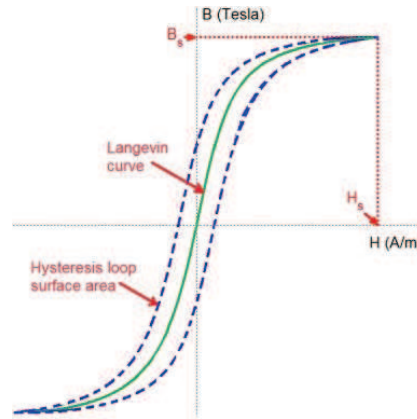


Figure 3-10 Representation of the hysteresis loop with the Langevin curve

$$B = B_s \left(\coth \frac{H}{a} - \frac{a}{H} \right) \quad (67)$$

The shape of experimental hysteresis loop changes when the frequency increases. This behavior of the hysteresis loop can be attributed to dynamic effects and the material capacitance as previously stated and can be taken into account by two models:

- (a) Frequency evolution of the parameter a .
- (b) Keep as a constant the parameter a and replace this frequency behavior with the material capacitance C_m .

The first approach consists in including the frequency evolution of the parameter a in the average magnetic behavior law by acting on its slope. This

solution is purely artificial but is quite easy to implement. The parameter evolution can be described, for example, by the exponential expression given in equation (68), where a_0 , b_0 and c_0 are coefficient to be determined.

$$a = a_0 [\log(f)^{b_0} + c_0] \quad (68)$$

The second approach consists in using an average B-H curve and an additional capacitance (C_m) in the equivalent circuit model of the material. This representation of the material allows decoupling the magnetic behaviour from the capacitive behaviour. The identification of this material capacitance is described in the section 3.3.4. However, the first approach results allow the calculation of the parameter a to be used within the second approach. This means that the average value of the parameter a is first identified and then the capacitance C_m is added to represent the frequency behavior of the hysteresis loop.

On the other hand, the BH losses are identified from BH hysteresis loop area obtained in different sinusoidal excitation field conditions (magnitudes and frequencies). This procedure is widely applied to characterize the hysteresis losses by the Steinmetz equation, for example in [92]. Others approaches has been made for arbitrary waveforms [91], where the Steinmetz parameters become functions of the waveform shape. In this average BH-curve model, sinusoidal waveforms have been used to calculate the power loss density P_h , which depends on the frequency and maximum magnetic flux density B_{max} . Two fitting stages are combined to get the three unknown parameters k_c , β and α of the expressions (69) and (70). The BH-surface, considering the quasi-static case, gives a relatively good idea of the losses that are involved in the magnetic material but only for sinusoidal signals.

$$P_h = k_{cf} B_{max}^\alpha \quad (69)$$

$$\text{with } k_{cf} = k_c f^\beta \quad (70)$$

The simplified procedure is summarized in Figure 3-11. First, two time-domain vectors of the B and H are obtained experimentally from different voltage levels and fundamental frequencies. Second, the hysteresis loop is split out into “maximum” values of B and H for each voltage level (B_{max} and H_{max}) and surface area of the hysteresis loop. Then, two fitting procedures are performed: the Langevin equation (a , B_s parameters) and the Steinmetz equation (k_c , α , β parameters). Both fitting procedures use implemented in MATLAB [®] scripts.

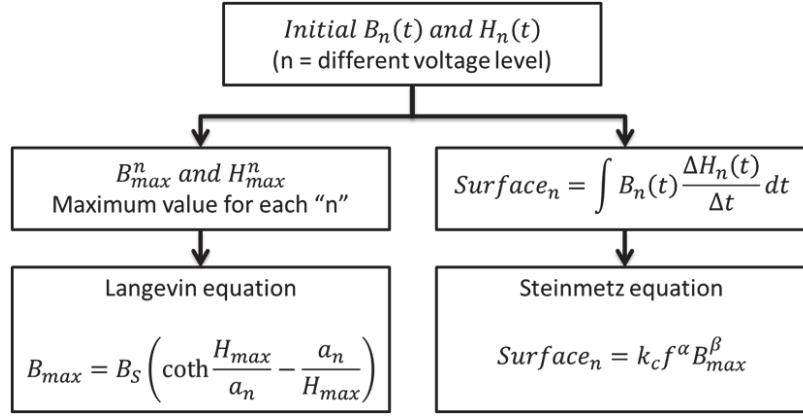


Figure 3-11 Calculation procedure of average BH-curve

3.3.3 Jiles-Atherton model

The Jiles-Atherton (J-A) model is well known in the modeling of the scalar magnetic hysteresis response of ferromagnetic materials. This model is built on the basis of the anhysteretic curve M_{an} that describes the process of magnetization without the hysteresis effect (71). Then, the magnetization process and hysteresis losses are introduced by both reversible (M_{rev}) (72) and irreversible (M_{irr}) (73) magnetization contributions.

In this model, the parameter k is related to the coercive field and $\delta = \pm 1$ is the signal function depending on the ascending or descending evolution of the magnetization. The parameters c and α are related to the reversible magnetization and to the effective magnetic field respectively. The interaction between the magnetic domains is described by the equation (74). The a parameter has the same meaning as in the average BH-curve model. Finally, the differential formulation of magnetization (dM/dH_e) is given by expression (75).

$$M_{an} = M_{sat} \left[\coth\left(\frac{H + \alpha M}{a}\right) - \frac{a}{H + \alpha M} \right] \quad (71)$$

$$M_{rev} = c(M_{an} - M_{irr}) \quad (72)$$

$$\frac{dM_{irr}}{dH_e} = \frac{M_{an} - M_{irr}}{k\delta - \alpha(M_{an} - M_{irr})} \quad (73)$$

$$H_e = H + \alpha M \quad (74)$$

$$\frac{dM}{dH_e} = c \frac{dM_{an}}{dH_e} + (1 - c) \frac{M_{an} - M_{irr}}{k\delta - \alpha(M_{an} - M_{irr})} \quad (75)$$

3.3.4 Stray capacitance due to the magnetic material

As previously described, the introduction of a capacitance C_m in the material model allows describing the frequency effect on the “apparent” magnetic behavior law. In fact, the frequency resonance of the material from impedance measurements can be used to estimate the capacitance C_m due to the material by the equation (76) that was introduced in chapter 2. The parameters of this expression are the geometric values, the initial permeability of the material μ_i , the resonance frequency of the material ($\sim 1\text{MHz}$) determined from the experiment (Figure 3-12), and the number of turns ($N=1$). The resulting material capacitance is of 400pF. Note that this value will be different if the ring core is changed (even for the same material) as non-negligible dispersion exists in the material properties from one sample to another [93].

$$C_m = \frac{1}{4\pi\mu_0\mu_i N^2 (2\pi f_m)^2} \left[\frac{\pi(D_e + D_i)}{H_g(D_e - D_i)} \right] \quad (76)$$

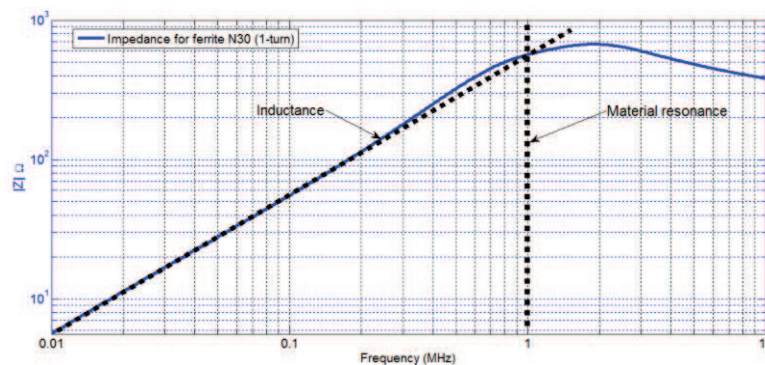


Figure 3-12 The impedance magnitude of the STC: The resonance of the N30 ferrite material occurs near 1MHz

3.3.5 Numerical resolution of the Jiles-Atherton model

The numerical procedure to compute the $B(H)$ behavior law is illustrated in Figure 3-13. The expressions (77) and (78) represent the coupling between the magnetic and the electrical domains. In these expressions, A_e is the cross sectional area of the ring core and l_e is the effective average magnetic path length. The nonlinear problem is then solved using the equivalent circuit model, given in Figure 3-6 together with the voltage and current in the inductor using a Newton-Raphson algorithm.

$$B = \frac{1}{NA_e} \int V dt \quad (77)$$

$$H = \frac{NI}{l_e} \quad (78)$$

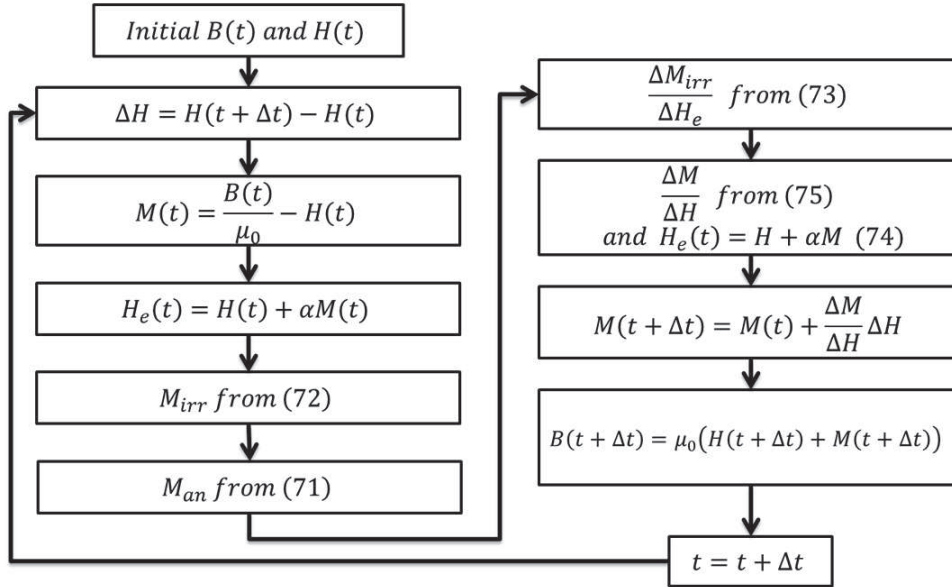


Figure 3-13 Calculation procedure of B(t) from H(t)

3.4 Experimental identification of model parameters

3.4.1 Specification of the magnetic material

Typically, the magnetic materials used in power converters and EMI filter applications are soft ferrites and nanocrystalline ones. In this chapter, three magnetic materials, listed in Table 2-9, are considered: N30 (MnZn ferrite), M43 (NiZn ferrite) and N6E3 (Nanophy nanocrystalline).

The parameters of the Jiles-Atherton hysteresis model are identified for these three magnetic cores. For each sample, some geometric parameters are defined, such as the effective length l_e (79), cross-section area A_e (80) and volume V_e (81). For the ring cores, it was reported that the effective cross-section area A_e and effective length l_e varies with the frequency mainly because of the skin effect above 1MHz [94]. Then, as the characterization method presented in this work is applied up to 1MHz, these parameters can be considered as constants.

$$l_e = \frac{2\pi \ln D_e/D_i}{2/D_i - 2/D_e} \quad (79)$$

$$A_e = H_g \frac{\left(\ln \frac{D_e}{D_i}\right)^2}{2/D_i - 2/D_e} \quad (80)$$

$$V_e = A_e l_e \quad (81)$$

Table 3-2 Magnetic materials under test

Geometric Characteristics of materials	N30 MnZn	M43 NiZn	Nanophy Nanocr.
D _e : Ex. Diameter [mm]	25.7	29.3	25.5
D _i : In. Diameter [mm]	14.5	19.1	16.0
H _g : Height [mm]	10.5	7.50	10.6
l _e : Eff. length [cm]	5.98	7.38	6.29
A _e : Eff. area [cm ²]	0.57	0.38	0.49
V _e : Eff. vol [cm ³]	3.41	2.81	3.10

For each material, the output voltage values of the RF amplifier (V₄) were identified when they were under the distortion levels of the power output (75W) by using the experimental setup shown in Figure 3-3. The other values (V₁ to V₃) are intermediate points. These voltage-frequency points are listed in Table 3-3 for N30 ferrite, in Table 3-4 for M43 ferrite and in Table 3-5 for N6E3 nanocrystalline.

Table 3-3 N30 MnZn material: amplitude of the voltage values

Freq.[kHz]	V ₁ [volt]	V ₂ [volt]	V ₃ [volt]	V ₄ [volt]
20	0.5	1	1.5	2
50	2	3	4	5
100	5	6	7.5	10
200	5	10	12.5	15
500	10	15	20	30
1000	10	20	30	40

Table 3-4 M43 NiZn material: amplitude of the voltage values

Freq. [kHz]	V ₁ [volt]	V ₂ [volt]	V ₃ [volt]	V ₄ [volt]
20	0.5	1	1.5	2
50	2	3	4	5
100	5	6	7.5	10
200	5	10	12.5	15
500	10	15	20	30
1000	10	20	30	40

Table 3-5 N6E3 nanocrystalline material: amplitude of the voltage values

Freq. [kHz]	V ₁ [volt]	V ₂ [volt]	V ₃ [volt]	V ₄ [volt]
20	0.5	1	1.5	2
50	2	3	4	5
100	5	6	7.5	10
200	5	10	12.5	15
500	10	15	20	30
1000	10	20	30	40

The voltage and current measurements (for each frequency) have been achieved within a short time frame shorter than 10 electrical periods to avoid the heating of the MDUT. Because the hysteresis loop is temperature dependent, the measurement has been performed at $27^{\circ} \pm 5^{\circ}\text{C}$.

3.4.2 Average BH-curve parameters identification

The average BH-curve model is obtained from the maximum points (H_{\max} , B_{\max}) of the measured hysteresis loops. From this average curve, the Langevin parameters B_s and a are obtained using a nonlinear least-squares curve fitting procedure illustrated in Figure 3-11. The procedure is repeated with all frequencies listed in Table 3-3 to Table 3-5.

As previously stated, the exponential evolution of the parameter a with the frequency is first identified. The Figure 3-14 shows this frequency-dependent evolution for the three MDUT. The coefficients of the analytical expression given by (68) are listed in Table 3-6. As aforementioned, the frequency influence on the

hysteresis loop is considered in the average BH-model by the parameter a . However, the *material capacitance* identified in Figure 3-12 can also be used. Then, the parameter a is kept as a constant value (from the low frequencies) plus the material capacitance C_m in the simulations. The calculated constant values are listed in Table 3-7 for the three materials

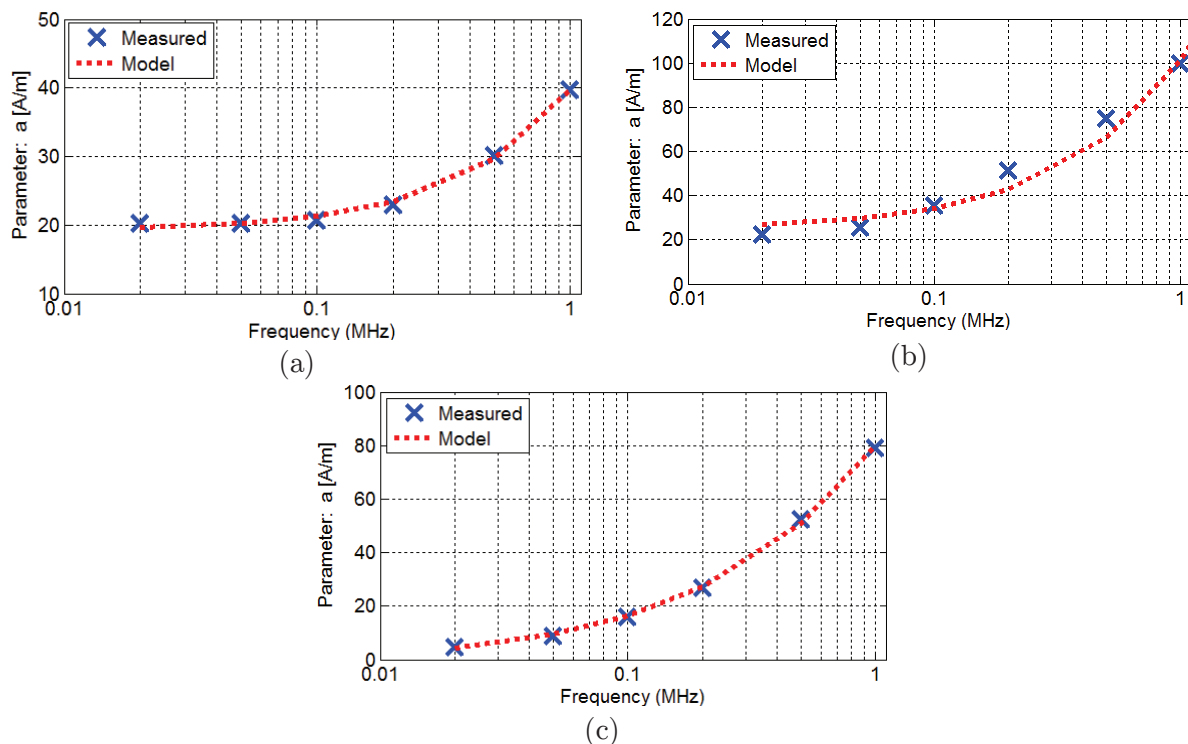


Figure 3-14 Evolution of parameter a : (a) N30 ferrite (b) M43 ferrite (c) N6E3 nanocrystalline

Table 3-6 Coefficients of the exponential expression of parameter a

Material	a_0 [A/m]	b_0	c_0 [A/m]
N30 (MnZn)	1.14×10^{-9}	13.18	19.45
M43 (NiZn)	4.85×10^{-8}	11.81	25.32
N6E3 (Nanocrystalline)	1.33×10^{-5}	8.71	2.70×10^{-3}

Table 3-7 Coefficients of the Langevin function

Material	B_s [Tesla]	a [A/m]
N30 (MnZn)	0.389	19.4
M43 (NiZn)	0.336	25.3
N6E3 (Nanocrystalline)	1.262	4.4

The experimental and simulation results are depicted in Figure 3-15. The identified maximum points of the measured hysteresis loops are fitted by Langevin equation for the three MDUT using the coefficients in the Table 3-7. Thus, the inductive behavior is taken into account within the average BH-curve model. Moreover, loss of the hysteresis loop is identified as following.

Because the losses are considered separately, they are extracted from the surface area of the hysteresis loop and modeled by the Steinmetz equation. The power loss density P_h obtained is the ratio between the BH area and the fundamental period T of the voltage signal. Then, the power loss density P_h obtained from measurement is fitted with (69) and (70). The three parameters k_c , α and β are calculated and summarized in Table 3-8.

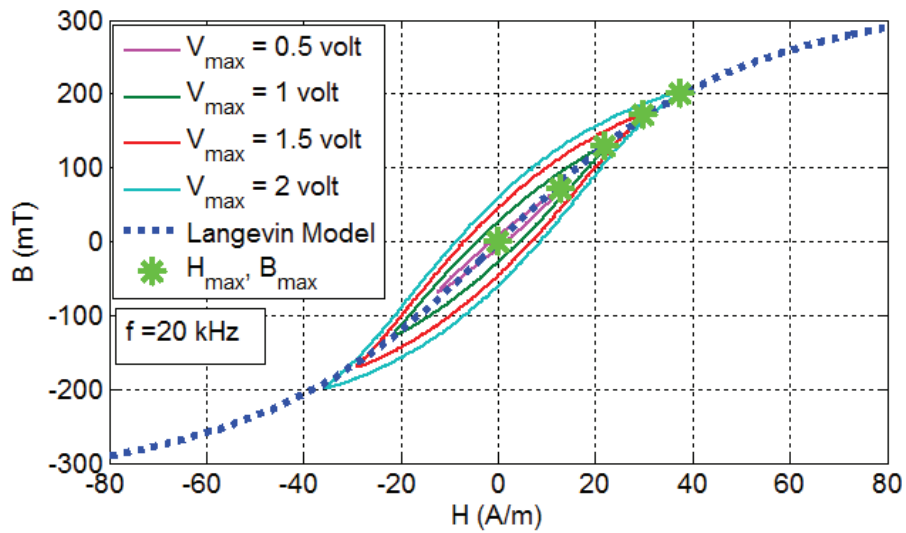
$$P_h \left[\frac{W}{m^3} \right] = \frac{(BH)_{surface}}{T} \quad (82)$$

Table 3-8 Steinmetz coefficients for power losses model

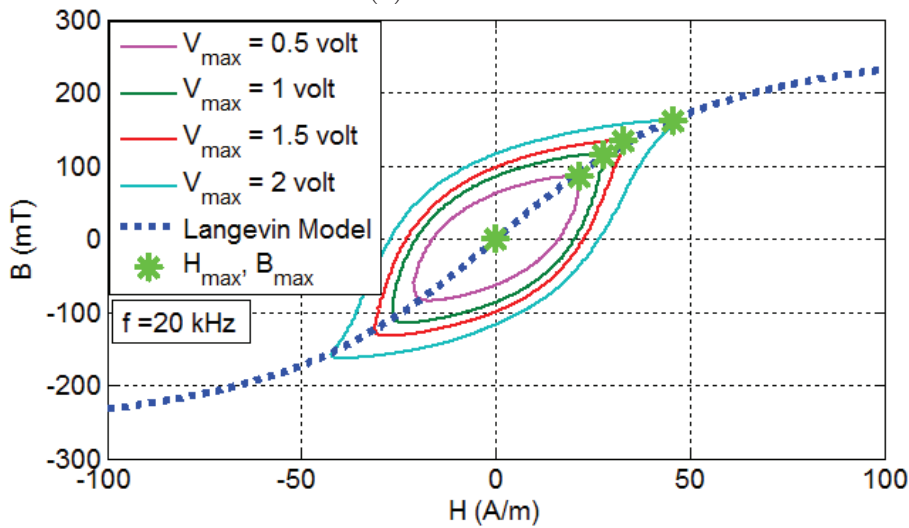
Materials	k_c	α	β
N30 (MnZn)	15.88	1.312	2.449
M43 (NiZn)	2.01	1.511	1.959
N6E3 (Nanocrystalline)	0.157	1.615	2.547

The power loss density of the three MDUT (P_h [W/dm³]) is shown in Figure 3-16. Alike other magnetic materials, the variations of power losses with the magnetic flux density are closely linear in a log-log representation. The symbol X represents the measured values and the lines belong to the Steinmetz model results.

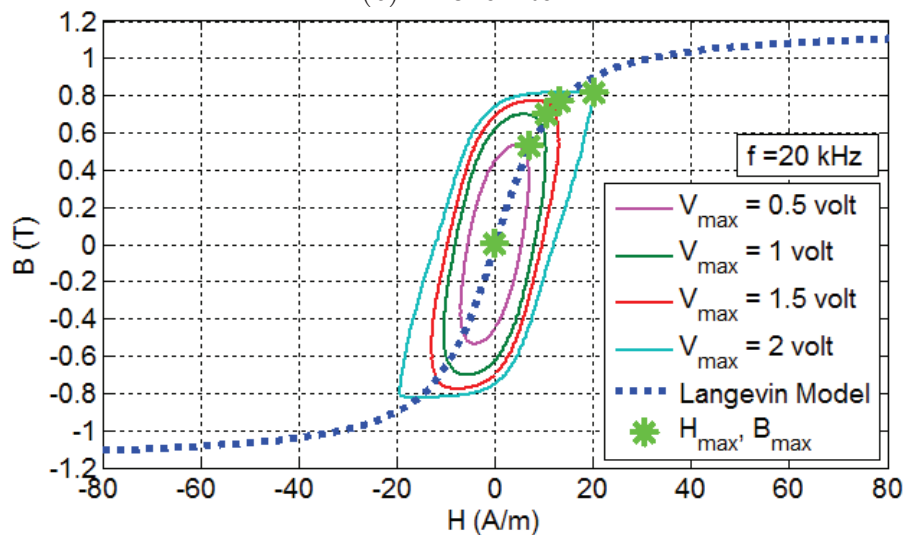
Note that, maximum magnetic flux density $B=200$ mT is obtained for the N30 (MnZn) material (Figure 3-16(a)) since the input current is limited in the configuration test. Meanwhile the maximum value specified in datasheets is 380mT at 25°C for 10kHz. Furthermore, the N6E3 Nanophy (nanocrystalline) material presents a higher permeability in frequencies below 1MHz with low losses. The maximum magnetic flux density achieved was just up to 800mT with this configuration setup while values of 1.2T are reported in the datasheets.



(a) N30 ferrite

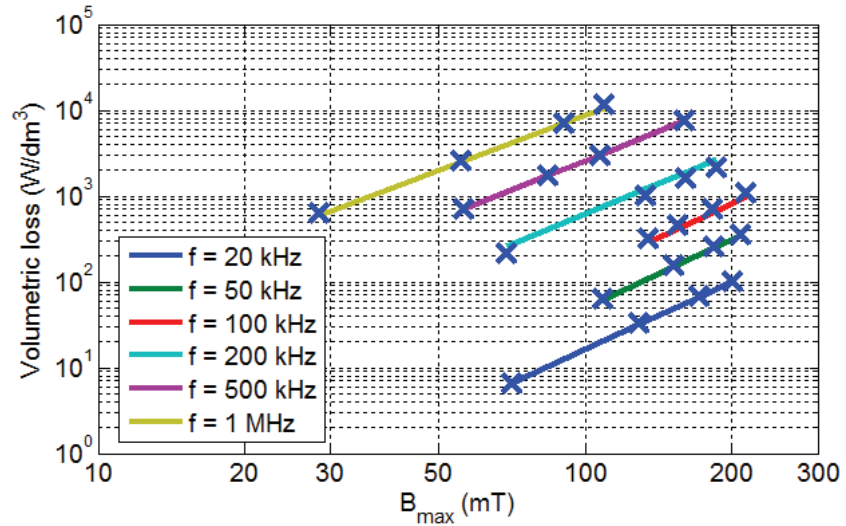


(b) M43 ferrite

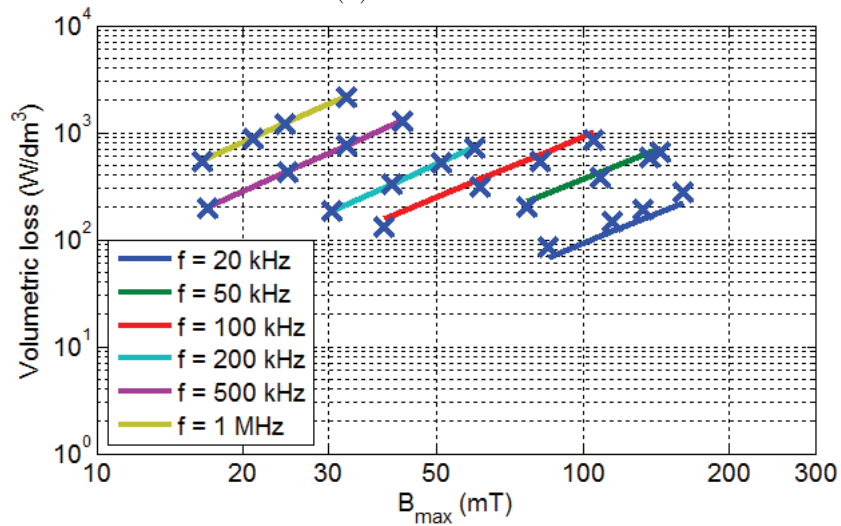


(c) N6E3 nanocrystalline

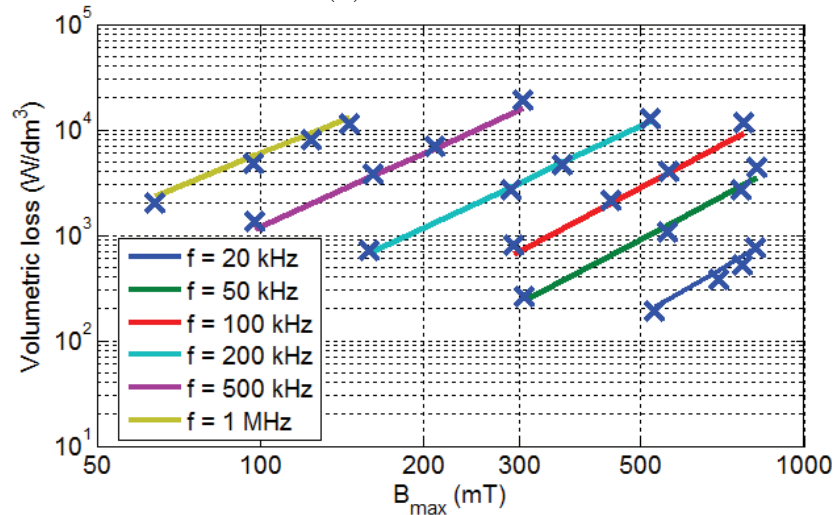
Figure 3-15 The average BH-curve model ($f=20$ kHz) (a) N30 ferrite (b) M43 ferrite and (c) N6E3 nanocrystalline



(a) N30 ferrite



(b) M43 ferrite



(c) N6E3 nanocrystalline

Figure 3-16 Measurement (X) and Steinmetz model result of power loss density for (a) N30 (MnZn) (b) M43 (NiZn) and (c) N6E3 Nanophy (Nanocrystalline) materials

3.4.3 Jiles-Atherton parameters identification

Efficient methods for identifying the J-A parameters have been studied in the literature, from nonlinear least-squares methods [95] to particle swarm optimization techniques [96]. In this section, the optimization of positive/negative branch of hysteresis loop, using the Nelder-Mead simplex direct search algorithm, is proposed. The main reason for this choice is related to simulation *stabilization time*.

The stabilization time is related to the number of periods that the procedure needs to get the simulation in a stable condition. Due to the low value of the resistance in the copper wire, the simulation gets a stable condition after several signal periods to have the DC bias close to zero. Therefore the number of periods is incremented. However, using the positive/negative branch of the signal allows the DC bias to be compensated and then the hysteresis loop can be approximated with less number of signal periods.

The measurements used for the J-A model identification are those obtained for the lowest frequency that is considered in this work, i.e. 20kHz, in order to reach the maximum magnitude of the BH loops for each material. Then the magnetic behavior-law parameters are extracted by a fitting algorithm. This one has been realized by reducing the gap between the measured and calculated hysteresis loops with the objective function f_{obj} given by (83).

$$f_{obj} = \sum |B_{sim} - B_{mea}| \quad (83)$$

The model equations (71) - (75) are used to identify the five parameters of the J-A model. The optimization process is realized from an initial vector with the parameter values. The measured magnetic field H_{mea} is used to calculate B_{sim} from the hysteresis model using $B = \mu_0(H + M)$. The objective function in (83) is then minimized using the Nelder-Mead simplex direct search algorithm. Once the convergence criterion is reached, the five parameters of the hysteresis model are obtained. The resulting parameters for the three materials are summarized in Table 3-9.

Table 3-9 Jiles-Atherton model parameters

Materials	Ms	a	K	α	c
N30 (MnZn)	0.302E6	18.7	23.9	0.55E-4	0.606
M43 (NiZn)	0.247E6	27.1	45	3.24E-4	0.289
Nanophy (Nanocr.)	0.955E6	10.9	17.6	0.42E-4	0.336

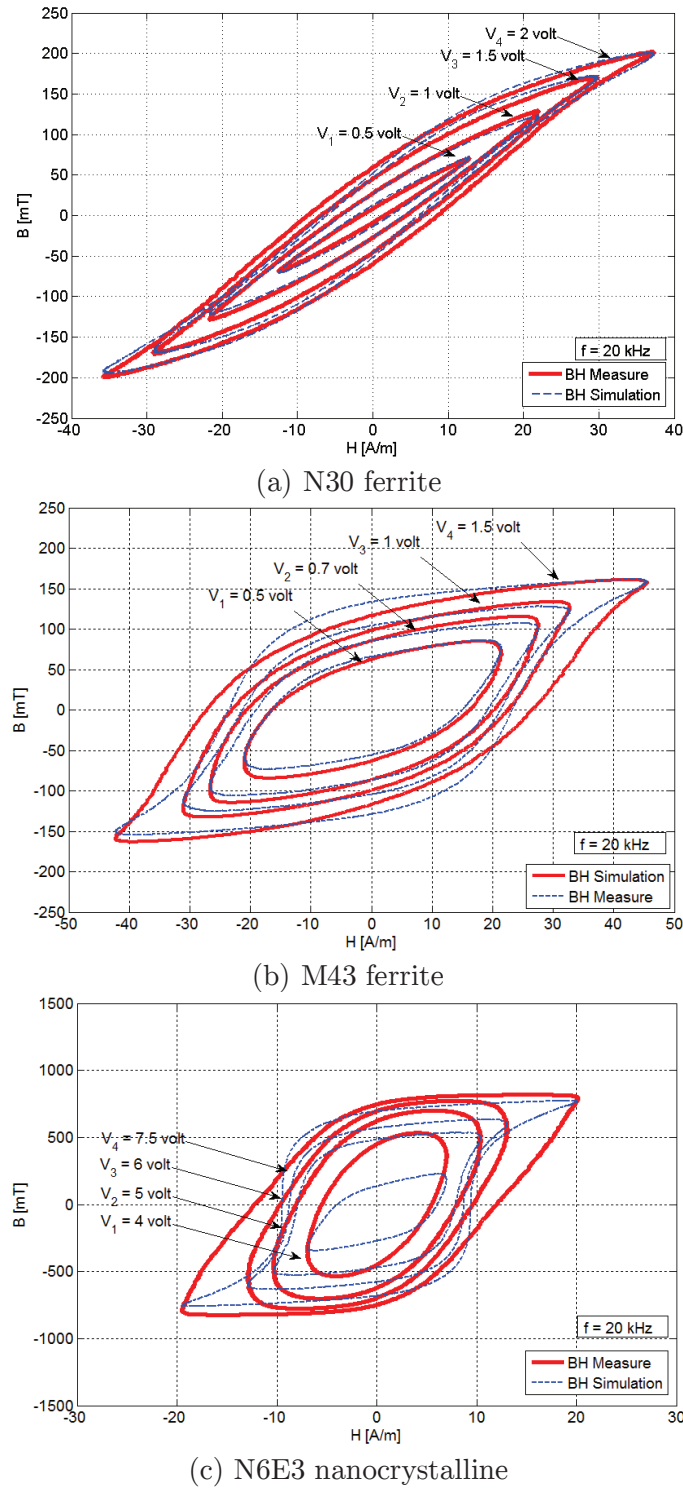


Figure 3-17 Measured and simulation results of the hysteresis loops for (a) N30 MnZn (b) M43 NiZn (c) N6E3 Nanocrystalline with J-A model

The simulation results and measurement data are reported in Figure 3-17 for the three studied materials. As illustrated in Figure 3-17(a) the N30 ferrite shows a good agreement between experimental and simulation results. The model for the M43 ferrite follows the experimental data with acceptable accuracy in the amplitude of the

induction field, but the core loss is still not accurate (Figure 3-17(b)). Then, another parameter can be added to take into account this variation [97]. Indeed, the used quasi-static model has some limitations to represent the shape variations of the BH loop. And, for the nanocrystalline material N6E3, the J-A hysteresis model presents some discrepancy with the experiment. The nanocrystalline material exhibits a particular hysteresis shape that the classical J-A model is not able to represent with accuracy (Figure 3-17(c)) [98]. The high slope of the BH loop (high value of the permeability) is difficult to follow by this model. Additional parameters could ameliorate the model such as a coefficient factor for weighting the H value or redefining the range of optimization for the nanocrystalline materials. For the sake of simplicity, the model is kept here in its original form.

3.4.4 Robustness of the hysteresis model

The robustness of the hysteretic and capacitive material behavior model (HCM) is studied with three parameters: the magnetic flux density, frequency and waveform shape.

Average magnetic flux density

In the aim to show the correlation of the model in other frequencies, the HCM was applied for different intermediary frequency values, as shown in Figure 3-18. The average slope is well followed by the model when increasing frequency.

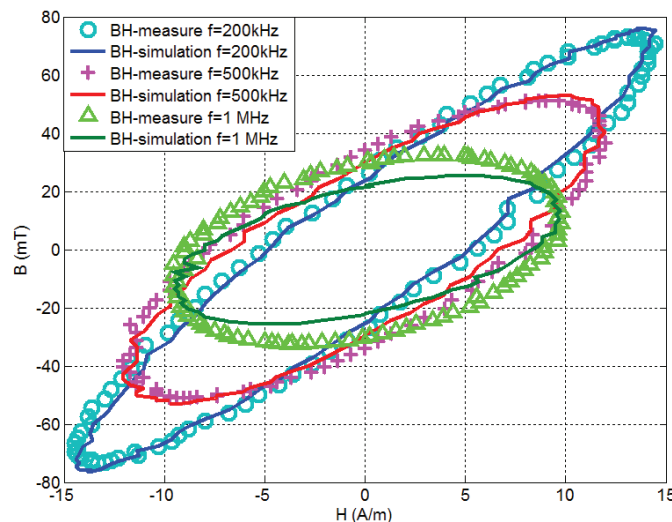


Figure 3-18 Hysteresis loop of N30 ferrite for frequencies of 200kHz, 500kHz and 1MHz

This slope variation (approaching to zero) is due to the *magnetic capacitance* included in the model. It means that our approach, the quasi-static hysteresis model plus the *material capacitance* can represent the frequency evolution of the hysteresis

in the frequency range under study. Already, it can be observed that the model cannot follow the hysteresis loop area with good accuracy. This limitation at losses estimation can be ameliorated with a dynamic hysteresis model, and it should be considered in a future work.

Low magnetic flux density

The HCM is compared to the classical CMP approach for the low magnetic flux density (<10mT) region, as shown in Figure 3-19. The real and imaginary parts of the classic CMP are given by equations (84) and (85) respectively [81]. In the proposed model (HCM), the volumetric loss (P_{vol}), maximum magnetic induction (B_m), and maximum magnetic field (H_m) are obtained from the hysteresis loop, which allow to compute then the equivalent real and imaginary parts. As shown in Figure 3-19, values calculated from the proposed model are close to the CMP that is obtained from the impedance analyzer characterization. The difference in low frequency is due to the high value of the magnetic field ($B > 50\text{mT}$), thus the magnetic permeability is not in the “initial” magnetization curve where the impedance analyzer works. In consequence, the CMP information can be obtained from the HCM if the small-signal characterization is required.

$$\mu' = \frac{\sqrt{\pi^2 f^2 H_m^2 B_m^2 - P_{vol}^2}}{\mu_0 \pi f H_m^2} \quad (84)$$

$$\mu'' = \frac{P_{vol}}{\mu_0 \pi f H_m^2} \quad (85)$$

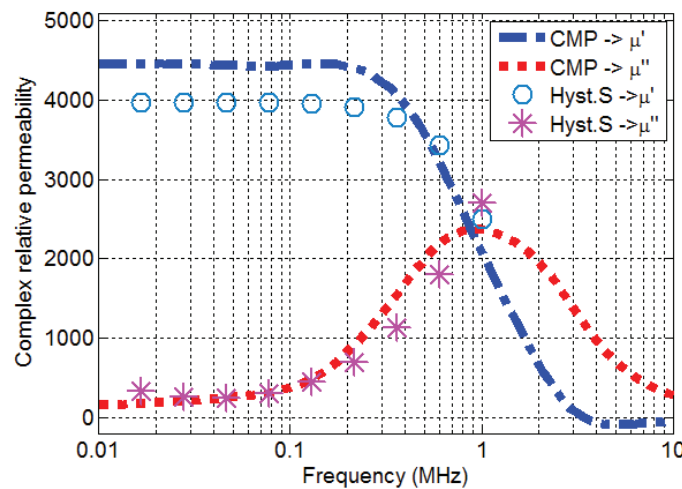


Figure 3-19 Complex magnetic permeability (CMP) for ferrite core N30 calculated with hysteresis loop (markers ‘o’ and ‘*’)

Test under different voltage shape

Until now, the parameter identification, the average BH-curve and J-A model have been studied using sinusoidal waveforms. The robustness of the proposed models is investigated by applying two different voltage waveforms (square and saw-tooth) to the MDUT. The average BH-curve and the HCM are tested, in the same conditions as described in Figure 3-3, with these different input-voltage (V_{in}) waveforms. The frequency is established to 500 kHz with a duty cycle of 50%. The material model is used to simulate the nonlinear behavior of the self-inductor (L_m) where the values of the equivalent circuit parameters (Figure 3-6) are summarized in Table 3-10.

Table 3-10 Values of equivalent circuit elements

Element	Average BH-curve	HCM
Supply output impedance (Z_{in})	50 Ω	50 Ω
Connector capacitance (C_{cn})	2pF	2pF
Wire resistance (R_w)	30m Ω	30m Ω
Voltage probe capacitance (C_{inst})	20pF	20pF
Voltage probe resistance (R_{inst})	8M Ω	8M Ω
Capacitance of the MDUT (C_m)	400pF	400pF
Resistance of the MDUT (R_m)	17 Ω	0 Ω

Two types of signals are studied; square and saw-tooth shapes. When the input voltage V_{in} is a square signal with a fundamental frequency at 500kHz, the current and voltage signal (N30 ferrite material) are depicted in Figure 3-20. In the same way, a saw-tooth signal is evaluated, experimental and simulation results are illustrated in Figure 3-21. The simulation is performed using the same procedure which is explained in the section by describing the numerical resolution of the nonlinear model. The experimental current data is used to calculate the magnetic field by (77) and the magnetic induction is obtained with the material model. The experimental voltage data of the self-inductor is then obtained by (78) together with the other elements of the equivalent circuit.

The comparison of the simulated and measured voltage waveforms show clearly that the HCM model can follow with a better accuracy the shape of the measured signal, whereas the average BH-curve model shows important discrepancy.

Nevertheless, some inaccuracies are observed in the leading-edge of the calculated square voltage (HCM). In fact, the leading-edge transient, linked to HF harmonics in the excitation signal, cannot be accurately represented with the proposed model, due to its limitations for higher frequencies (above 1MHz). However, the use of a hysteresis model, together with the capacitance of the material, is able to represent with an acceptable accuracy the behavior of the core under square signal excitation in the considered frequency range (~ 1 MHz).

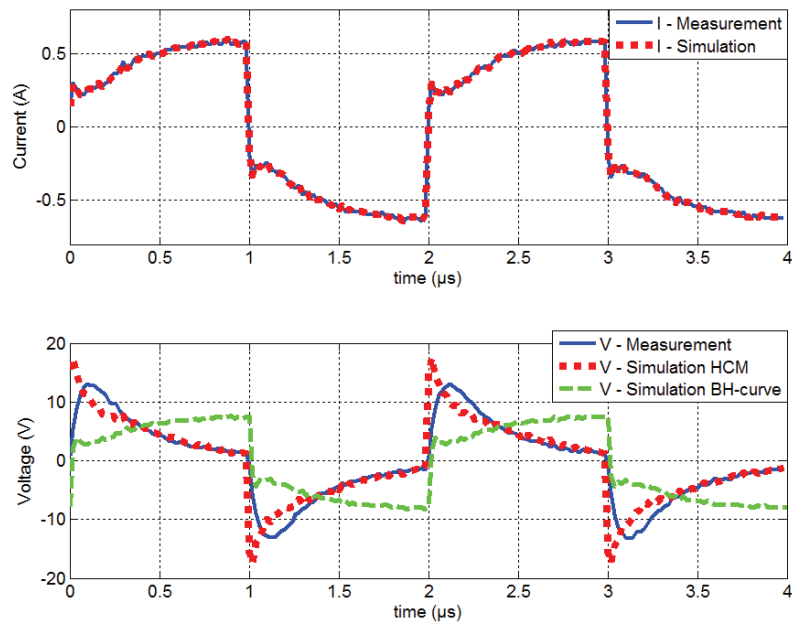


Figure 3-20 Square signal; Current and Voltage in self-inductor of N30 (MnZn) at 500kHz

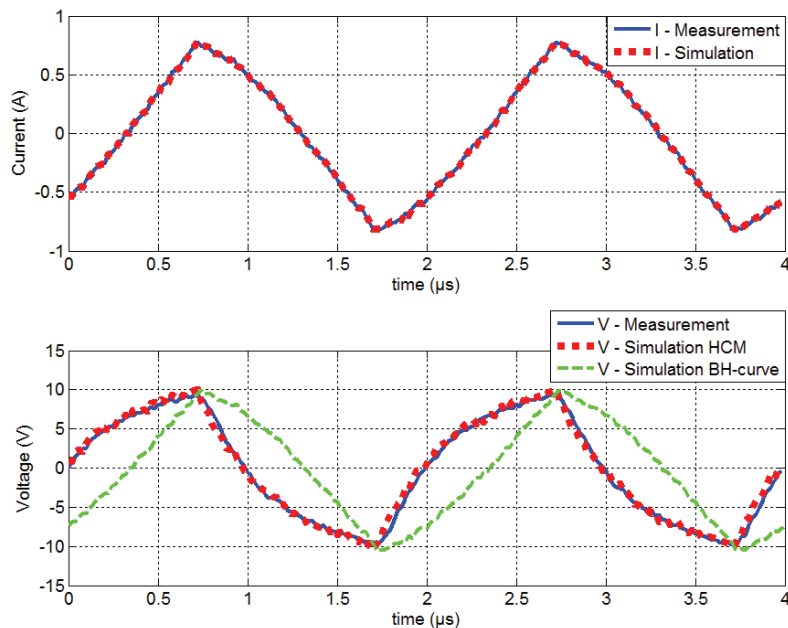


Figure 3-21 Saw-tooth signal; Current and Voltage in self-inductor of N30 (MnZn) at 500kHz

DC-bias

In the literature, there are different approaches to take into account for the DC-bias behavior. To that end, specific characterization methods of the ferrite materials are developed as reported in [99]. In these references, the permeability and core losses were measured by a resonance technique using a DC-bias level to magnetize the material. However, the proposed characterization with STFC and the proposed material model (HCM), identified from measurements without DC-bias, can also be used to estimate the variation of the permeability with the DC-bias level.

The first test, with the N30 ferrite, was performed with an arbitrary saw-tooth waveform ($\Delta I = 0.8A$), a DC component ($I = 2.1A$) and operating frequency equal to 100 kHz. The simulated voltage, in Figure 3-22, is within the amplitude range of the measured one. Note that a numerical transient is observed at the initial part on the voltage waveform. It can be concluded that the HCM represents with acceptable accuracy the waveform in DC-bias conditions.

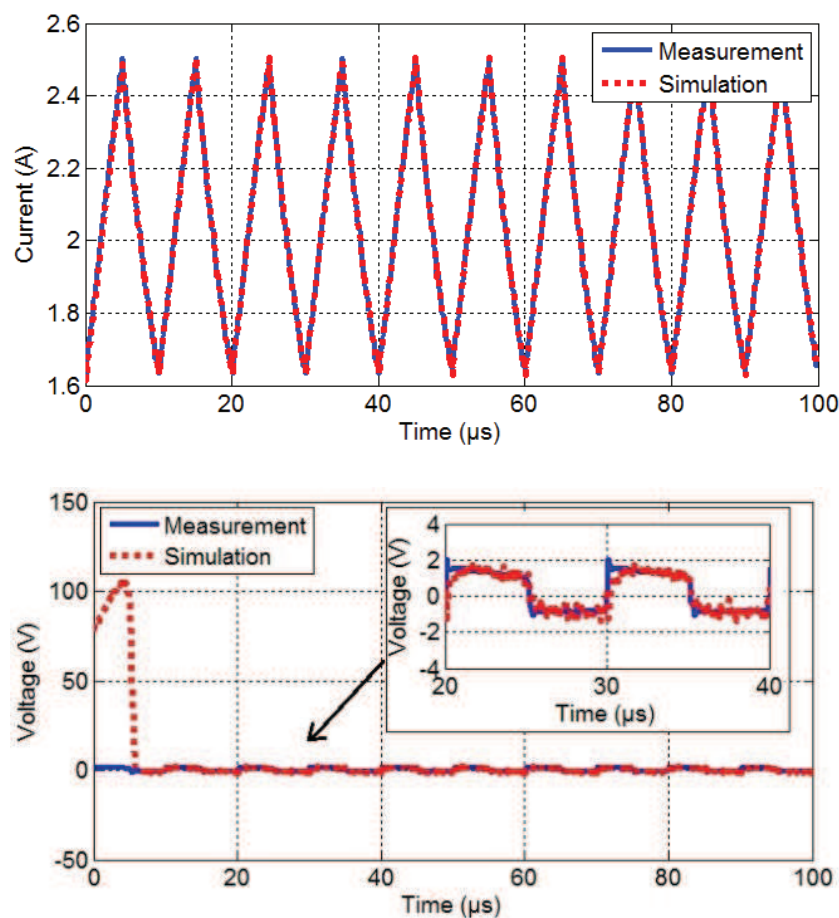


Figure 3-22 Arbitrary waveform with DC-bias: Current and Voltage in self-inductor of N30 (MnZn) at 100kHz (simulation with HCM)

The second test, still with the N30 ferrite, is achieved with a small sinusoidal AC current ($\Delta I=3.2\text{mA}$) and a DC current component (I_{DC}) varies from 12mA to 2.4A. In order to use the model in the same conditions as those given in the datasheet, an inductor with $N=5$ turns is used. Therefore, for two different frequencies (20 kHz ad 200 kHz), the simulation results are compared with the datasheet DC-bias curve (given for 10 kHz) as illustrated in Figure 3-23. The tendency of the relative permeability (μ_r) is well followed by the model, and predictions of higher H_{dc} values can be obtained. Even if the simulated data do not correlate with the datasheet curve, which is given with a dispersion of $\pm 25\%$, it can be useful for the first simulation approach. This cannot be achieved if the CMP is used instead of the proposed HCM.

3.4.5 Core loss and copper losses

It is well known that the core losses can be determined experimentally by different techniques (e.g. resonance technique). In our case, the core losses are directly calculated from the hysteresis loop but will be under-estimated for higher frequencies due to the quasi-static hypothesis. This point is addressed further in the present section.

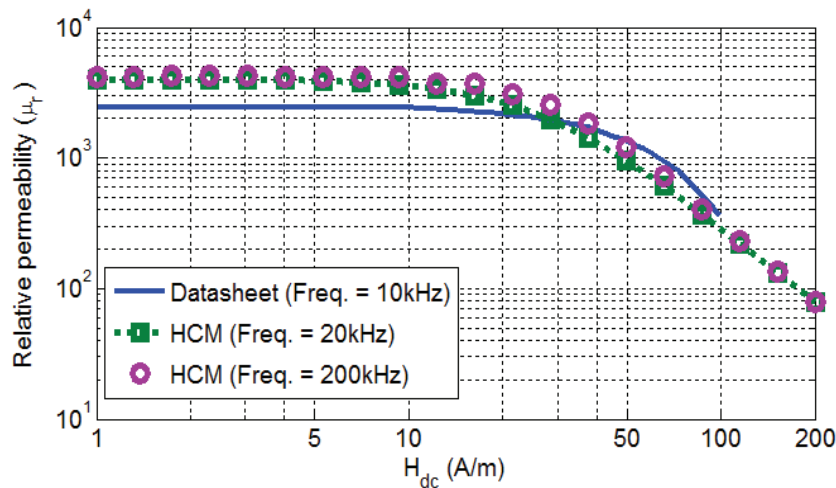


Figure 3-23 (a) Relative permeability of N30 ferrite with DC-bias magnetic field

The results of the simulation with HCM are compared with the experiment in Figure 3-24 representing the volumetric loss evolutions that are almost straight lines in the log-log scale representation. At low magnetization level (e.g. 50mT) the measured values of the volumetric loss (W/dm^3) are close to those given in [84]. Moreover, and as expected, the HCM is able to calculate the volumetric losses with

accuracy for the frequency used for the parameter identification (20 kHz). Nevertheless, as the dynamic losses are not taken into account in the HCM approach, some discrepancies are observed when the frequency increases. This is the main limitation in the proposed HCM approach that can be further improved by using a dynamic hysteresis model.

In the other hand, the copper losses, measured at 20 kHz and 500 kHz frequencies are illustrated in Figure 3-25. This emphasizes the higher ratio of the copper loss to the core loss for low frequencies, about 30% at 20 kHz, with regard to high frequencies, less than 5% at 500 kHz.

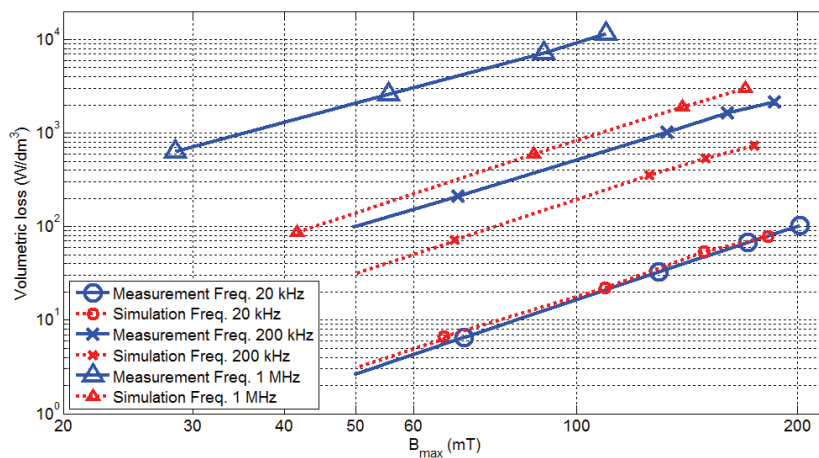


Figure 3-24 Extrapolation of the volumetric loss for ferrite core N30 ($B_{\max}=50\text{mT}$)

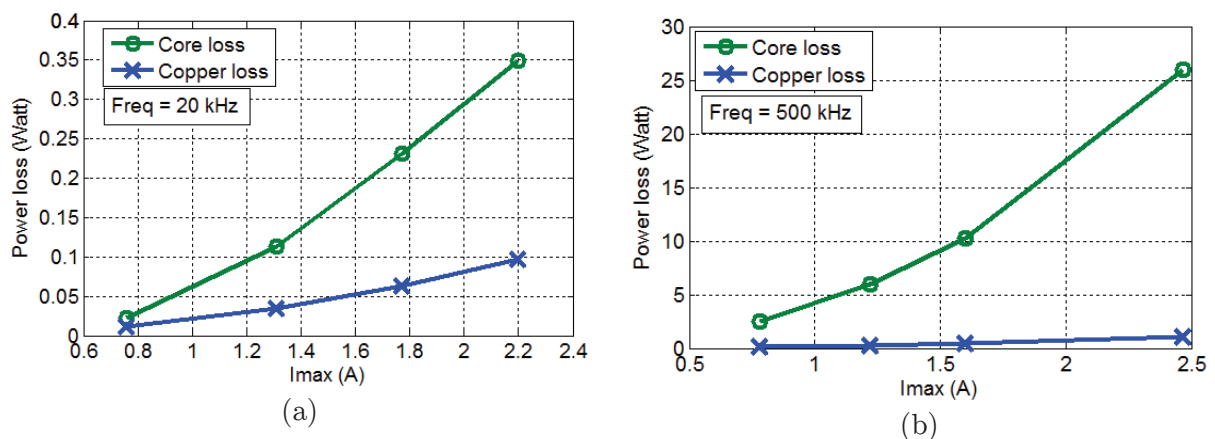


Figure 3-25 Core loss of N30 ferrite and copper loss in the STFC

3.5 Application: EMI filter for power converter

In the previous section, the robustness of the proposed model was verified in different excitation conditions (voltage waveform, frequency, DC component). Now the model will be used to calculate the insertion loss of EMI filters in different operating conditions. In fact, in EMI filter design, the coupled inductors configuration is frequently used for inductive components in common mode (CM) and differential mode (DM) filtering configurations. The LC (inductor-capacitor) low-pass filter configuration (one or more stages) is usually adopted. The capacitor values are defined using standardized values. The inductive component of the CM and DM filter (Figure 3-26) is simulated using the proposed inductor model.

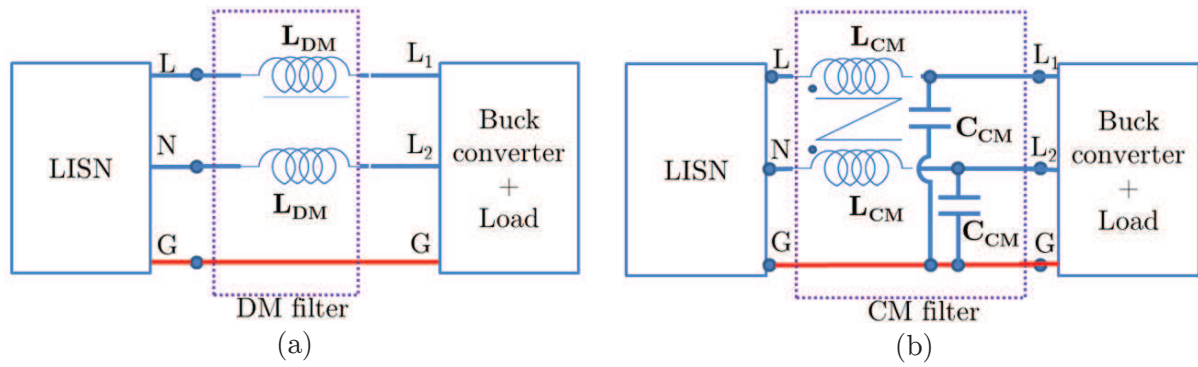


Figure 3-26 Equivalent circuit of the (a) DM filter and (b) CM filter

3.5.1 Differential mode filter

In this section, the case of a differential mode LC filter associated with a buck converter is presented. The objective is to evaluate the modification of the insertion losses of the EMI filter due to the inductance variation in high level of magnetization and/or DC-bias conditions. Then, the inductor L_{DM} of the filter uses the high-level magnetic material and the capacitance is the value of DC-Bus capacitor C_{DM} (inside the buck converter block in Figure 3-26(a)). Two tests are performed: with and without the coupled inductance in the DM filtering configuration. The buck converter is illustrated in Figure 3-27(a) and its characteristics are summarized in Table 3-11.

The differential mode emission is represented by a Norton equivalent circuit I_{DM} in parallel with impedance Z_{DM} . The DM current I_1 is measured with the F-35 current probe and the spectrum analyzer (ESA 1500A). Then, by multiplying this current by the LISN (Line Impedance Stabilization Network) impedance (Z_{LISN}), the equivalent DM voltage spectrum (in dB μ V) is obtained. The voltage at the converter input $V_{OSC} = V_1 - V_2$, shown in Figure 3-27(b), is considered the same input voltage as the one in the circuit in Figure 3-27(c) ($V_{OSC} = V_{OSC}'$) for each load impedance.

Therefore, to evaluate the attenuation due to DM filter under the LISN impedance Z_{LISN} , the voltage drop in the inductance is simulated and compared with measurements. The simulation of the equivalent circuit (Figure 3-27) with and without the filter is performed by solving the equation (86) with Newton-Raphson method. The number of turns (N) of the coupled inductor is equal to 4 and the HCM is used to calculate $\phi(I_1)$.

$$V_{osc} + N \frac{d\phi(I_1')}{dt} - I_1' Z_{LISN} = 0 \quad (86)$$

The voltage V_{osc} in the simulation is obtained from the FFT of the time-domain signal. The amplitude of each harmonic is the amplitude of sinusoidal signal which is injected in the model. Then, the calculated current I_1' is used to predict the attenuation in the Z_{LISN} .

The noise harmonic (at 100 kHz) without DM inductor configuration (Figure 3-27(b)) is measured for three different operating points of the buck converter. The current is varied by changing the load resistance value and keeping the DC input voltage constant (50V). The direct current values are 0.8A, 0.4A and 0.2A for the load resistances 15 Ω , 30 Ω and 60 Ω , respectively. Note that the DM current is composed by a direct current and HF disturbances. The experimental results obtained without the DM inductor are shown in Figure 3-28. Then, the DM inductor is connected as illustrated in Figure 3-27(c). It appears clearly on the experimental results shown in Figure 3-28 that the attenuation of the filter is different for the three operating points. This attenuation is lower when the DC current is higher, as it was expected because the material is magnetized in its non-linear region where the relative permeability decreases (Figure 3-23). It must be pointed out that the usual approach based on the CMP cannot take into account this phenomenon as the self-inductor remains constant when the DC current changes

From the simulation of the inductor with HCM, and using the FFT, the harmonic components at frequency 100 kHz are obtained, as shown in Figure 3-29. As expected, the observed attenuation of the DM noise decreases when the DC current increases. The experiment result confirms that the inductance value of the coupled inductor depends on the level of magnetization of the ring core under DC bias operating condition. It must be pointed out that the classical approach that uses the CMP cannot take into account this phenomenon as the self-inductor remains constant when the level of the DC current increases.

Another aspect is the behavior of the noise level without the DM inductor. The experimental data shows that the noise level varies whereas in the simulation it

remains constant. This phenomenon can be explained by the non-perfect behavior of the experimental setup as other elements introduce noise with the increase of the current like external coupling or temperature. At the opposite, the equivalent circuit used in the simulation, without the DM filter, is supposed to be the same whatever the level of current. Moreover, the comparison of the experimental and the simulation results of the noise attenuation with the DM filter show a low difference. Nevertheless, the global tendency is respected and is useful if one wants to have an estimation of the attenuation.

Table 3-11 Elements of DC DC buck converter

Element	Description
Input DC voltage (V_{in})	50 volt
DC bus capacitor (C_{DM})	10 μ F
Diode	STH15R06
IGBT	IXGR40N60
Load impedance	15 Ω /30 Ω /60 Ω
Operating frequency	100 kHz
Duty cycle	50%
IGBT driver supply	Battery cell

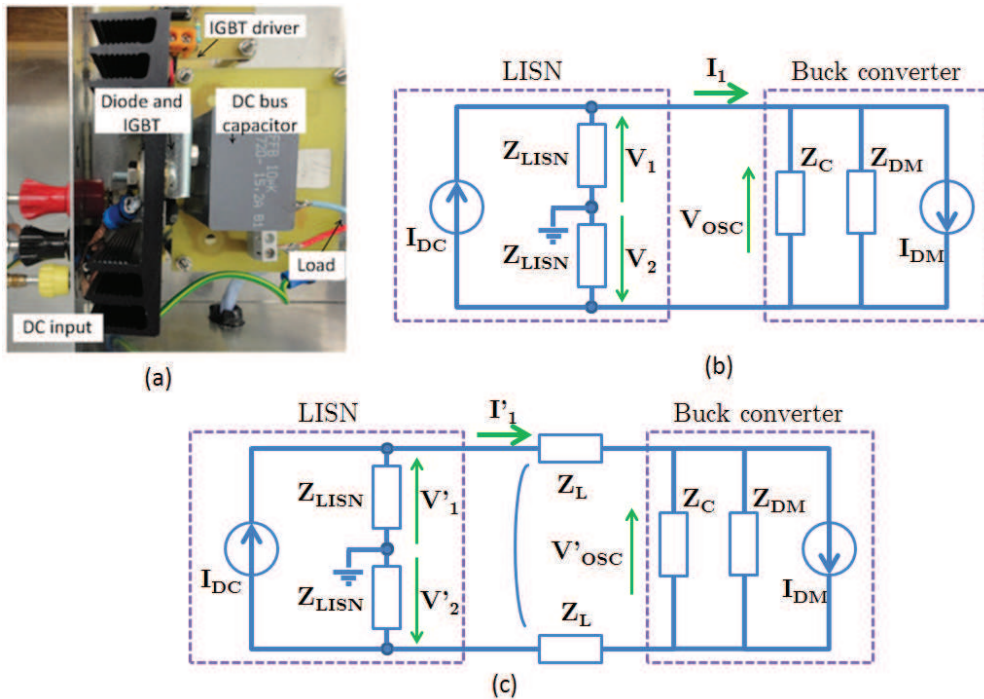
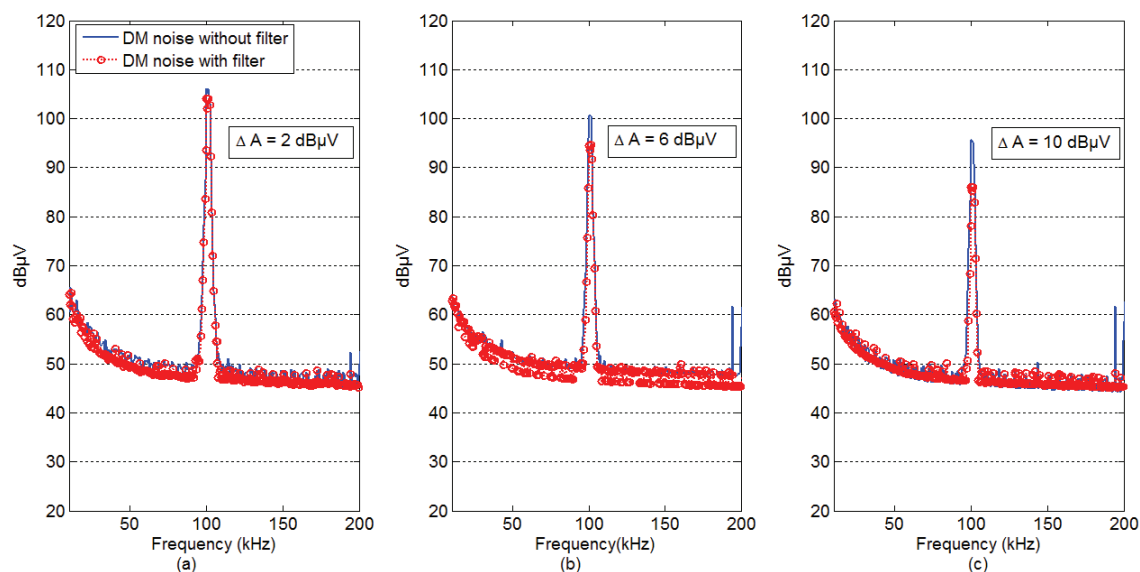
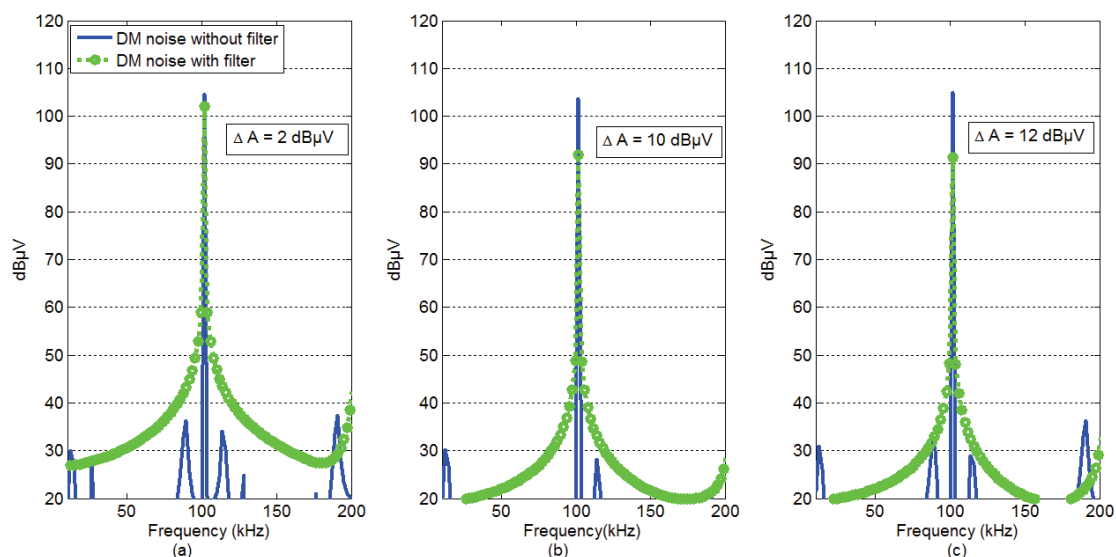


Figure 3-27 Buck converter and DM equivalent circuit (b) without coupled inductor (c) with coupled inductor (separator, DC-DC)

Figure 3-28 Measured DM noise attenuation with load resistor (a) 15Ω (b) 30Ω and (c) 60Ω Figure 3-29 Simulated DM noise attenuation with load resistor (a) 15Ω (b) 30Ω and (c) 60Ω

3.5.2 Common mode filter

The insertion loss (IL) of the common mode filter, given by expression (87), is obtained with a $50\Omega/50\Omega$ (Z_{in}/Z_{out}) impedance test and also it is realized with a vector network analyzer (Agilent-E5071C). Because the characterization was performed to small-signal conditions, only one measured curve is presented. The influence of the magnetic material on the IL is predominant below 1MHz, before the resonance due to the HF parasitic elements, such as the "material capacitance" or the inter-turns capacitances. The value of the capacitance C_{CM} is 4.7nF and the CM inductor value is 0.8mH at low frequencies. These values have been characterized from the impedance analyzer. Then the equivalent circuit, illustrated in Figure

3-30(a), is simulated with the HCM instead of the classical linear inductance value. The results are presented in Figure 3-30(b). These simulation results show that the IL is deformed when the current increases (changed with voltage input) due to saturation effects in the material.

As observed in the insertion loss (Figure 3-30(b)), the CM inductor impedance (Z_L) is close to zero (due to the saturation effect) when the voltage increases. Moreover, if the capacitor impedance is high enough (Z_C), the equation (87) is close to zero. Therefore, the real insertion loss will not be correctly predicted by the small-signal characterization approach, i.e. by a constant inductance representing the material. However, when the current that flows through the inductor does not saturate the material (low voltage), the insertion loss is very close to the measurement obtained with the small signal characterization, as expected in this operating condition. Moreover, simulation results in Figure 3-30(b) can be used as the non-linear evolution of the insertion loss of the filter, depending on the voltage level, a point that is not treated in the literatures.

$$IL = -20 \log \left| \frac{Z_{OUT}}{Z_{IN} + Z_{OUT}} \left(1 + (Z_L + Z_{IN}) \left(\frac{1}{Z_C} + \frac{1}{Z_{OUT}} \right) \right) \right| \quad (87)$$

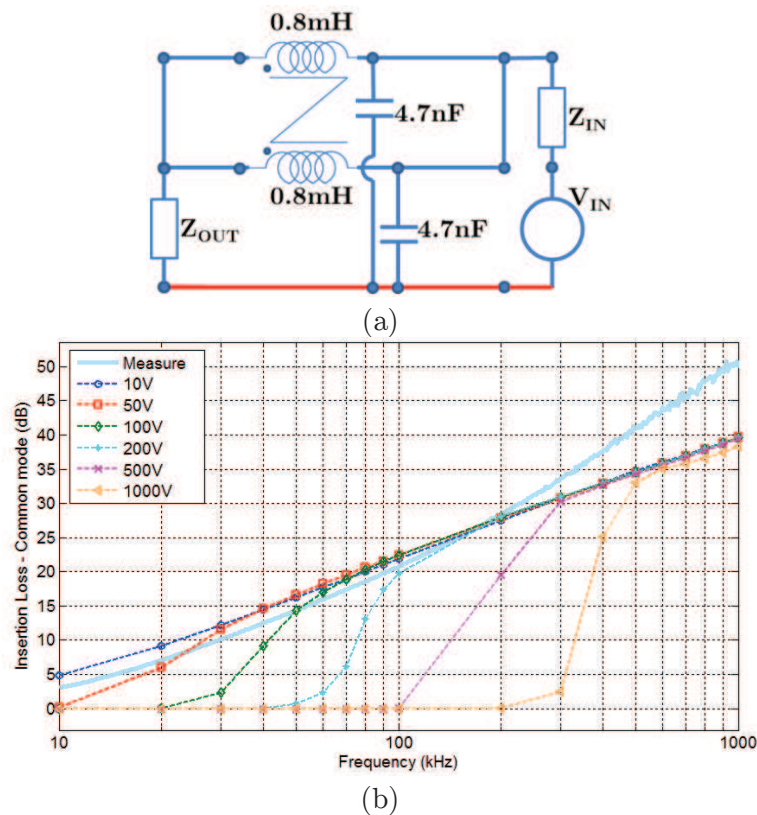


Figure 3-30 Simulation of CM filter (a) equivalent circuit (b) insertion loss for different input voltage (V_{in})

In summary, the *high-signal* magnetic material model developed can represent the material behavior in different operating conditions. The robustness of the model and the application results are good arguments that can justify the HCM use in modeling the magnetic materials. Even if this model has some limitations (dynamic effect, frequency ...), it is a first approach that opens the possibility to improvements and extensions. For example, the temperature influence in the magnetic material model shows in the next section that effectively the model can be updated to take into account this influence.

3.6 Temperature influence in the magnetic material

3.6.1 Overview

In the previous section, the proposed approach, quasi-static J-A model together with the material capacitance, showed a good agreement with the experiment characterization that was realized under ambient temperature that do not impact significantly the magnetic behavior of the material (temperature range between 20°C and 30°C). Nevertheless, the heat dissipation, due to power loss in the magnetic core, winding and surrounding components, can lead to high temperature levels. In the case of the N30 ferrite, the impact can be significant as the Curie temperature of this material is about 130°C. Therefore, it is more interesting to evaluate the temperature influence on the material properties and build an adequate modeling approach. In the literature, different approaches are proposed to take into account the temperature effect on magnetic cores, in the experiment characterization and/or in the magnetic model. In [100], an automatic test system was presented to measure the hysteresis loop of MnZn ferrites. The test system is equipped with an isolation transformer to prevent any DC offset. The Basso-Bartotti model is applied to take into account the hysteresis loop and the temperature effects. The five parameters of the model were optimized and their temperature-dependent expressions evaluated up to the Curie temperature. The power expression (88) was introduced to represent the saturation magnetic flux density when the temperature varies (T). Three parameters (T_c , b_1 and b_2) are identified by fitting procedure.

$$B_s(T) = b_1 \left(1 - \frac{T}{T_c}\right)^{b_2} \quad (88)$$

In [63], the magnetic behavior that takes into account the temperature of the nanocrystalline materials is investigated. The dynamic hysteresis model is described by the homogenized diffusion equation (89). Where the polynomial law $P(H)$ is used to define $B(H)$ as given in (90). The parameter γ was defined as the lumping eddy current which models the dynamic effect in the expression (89). In this model there are five parameters to be identified: H_b , γ and the three polynomial coefficients.

$$H_{tot} = H_{stat}(B(t)) + \frac{\gamma dB(t)}{dt} \quad (89)$$

$$B(t) = \begin{cases} \mu_0(H - H_b) + P(H_b) & \text{for } H \geq H_b \\ P(H) & \text{for } |H| < H_b \\ \mu_0(H + H_b) - P(H_b) & \text{for } H \leq -H_b \end{cases} \quad (90)$$

Two methods have been proposed in [101]. First, the Jiles-Atherton parameters have been characterized: the expression (88) and exponential functions were applied to represent the saturation magnetization M_s , domain density a and pinning factor k as functions of the temperature, while the other parameters are functions of the precedent parameters. Second, the five parameters in the Jiles-Atherton model have been identified for each temperature point. Even if the second method presents better results than the first one, it is not advisable to generalize this method due to the non-homogeneity of the parameters variation.

In this work, the expression (88) will be applied to represent the temperature dependency of the Jiles-Atherton parameters. This procedure is a first contribution to the temperature characterization of the magnetic material.

3.6.2 Test bench

The first measurement test is performed, with a small-signal, in order to study the variation of the material impedance with the temperature. Thus, the MDUT (inside of the temperature chamber) is plugged to the impedance analyzer (4294A), as shown in Figure 3-31. The material temperature chamber from BINDER® M series offers the mechanical convection for the material testing tasks. The programming and slow heating option can assure a homogeneous heat distribution over the MDUT. The temperature is monitored by a thermocouple up to a maximum of 300°C. Nevertheless, one has to limit the temperature because of the welding in the connector element.

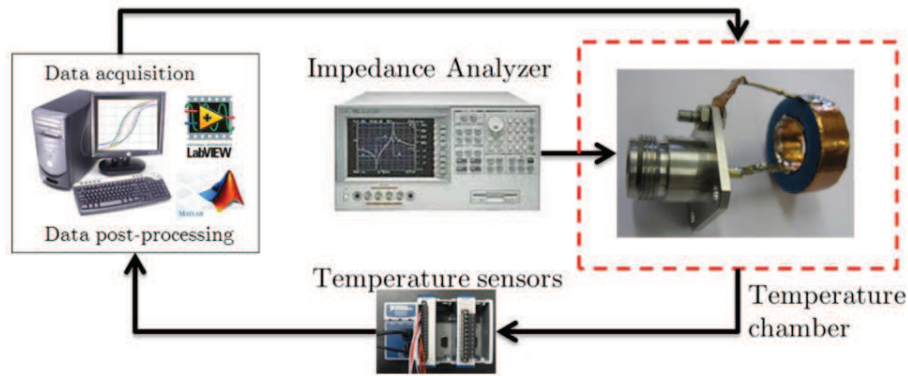


Figure 3-31 Test bench for temperature influence

The slot from National Instrument® NI-cDAQ-9174 and the module NI-9217 (4-Channel, 100 Ω RTD, 24-Bit Analog Input Module) have been configured as acquisition block to monitor the material core and the surrounding temperature of the MDUT. In fact, two probes PTC-100 (type J – 3 wires) and two additional PTC-100 (type J – 2 wires) are distributed as in Figure 3-32.

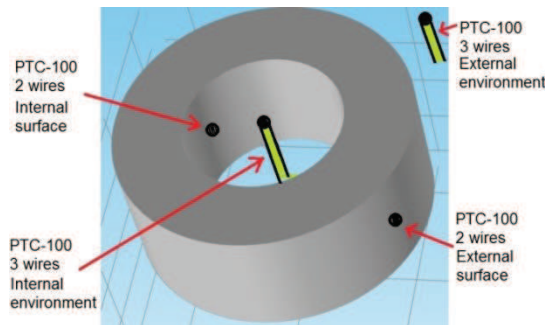


Figure 3-32 Temperature sensor distribution

The protocol of measurement is as follow:

- The MDUT with STFC is placed inside the temperature chamber
- The four temperature sensors are positioned
- The impedance analyzer is configured to measure the impedance of the MDUT in the frequency range from 100 kHz to 100 MHz.
- The temperature reference is send to the temperature chamber
- When the four temperature sensors shows the desired temperature of measurement (with a delta of +/- 10%) the acquisition starts
- The experimental data is saved

The measured impedance for the N30 ferrite and the N6E3 nanocrystalline are illustrated in Figure 3-33. The N30 ferrite loses its properties when the temperature reaches 200°C (above the Curie temperature = 130°C as indicated in datasheet). The measured impedance at 200°C reflects the leakage inductance and the copper loss in the STFC connector.

In addition, the datasheet of N30 ferrite at 10 kHz shows an increasing evolution of the initial permeability with the rise of temperature (below the Curie temperature). Nevertheless, the measurements show that the increasing evolution is not in all the frequency range. For example, as illustrated in Figure 3-33(a), the equivalent impedance is lowered above 300 kHz.

The N6E3 nanocrystalline was also measured up to 250°C. The Curie temperature of this material is reported at more than 600°C. Therefore the impedance variation with the temperature, as shown in Figure 3-33(b), is less affected in the considered temperature range. In fact, when the temperature reaches 250°C, the impedance decreases by about 10%.

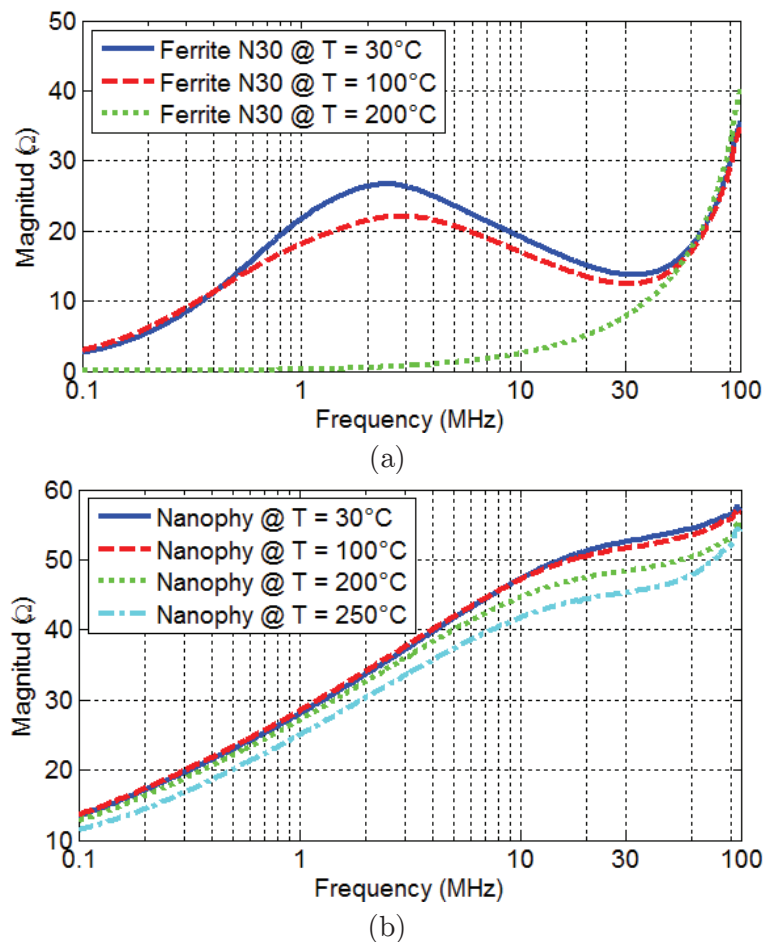


Figure 3-33 Frequency-dependent impedance (a) N30 ferrite and (b) N6E3 nanocrystalline

Furthermore, a second measurement setup is implemented but this time in high-signal excitation conditions. The previous setup (Figure 3-31) is extended with a function generator and a RF amplifier. The test bench is configured and programmed into the Labview® environment to perform an automatic excitation and acquisition of the experimental data to extract the hysteresis loop. The following tasks are implemented:

- Fix the frequency of the sinusoidal signal (Function generator)
- Fix the voltage level of the amplified signal (RF amplifier)
- Fix the surrounding temperature (Temperature chamber)
- Configure the acquisition setup (Oscilloscope)
- Monitor the temperature probes (Temperature sensor)

The automatic characterization of hysteresis loop under temperature variation is illustrated in Figure 3-34.

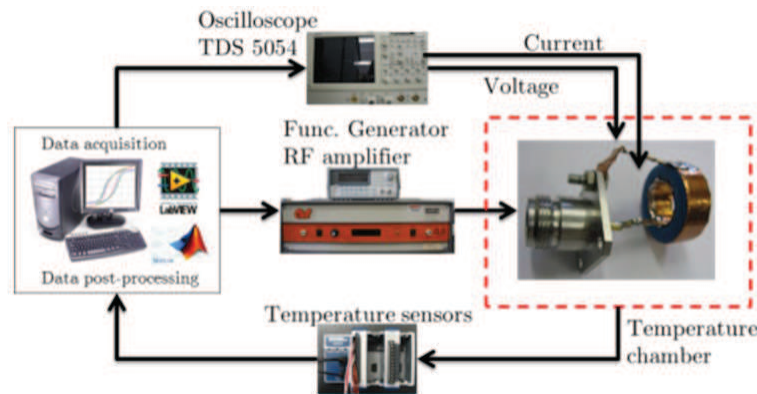


Figure 3-34 Temperature test configuration

3.6.3 Evolution of the J-A parameters with the temperature

The measuring procedure and the identification of the Jiles-Atherton model parameters are performed for different temperature levels. It is observed that the parameters M_s and a are most affected by the temperature variation. Indeed, it is reported that the parameter a is linked to the temperature in the Langevin expression. And the saturation of the material M_s represents the ability of magnetic moment alignment in the saturation state, which decreases with the temperature as shown in Figure 3-35. In fact, these parameters have been modeled by expressions (91) and (92). The *Model 1* is a third degree polynomial expression with coefficients a_0 and a_1 , whereas the *Model 2* is a rational function with coefficients b_0 and b_1 . These expressions of the parameter evolutions are fitted with the experimental data at temperatures of 30°C, 60°C, 90°C and 120°C at 100 kHz. The results of the

fitting are listed in the Table 3-12 and illustrated in Figure 3-36.

$$\text{Model 1} = a_0 - a_1 T^3 \quad (91)$$

$$\text{Model 2} = \frac{b_0}{1 + \left(\frac{T}{b_1}\right)^5} \quad (92)$$

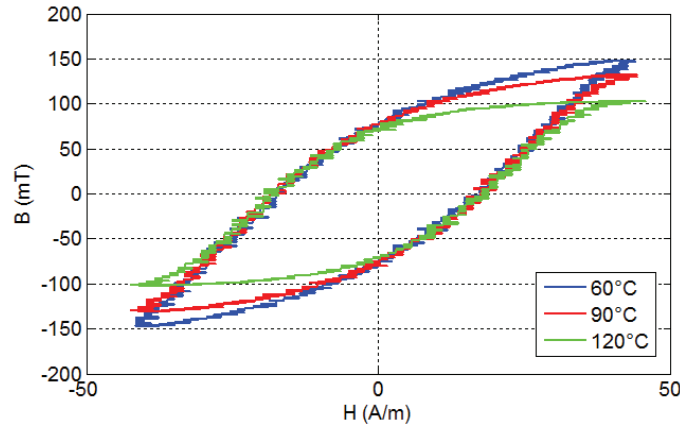


Figure 3-35 Hysteresis loop variation with temperature (N30 ferrite at 100 kHz)

The second model follows the tendency of the parameters with more accuracy for the N30 ferrite (Figure 3-36(a) and (b)). However, the parameters of N6E3 nanocrystalline are more difficult to ensure.

In this first study of the temperature over the hysteresis loop, two of the five parameters from Jiles-Atherton model show an evolution with temperature (parameter a and M_S). The model of these parameters can be included in the average BH-curve model and HCM model by updating their coefficients. That opens the possibility to improve the model in a future work in order to include the temperature issue.

Table 3-12 Coefficients of the models

Materials	Parameters	Model 1		Model 2	
		a_0	a_1	b_0	b_1
N30 ferrite	a	2.55×10^5	0.077	2.55×10^5	117
	M_S	42.7	1.69×10^{-5}	42.7	106.5
Nanocrystalline N6E3	a	9.55×10^5	0.1152	9.55×10^5	145
	M_S	25.05	0.319×10^{-5}	25.05	114

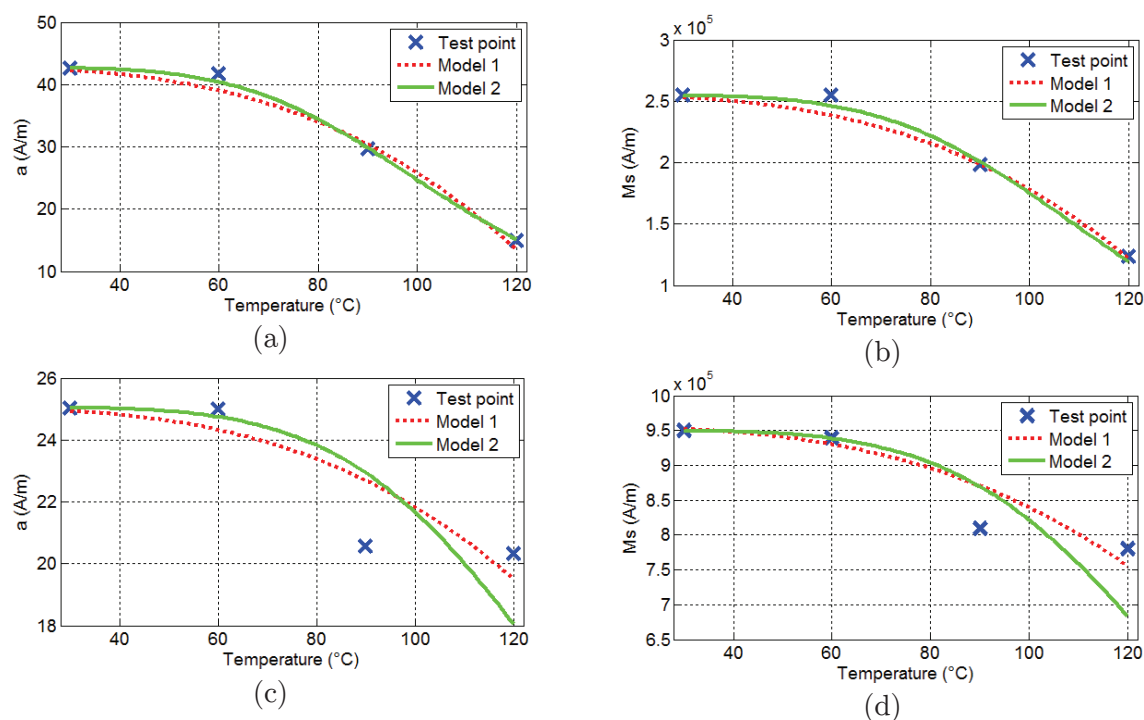


Figure 3-36 Jiles-Atherton parameters: N30 ferrite (a) parameter “ a ” (b) “ M_s ”; and N6E3 nanocrystalline (c) “ a ” (d) “ M_s ”

3.7 Conclusion

In this chapter, an experimental setup based on a single turn flat coil was proposed to characterize the magnetic hysteresis loop in HF up to 1MHz. This was motivated by the use of an alternative technique to the classic two winding transformer configuration that introduces additional parameters that must be identified (inter-turns capacitance, magnetic coupling between primary and secondary windings and proximity effects in the winding). The remaining elements that have to be characterized are the probes and connector parameters.

The second point, concerning the hysteresis loop modeling, has been achieved by considering the material behavior associated to a quasi-static hysteresis model together with a material capacitance identified from the impedance response of the material. The Jiles-Atherton model is chosen in our case as it is quite easy to implement and to identify it. The main limitation of this approach is related to the neglecting of the dynamic losses as illustrated by the core loss evolution at high frequency. Nevertheless, it still remains an interesting alternative to the classical complex magnetic permeability approach that does not take into account the nonlinearity and the DC-bias operating condition. In that last case, the proposed

hysteresis model has been tested with satisfactory results in comparison with the experiment. The magnetic model, including hysteresis and material capacitance, has been also tested with acceptable accuracy when magnetizing the material with different waveforms (saw-tooth, square) and frequencies than those used in the identification step. Finally, by imposing an arbitrary signal with DC-bias to saturate the material, the robustness of the model has been shown. These results allow then to validate the proposed method and emphasize its ability to represent the material when it is magnetized within its nonlinear region.

In addition, the model has been applied to the case of an EMI filter in order to simulate its attenuation in differential mode. This attenuation varies with the DC current level due to the saturation of the magnetic core as expected. Moreover, when comparing these results with the experiment, the same tendency for the decrease of the attenuation when the DC current level increases, is observed. There are still some improvements to be added to the modeling of the system, especially for the environment of the filter that has been considered ideal (no variation of its properties with the level of DC current). Another example of application was simulated with the model. It reflects the insertion loss of common mode filter by showing the impact of the nonlinear model on the filter effectiveness.

The proposed approach is quite interesting when one wishes to estimate the behavior of an EMI filter under DC-bias component together with the hysteresis effect. Nevertheless, some improvement can still be realized in this approach by including the dynamic effects in the hysteresis model, which would be part of a future work.

In the last section, the temperature influences over the magnetic material was investigated. Thus, an automatic test bench was developed. Two experimental procedures have been detailed to measure the CMP and the hysteresis loop respectively. In the case of the HCM model, it was observed that two parameters can be modeled in order to take into account the temperature in the model. These two parameters can be updated following the material temperature evolution and environment during simulations. However, this aspect could also be part of a future work.

Chapter 4. EMI filter design

The previous chapters describe the characterization and modeling of magnetic materials in wide frequency band. The small-signal and high-signal characterization of two kinds of magnetic materials have been developed in order to use their models in EMI filter design. However, the effectiveness of the EMI filters depends not only on its internal components, the input and output impedances linked to the EMI filter also have an influence. Then, measuring or estimating these impedances becomes important to optimize the EMI filter design.

4.1 Introduction

In order to predict the insertion loss and effectiveness of the EMI filter, it is necessary to know the required conducted emissions level that will be reduced to meet the EMC standards. Additionally, it is necessary to know the input/output impedances connected with the filter and the characteristics of passive components.

In this chapter, the conducted emissions of static converters quantified by measurement are firstly studied. The level of these emissions is estimated by regarding the EMC standard limits. Second, the LISN and static converter input impedances are characterized by the current injection method (CIM). Third, new current probes are designed to improve the accuracy of the measurement method. These impedances, together with the small and high-signal material model, developed in previous chapters, are used to predict the insertion loss of the EMI filter associated to a buck converter. Finally, the procedure to characterize the insertion loss of realized filters by S-parameters is addressed.

4.2 Equipment under test – buck converter

In this chapter different static converters are considered as equipment under test (EUT) to validate the proposed methods. For example the buck converter based on IGBT (Figure 4-1), with their characteristics listed in Table 4-1. The battery cell, in the schematic, provides the power for the driver and that cancels the CM emissions that could be closed by the power supply.

The printed circuit board (PCB) of the buck converter (with dimension 10x6 cm²) and the complete view of the global system are shown in Figure 4-2. The load is composed of a resistor of 16.5Ω (two resistors of 33Ω connected in parallel) and one

inductor of 200 μH (at 100 kHz) made with an iron powder ring core with dimensions of $D_E=39\text{mm}$, $D_I=21\text{mm}$, $H_E=11\text{mm}$ and 40 turns.

Table 4-1 Characteristics of the buck converter

	Description		Description
IGBT	IXGR40N60	Duty cycle	25%
Diode	STTH15R06D	Capacitor Bus	4.7 μF (X7R)
Switching frequency	60 kHz	Power supply	100 V

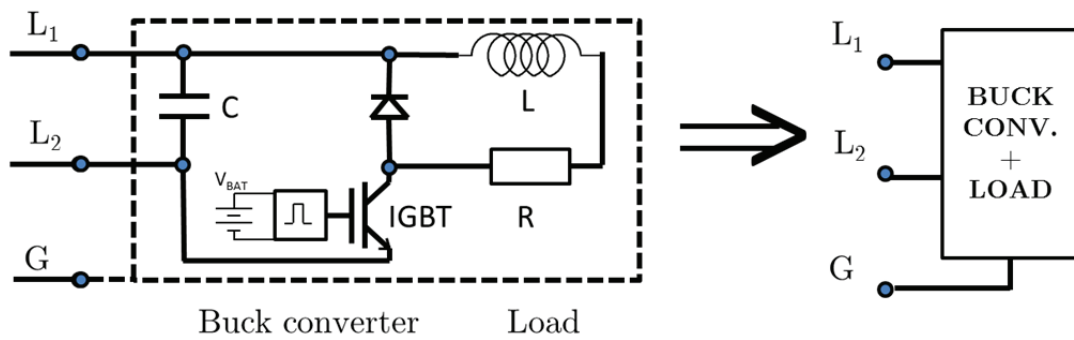
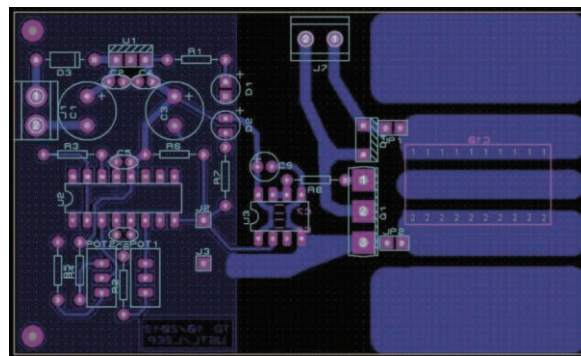
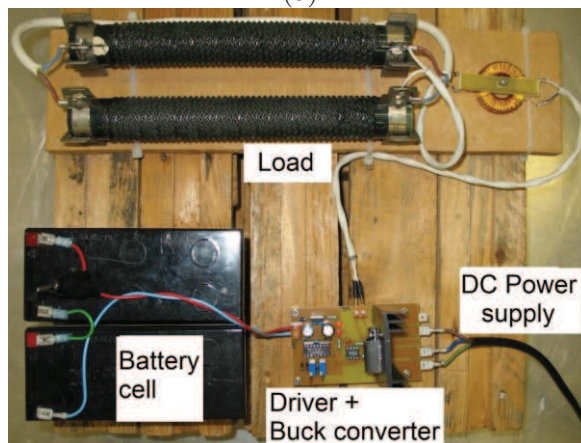


Figure 4-1 Schematic of IGBT Buck converter



(a)



(b)

Figure 4-2 Buck converter (a) drive and power PCB and (b) global view of the system

4.3 Conducted emissions measurement

4.3.1 Overview

The conducted emissions, generated by static converters, are measured to know the spectral content in the frequency bandwidth of interest. These emissions are compared with the limits established by EMC standard and thereby to identify the frequencies where EMI has to be reduced. Three methods to measure the conducted emissions can be used:

- Indirect measurement with FFT of time-domain input voltage
- Direct measurement at LISN's 50Ω terminals
- Direct measurement on the spreading paths with current probes

The indirect method with FFT is not developed in this work but additional information can be found in [102].

4.3.2 Measurement with LISN

The Line Stabilization Network (LISN) is a low pass filter. It is used to separate the equipment under test (EUT) from the power supply, and it establishes constant impedance ($Z_{LISN} = 50\Omega$) at the output terminals. The drop voltage over Z_{LISN} is measured to get the conducted emissions generated by EUT; for example, the voltages V_{L1} and V_{L2} in LISN (EMCO 3810/2) shown in Figure 4-3.

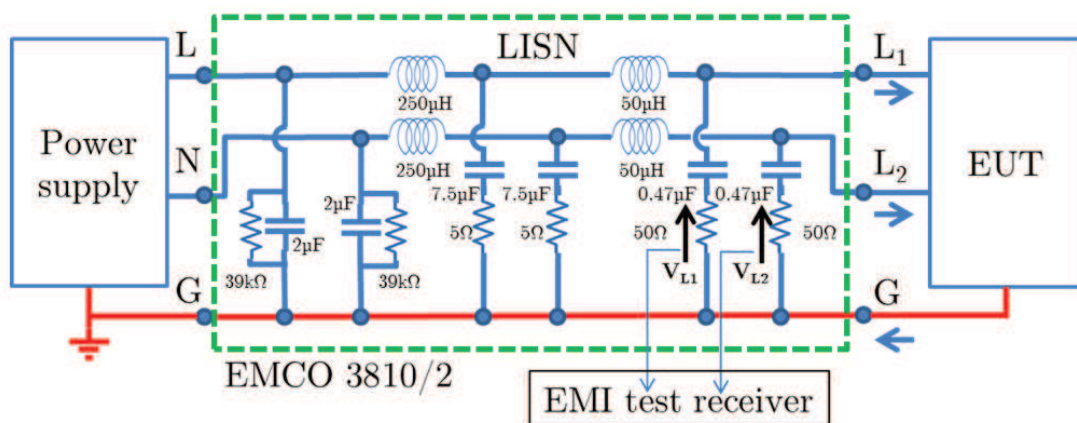


Figure 4-3 Equivalent circuit of mono-phase LISN (EMCO 3810/2)

The common mode ($V_{CM-LISN}$) and differential mode ($V_{DM-LISN}$) voltages can

be expressed in function of the measured voltages by the software separation technique using (93) and (94) [6]. Even though, these expressions are not adapted to arithmetic operations because the phase information of the measured drop voltages are unknown. In this case, the EMC standard requires evaluating the conducted emissions only in one phase (measured emissions voltage V_{L1} or V_{L2}).

$$V_{CM-LISN} = \frac{V_{L1} + V_{L2}}{2} \quad (93)$$

$$V_{DM-LISN} = V_{L1} - V_{L2} \quad (94)$$

Another technique based on RF transformers, known as the hardware separation method, can be also applied [103]. An extra device connected to both 50 Ω -outputs of the LISN is required in order to split the conducted emissions into DM and CM. However, it is limited to some LISN models where both 50 Ω -outputs are accessible. This technique is not developed here.

4.3.3 Measurement with current probe

The diagram depicted in Figure 4-4(a) represents the composition of the currents on each phase line (I_{L1} , I_{L2}) and the ground line (I_G) versus DM and CM currents (I_{DM} , I_{CM}). The technique of current probe allows splitting the current into DM and CM by clamping the probe between the phase and ground lines as shown in Figure 4-4(b) and (c). The currents I_{CM} and I_{DM} are multiplied by the LISN impedance (Z_{LISN}) to calculate the CM and DM voltage, as given in (95) and (96).

$$V_{CM-LISN} = \frac{Z_{LISN}}{2} I_{CM} \quad (95)$$

$$V_{DM-LISN} = 2Z_{LISN} I_{DM} \quad (96)$$

The current probe method allows measuring the current with an equivalent voltage value given in decibels ($dB\mu V_{mea}$). Then, these voltages are compensated with the current probe factor or impedance transfer ($dB\Omega$) to extract the current information ($dB\mu A_{mea}$) as given by (97).

$$dB\mu A_{mea} = dB\mu V_{mea} - dB\Omega \quad (97)$$

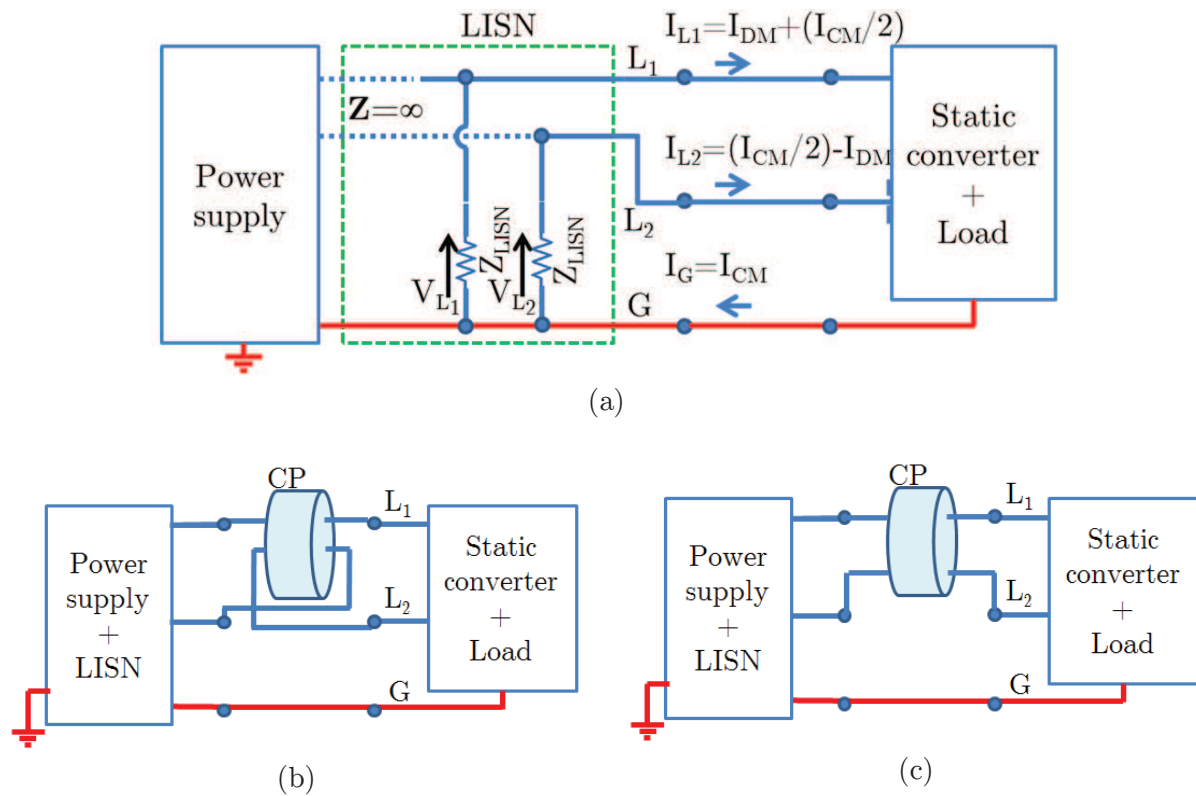


Figure 4-4 (a) Conducted emissions over the spreading paths (b) DM current and (c) CM current measurement setup

4.4 Conducted emissions of the buck converter

The EMI measurement setup of the conducted emissions are composed of the EUT (buck converter), the LISN (EMCO 3810/2) and the EMI test receiver (R&S ESPI3), as shown in Figure 4-5. The spectrum of conducted emissions (V_{L1} and V_{L2}) are presented in Figure 4-6 with the limit in quasi-peak (QP) given by the EMC standard CISPR-11 (class B) in the frequency range from 150 kHz to 30 MHz. Already, it is observed that the conducted emissions measured in both terminals are not identical in all the frequency range.

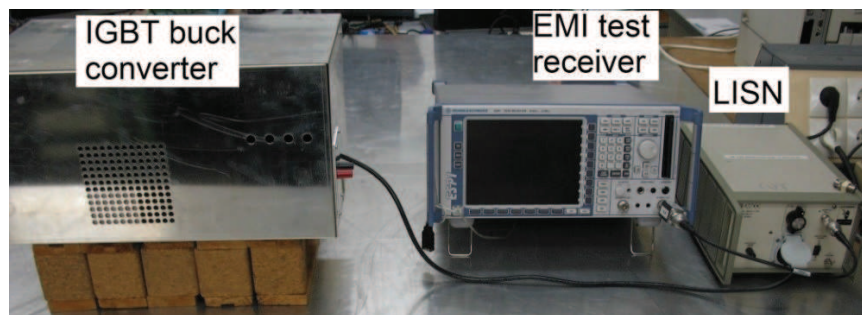


Figure 4-5 Conducted emissions measurement setup

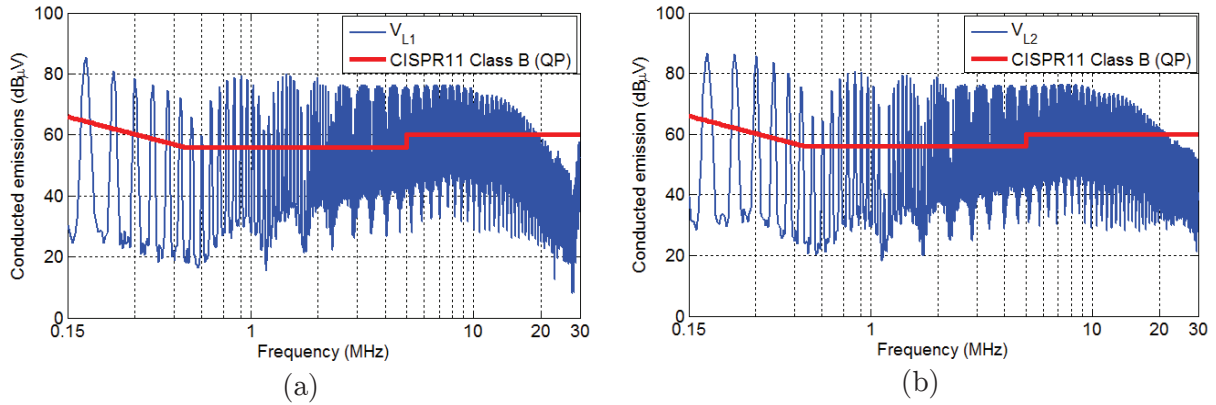


Figure 4-6 Conducted emissions (QP) of the buck converter with LISN (a) V_{L1} and (b) V_{L2}

The current probes method is used as shown in the configuration presented in Figure 4-4(b) and (c) (current probe FCC F-35 (100 Hz -100 MHz)). The measured DM and CM emissions are given in Figure 4-7. In low frequency, it is observed that the influence of the DM, close to the switching frequency (60 kHz), is more pronounced than in the high frequencies, for example the third harmonic at 180 kHz can reach 100dB μ V.

The CM emissions presents a large spectral content distributed in almost the entire frequency range (150 kHz – 30 MHz). The harmonic amplitudes are close to 90dB μ V. All these excess emissions will be used in the design process of the EMI filter, and for the prediction of its insertion loss.

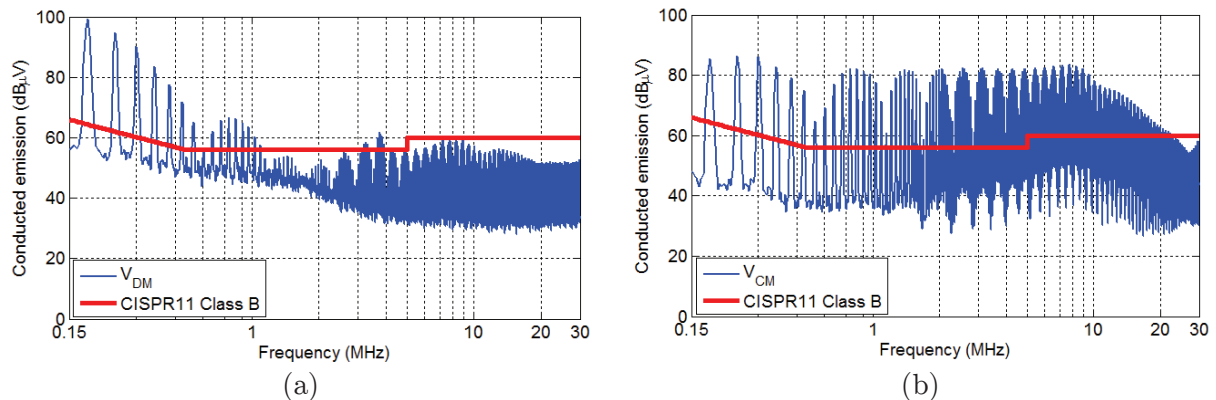


Figure 4-7 Conducted emissions of the buck converter (a) V_{DM} and (b) V_{CM}

4.5 EMI source impedance measurement

4.5.1 Overview

The insertion loss of the filters is typically characterized by apparatus with standardized impedance of 50 Ω . Thus, the impedances connected to the input-output

of EMI filter in the characterization procedure are 50Ω - 50Ω . These values are different from the input-output impedances connected to the filter in operating conditions. Then, it is necessary to know the input impedance of the converter (Z_{SDM} and Z_{SCM}) and the impedance of the LISN (Z_{LISN}). In this section, two measurement methods are used to identify these impedances. The first is based on impedance analyzer (converter in off-state) and the second is based on current injection probes (in operating conditions).

4.5.2 Measurement in off-state

The typical impedance measurement procedure is based on the impedance analyzer. The buck converter is characterized between the terminals L_1 , L_2 and G . The six measurement configurations are shown in Figure 4-8: between the line L_1 to line L_2 (Z_{L1-L2}), line L_1 short-circuited with ground line G to line L_2 (Z_{L1G-L2}), line L_2 short-circuited with ground line G to line L_1 (Z_{L2G-L1}), line L_1 to ground line G (Z_{L1-G}), line L_2 to ground line G (Z_{L2-G}) and line L_1 short-circuited with line L_2 to ground line G (Z_{L1L2-G}). The measured impedances are compared in Figure 4-9(a) for the DM configuration.

The impedance Z_{L1-L2} is equivalent to the converter impedance in differential mode Z_{SDM} . The two additional measurements (Z_{L1G-L2} and Z_{L2G-L1}) are identical up to 400 kHz. Above this frequency the asymmetrical impedances put in evidence the parasitic elements in HF. Moreover, the measured impedance Z_{L1L2-G} is equivalent to the converter impedance in common mode Z_{SCM} . In this case, the two other measures (Z_{L1-G} and Z_{L2-G}) have closely the same measurement result. In fact, this method allows measuring the impedance of the converter in the off-state which becomes the main inconvenience of this method.

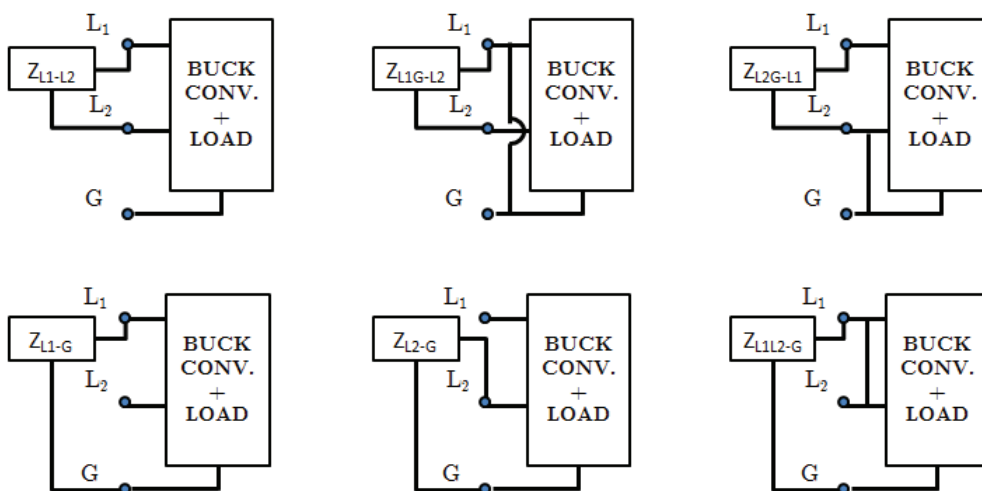


Figure 4-8 Measurement configurations of the converter impedance in off-state

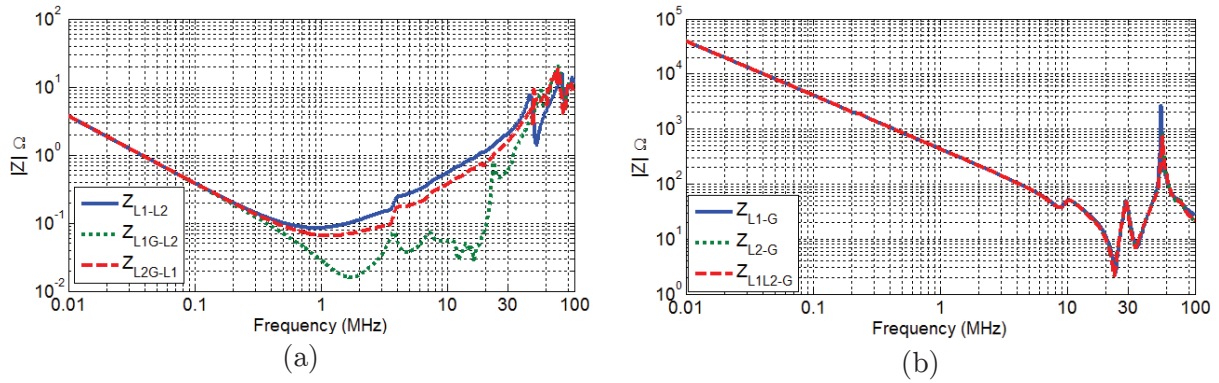


Figure 4-9 Impedances of the buck converter measured with impedance analyzer in off-state

4.5.3 Current injection method

The current injection method (CIM) for impedance characterization was introduced in [104]. The small level signal generated by the vector network analyzer is injected through current probes to measure the unknown impedance branched to the terminals of the setup. In [105], the impedance measurement procedure based on the CIM is applied for DM and CM configurations of the static converter. Then in [106], these impedances are included in the filter design process. The EMI filter insertion loss, unlike the traditional process, where the EMI filter is characterized under 50Ω - 50Ω , replaces these impedances by the LISN impedance Z_{LISN} and the static converter impedances (Z_{SDM} and Z_{SCM}). Thus, the insertion loss and optimizing the choice of the components for the filter are improved.

First, the current injection method is studied in order to validate the measurement procedure. Second, the input impedance of a static converter is measured, which is considered as a three-line terminal (L_1 , L_2 and G).

The principle is as follows: the current I_w is injected through the current injection probe (FCC : F120-3) to the loop containing the unknown impedance Z_X while a second current probe (FCC : F35) measures this current, as shown in Figure 4-10(a). The vector network analyzer (VNA - E5071C) generates the power signal in port 1 and port 2 captures the current injected measured by the CP. The output power of port 1 is set to 10 dBm, and the frequencies range from 10 kHz to 30MHz.

Following the analogy of a two-port network, the equivalent impedance of the circuit in Figure 4-10(a) can be determined by S-parameters. This method needs two calibration measurements (short circuit and 50Ω) then it enables the calculation of the unknown impedance Z_X based on the schematic shown in Figure 4-10(b). The equivalent circuit of the measurement setup considers the two probes and the wire

impedance Z_{wire} as a transformer model. The main advantage of this method is the insulation between the measurement equipment and the unknown power network. Moreover, both magnitude and phase information of the measured impedances can be obtained in the frequency domain.

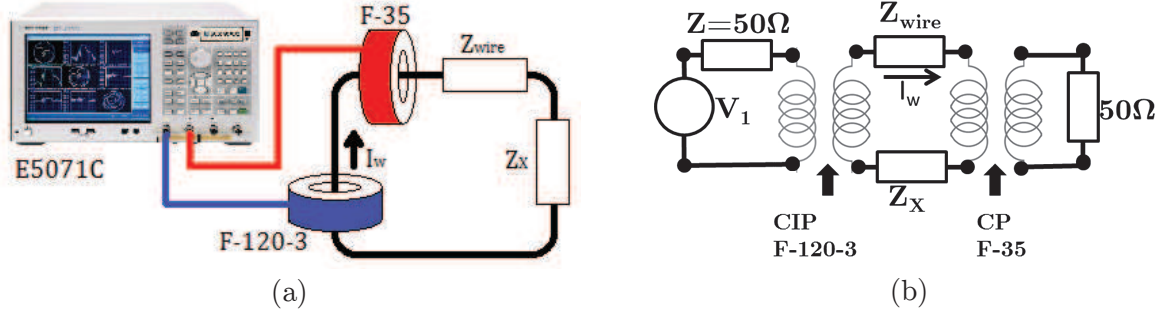


Figure 4-10 CIM to measure the unknown impedance Z_X (a) connection (b) equivalent circuit

The FCC current probe F-120-3 (10 kHz to 100 MHz) (CIP) is connected to the port 1 of VNA to inject the current and the FCC current probe F-35 (10 kHz to 100 MHz) (CP) connected to port 2 measures the current. The calibration of a two-port network is performed between ports 1 and 2. The output power of port 1 is set to 10 dBm, and the frequencies range from 10 kHz to 30 MHz.

The frequency dependent variables, K and Z_{setup} in (98), are determined from the two calibration measurements ($Z_X = 0\Omega$ and $Z_X = 50\Omega$). Then, both expressions (99) and (100) are solved and replaced in the equation (98). The parameter D_{p1p2} represents the input voltage source (port1) over the measured voltage (port 2) and it is obtained experimentally from the S-parameters, as given by (101). This parameter is a frequency dependent complex number (without units) because it is obtained from the ratio of the S-parameters S_{11} and S_{21} . The parameter Z_{setup} includes the impedance of the measurement setup, and the unknown impedance Z_X is a complex number and also frequency dependent.

$$Z_X = KD_{p1p2} - Z_{\text{setup}} \quad (98)$$

$$K = \frac{(Z_{X=50} - Z_{X=0})}{D_{p1p2, X=50} - D_{p1p2, X=0}} \quad (99)$$

$$Z_{\text{setup}} = KD_{p1p2, X=50} - Z_{X=50} \quad (100)$$

$$D_{p1p2} = \frac{1 + S_{11}}{S_{21}} \quad (101)$$

4.5.4 Measurement of passive components

In order to validate the procedure, a single loop of wire (20 cm) is used with the current probes (Figure 4-10). Both parameters, K and Z_{setup} , are shown in Figure 4-11. The phase of the parameter K is linked to the transfer impedance of the current probes, which also explains its evolution in frequency that changes to negative values around 2 MHz (Figure 4-11(a)).

From the Figure 4-11(b), Z_{setup} can be considered as an inductance (because the phase is $\sim 90^\circ$) between 150 kHz and 30 MHz. It includes the impedance of the network (wire and coupled impedance of the probes) that connects to the unknown impedance. The average value measured with the impedance analyzer is $0.75\mu\text{H}$. This value remains stays valid only if the configuration is kept constant. That means, if the wire is changed (position or dimension), a new calibration of the measurement setup has to be performed.

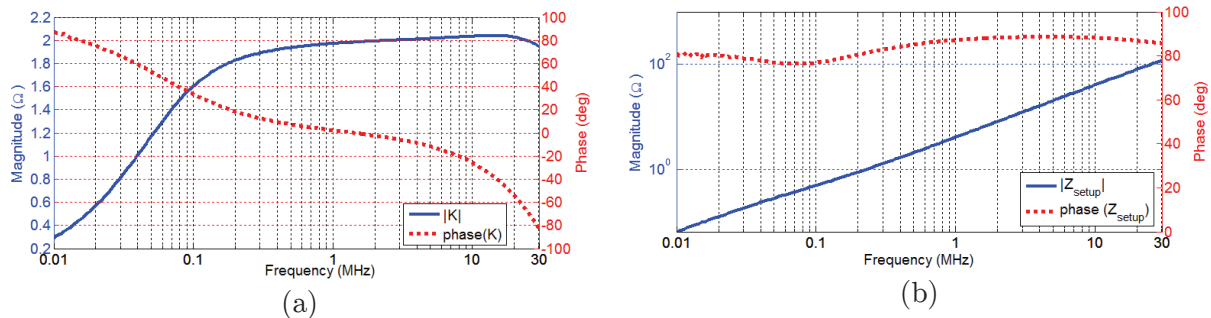


Figure 4-11 Frequency evolution (a) parameter K and (b) Z_{setup}

Now, this method is evaluated with some passive components. First, the unknown impedance Z_X is replaced by precision resistors with values 82Ω , 470Ω and $1.2\text{k}\Omega$. And then, it is replaced by a capacitor and inductor.

The precision resistors are measured in the frequency range from 10 kHz to 30 MHz, and the results are shown in Figure 4-12. In low frequencies (below 50 kHz), the accuracy of this method is not enough to represent the correct value of the resistor. Basically, that discrepancy is related to the transfer impedance of the probe that has low values. The accuracy is then affected by the value of the unknown impedance. The same result can be obtained when the unknown impedance is lower than the impedance of calibration (50Ω). This inconvenience can be partially ameliorated if this impedance is changed with a value in the same order of the unknown impedance. It means that better results could be accomplished when Z_X is close to the calibration impedance.

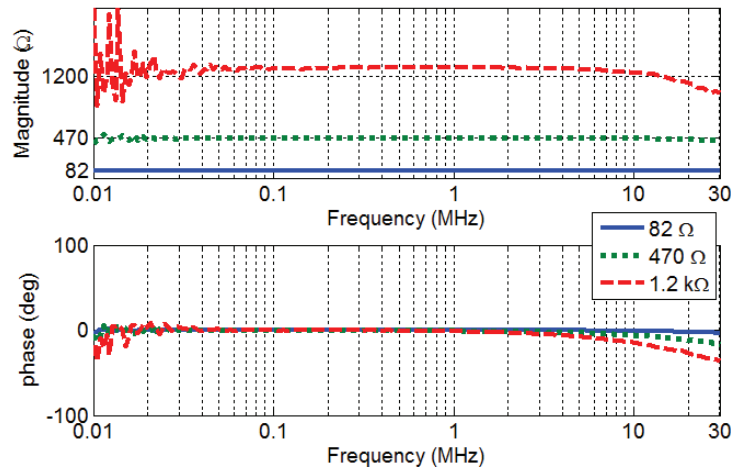


Figure 4-12 Impedance of precision resistors measured with CIM

On the other hand, the impedance of a capacitor and inductor were measured and compared with the experimental results obtained with the impedance analyzer. These curves are compared in Figure 4-13. The capacitor impedance shows a good agreement in HF with some oscillations at low frequencies. That is attributed to the high impedance value below 100 kHz. Besides, the inductor impedance correlates with the impedance analyzer measurement up to 30 MHz.

In consequence, the CIM can measure the impedance of one unknown element with some limitation regarding the value of impedance. The main advantage of this method is that it allows a measurement of the unknown impedance in operating condition with isolation between VNA and EUT, as described in the following section, where the CIM is used to measure the input converter impedance (Z_{SCM} and Z_{SDM}).

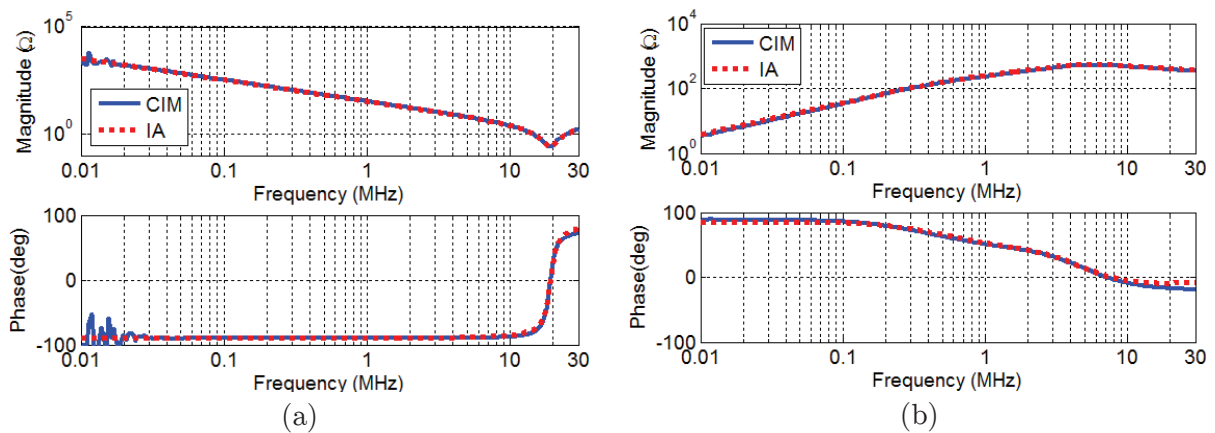


Figure 4-13 Impedance measurement of (a) a capacitor and (b) an inductor

4.5.5 Measurement of static converter impedances

The procedure of impedance measurement detailed in the previous section was applied to two terminal devices (resistor, capacitor and inductor). In the case of the static converters, for example the SiC buck converter (input voltage 100V, switching frequency of 100 kHz and output current 2A) illustrated in Figure 4-14, different configurations are observed, then some arrangements have to be done. Indeed, for each configuration (CM and DM) a specific calibration has to be carried out. The differential mode (Z_{SDM}) and the common mode (Z_{SCM}) impedances will be identified independently. The objective is to measure these impedances of the converter in operating conditions.

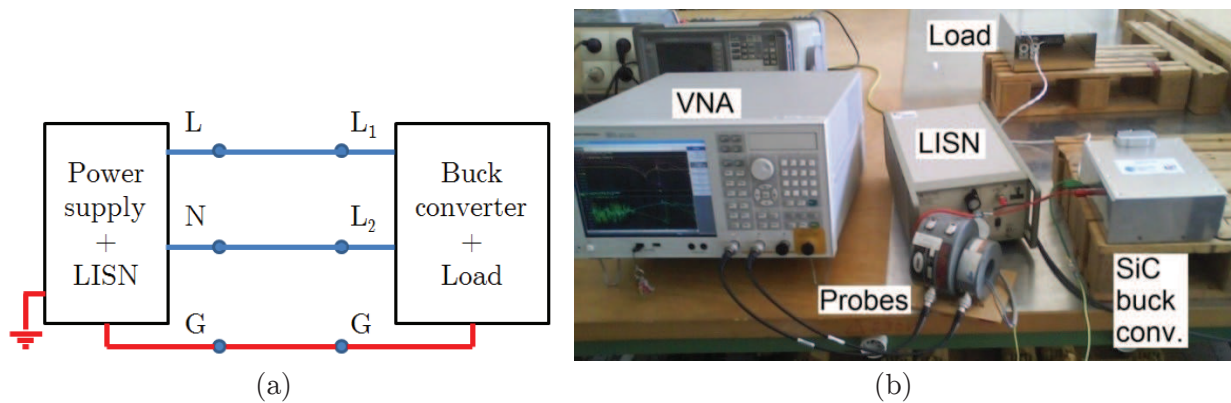


Figure 4-14 Impedance measurement of SiC buck converter in operating conditions by CIM

Differential mode impedance

The DM configuration characterizes the input impedance of the buck converter following the diagram shown in Figure 4-15. The current injection probe and current measuring probe are clamped around both lines (L_1 and L_2). Thus, the current injected by CIP will follow the DM paths of the buck converter and the LISN. By hypothesis, there is no coupling between the lines L_1 , L_2 and ground line G .

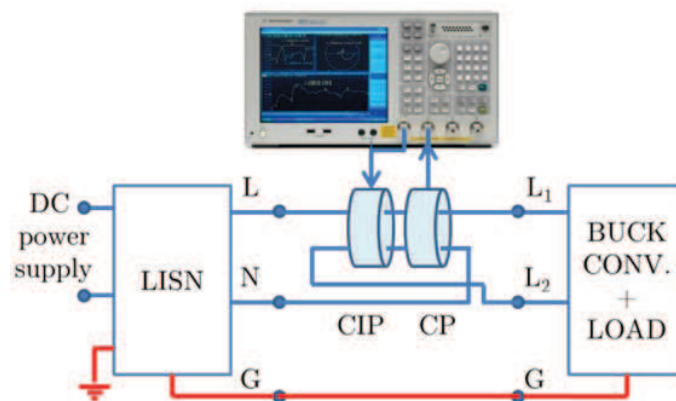


Figure 4-15 Measurement of the DM impedance of the buck converter and load

The measurement steps to determine the equivalent impedance Z_{SDM} are:

1. Determination of the parameters K and Z_{setup} .
2. Determination of the equivalent impedance of LISN in DM.
3. Determination of the equivalent impedance of buck converter in DM.

The first step was described in the previous section. However, the second step needs an additional capacitor connected instead of static converter to emulate a short circuit at HF, as shown in Figure 4-16. The capacitor value ($C = 2.2 \mu\text{F}$; $\text{ESL} = 66\text{nH}$; $\text{ESR} = 22\text{m}\Omega$) is chosen larger in order to have a resonance in low frequencies (600 kHz). This resonance is shifted to low frequencies (70 kHz) because of the wire inductance connected. The configurations for a $Z_X = 0\Omega$ and $Z_X = 50\Omega$ are shown in Figure 4-16 and the evolution of K and Z_{setup} are illustrated in Figure 4-17.

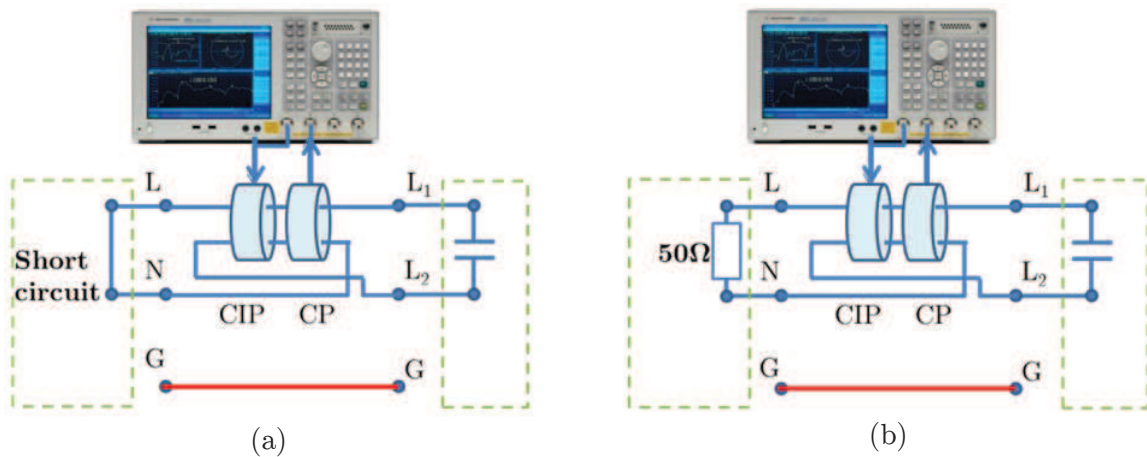


Figure 4-16 DM configuration test to determine K and Z_{setup} (a) $Z_X = 0\Omega$ (b) $Z_X = 50\Omega$

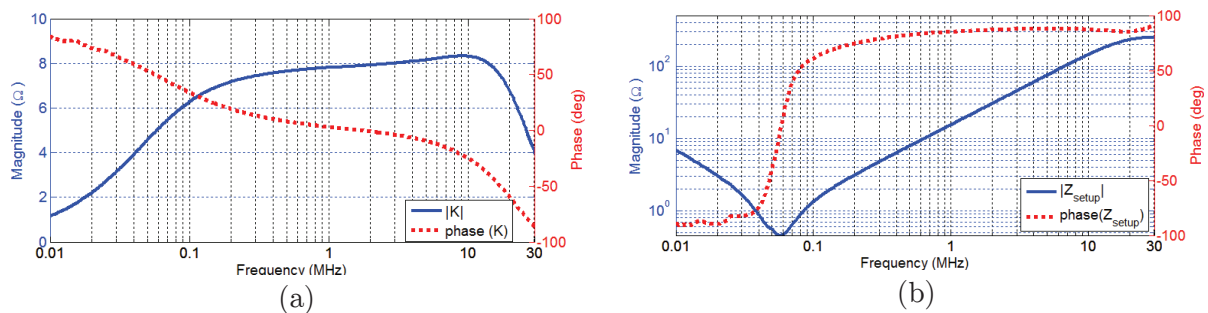


Figure 4-17 Frequency evolution of (a) K and (b) Z_{setup} in the DM configuration

The magnitude of the parameter K drops above 10 MHz as a product of the change in phase (Figure 4-17(a)). Meanwhile, Z_{setup} defines the low frequency limit of the measurement due to the inductive behavior above 70 kHz.

The second step is the LISN characterization, which is carried out with a capacitor (known impedance) and the power supply connected to the LISN (Figure 4-18(a)). The difference between the CIM and the impedance analyzer measurement on the LISN impedance is the possibility to apply a voltage level at LISN input. The comparison between the measured impedances with these two methods is shown in Figure 4-18(b). A good agreement is observed up to 30 MHz. These results show that the impedance of the LISN in DM ($Z_{LISN-DM}$) is 100Ω in most of the frequency range. The phase of $Z_{LISN-DM}$ in HF starts to increase due to parasitic effects from the connections or coupling in the measurement setup.

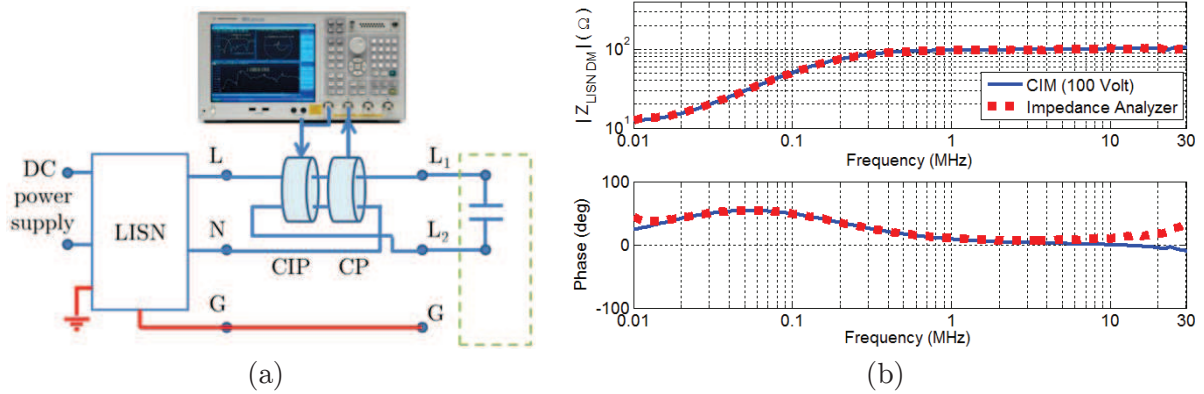


Figure 4-18 Impedance measurement of the LISN (a) DM configuration setup and (b) Comparison of measurement results

The third, and last step, consists of measurement of the impedance of the static converter. The input impedance of a buck converter is nonlinear because it varies over time due to the switching components. The impedance measurement with CIM is performed in a time duration considered much greater than the switching period. In fact, the VNA performs a data acquisition in the order of milliseconds while the period of the buck converter is of 0.1mSec. Consequently, the measured impedance value is an average of two impedances: the off-state (Z_{OFF}) and on-state (Z_{ON}) that vary in time. In this configuration the buck converter is connected as described in Figure 4-15.

The measured impedance (Z_{mea}) is the combination of the static converter impedance (Z_{SDM}) plus the impedance of the LISN in DM ($Z_{LISN-DM}$). Then the converter input impedance in DM is given by (102).

$$\overline{Z_{SDM}} = \overline{Z_{mea}} - \overline{Z_{LISN-DM}} \quad (102)$$

Three tests are performed and compared to investigate the influence of the on-operating conditions over the impedance measurement. It is necessary to state that the control circuit of the converter (driver) has its own power supply. Then, the impedance is measured under the following conditions:

- The DC power supply = 0V and power supply of the driver = OFF.
- The DC power supply = 0V and power supply of the driver = ON.
- The DC power supply = 100V and power supply of the driver = ON.

As shown in Figure 4-19 the values of the measured impedance with CIM (on-operating) of buck converter in DM is compared with those measured by an impedance analyzer (off-state). A phase of 90° degrees indicates an inductive element by almost the entire frequency bandwidth 100 kHz to 10 MHz. The equivalent impedance without input voltage (DC=0 V and Driver OFF) approaches the value obtained by the impedance analyzer, approximately 318nH.

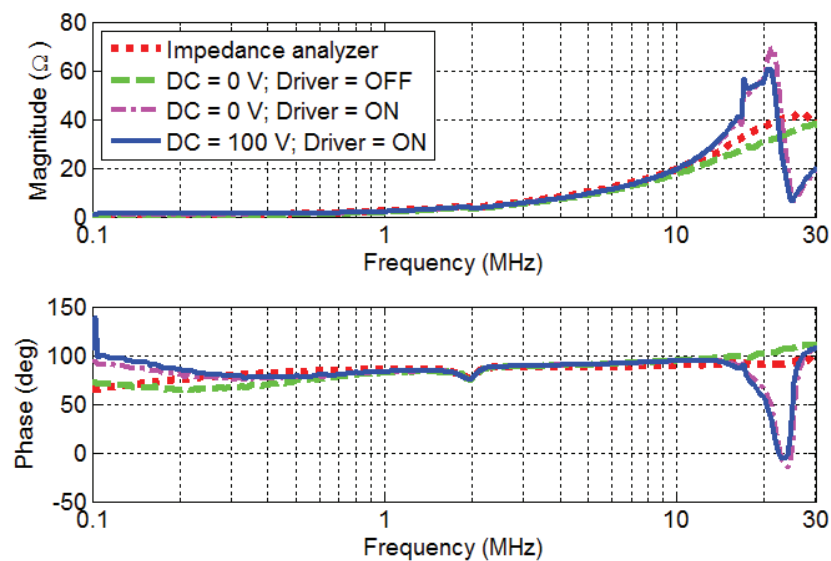


Figure 4-19 Evolution of Z_{SDM}

Between 10 MHz and 30 MHz, resonances occur when static converter is fed with 100V. Those resonances can be attributed to parasitic effects that become more evident when buck converter elements are polarized. Even though, it has to stand out that the impedance measured in off-state conditions (impedance analyzer) do not represent the impedance in HF when the static converter is in operating condition.

Common mode impedance

The CM configuration measures the impedance of the static converter when the injected current flow through the supply wires (L_1 and L_2) and is closed by the ground line (G). In Figure 4-20, the CM configuration is presented where two current probes are used. Following the same steps of the DM impedance measurement, the CM configuration is calibrated to obtain the K and Z_{setup} parameters. Thus, the LISN impedance and the static converter impedance (Z_{SCM}) are determined.

The configuration test to obtain the K and Z_{setup} parameters are shown in Figure 4-21. Two capacitors of $C = 2.2 \mu\text{F}$ are placed between the lines (L_1, L_2) and the ground line, while in the other side, the $Z_X=0\Omega$ and $Z_X=50\Omega$ are connected respectively in order to have the two measurement configurations. The measurement results are illustrated in Figure 4-22. The frequency evolution of these parameters has similarities to the DM configuration; however, they do not have the same magnitude values. The first resonance of Z_{setup} at 70 kHz is defined by the resonance of the additional capacitor and the equivalent inductance of the measurement configuration.

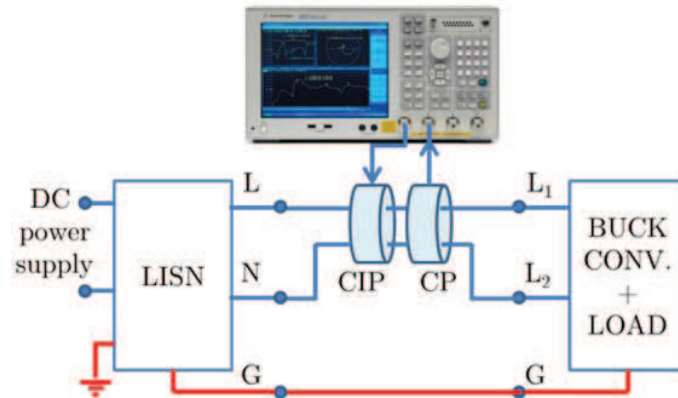


Figure 4-20 Measurement of the CM impedance of the buck converter and load

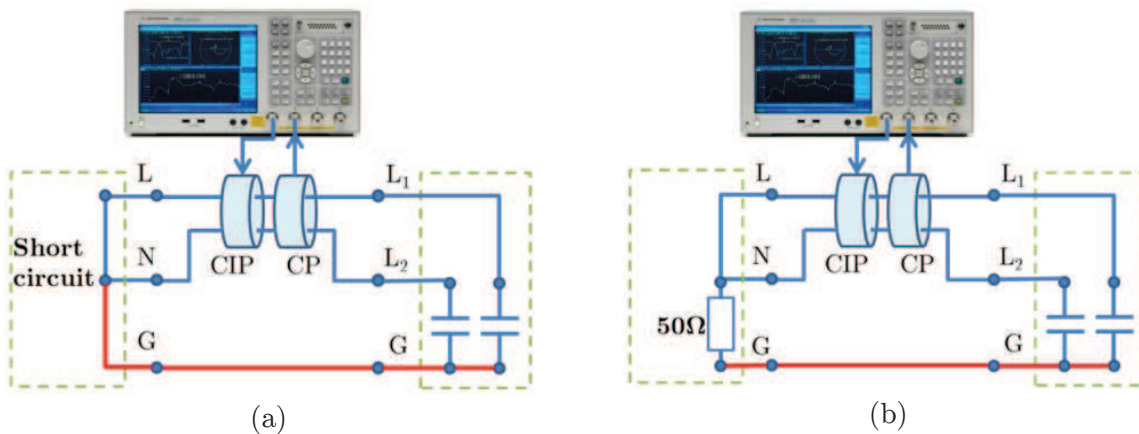


Figure 4-21 CM configuration test to determine K and Z_{setup} (a) $Z_X = 0\Omega$ (b) $Z_X = 50\Omega$

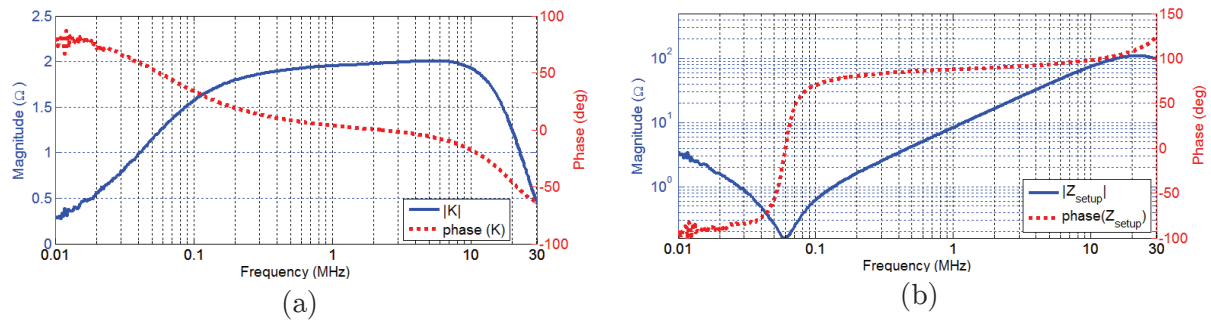


Figure 4-22 Frequency evolution of (a) K and (b) Z_{setup} in the CM configuration

The impedance Z_X is replaced by the LISN as shown in Figure 4-23(a). Like in operating conditions, a DC power supply of 100 V is connected to LISN. The measured impedance (Figure 4-23 (b)) shows an evolution in frequency with an average value of 25Ω up to 10MHz. Above 10 MHz, close to 22MHz, the resonances start to appear. These resonances can be linked to parasitic elements of the connection wire between the LISN and the static converter. The loop area of the setup configuration must be reduced at the minimum area. One solution that consists of reducing the probe size will be addressed in the next section.

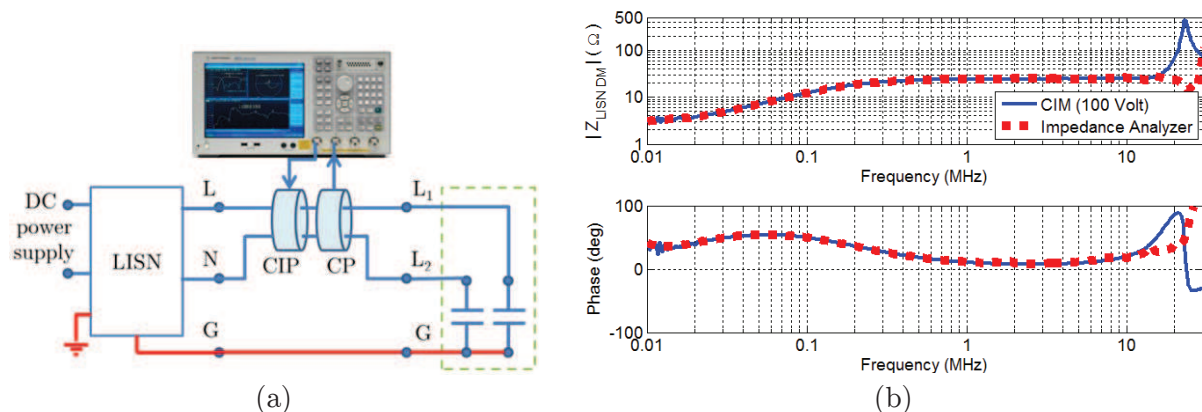


Figure 4-23 Impedance measurement of the LISN (a) CM configuration setup and (b) Comparison of measurement results

Now, the capacitors are replaced by the static converter and different measurements of the common mode impedance (Z_{SCM}) are evaluated:

- The DC power supply = 0V and power supply of the driver = OFF.
- The DC power supply = 0V and power supply of the driver = ON.
- The DC power supply = 100V and power supply of the driver = ON.

The measurement results of the CM impedance of the static converter are shown in Figure 4-24. The value of the equivalent capacitance of the converter below

10MHz compared with the value obtained with the impedance analyzer has increased. For example at 1 MHz, the impedance Analyzer gives 191.4pF, while in the other three tests $C = 232.8\text{pF}$ (0V - OFF), $C = 252.9\text{pF}$ (0V - ON) and $C = 299.4\text{pF}$ (100V - ON), over 50% of the value obtained with the impedance analyzer. Above 10MHz a different resonance appears linked to the parasitic elements of the setup.

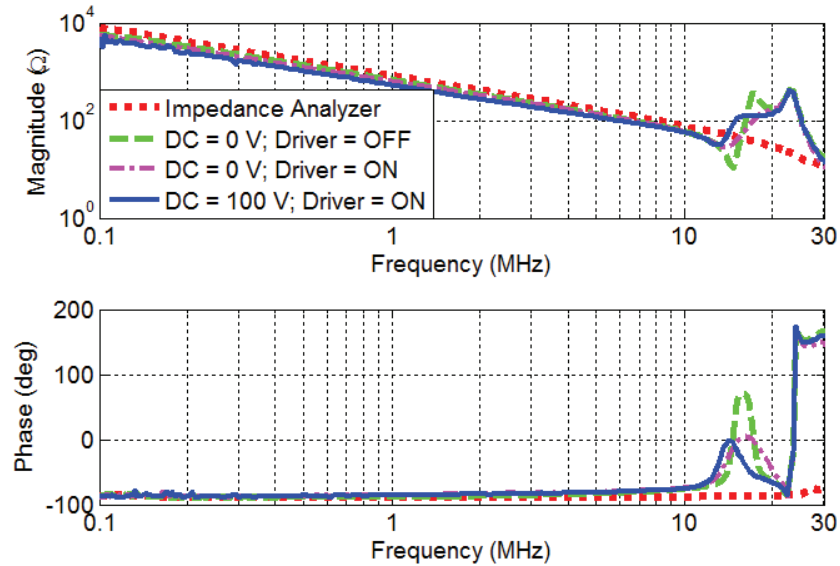


Figure 4-24 Evolution of the buck converter impedance Z_{SCM}

In this section, the impedance measurement method of the static converter has been presented. Both configuration, DM and CM, are employed to determine the impedances Z_{SDM} and Z_{SCM} of the buck converter. In consequence, the current injection method can measure effectively the input impedance of these static converters on operating conditions, but it can be improved by increasing the accuracy of the setup. In the purpose of reducing the parasitic elements of the experimental setup, one solution is proposed. The current probes used until now were commercial probes. The size of these probes increases the loop area of the setup, and in consequence, that increases the parasitic effects. In order to improve the CIM, new current probes are proposed and detailed in the following section.

4.6 Current probes

Two new current probes (NCP) are designed with appropriate high frequency magnetic material to improve the accuracy of the impedance measurement using the current injection method. Because this impedance is relevant for the EMI filter design, the NCP are used to measure the common mode impedance of static converters in operating conditions. To determine the transfer impedance of the

probes, a simple formulation using S-parameters is proposed. Thus, the NCP allows improving the accuracy of the impedance measurement in a wide frequency band up to 100 MHz. Finally, different measurements of common mode configurations are detailed and discussed.

The measurement of the common mode impedance Z_{SCM} of the converter in operating conditions, using the CIM, was described previously. This method needs two calibration measurements (short circuit and 50Ω) to calculate the unknown impedance Z_X . The main advantage of this method is the insulation between the measurement equipment and the power converter in operating conditions. Moreover, both magnitude and phase information of the measured impedances can be obtained in frequency domain. The accuracy of the experimental setup in low frequency (below 1 MHz) is affected by the low transfer impedance of the probes. In high frequency (above 10MHz), the accuracy of the measurement is also affected by the setup impedance linked to the length of the wire and characteristics of the probes.

In order to reduce the impedance of the connection wire Z_{wire} , that considerably influences the accuracy of the measurement, and increase the transfer impedance in low frequency, two new small probes with appropriate magnetic material properties regarding the desired impedance value and frequency range, are realized. These probes (Figure 4-25) are designed in order to improve the measurement accuracy mainly in the frequency range from 150 kHz to 30MHz.

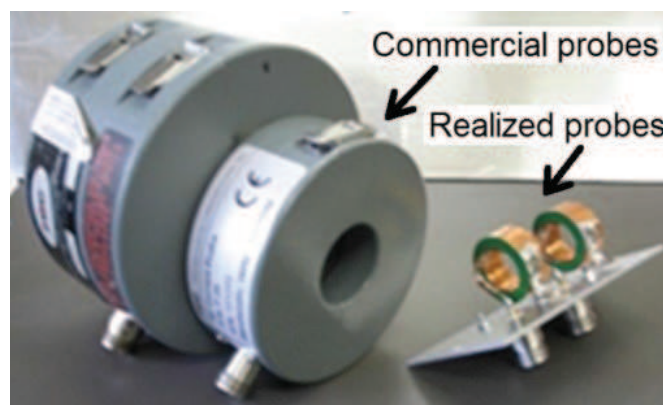


Figure 4-25 Commercial and proposed current probes

4.6.1 Transfer impedance of the current probe

In order to identify the transfer impedance of the commercial probes a three-port structure is built, as shown in Figure 4-26(a). In [107-109], this method was used to identify the transfer impedance of the current probe for RF applications up to GHz. In the frequency range from 150 kHz to 30 MHz a more simple expression is proposed in [107-109]. The probe and wire are modeled as a transformer. The transfer

impedance determines the relation between the current in the secondary (current through Z_{wire}) and the voltage in the primary (voltage in Port 1).

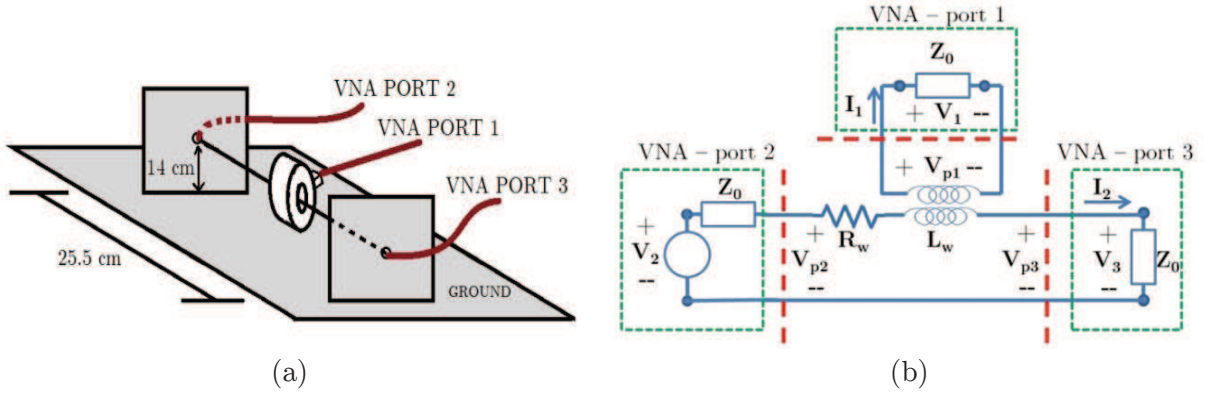


Figure 4-26 (a) Structure to measure the transfer impedance of the current probe (b) The equivalent circuit of the structure

The structure illustrated in Figure 4-26(a) has the characteristic impedance that is equal to 197Ω up to 100 MHz (measured with the Agilent impedance analyzer 4294A). Thus, it will be considered as a transmission line. Moreover, this method allows measuring the phase information that is not usually given by datasheets of commercial current probes.

The equivalent circuit of the structure, based on a transformer model, is shown in Figure 4-26(b). Port 1 of the VNA is connected to the current probe under test (CPUT). The signal in port 2 (10dBm) produces the current I_2 (103) that flows through Z_0 (50Ω) of port 3 generating the voltage V_{p3} (104). On the other side, the induced current I_1 (106) in the current probe generates the voltage V_{p1} (107) over the Z_0 of port 1.

$$I_2 = \frac{V_{p3}}{Z_0} \quad (103)$$

$$V_{p3} = S_{32}V_{p2}^+ \quad (104)$$

$$I_1 = \frac{V_{p1}}{Z_0} \quad (105)$$

$$V_{p1} = S_{12}V_{p2}^+ \quad (106)$$

$$K = \frac{V_1}{I_2} = Z_0 \left(\frac{S_{12}}{S_{32}} \right) = Z_0 \left(\frac{S_{13}}{S_{23}} \right) \quad (107)$$

The relation between the measured current (I_2) and the equivalent voltage of the current probe ($V_1=V_{p1}$) is given by the parameter K (107). This ratio is a complex function calculated from the magnitude and phase of the CPUT transfer impedance. The transfer parameters S_{12} and S_{32} describe, respectively, the voltage in the probe (port 1) and the current in the wire (port 3) produced by the source of signal (port 2). Also, the symmetrical characteristic of the S-parameters allows expression of the K parameter with S_{13} and S_{23} , as given by (107).

This method is used to characterize two commercial probes: the current measurement probe (CP : F-52A) and the current injection probe (CIP : F-120-3). Their obtained transfer impedances are compared with the datasheet information in the aim to validate this method. The results of the transfer impedances are shown in Figure 4-27 for both current probes. The magnitude shows a good agreement in both cases. In addition, the phase information reveals that the probes become capacitive above 40MHz for CP and above 2MHz for CIP.

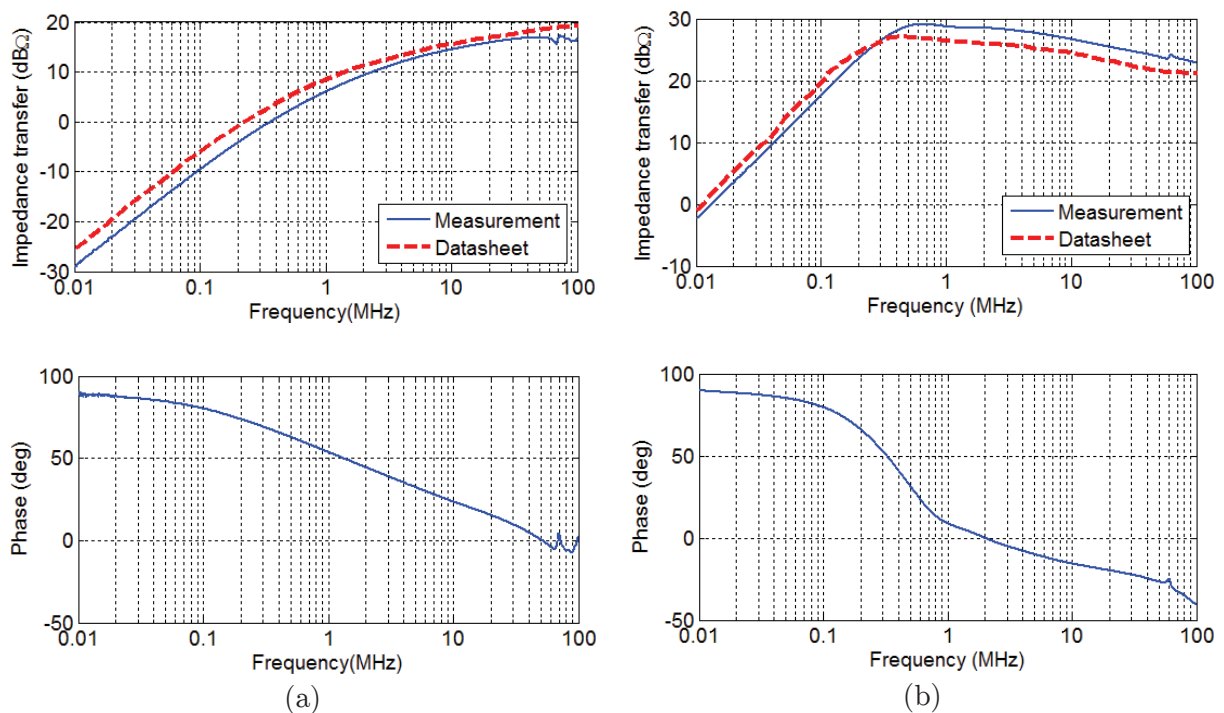


Figure 4-27 Transfer impedance of: (a) F-52A current probe and (b) F-120-3 current injection probe

4.6.2 New current probes

In the following, the design of the CP and CIP is considered on the basis of two key points: the size of the probe and the magnetic material properties of the core. In fact, a small size of the core means low wire impedance Z_{wire} and, the

adequate properties of the magnetic core in order to avoid saturation. In [39], the N30 ferrite ring core (from EPCOS®) has been adapted with an air-gap to reduce the impact of saturation. Nevertheless, the size of the core increases because the intrinsic relative permeability of the magnetic core has been significantly decreased due to the air-gap.

In power electronics, other magnetic materials are used to replace ferrite [54]. For example, nanocrystalline material, which becomes a good alternative in power devices such as inductors in EMI filters [29].

Therefore, in the present work, the nanocrystalline material is chosen for the magnetic core of the current probes because of its high value of the saturation flux and high intrinsic relative permeability. Thus, the nanocrystalline ring core 097-12-1-E2 from Aperam®, with magnetic flux saturation = 1.2T and $\mu_i \approx 50000$ at low frequency is selected. The dimensions of the core are chosen according to the constraint of the test bench (external diameter $D_E = 30\text{mm}$, internal diameter $D_I = 20\text{mm}$ and height $H_E = 12\text{mm}$).

As the datasheet of the nanocrystalline materials does not provide all the information about its complex permeability, measurements have been carried out following the procedure detailed in chapter 2. The complex permeability deduced from expression (108) is illustrated in Figure 4-28. This high permeability value at low frequencies increases the impedance of the current probe without requiring lot of turns. Thus, the single-turn coil ($N=1$) has been used.

$$Z_{probe} = j\omega \left(\frac{(\mu' - j\mu'') \mu_o}{2\pi} N^2 H_E \ln \left(\frac{D_E}{D_I} \right) \right) \quad (108)$$

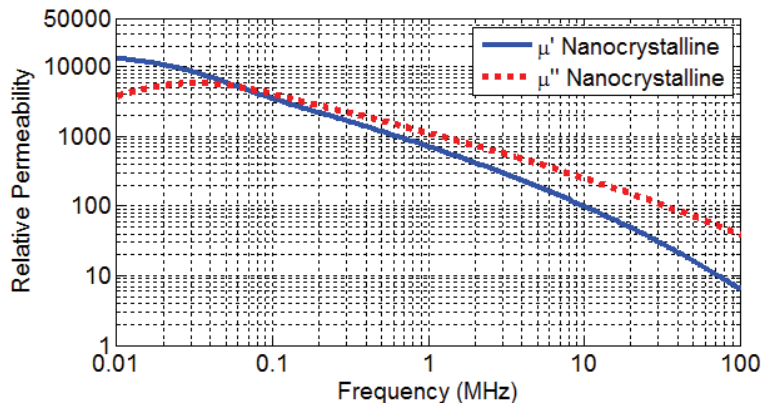


Figure 4-28 Magnetic permeability of the nanocrystalline material (097-12-1-E2 from Aperam®)

The new current probe (NCP) has been introduced in the characterization structure shown in Figure 4-26 to measure the transfer impedance. The measured results are presented in Figure 4-29. The NCP has high impedance transfer values at low frequency and also an inductive characteristic up to 80MHz, as illustrated in the phase information (Figure 4-29(b)). In addition, the size of the measurement probes was reduced by 98.8% for the CIP and 96.6% for the CP as shown in Figure 4-25. These NCPs are put together in the same ground plane to perform the current injection method to measure the CM impedance of the static converter as described in the following.

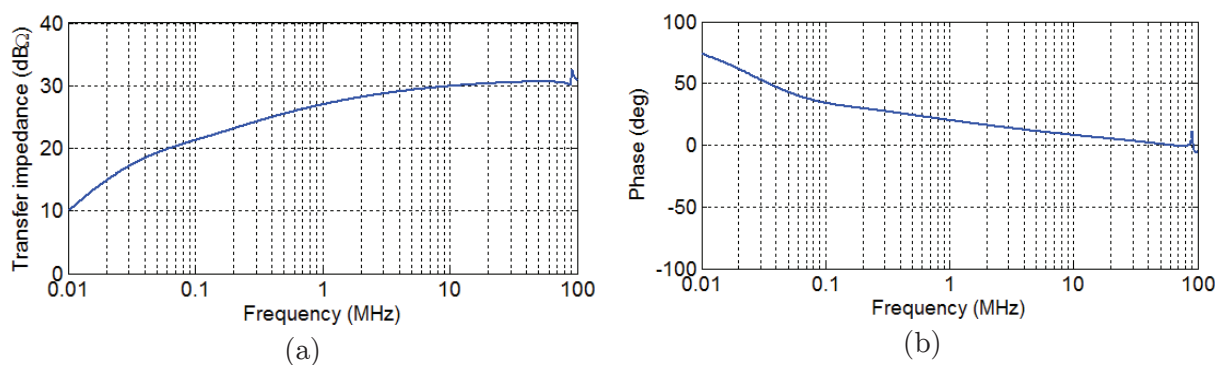


Figure 4-29 The new current probe transfer impedance with nanocrystalline material

In this section, a buck converter was chosen to be characterized. The switching frequency is 100 kHz, with a duty cycle of 25%. The input voltage is 200 V_{DC}, and the load is composed by a resistor (30Ω) and inductor (3mH).

The calibration equation is given by (98) - (101). Unlike the method proposed by [110] where the LISN impedance is subtracted from the final measurement, here, it is part of the calibration parameter equation Z_{setup} . Thus, two measures with the known impedances $Z_X = 0\Omega$ and $Z_X = 50\Omega$ for the calibration procedure are performed. Unfortunately, even if the characterization of the current probes treated in the previous section was as much as 100 MHz, the maximum valid frequency of the LISN impedance is 30MHz.

In order to present the advantages of proposed current probes, the common mode impedance of the SiC buck converter in off-state is considered. The measurements are realized with the commercial probes and the proposed probes. The impedance and phase curves are compared with those obtained from the impedance analyzer (4294A).

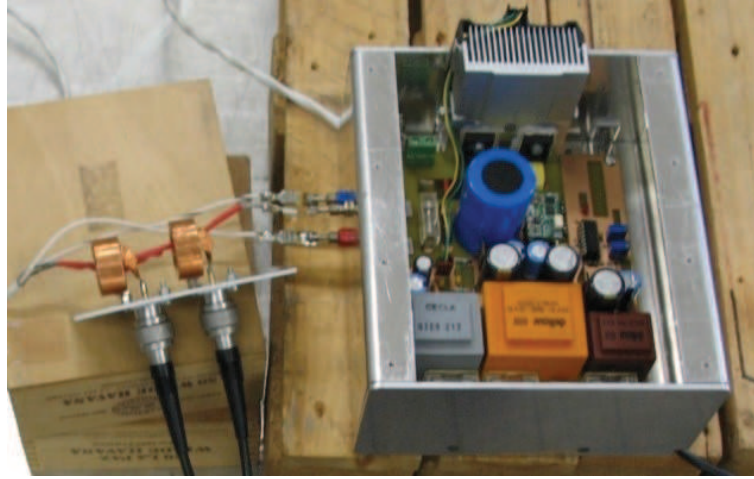


Figure 4-30 Measurement of the SiC buck converter impedance with new current probes

The measured CM impedance with the commercial probes (Figure 4-31(a)) is affected by the measurement noise in low frequency, while the high frequency is attenuated. However, the CM impedance measured with the new probes shown in Figure 4-31(b) presents a better accuracy at low and high frequency. Globally, there is better agreement between the impedance analyzer and the CIM results in the considered frequency bandwidth with the new current probes.

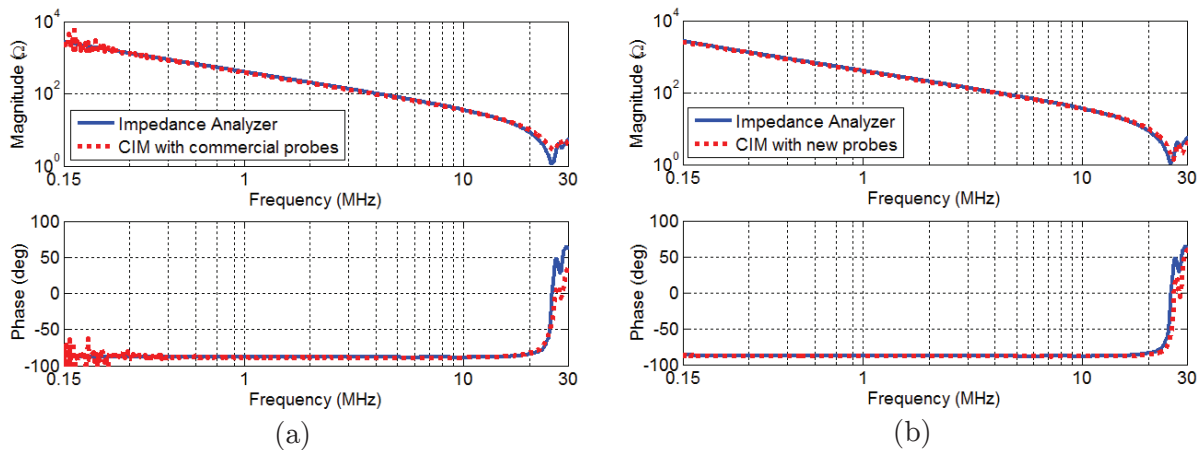


Figure 4-31 Common mode impedance of buck converter in off-state measured with (a) commercial current probes and (b) with new current probes

4.6.3 Measurement of the common mode source impedance

The common mode impedance measurement is carried on a SiC buck converter, illustrated in Figure 4-30. Six configurations are proposed to measure the CM buck converter impedance as shown in Figure 4-32. In all cases, the dashed line named “calibration point” represents the initial point from where the impedance is measured.

Configuration (a) and (b)

For the configuration (a), the converter phases (L_1 and L_2) are short-circuited and the impedance between them and the ground line G is measured. The measurements carried out with the impedance analyzer 4294A in configuration (a) and with the NCP in configuration (b) are shown in Figure 4-33. The results show a good agreement. The measured impedance corresponds to a capacitance (up to 20 MHz) with a value equal to 407pF.

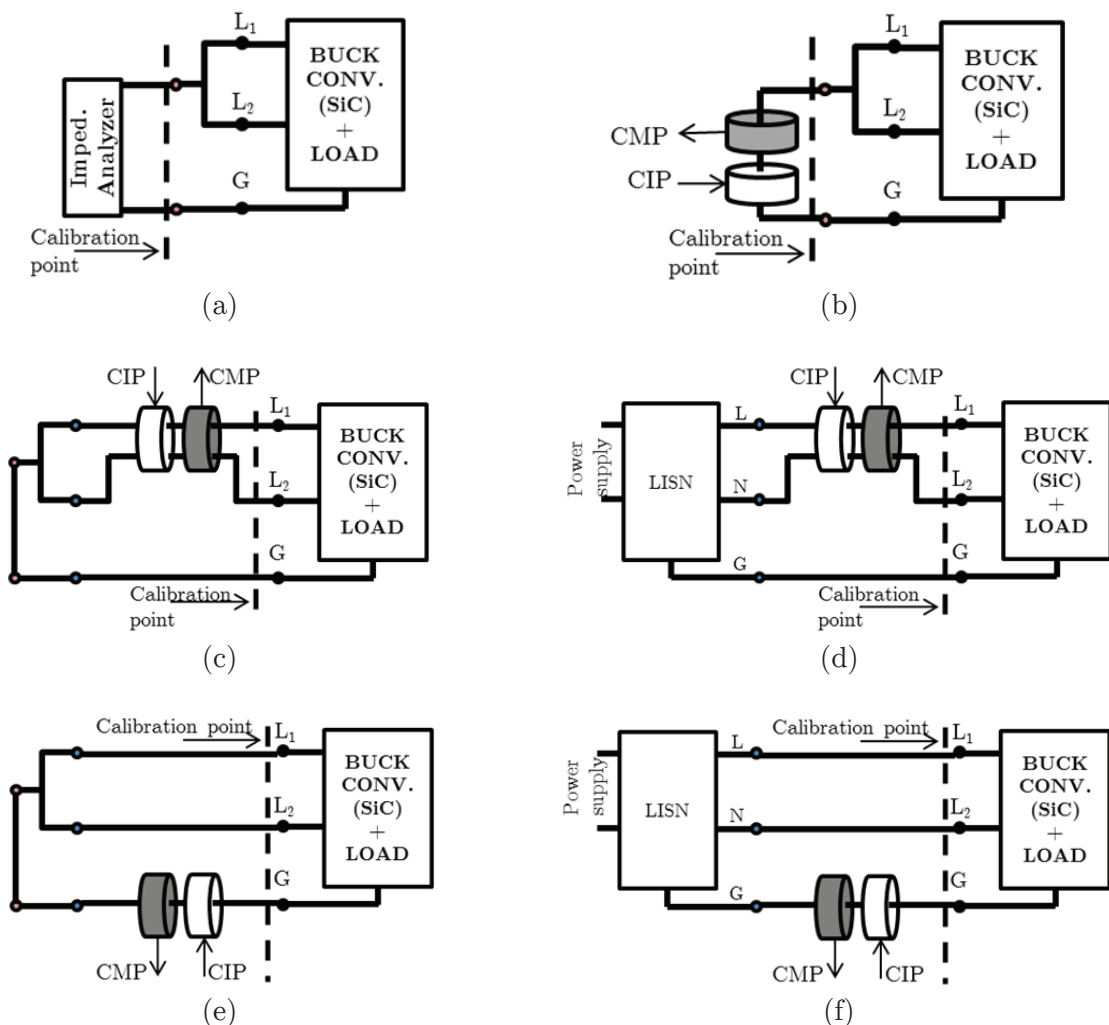


Figure 4-32 Different test configurations to measure the common mode impedance of a SiC buck converter + load

Configuration (c) and (d)

The configuration (c) uses two wires in parallel to inject the current. Both wires are similar, with the same wire length (40cm) and cross section area (2mm²). They are short-circuited before the two probes as shown in Figure 4-32(c). The

calibration procedure was performed at the other end of the wire. Due to short circuit in the wires, the converter is in off-state.

In the configuration (d) the LISN is added. As mentioned before, the LISN impedance is part of the calibration process and included in the parameter Z_{setup} . The measurement results for the buck converter in off-state and on-state are depicted in Figure 4-34.

Both measurements reflect the capacitive behavior (407 pF) in a frequency band from 150 kHz to 18MHz. The measurement noise that appears in the configuration (d) is more evident below 1MHz due to the presence of the switching frequency harmonics of the power converter. In fact, the amplitude of these harmonics is greater than the magnitude of the injected current. Note that, even if the maximum power (10dBm) of the VNA E5071C was applied in the measurement configurations, the power in port 1 (where CIP is connected) can be amplified with additional equipment in order to increase the injected current value, but this solution is out of the scope of this work.

Moreover, in the configuration (d), above 18MHz two effects can be described. First, the resonance frequency has shifted down in comparison with the configuration (c). In fact, the variation of high frequency response, when the converter is in operating condition, is due to the interactions between the converter impedance and the setup impedance (Z_{setup}). Secondly, the setup impedance increases with the frequency whereas the converter impedance Z_{SCM} decreases. It means, that it is more difficult to identify the low values impedance in high frequency, as explained in [111]. Even though, the length of the wire was kept short enough to reduce the impedance Z_{setup} , the LISN impedance still remains large.

Configuration (e) and (f)

These two configurations were evaluated based on the hypothesis that the current injected in the two lines (L_1 and L_2) is the same current over the ground wire. The configuration (e) in off-state is close to configurations (b) and (c). However, the difference appears when the LISN is connected in the setup of the configuration (f). As explained before, the increase over the impedance setup affects the accuracy of the measurement results in high frequency. As shown in Figure 4-35, the configuration (f) with the converter in the off-state and on-state follows the capacitance impedance value up to 18 MHz. Above this frequency the measurement differs from configuration (d).

The two NCPs reduce the size of the measurement setup and increase the accuracy of the results compared to the commercial current probes. All configurations are able to measure the CM impedance of the buck converter using the two proposed probes. At this step, the impedance of the converter can be measured in operating condition with a good accuracy. The impedances of the converter (Z_{SCM} and Z_{SDM}) have been measured with the CIM and they are used in the design of the EMI filter in the following section.

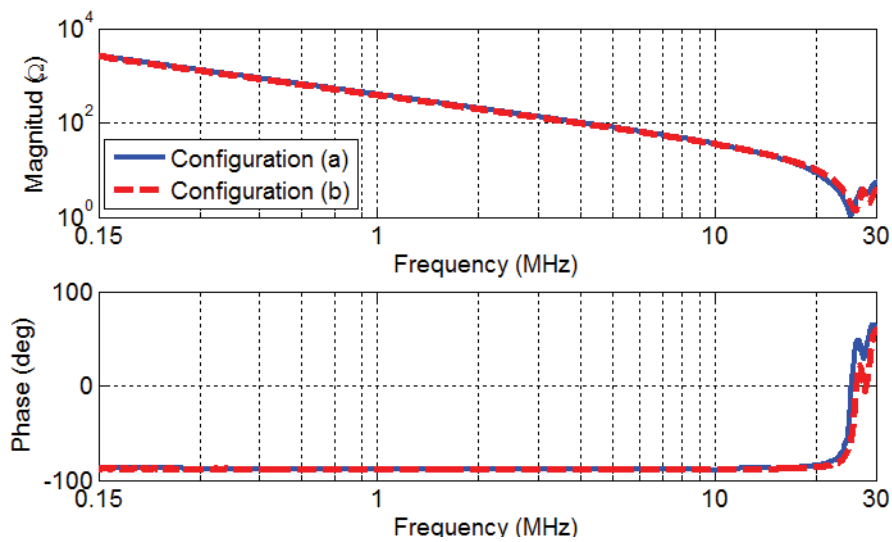


Figure 4-33 CM impedance with configurations (a) and (b)

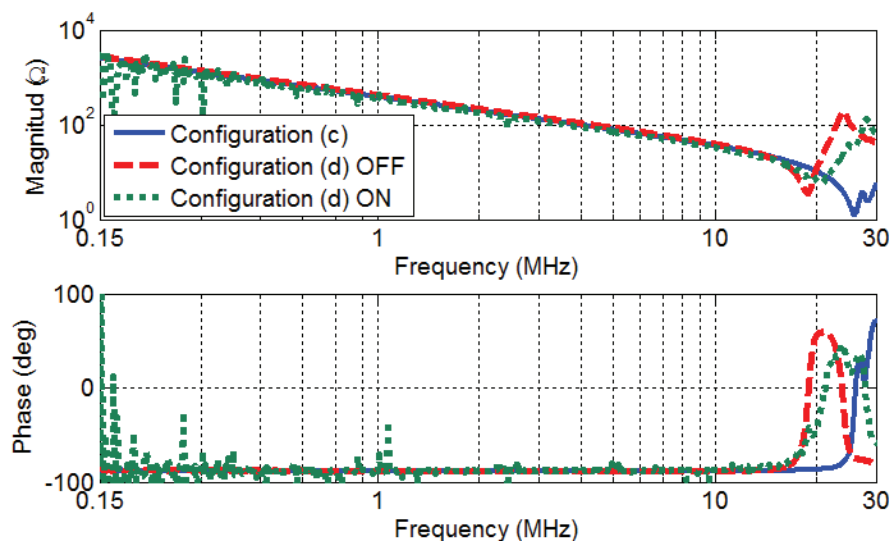


Figure 4-34 CM impedance with configurations (c) and (d) with converter in off-state and on-state

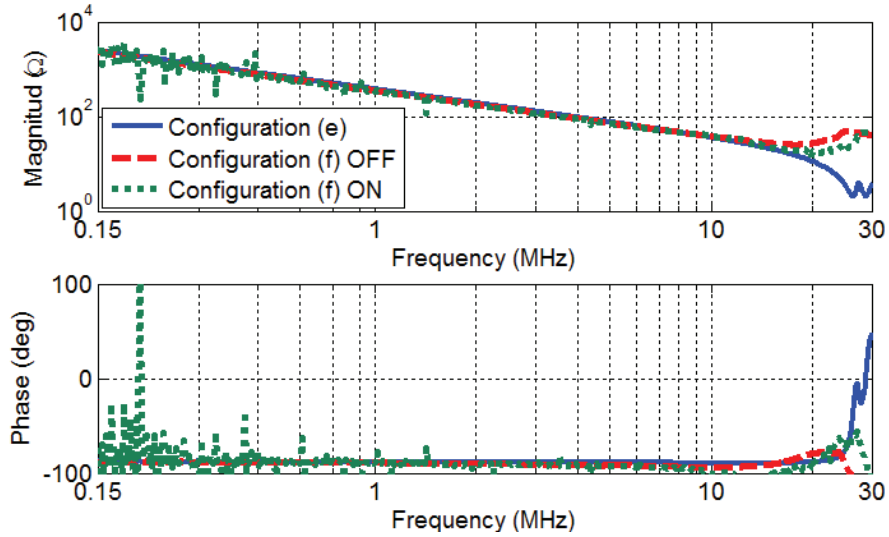


Figure 4-35 CM impedance with configurations (e) and (f) in off and on-operating conditions

4.7 EMI filter design

In this work, the EMI filter is used to reduce the conducted emissions induced by the power converters. The static converter (EMI source) and LISN (Load) are presented in a simplified circuit (Thévenin equivalent circuit) in the Figure 4-36(a). The structure of the EMI filter could be represented with Π or T network. For example, the single stage EMI filter with a T network is shown in Figure 4-36(b). The insertion loss of the EMI filter (109) associated with this schema is the ratio of the voltage *without filter* (110) over the voltage *with filter* (111) under the load impedance (Z_{out}). Therefore, the derived schemas like LC and CL can be easily calculated replacing the missing impedances by short-circuits.

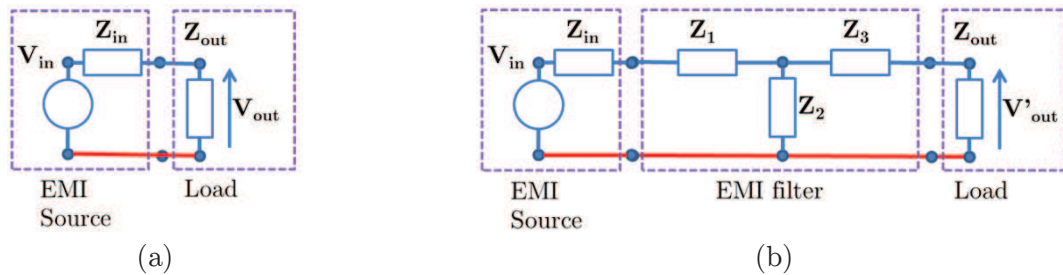


Figure 4-36 (a) Thévenin equivalent circuit of the converter (b) T-network of the EMI filter

$$IL = -20 \log \left| \frac{V_{out}}{V'_{out}} \right| \quad (109)$$

$$V_{out} = V_{in} \frac{Z_{out}}{Z_{out} + Z_{in}} \quad (110)$$

$$V'_{out} = \frac{V_{in}Z_{out}Z_2}{Z_2(Z_{out} + Z_3) + Z_2(Z_1 + Z_{in}) + (Z_{out} + Z_3)(Z_1 + Z_{in})} \quad (111)$$

The diagram shown in Figure 4-37 summarizes the different steps to design an EMI filter. First, the conducted emissions are measured to define the minimum insertion loss required for the filter. The DM and CM conducted emissions of the buck converter measured with the current probe are given in Figure 4-7. Thus, the minimum attenuations required for the DM and CM filters are shown in Figure 4-38. These attenuations are obtained by making the difference between the limit given by EMC standard (CISPR-11 Class B) and the CM and DM measured conducted emissions. The DM emissions are basically at low frequencies and the CM emissions up to 30 MHz

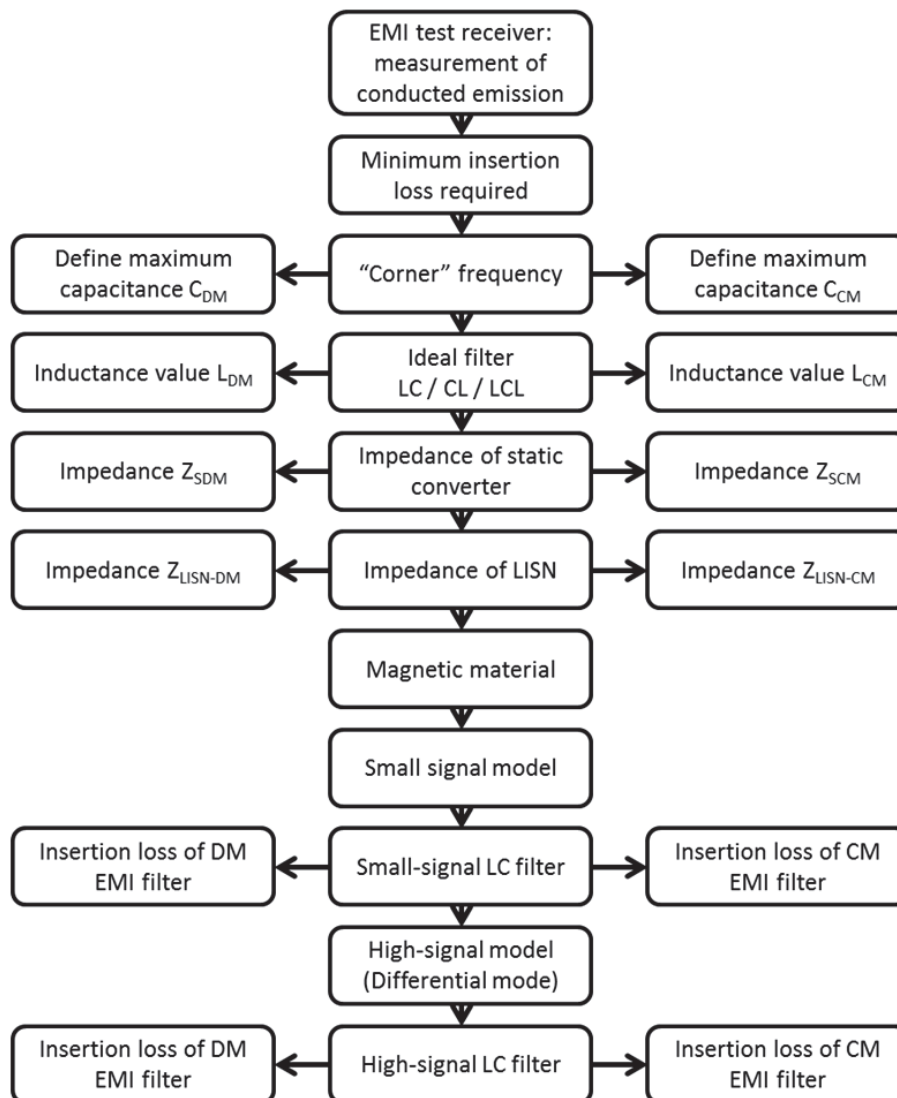


Figure 4-37 Steps in EMI filter design

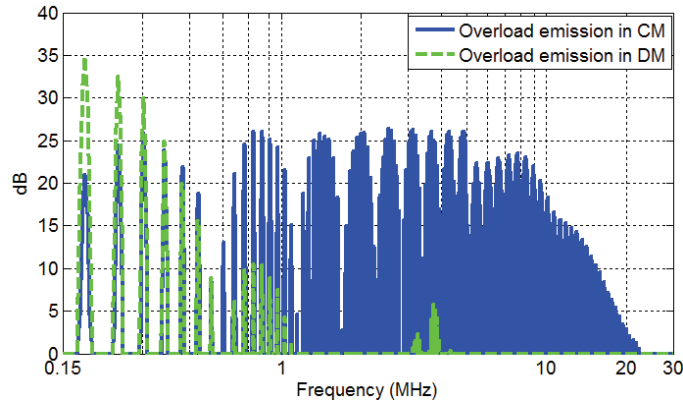


Figure 4-38 Required level of conducted emission attenuation in DM and CM

Second, the “corner” frequency is the intersection between the straight line of 40dB/dec and the horizontal axis. The principle is that all the required emissions levels stay under this straight line [36]. The slope of these lines will depend on the number of stages of the filter. Each of the stages represents a straight line of 40dB/dec. Based on this corner frequency, the value of inductors (L_{DM} and L_{CM}) could be estimated with the expression (112). Usually the capacitors (C_{DM} and C_{CM}) are the first elements to be determined. Their values are limited by the size and security issues. Two capacitors are employed in the present application: $C_{CM} = 4.7\text{nF}$ and $C_{DM} = 2.2\mu\text{F}$. These values can be changed in order to optimize the final version of the filter in order to fulfill a specific objective (size, weight, technology). However, this procedure remains as a future extension of the work.

$$f_{corner} = \frac{1}{2\pi\sqrt{CL}} \quad (112)$$

The CM and DM filters are calculated independently. Three topologies (LC, CL, LCL) are applied in order to choose the best. In the general expression of the insertion loss (111), the impedance Z_1 (Figure 4-36(b)) is short-circuited for a LC filter and Z_3 for a CL filter.

The aim of the present work is to avoid the prototyping of the filter and to find the most appropriate filter for each application. Here, three kinds of filters are simulated in three different scenarios:

1. Ideal filters,
2. With only the model of the components
3. With the model of components and the measured impedance of the converter and LISN based on the current injection method.

Finally, the adequate filter will be designed based upon the insertion loss information obtained.

The measured impedances of the buck converter with CIM are depicted in Figure 4-39. The impedances Z_{SDM} and Z_{SCM} are modeled by lumped circuits which are obtained with fitting procedures. In the same way, the impedance of the LISN is modeled and illustrated in Figure 4-40.

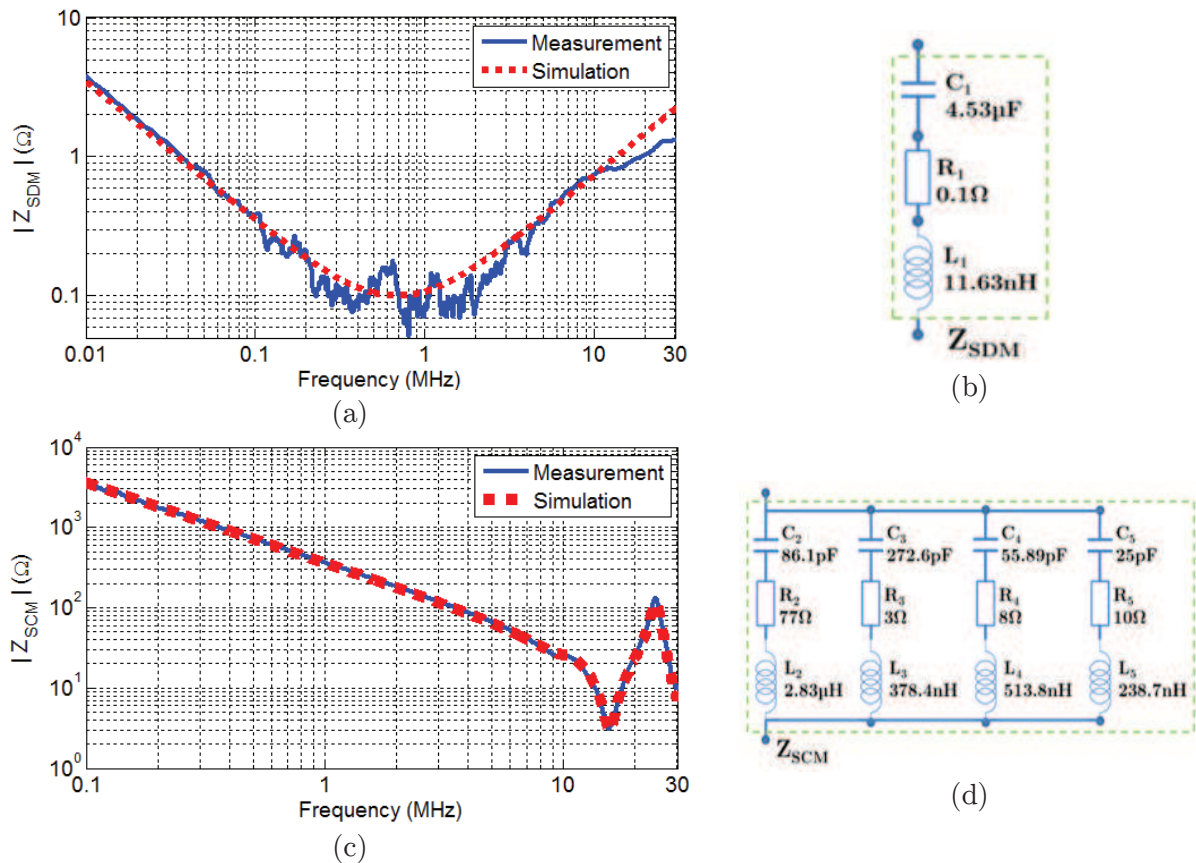


Figure 4-39 Buck converter impedances (a) Z_{SDM} impedance (b) Z_{SDM} equivalent circuit (c) Z_{SCM} impedance and (d) Z_{SCM} equivalent circuit

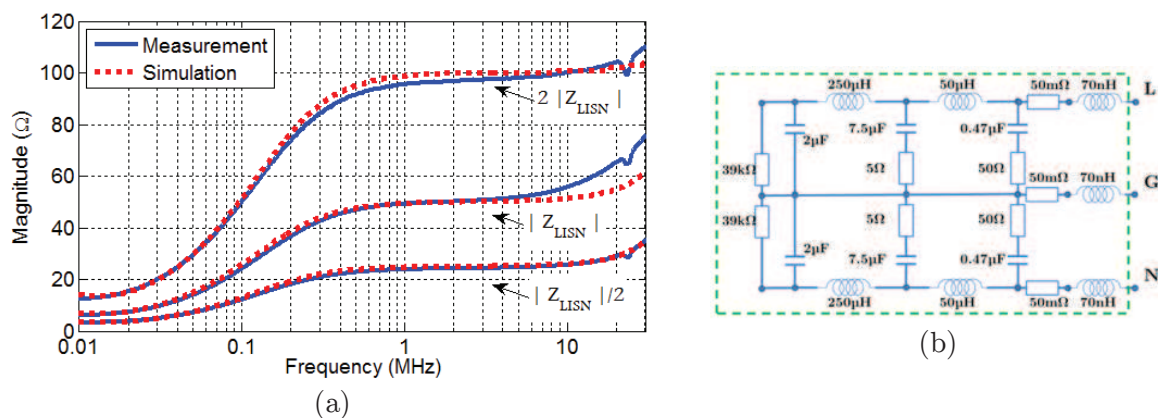


Figure 4-40 LISN impedance (a) measured and simulation results (b) equivalent circuit

4.7.1 Common mode filter

The simplified equivalent circuits of the CM filter, based on the T network, are illustrated in Figure 4-41. The simulation of the insertion loss was developed in Matlab®. The noise level has been modified to take into account a tolerance of 6dB.

The conditions of the simulation are summarized in Table 4-2 and graphically illustrated in Figure 4-42. As previously stated, three topologies are studied for three different scenarios.

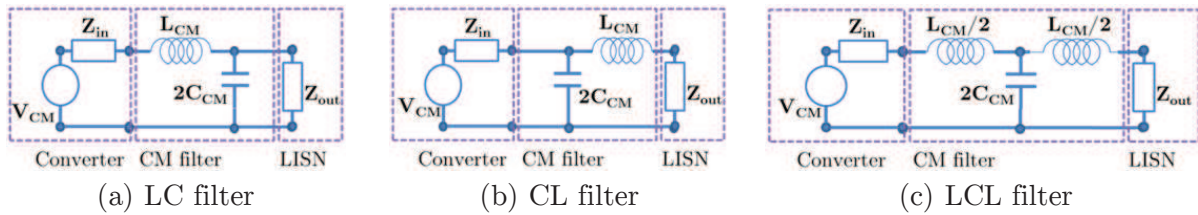
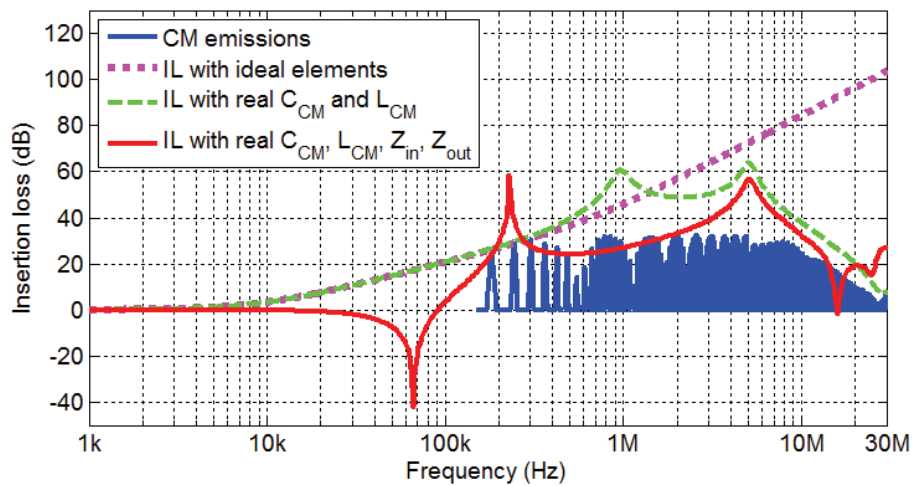


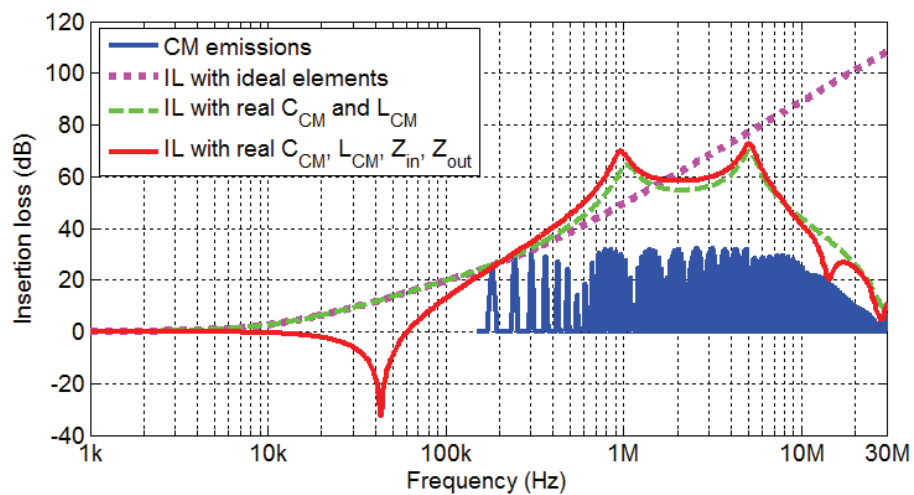
Figure 4-41 Common mode filter structures

Table 4-2 Characteristics of the three CM filters

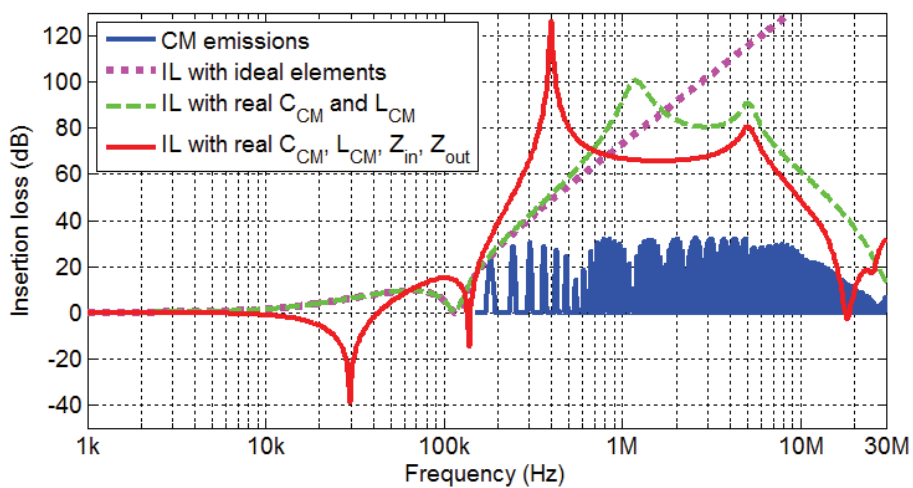
		Z_{IN}	Z_{OUT}	$Z_{C_{CM}}$	$Z_{L_{CM}}$	f_{corner}
LC filter	Ideal elements	50Ω	50Ω	$C_{CM} = 4.7\text{nF}$	$L_{CM} = 1.28\text{mH}$	64.9 kHz
	Real C_{CM} and L_{CM}	50Ω	50Ω	$C_{CM} = 4.87\text{nF}$; ESR=886.7mΩ; ESL=200.6nH;	$L_{CM} = 1.28\text{mH}$ N = 23 (mat. N87) 25.3mm/14.8mm/10mm	63.7 kHz
	Real C_{CM} , L_{CM} , Z_{IN} and Z_{OUT}	Z_{SCM}	$Z_{LISN}/2$	$C_{CM} = 4.87\text{nF}$; ESR=886.7mΩ; ESL=200.6nH;	$L_{CM} = 12\text{mH}$ N = 73 (mat. N87) 25.3mm/14.8mm/10mm	20.8 kHz
CL filter	Ideal elements	50Ω	50Ω	$C_{CM} = 4.7\text{nF}$	$L_{CM} = 1.1\text{mH}$	69.7 kHz
	Real C_{CM} and L_{CM}	50Ω	50Ω	$C_{CM} = 4.87\text{nF}$; ESR=886.7mΩ; ESL=200.6nH;	$L_{CM} = 1.10\text{mH}$ N = 22 (mat. N87) 25.3mm/14.8mm/10mm	68.8 kHz
	Real C_{CM} , L_{CM} , Z_{IN} and Z_{OUT}	Z_{SCM}	$Z_{LISN}/2$	$C_{CM} = 4.87\text{nF}$; ESR=886.7mΩ; ESL=200.6nH;	$L_{CM} = 1.32\text{mH}$ N = 24 (mat. N87) 25.3mm/14.8mm/10mm	62.8 kHz
LCL filter	Ideal elements	50Ω	50Ω	$C_{CM} = 4.7\text{nF}$	$L_{CM} = 0.76\text{mH}$	84.2 kHz
	Real C_{CM} and L_{CM}	50Ω	50Ω	$C_{CM} = 4.87\text{nF}$; ESR=886.7mΩ; ESL=200.6nH;	$L_{CM} = 0.76\text{mH}$ N = 18 (mat. N87) 25.3mm/14.8mm/10mm	82.7 kHz
	Real C_{CM} , L_{CM} , Z_{IN} and Z_{OUT}	Z_{SCM}	$Z_{LISN}/2$	$C_{CM} = 4.87\text{nF}$; ESR=886.7mΩ; ESL=200.6nH;	$L_{CM} = 5.58\text{mH}$ N = 50 (mat. N87) 25.3mm/14.8mm/10mm	30.5 kHz



(a) LC filter



(b) CL filter



(c) LCL filter

Figure 4-42 Simulation results of the insertion loss of the three CM filter topologies (a) LC filter, (b) CL filter and (c) LCL filter

Different analysis can be addressed from the simulation results as shown in Figure 4-42.

- First, the insertion losses are obtained from the simulations carried out with the ideal elements of the LC, CL and LCL filters.
- Second, the insertion losses are obtained from the simulations carried out with the high frequency models of the L and C components (named real components).
- Third, the insertion losses are obtained from the simulations carried out taking into account the LISN's impedance, static converter impedance Z_{SCM} and the models of HF models of the filter components.

The simulation results show that the CL structure is enough to obtain the necessary insertion loss of the CM filter. The insertion loss of the filter shows that it allows reduction of the conducted emissions as shown in Figure 4-42(b). These simulations allowed finding a new value of the inductance (L_{CM}). The inductance value of CL structure is lower in comparison with the other ones. However, the obtained filter model includes the high frequency behavior of the passive components and the input/output impedances. In addition, the magnetic material was changed in order to compare its performances with the ferrite N87, previously used. The CM inductance $L_{CM} = 1.32\text{mH}$ (with $N=10$ turns) was simulated with the nanocrystalline core (N6E3 -25.5mm/16mm/10.6mm). Thus, the number of turns was reduced from 24 to 10 and in consequence the insertion loss was also modified, as shown in Figure 4-43. The ferrite material is kept in our case to design the CM inductor because it has a larger leakage inductance that will be used in the design of the DM filter that will be detailed in the next section.

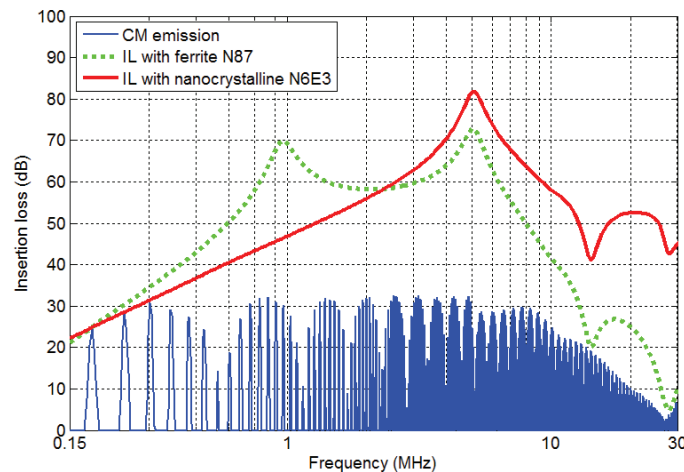


Figure 4-43 Insertion losses of CM filter with ferrite N87 and N6E3 nanocrystalline material

4.7.2 Differential mode filter

The DM filter is composed from capacitor C_{DM} , usually with a large value, and the inductance L_{DM} . Often, this inductance is the leakage inductance of the CM inductor (choke inductor). As in the previous case, three filter topologies are evaluated with three different scenarios (Figure 4-44). In Table 4-3 are listed the components characteristics for each filter. The simulations' results are illustrated in Figure 4-45. Notice that the inductance value (L_{DM}) is maintained as a constant because it is linked to the leakage inductance of the common mode inductor.

The simulation with the LISN's impedance, converter impedance Z_{SDM} and the model of the passive components shows that the topology LC is enough for the DM filter.

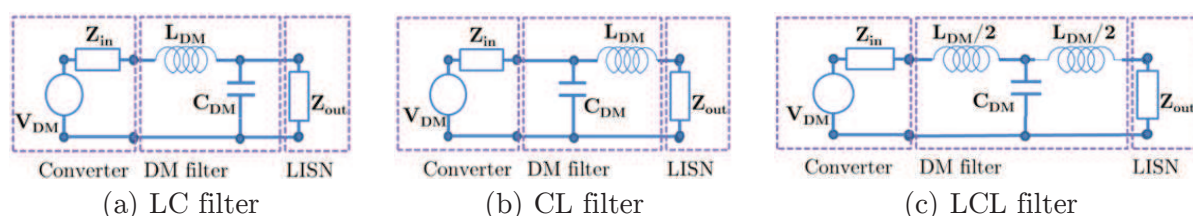
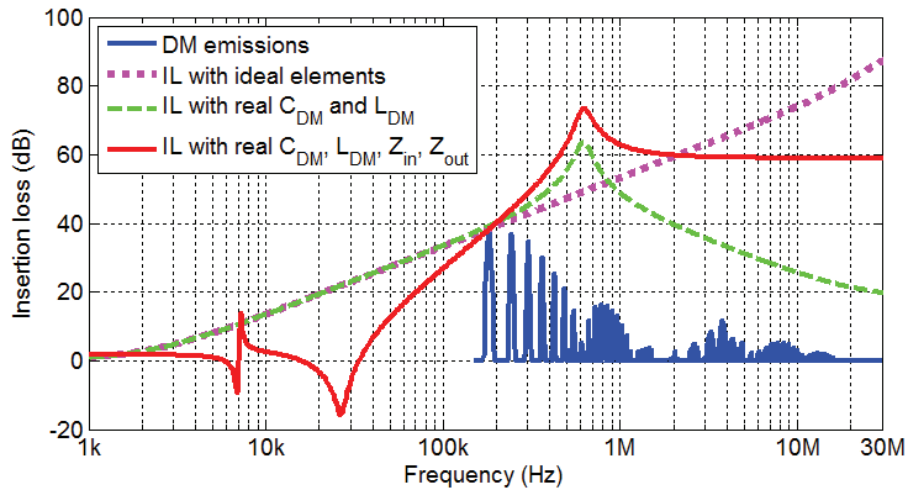


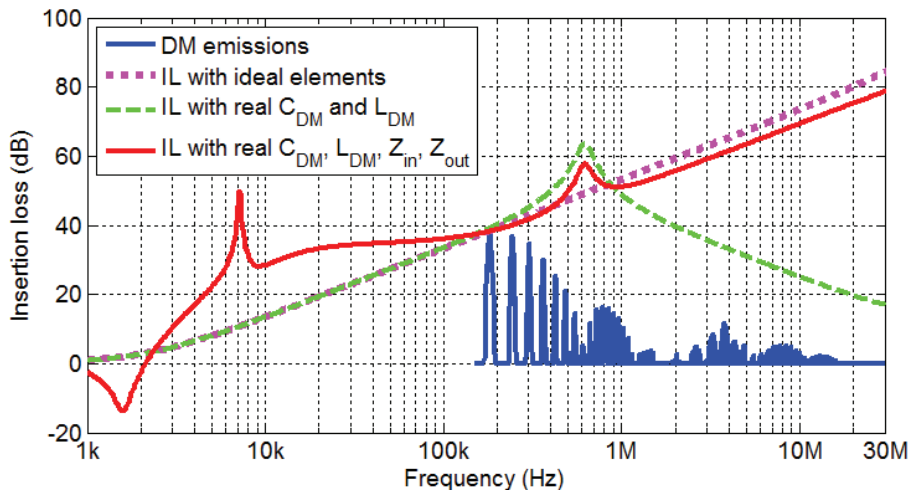
Figure 4-44 Differential model filter structures

Table 4-3 Characteristics of the three calculated DM filters

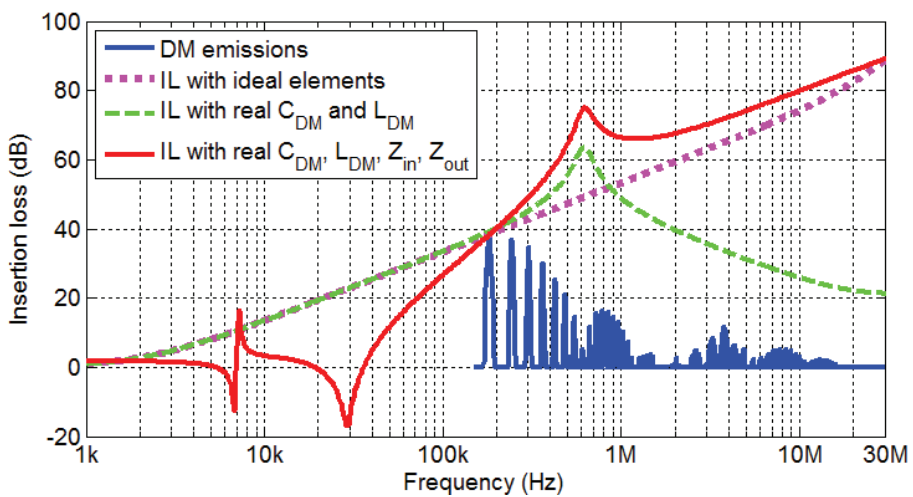
		Z_{IN}	Z_{OUT}	$Z_{C_{DM}}$	$Z_{L_{DM}}$	f_{corner}
LC filter	Ideal elements	50Ω	50Ω	$C_{DM} = 2.2\mu F$	$L_{DM} = 0.35\mu H$	181.3 kHz
	Real C_{DM} and L_{DM}	50Ω	50Ω	$C_{DM} = 2.2\mu F$; ESR = 22m Ω ; ESL = 30nH;	$L_{DM} = 0.32\mu H$	181.7 kHz
	Real C_{DM} , L_{DM} , Z_{IN} and Z_{OUT}	Z_{SDM}	$2*Z_{LISN}$	$C_{DM} = 2.2\mu F$; ESR = 22m Ω ; ESL = 30nH;	$L_{DM} = 26.5\mu H$	20.8 kHz
CL filter	Ideal elements	50Ω	50Ω	$C_{DM} = 2.2\mu F$	$L_{DM} = 0.35\mu H$	181.3 kHz
	Real C_{DM} and L_{DM}	50Ω	50Ω	$C_{DM} = 2.2\mu F$; ESR = 22m Ω ; ESL = 30nH;	$L_{DM} = 0.32\mu H$	181.7 kHz
	Real C_{DM} , L_{DM} , Z_{IN} and Z_{OUT}	Z_{SDM}	$2*Z_{LISN}$	$C_{DM} = 2.2\mu F$; ESR = 22m Ω ; ESL = 30nH;	$L_{DM} = 3.4mH$	1.8 kHz
LCL filter	Ideal elements	50Ω	50Ω	$C_{DM} = 2.2\mu F$	$L_{DM} = 0.7\mu H$	128.3 kHz
	Real C_{DM} and L_{DM}	50Ω	50Ω	$C_{DM} = 2.2\mu F$; ESR = 22m Ω ; ESL = 30nH;	$L_{DM} = 0.64\mu H$	134.1 kHz
	Real C_{DM} , L_{DM} , Z_{IN} and Z_{OUT}	Z_{SDM}	$2*Z_{LISN}$	$C_{DM} = 2.2\mu F$; ESR = 22m Ω ; ESL = 30nH;	$L_{DM} = 43.2\mu H$	163.2 kHz



(a) LC filter



(b) CL filter



(c) LCL filter

Figure 4-45 Insertion loss of three DM EMI filter topologies

Finally, the simulation of three different structures for both filters (CM and DM) has shown that the CL filter is enough for the CM filter, and the LC filter is for the DM filter. In the next section, the first prototype of the obtained EMI filter is built. Then, the EMI tests are performed in order to meet the CISPR-11 Class B (QP) standard. This study shows that the design of the EMI filter can be achieved by HF simulations of the energy conversion system.

4.7.3 Realization of the EMI Filter

The equivalent circuit for EMI filter including the DM and CM filters is shown in Figure 4-46. The impedance of capacitors (C_{CM} and C_{DM}) can be extracted with direct measurements. The input and output impedances are the static converter impedances (Z_{SDM} and Z_{SCM}) and the LISN impedance (Z_{LISN}) respectively.

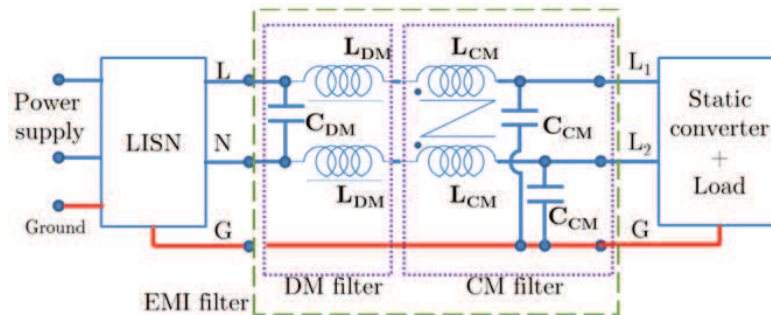


Figure 4-46 EMI filter schematic connected to the LISN and to the static converter + load

The EMI filter components are mounted in a double-face PCB, as illustrated in Figure 4-47. The distribution of the components was arbitrary following the symmetrical distribution without constraints about the space. The measurement of the conducted emission is carried out with the EMI test receiver (R&S ESPI3). The EMC standard CISPR-11 class B (equivalent to the EN55011 class B) is met by the converter as shown in Figure 4-48.

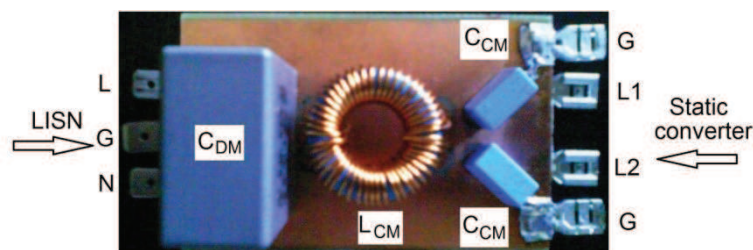


Figure 4-47 EMI filter prototype with ferrite N87

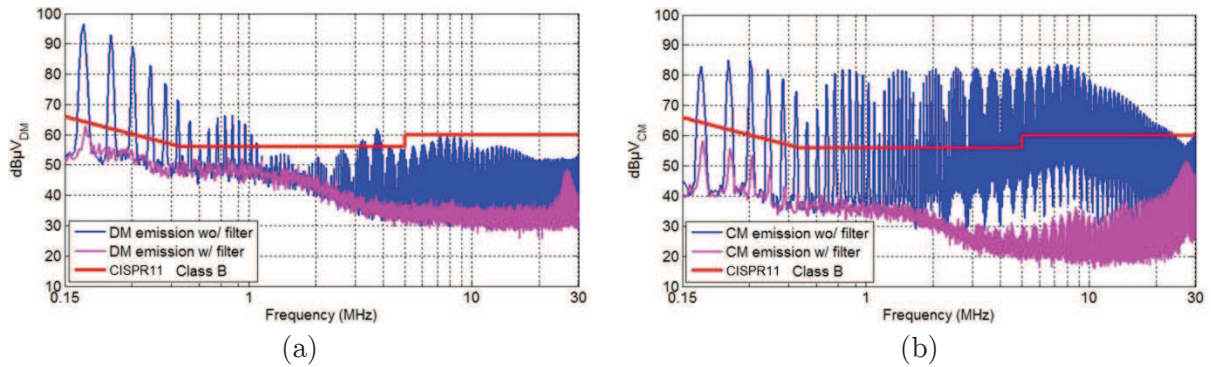


Figure 4-48 Reduction of conducted emissions using the designed EMI filter in (a) DM emission (b) CM emission

The EMI filter has been designed using the elements previously provided such as the magnetic material model and input/output impedances. The magnetic material in the EMI filter is more preponderant in the lower frequencies below the capacitors resonance. In fact, if higher levels of emission are measured in frequencies above 1MHz the filter risks failing to meet the standard even if the magnetic material is changed. Above this frequency, the parasitic effect of the other components will define the effectiveness of the filter.

Until now, the design of the filter was focused on the constitutive elements, such as the inductors and magnetic materials. It is done when the EMI filter is a custom-made design, previous to prototyping. In the case of pre-fabricated EMI filters, the evaluation of its insertion loss was also part of our research work. Indeed, the typical IL identification is performed by apparatus with 50Ω as characteristic impedance. It means that the insertion loss of the filter is measured in the case of ideal input/output impedances (50Ω).

In the next section, a measurement method of the IL, based on scattering parameters, was evaluated in the case of impedances different to the classic 50Ω .

4.8 Insertion loss with S-parameters

The performance of the EMI filter is characterized by the insertion loss. This IL depends on the main network and the power converter impedances. In this work, an experimental method is proposed to determine the insertion loss for arbitrary (input/output) impedances. The proposed method is based on the utilization of the black-box model of the filter, obtained from S-parameter measurements, with $50\Omega/50\Omega$ using the scattering parameters. The black-box model is then used to characterize the EMI filter with more complex impedances.

4.8.1 Introduction

Another aspect of the insertion loss characterization is the kind of input and output impedances connected to the filter which impact the performance of the filter due to the mismatch impedance problem [112]. In most cases, the input and output impedances are replaced by 50Ω because of the measurement instrument's impedances, such as spectrum analyzer (SA) or vector network analyzer (VNA). Also, the “worst case” procedure can be used with transformer baluns (balanced-unbalanced) to evaluate the insertion loss when the output (input) impedance is 0.1Ω or 100Ω [8]. This procedure is justified when information of the final application of the filter is unknown.

In actual test setups of the filter performance, the output impedance is fixed by the LISN, as shown in Figure 4-49(a). However, the input impedance has to be replaced by the static converter impedance which is measured by the current injection method. In those conditions, an experimental method is proposed to measure the insertion loss of the filter. Thus, the black box model can replace the EMI filter for common mode and differential mode into a quadripole as shown in Figure 4-49(b). In both cases, the CM and DM impedances of the power converter must be measured.

First, the characterization of the filter is carried out in $50\Omega/50\Omega$ conditions using a VNA. Thus, the black box model is obtained based on the scattering parameters. This model is then validated using other measurement instruments (i.e. spectrum analyzer).

The black box model of the filter is adapted to take into account different values of the input/output impedances emulating its real operating conditions. This method allows us to estimate directly by simulation the insertion loss of the filter. The converter's impedance is measured using the current injection probes detailed previously. The equivalent impedance obtained is then introduced in the specific expressions to estimate the insertion loss of the filter. Usually, the insertion loss can be obtained by two models: the electrical equivalent circuit and the black-box models. The electrical circuit model that has been investigated in previous chapters (small-signal and high-signal models) is used to design and to optimize the performance of the filter before its realization. In contrast, the black box model is used to study the influence of the Z_{in} and Z_{out} in the insertion loss based on measurements of a realized filter.

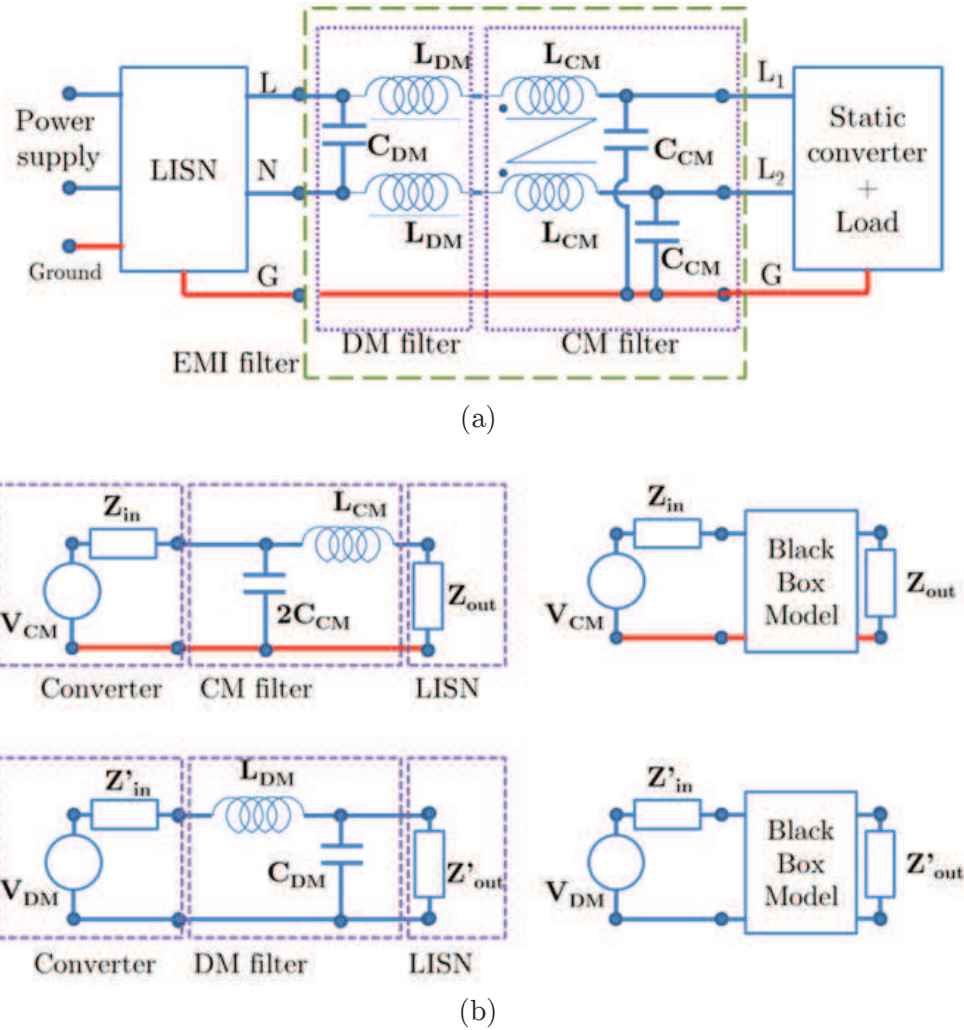


Figure 4-49 (a) CM and DM filters (a) equivalent circuits (b) black box models

4.8.2 Insertion loss with arbitrary input and output impedances

For the black box model, the EMI filter is considered as a component with two ports (quadripole). The filter is described by equations that represent its global behavior. Based on scattering parameters measured by VNA, the equivalent two-port quadripole mode is obtained, in the first step, under $50\Omega/50\Omega$. Then, the equivalent model (in Z parameters) can be extracted [113]. For that, a transfer function conversion between S-matrix to ABCD-matrix is given by (113) - (116). The ABCD-matrix representation is widely used in the concatenation of microwave models of devices. This ABCD-matrix represents the relation between currents and voltages of the filter. The characteristic impedance (Z_0) is 50Ω due to the instrument's impedance. Then, the insertion loss is expressed by (117).

This expression is validated with experimental results of the LC filter composed of an inductor of 0.8mH and a capacitor of 1nF. Insertion loss obtained with the black-box model and that measured with the spectrum analyzer (under 50Ω/50Ω) are illustrated in Figure 4-50. Now, for extra impedance (Z_q) connected to the input or output of the filter, the expression (117) can be modified.

$$A = \frac{(1 + S_{11})(1 - S_{22}) + S_{12}S_{21}}{2S_{21}} \quad (113)$$

$$B = Z_o \frac{(1 + S_{11})(1 + S_{22}) - S_{12}S_{21}}{2S_{21}} \quad (114)$$

$$C = \frac{1}{Z_o} \frac{(1 - S_{11})(1 - S_{22}) - S_{12}S_{21}}{2S_{21}} \quad (115)$$

$$D = \frac{(1 - S_{11})(1 + S_{22}) + S_{12}S_{21}}{2S_{21}} \quad (116)$$

$$IL(f) = -20 \log \left| \frac{AZ_{out} + B + Z_{in}D + Z_{out}Z_{in}C}{Z_{out} + Z_{in}} \right| \quad (117)$$

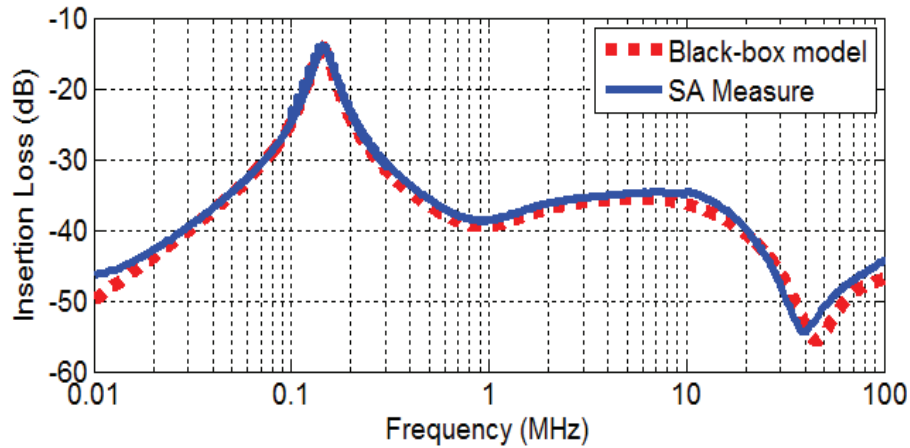


Figure 4-50 Insertion loss of the black-box and spectrum analyzer (under 50Ω/50Ω)

Four schemes are investigated depending on the extra impedance connection Z_q , as shown in Figure 4-51. The interest of these configurations are their close similitude with the real input and output impedances when the filter is linked to the static converter and power supply. Thus, the insertion loss expression given by (117) has to be changed in order to take these new configurations into account. However,

four expressions are proposed to make direct simulations. The insertion loss of the (a) parallel output IL_{po} , (b) serial output IL_{so} , (c) parallel input IL_{pi} and (d) serial input (IL_{si}) are expressed by (118) to (121) respectively.

In this work, only the capacitive impedance Z_q is considered and evaluated in the four cases. This method will be applied to identify the insertion loss in different input and output impedance conditions.

$$IL_{po} = -20 \log \left| \frac{AZ_q R_0 + B(R_0 + Z_q) + R_0 D(Z_q + R_0) + Z_q R_0^2 C}{2R_0 Z_q} \right| \quad (118)$$

$$IL_{so} = -20 \log \left| \frac{AR_0 + AZ_q + B + R_0 C Z_q + R_0 D + R_0^2 C}{2R_0} \right| \quad (119)$$

$$IL_{pi} = -20 \log \left| \frac{AZ_q R_0 + BR_0 + BZ_q + R_0^2 A + R_0 Z_q D + Z_q R_0^2 C}{2R_0 Z_q} \right| \quad (120)$$

$$IL_{si} = -20 \log \left| \frac{AR_0 + CR_0 Z_q + B + DZ_q + R_0 D + R_0^2 C}{2R_0} \right| \quad (121)$$

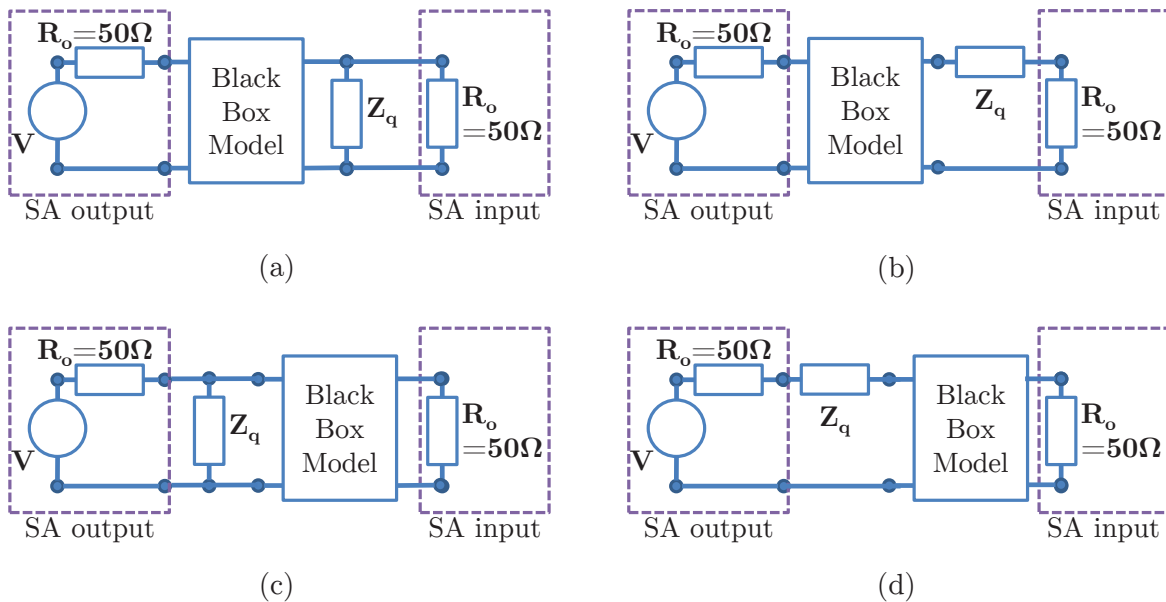


Figure 4-51 Characterization setup with additional impedance (a) parallel output (b) series output (c) parallel input (d) series input

A first approach to validate the proposed method in the four cases presented in Figure 4-51 is replacing the additional impedance Z_q by a capacitor with a closer value of the CM static converter impedance. In fact, the CM impedance of buck converter was measured by the CIM and it is illustrated in Figure 4-52. The equivalent capacitance (up to 10 MHz) is approximately 430pF. Then, an equivalent capacitor of 490pF with parasitic elements $ESR = 1.55\Omega$ and $ESL = 22.3nH$ measured with an impedance analyzer will be used in the experimental validation.

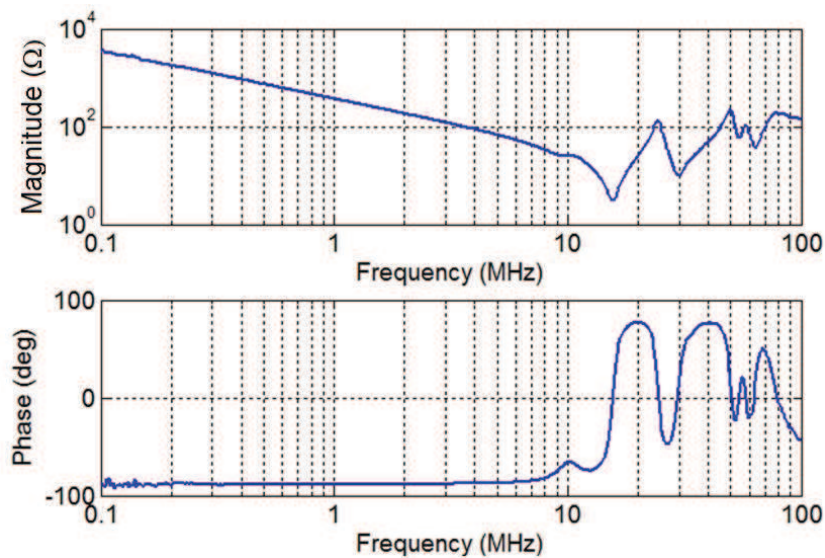


Figure 4-52 Measured CM impedance of the buck converter

When the capacitor (490pF) is replaced in the expressions (118) to (121), four IL are revealed as shown in Figure 4-53. The simulation results present a good agreement with experimental.

A second validation test is developed using the measured CM impedance of the buck converter (Figure 4-52). This impedance describes the parasitic element between the two input lines of the converter and the ground line. The setup is illustrated in Figure 4-54(a). The impedance Z_q , in the expression (121), is replaced by the impedance of the buck converter in off-state. The measured insertion loss and the simulation results are compared in Figure 4-54(b). The agreement of the insertion loss validates the proposed method.

The insertion loss of the EMI filter, based on the black box model, was investigated in this section. The only characterization of the filter with $50\Omega/50\Omega$ is not enough to estimate the real insertion loss of the filter when it is connected to the static converter and power supply.

Four expressions are proposed and used to evaluate the insertion loss of the filter when it is connected to arbitrary input and output impedances. The model was validated with $50\Omega/50\Omega$, and with different configurations. In addition, the input impedance of a buck converter, measured with the current injection probe method, is used to validate this method

This study is a first step of a huge work because the proposed method must be ameliorated.

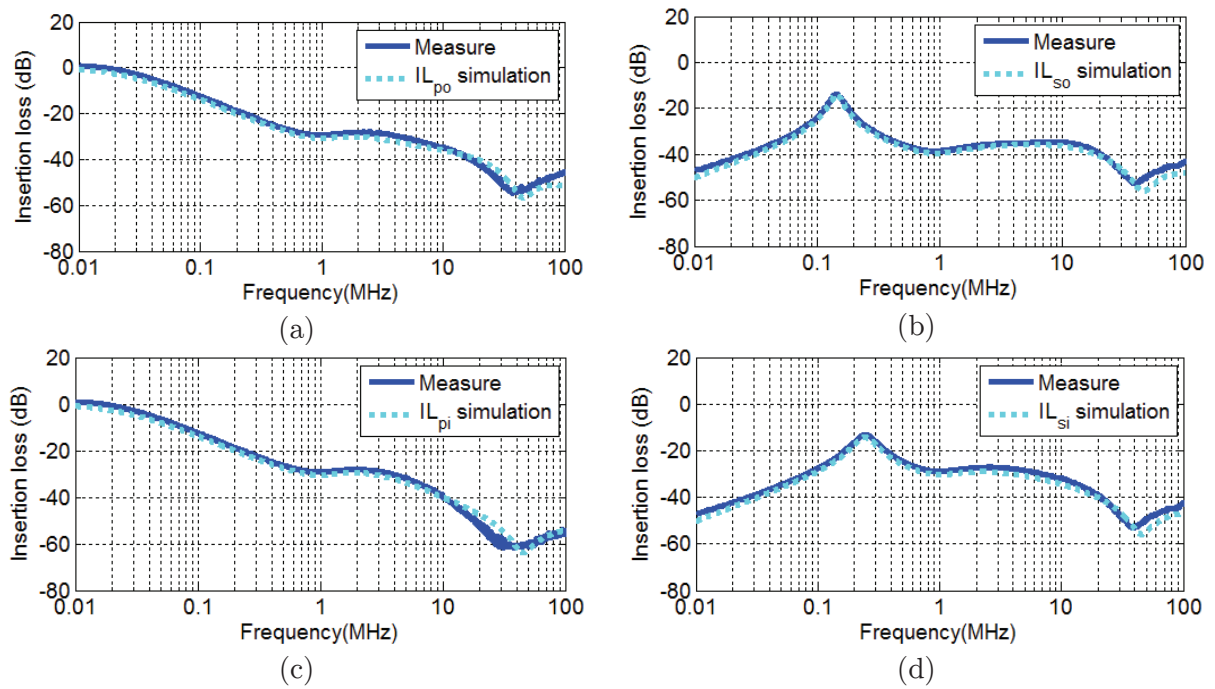


Figure 4-53 Validation of the additional impedance (a) for parallel output IL_{po} (b) series output IL_{so} (c) parallel input IL_{pi} (d) and series input IL_{si}

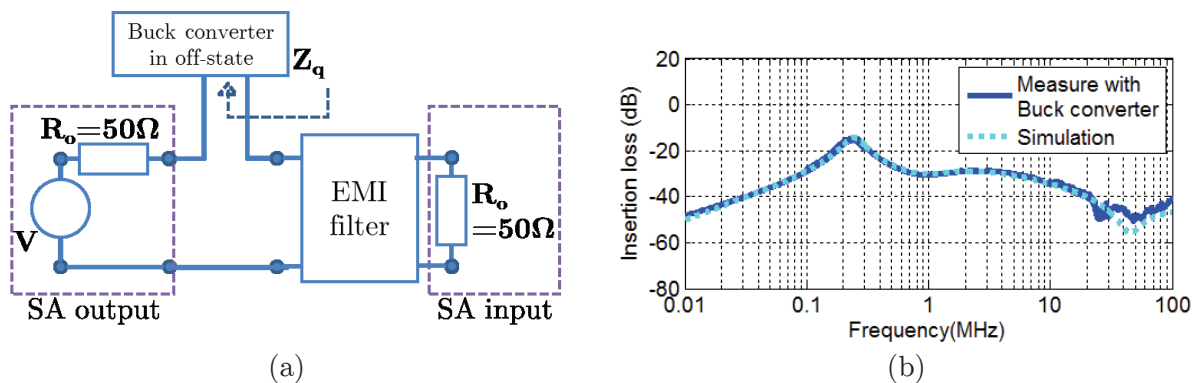


Figure 4-54 (a) Measurement of the insertion loss with buck converter input impedance in series with the EMI filter, and (b) insertion loss measured and simulated

4.9 Conclusion

In this chapter, the principles of the conducted emission measurement of the static converters have been presented. The DM and CM emissions have been measured using a current probe. The design method of the CM and DM filter is detailed.

In order to well determine the insertion loss, the input and output impedances connected to the EMI filter have to be known. Therefore, the current injection method (CIM) to measure the impedance of the static converter in operating conditions was studied. Different configurations have been proposed and investigated to study the configuration impact over the measurement.

The improvement of the CIM was obtained by designing new current probes that increase the accuracy in low and high frequencies. Moreover, the size of the measurement setup with commercial probes was reduced by more than 90% when new current probes are applied.

In the EMI filter design, the electrical equivalent circuit model developed in the previous chapters and the impedances measured with the CIM are used to predict the insertion loss of the EMI filter associated with a buck converter. The obtained values are then used to build the EMI filter and evaluate the attenuation of the conducted emission.

Finally, the insertion loss of the EMI filter is modeled with S-parameters to evaluate, by simulation and measurement, the influence of the arbitrary input/output impedances connected to the filter.

The electrical circuit model of the filter, using the magnetic material model, allows the prediction of the insertion loss and optimization of the dimensions of the filter. Once the filter is realized, the black box model can be employed to determine the IL for different input and output impedances.

General Conclusion

With the increase of switching frequency of the static converter based on the wide band gap semiconductors, the development of EMI filters that intends to reduce the conducted emissions, is still a challenging research area. The design of such filter requires detailed characterization and investigations related to its passive components as well as the input/output impedances which are also really important parameters.

In this dissertation, the magnetic materials for inductive components are studied first. This kind of material is very difficult to model due to nonlinearity effects that depend on frequency, current values and also temperature. In this work, different approaches are developed to study the characterization of the magnetic material in order to introduce a useful model to design and optimize the EMI filter for power electronic applications. Different studies were necessary to achieve this goal.

A specific complex magnetic permeability (CMP) measurement setup is developed to characterize the magnetic cores in HF. The number of turns, the leakage inductance and the material dispersion are taken into account to increase the measured parameters accuracy. The single turn flat coil presents less parasitic effects that usually mask the core's main effects. The CMP measurement realized on different magnetic materials reveals that the dispersion among the same ferrite cores can reach up to 40% above 1MHz and up to 30% for the nanocrystalline material. However, the ferrite material stays in the linear region of its characteristic while the nanocrystalline one presents different magnetization curves.

Once the CMP is measured, it is then modeled by two approaches: A mathematical model based on the rational functions and an electrical equivalent circuit. Both are finally validated with experimental data up to 100MHz. These models can describe only the CMP evolution with frequency.

In order to take into account the influence of the current level and temperature in the operating condition of the power converter, another model, called hysteresis model, is adopted. Thus, to characterize the material in the high-signal condition, a single turn flat coil is introduced instead of the commonly method with two coils. This solution allows reducing the magnetic coupling, inter-turning capacitances and proximity effects. Then, to model the hysteresis loop, two different representations are also developed: the average BH-curve and the Jiles-Atherton model. The latter enables a better depiction of the signal waveform in comparison with the average BH-curve. Furthermore, this model can also represent the CMP

evolution in low magnetization levels as well as the DC-bias effect on the magnetic material.

The obtained models of the two magnetic materials studied (ferrite and nanocrystalline) are tested to design EMI filter. The insertion loss of the filter, in common and differential mode, shows that the nonlinearity of the material can justify the attenuation's decrease when the electric current level increases. Additionally, the study of the temperature's influence on the magnetic material characteristics, with a developed test bench, shows that the electrical parameters strongly depend on the temperature. These results demonstrate the necessity to take into account the temperature when using such model of magnetic material.

To determine the EMI filter insertion losses, it is necessary to know the input impedance (EMI source) and the output one (load). The measurements carried out with the current injection method reveals that the high frequency impedance of the static converter changes with the operating conditions. The accuracy of this method is improved by using two small current probes. Their transfer impedances are identified with a developed characterization method. At the end, these probes are utilized to measure the common mode impedance of the static converter in different test configurations.

Finally, the EMI filter design procedure was described. The elements of the filters, in common and differential mode, are calculated. In both cases, three kinds of topologies were simulated in order to predict their insertion losses. The inductor model and the measured impedances of the static converter, in operating conditions, are used to determine by simulation the insertion loss of the filter. A large difference can be observed between the insertion loss obtained with 50Ω and the one obtained with the real measured impedance of the power converter. The simulation results show that the insertion loss of the filter is calculated with an acceptable accuracy considering that the influence of the temperature on the magnetic material model is neglected. The EMI filter prototype and the associated converter are evaluated to meet the EMC standard. Then, good attenuation results are obtained. This procedure of EMI filters design has been performed starting from the magnetic materials until realization of the filter prototype.

In case of using a manufactured filter, the insertion loss is measured with scattering parameters. The black box model, obtained by vector network analyzer, replaces the electrical equivalent model of the EMI filter to include impedances different to 50Ω during the simulations. Finally, the predicted insertion loss with arbitrary impedances is validated with measurement. This is a starting point to

improve the measurement of insertion loss with arbitrary input/output impedances.

Even if magnetic materials are widely used in power electronics for many years, a lot of scientific researchers are still working in this specific field. As a preliminary work in the L2EP on HF magnetic material, this PhD enables to deal with a lot of subjects related to characterization, modeling, simulation and experimentation of magnetic materials and more generally on EMI Filters. Of course, this work is not finished with this dissertation and a lot of enhancements can be considered.

Future work

The work realized in this dissertation is a contribution towards a better design of EMI filters and improvements are expected in the future regarding the accuracy of the developed models and measurement methods. Some key points for future works are suggested in the following paragraphs.

Regarding the small signal characterizations, a special effort is needed for parasitic capacitance analysis. Indeed, for ring core inductors, such capacitance is still difficult to estimate, even if a lot of approaches can be found in the literature. The main problem is linked to the inhomogeneity on the winding that distort the different computations. Then, uniformly wound around ring core need to be addressed with better winding techniques or special sockets. Additionally, stochastic analysis could be performed to estimate de margin of the capacitance value, which may further lead to better calculation for the electrical equivalent circuit.

Moreover, CMP models (analytical and electrical equivalent circuit) can be improved including additional parameters linked to temperature's influence or by updating the latter. Such temperature information will be very interesting because it will enable to take into account its influence in a design phase, which is obviously essential when designing filters for highly-constrained environment (in avionics, trains or automotive vehicles, etc...)

Regarding the high signal characterization aspects, specific works can be done on the measuring and the modeling parts. For example, the measurement test bench for automatic hysteresis loop characterization can be optimized to obtain directly the characteristic curves of the material (hysteresis loop, CMP curve, DC-bias ...) by a specific user-friendly interface. Thereby, reduce the time in the material characterization and also create a magnetic material database. This technique can be extended to measure different core shapes with and without a gap.

Furthermore, in the modeling part, the Jiles-Atherton model, that was applied to describe the hysteresis loop, can be improved by adding some different aspects describes below:

- Firstly, some additional parameters can be applied in order to introduce the dynamic effect to compute the core losses with better accuracy.
- Secondly, the maximum frequency (1MHz) has to be increased. This could be possible with a variable material capacitance instead of the constant one used in the model.

- Thirdly, the model can be extended to fit with better accuracy the hysteresis loop of nanocrystalline materials. The use of variable parameters in the model, as suggested in the literature, could be a solution, or the development of some specific hysteresis model.
- Finally, the last improvement linked to Jiles-Atherton model deals with temperature's impact. It could be interesting to include a feedback of the temperature in the model to update the parameters with the temperature evolution.

Considering the EMI filter part of this dissertation, some enhancements could also be done related to characterization and measurement methods. For example, the current probes designed for current injection method have been applied only in the common mode configuration. Thus, an extension to differential mode configuration could be addressed considering the DC-bias and the saturation of the material. In that case, materials with high magnetic density saturation could be applied.

In the aim of improvement the CM and DM filters design during the conception stage, some other operating conditions need to be included such as the network stability, and higher power densities. Finally, this procedure should be automated by programs that can reduce the EMI filter design process.

Bibliography

- [1] F. C. Lee and Q. Li, "High-Frequency Integrated Point-of-Load Converters: Overview," *IEEE Trans. Power Electron.*, vol. 28, pp. 4127-4136, 2013.
- [2] F. Costa and D. Magnon, "Graphical analysis of the spectra of EMI sources in power electronics," *IEEE Trans. Power Electron.*, vol. 20, pp. 1491-1498, 2005.
- [3] "American National Standard Dictionary of Electromagnetic Compatibility (EMC) including Electromagnetic Environmental Effects (E3)," *ANSI Std C63.14-2009*, pp. 1-46, 2009.
- [4] K. Kaiser, *Electromagnetic Compatibility Handbook*, 1 ed. U.S.A.: CRC Press, 2004.
- [5] N. J. Carter, "The past, present and future challenges of aircraft EMC," *IEEE Electromagn. Compat. Magazine*, vol. 1, pp. 75-78, 2012.
- [6] C. Po-Shen and L. Yen-Shin, "Effective EMI Filter Design Method for Three-Phase Inverter Based Upon Software Noise Separation," *IEEE Trans. Power Electron.*, vol. 25, pp. 2797-2806, 2010.
- [7] W. Shuo, "Modeling and Design of EMI Noise Separators for Multiphase Power Electronics Systems," *IEEE Trans. Power Electron.*, vol. 26, pp. 3163-3173, 2011.
- [8] "CISPR 11 - Industrial, scientific and medical equipment - Radio-frequency disturbance characteristics - Limits and methods of measurement," ed: IEC, 2009.
- [9] K. Mainali and R. Oruganti, "Conducted EMI Mitigation Techniques for Switch-Mode Power Converters: A Survey," *IEEE Trans. Power Electron.*, vol. 25, pp. 2344-2356, 2010.
- [10] N. Idir, R. Bausiere, and J. J. Franchaud, "Active gate voltage control of turn-on di/dt and turn-off dv/dt in insulated gate transistors," *IEEE Trans. Power Electron.*, vol. 21, pp. 849-855, 2006.
- [11] F. Mihalic and D. Kos, "Reduced Conductive EMI in Switched-Mode DC-DC Power Converters Without EMI Filters: PWM Versus Randomized PWM," *IEEE Trans. Power Electron.*, vol. 21, pp. 1783-1794, 2006.
- [12] A. Bhargava, D. Pommerenke, K. W. Kam, F. Centola, and L. Cheng Wei, "DC-DC Buck Converter EMI Reduction Using PCB Layout Modification," *IEEE Trans. Electromagn. Compat.*, vol. 53, pp. 806-813, 2011.
- [13] X. Lei and S. Jian, "Conducted Common-Mode EMI Reduction by Impedance Balancing," *IEEE Trans. Power Electron.*, vol. 27, pp. 1084-1089, 2012.
- [14] M. L. Heldwein, H. Ertl, J. Biela, and J. W. Kolar, "Implementation of a Transformerless Common-Mode Active Filter for Offline Converter Systems," *IEEE Trans. Industrial Electronics* vol. 57, pp. 1772-1786, 2010.
- [15] M. Ali, E. Laboure, F. Costa, and B. Revol, "Design of a Hybrid Integrated EMC Filter for a DC-DC Power Converter," *IEEE Trans. Power Electron.*, vol. 27, pp. 4380-4390, 2012.

-
- [16] V. Tarateeraseth, "EMI filter design: Part III: Selection of filter topology for optimal performance," *IEEE Electromag. Compat. Magazine*, vol. 1, pp. 60-73, 2012.
- [17] Y. Maillat, L. Rixin, W. Shuo, W. Fei, R. Burgos, and D. Boroyevich, "High-Density EMI Filter Design for DC-Fed Motor Drives," *IEEE Trans. Power Electron.*, vol. 25, pp. 1163-1172, 2010.
- [18] B. Toure, J. L. Schanen, L. Gerbaud, T. Meynard, J. Roudet, and R. Ruelland, "EMC Modeling of Drives for Aircraft Applications: Modeling Process, EMI Filter Optimization, and Technological Choice," *IEEE Trans. Power Electron.*, vol. 28, pp. 1145-1156, 2013.
- [19] J. Meng and W. Ma, "A new technique for modeling and analysis of mixed-mode conducted EMI noise," *IEEE Trans. Power Electron.*, vol. 19, pp. 1679-1687, 2004.
- [20] F. Costa, C. Gautier, B. Revol, J. Genoulaz, and B. Demoulin, "Modeling of the near-field electromagnetic radiation of power cables in automotives or aeronautics," *IEEE Trans. Power Electron.*, vol. PP, pp. 1-1, 2012.
- [21] H. Bishnoi, A. C. Baisden, P. Mattavelli, and D. Boroyevich, "Analysis of EMI Terminal Modeling of Switched Power Converters," *IEEE Trans. Power Electron.*, vol. 27, pp. 3924-3933, 2012.
- [22] C. Marlier, A. Videt, N. Idir, H. Moussa, and R. Meuret, "Modeling of switching transients for frequency-domain EMC analysis of power converters," in *Power Electronics and Motion Control Conference (EPE/PEMC), 2012 15th International*, 2012, pp. DS1e.1-1-DS1e.1-8.
- [23] "IEEE Standard for Methods of Measurement of Radio Frequency Power Line Interference Filter in the Range of 100 Hz to 10 GHz," *IEEE Std 1560-2005*, pp. 1-92, 2006.
- [24] H. Kosai, J. Scofield, S. McNeal, B. Jordan, and B. Ray, "Design and Performance Evaluation of a 200°C Interleaved Boost Converter," *IEEE Trans. Power Electron.*, vol. 28, pp. 1691-1699, 2013.
- [25] A. Roc'h and F. Leferink, "Nanocrystalline Core Material for High-Performance Common Mode Inductors," *IEEE Trans. Electromagn. Compat.*, vol. 54, pp. 785-791, 2012.
- [26] D. Cochrane, D. Y. Chen, and D. Boroyevic, "Passive cancellation of common-mode noise in power electronic circuits," *IEEE Trans. Power Electron.*, vol. 18, pp. 756-763, 2003.
- [27] W. Shuo, F. C. Lee, and J. D. Van Wyk, "A Study of Integration of Parasitic Cancellation Techniques for EMI Filter Design With Discrete Components," *IEEE Trans. Power Electron.*, vol. 23, pp. 3094-3102, 2008.
- [28] R. Wang, H. Blanchette, M. Mu, D. Boroyevich, and P. Mattavelli, "Influence of High-Frequency Near-Field Coupling between Magnetic Components on EMI Filter Design," *Power Electronics, IEEE Transactions on*, vol. PP, pp. 1-1, 2013.
- [29] T. Wenhua, C. Cuellar, X. Margueron, and N. Idir, "A Common-Mode Choke Using

- Toroid-EQ Mixed Structure," *IEEE Trans. Power Electron.*, vol. 28, pp. 31-35, 2013.
- [30] J. Aime, B. Cogitore, G. Meunier, E. Clavel, and Y. Marechal, "Numerical Methods for Eddy Currents Modeling of Planar Transformers," *IEEE Trans. Magnetics*, vol. 47, pp. 1014-1017, 2011.
- [31] EPCOS, "Ferrite and Accessories," EPCOS, Ed., ed, 2007.
- [32] C. Henglin, Q. Zhaoming, Y. Shaodong, and C. Wolf, "Finite-Element Modeling of Saturation Effect Excited by Differential-Mode Current in a Common-Mode Choke," *IEEE Trans. Power Electron.*, vol. 24, pp. 873-877, 2009.
- [33] J. L. Schanen, J. Roudet, É. Clavel, and J. M. Guichon, "Modélisation PEEC des connexions dans les convertisseurs de puissance," *Techniques de l'ingénieur Outils d'analyse en électronique de puissance et métrologie*, vol. base documentaire : TIB278DUO, 2004.
- [34] I. Kovacevic, T. Friedli, A. Muesing, and J. Kolar, "3D Electromagnetic Modeling of EMI Input Filters," *IEEE Trans. Industrial Electronics* vol. PP, pp. 1-1, 2013.
- [35] T. Wenhua, C. Cuellar, X. Margueron, and N. Idir, "A High Frequency Equivalent Circuit and Parameter Extraction Procedure for Common Mode Choke in the EMI Filter," *IEEE Trans. Power Electron.*, vol. 28, pp. 1157-1166, 2013.
- [36] J. L. Kotny, X. Margueron, and N. Idir, "High-Frequency Model of the Coupled Inductors Used in EMI Filters," *IEEE Trans. Power Electron.*, vol. 27, pp. 2805-2812, 2012.
- [37] I. Stevanovic, S. Skibin, M. Masti, and M. Laitinen, "Behavioral Modeling of Chokes for EMI Simulations in Power Electronics," *IEEE Trans. Power Electron.*, vol. 28, pp. 695-705, 2013.
- [38] M. Kovacic, Z. Hanic, S. Stipetic, S. Krishnamurthy, and D. Zarko, "Analytical Wideband Model of a Common-Mode Choke," *IEEE Trans. Power Electron.*, vol. 27, pp. 3173-3185, 2012.
- [39] L. Dalessandro, W. G. H. Odendaal, and J. W. Kolar, "HF Characterization and Nonlinear Modeling of a Gapped Toroidal Magnetic Structure," *IEEE Trans. Power Electron.*, vol. 21, pp. 1167-1175, 2006.
- [40] J. P. Keradec, P. Fouassier, B. Cogitore, and F. Blache, "Accounting for resistivity and permittivity in high frequency permeability measurements: application to MnZn ferrites," in *Instrumentation and Measurement Technology Conference, 2003. IMTC '03. Proceedings of the 20th IEEE*, 2003, pp. 1252-1256 vol.2.
- [41] R. Prieto, V. Bataller, J. A. Cobos, and J. Uceda, "Influence of the winding strategy in toroidal transformers," in *Industrial Electronics Society, 1998. IECON '98. Proceedings of the 24th Annual Conference of the IEEE*, 1998, pp. 359-364 vol.1.
- [42] C. R. Sullivan, "Optimal choice for number of strands in a litz-wire transformer winding," *IEEE Trans. Power Electron.*, vol. 14, pp. 283-291, 1999.
- [43] V. Dubickas and H. Edin, "High-Frequency Model of the Rogowski Coil With a Small Number of Turns," *IEEE Trans. Instrum. and Meas.*, vol. 56, pp. 2284-2288, 2007.

-
- [44] C. R. Sullivan, W. Li, S. Prabhakaran, and L. Shanshan, "Design and Fabrication of Low-Loss Toroidal Air-Core Inductors," in *Power Electronics Specialists Conference. IEEE PESC 2007*, 2007, pp. 1754-1759.
- [45] C. Hebedean, C. Munteanu, A. Racasan, and O. Antonescu, "Technologies to increase HF losses in planar structures and their limitations," in *Optimization of Electrical and Electronic Equipment (OPTIM), 2012 13th International Conference on*, 2012, pp. 48-53.
- [46] G. Grandi, M. K. Kazimierczuk, A. Massarini, and U. Reggiani, "Stray capacitances of single-layer solenoid air-core inductors," *IEEE Trans. Industry Applications*, vol. 35, pp. 1162-1168, 1999.
- [47] A. Massarini and M. K. Kazimierczuk, "Self-capacitance of inductors," *IEEE Trans. Power Electron.*, vol. 12, pp. 671-676, 1997.
- [48] L. Hai Yan, Z. Jian Guo, and S. Hui, "Experimental determination of stray capacitances in high frequency transformers," *IEEE Trans. Power Electron.*, vol. 18, pp. 1105-1112, 2003.
- [49] S. Wang, Z. Liu, and Y. Xing, "Extraction of parasitic capacitance for toroidal ferrite core inductor," in *Industrial Electronics and Applications (ICIEA), 2010 the 5th IEEE Conference on*, 2010, pp. 451-456.
- [50] W. Shuo, F. C. Lee, and J. D. Van Wyk, "Inductor winding capacitance cancellation using mutual capacitance concept for noise reduction application," *IEEE Trans. Electromagn. Compat.*, vol. 48, pp. 311-318, 2006.
- [51] M. J. Nave, "On modeling the common mode inductor," in *Electromagnetic Compatibility, 1991. Symposium Record., IEEE 1991 International Symposium on*, 1991, pp. 452-457.
- [52] A. Goldman, *Modern ferrite technology*, 2 ed. U.S.A.: Springer Science, 2006.
- [53] E. C. Snelling, *Soft ferrites properties and applications*, 2 ed. England: Butterworth-Heinemann, 1988.
- [54] T. Waeckerlé, "Matériaux magnétiques doux cristallins Choix des matériaux," *Techniques de l'ingénieur Matériaux magnétiques en électrotechnique*, vol. base documentaire : TIB259DUO, 2011.
- [55] R. Lebourgeois, "Ferrites doux pour l'électronique de puissance," *Techniques de l'ingénieur Matériaux magnétiques*, vol. base documentaire : TIB537DUO, 2005.
- [56] X. Jianfeng, M. Koledintseva, Z. Yaojiang, H. Yongxue, B. Matlin, R. E. DuBroff, J. L. Drewniak, and Z. Jianmin, "Complex Permittivity and Permeability Measurements and Finite-Difference Time-Domain Simulation of Ferrite Materials," *IEEE Trans. Electromagn. Compat.*, vol. 52, pp. 878-887, 2010.
- [57] H. Kai Meng, "Error correction for diffraction and multiple scattering in free-space microwave measurement of materials," *IEEE Trans. Microwave Theory and Techniques*, vol. 54, pp. 648-659, 2006.
- [58] R. B. Yang, C. Y. Tsay, D. S. Hung, W. F. Liang, Y. D. Yao, and C. K. Lin, "Complex

- permeability and permeability of iron-based composite absorbers measured by cavity perturbation method in X-band frequency range," *Journal of Applied Physics*, vol. 105, pp. 07A528-3, 2009.
- [59] H. Ruifeng and Z. Daming, "Using a Single Toroidal Sample to Determine the Intrinsic Complex Permeability and Permittivity of Mn-Zn Ferrites," *IEEE Trans. Magnetics*, vol. 43, pp. 3807-3815, 2007.
- [60] "IEEE Standard for Test Procedures for Magnetic Cores," *IEEE Std 393-1991*, 1992.
- [61] P. Nakmahachalasint, K. D. T. Ngo, and V.-Q. Loc, "A static hysteresis model for power ferrites," *IEEE Trans. Power Electron.*, vol. 17, pp. 453-460, 2002.
- [62] S. Lizon-Martinez, B. Tellini, R. Giannetti, and G. Robles, "Measurement of Asymmetric Minor Loops in Soft Ferrites Up to Medium Frequencies," *IEEE Trans. Instrum. and Meas.*, vol. 58, pp. 423-428, 2009.
- [63] T. Chailloux, M. Raulet, C. Martin, C. Joubert, F. Sixdenier, and L. Morel, "Magnetic Behavior Representation Taking Into Account the Temperature of a Magnetic Nanocrystalline Material," *IEEE Trans. Magnetics*, vol. 48, pp. 455-458, 2012.
- [64] F. Preisach, "Uber die magnetische Nachwirkung," *Zeitschrift fur Physik*, vol. 94, pp. 277-302, May 1935.
- [65] D. C. Jiles and D. L. Atherton, "Theory of ferromagnetic hysteresis (invited)," *Journal of Applied Physics*, vol. 55, pp. 2115-2120, 1984.
- [66] P. L. Dowell, "Effects of eddy currents in transformer windings," *Electrical Engineers, Proceedings of the Institution of*, vol. 113, pp. 1387-1394, 1966.
- [67] T. Tsutaoka, T. Nakamura, and K. Hatakeyama, "Magnetic field effect on the complex permeability spectra in a Ni--Zn ferrite," *Journal of Applied Physics*, vol. 82, pp. 3068-3071, 1997.
- [68] B. Cullity and C. Graham, *Introduction to magnetic materials*, 2nd ed. United States of America: Wiley-IEEE Press, 2009.
- [69] T. Tsutaoka, "Frequency dispersion of complex permeability in Mn--Zn and Ni--Zn spinel ferrites and their composite materials," *Journal of Applied Physics*, vol. 93, pp. 2789-2796, 2003.
- [70] P. G. Blanken, "A lumped winding model for use in transformer models for circuit simulation," *IEEE Trans. Power Electron.*, vol. 16, pp. 445-460, 2001.
- [71] R. Huang, D. Zhang, and K. J. Tseng, "Determination of Dimension-Independent Magnetic and Dielectric Properties for Mn-Zn Ferrite Cores and Its EMI Applications," *IEEE Trans. Electromagn. Compat.*, vol. 50, pp. 597-602, 2008.
- [72] H. Ruifeng, Z. Daming, and T. King Jet, "An efficient finite-difference-based Newton-Raphson method to determine intrinsic complex permeabilities and permittivities for Mn-Zn ferrites," *IEEE Trans. Magnetics*, vol. 42, pp. 1655-1660, 2006.
- [73] E. C. Levy, "Complex-curve fitting," *Automatic Control, IRE Transactions on*, vol. AC-4, pp. 37-43, 1959.

-
- [74] G. Golub and C. Van Van Loan, *Matrix Computations*, 3rd edition ed. Baltimore: The Johns Hopkins University Press, 1996.
- [75] W. Shuo, F. C. Lee, and W. G. Odendaal, "Characterization and parasitic extraction of EMI filters using scattering parameters," *IEEE Trans. Power Electron.*, vol. 20, pp. 502-510, 2005.
- [76] A. Davoudi, P. L. Chapman, J. Jatskevich, and H. Behjati, "Reduced-Order Dynamic Modeling of Multiple-Winding Power Electronic Magnetic Components," *IEEE Trans. Power Electron.*, vol. 27, pp. 2220-2226, 2012.
- [77] C. Henglin and Q. Zhaoming, "Modeling and Characterization of Parasitic Inductive Coupling Effects on Differential-Mode EMI Performance of a Boost Converter," *IEEE Trans. Electromagn. Compat.*, vol. 53, pp. 1072-1080, 2011.
- [78] I. F. Kovacevic, A. M. Musing, and J. W. Kolar, "An Extension of PEEC Method for Magnetic Materials Modeling in Frequency Domain," *IEEE Trans. Magnetics*, vol. 47, pp. 910-913, 2011.
- [79] S. Sander, "Buck and Boost Converters With Transmission Lines," *IEEE Trans. Power Electron.*, vol. 27, pp. 4013-4020, 2012.
- [80] C. Labarre and F. Costa, "Circuit Analysis of an EMI Filter for the Prediction of its Magnetic Near-Field Emissions," *IEEE Trans. Electromagn. Compat.*, vol. 54, pp. 290-298, 2012.
- [81] F. Mesmin, B. Ahmadi, H. Chazal, A. Kedous-Lebouc, and F. Sixdenier, "Improving reliability of magnetic mutual impedance measurement at high excitation level," in *Instrumentation and Measurement Technology Conference (I2MTC), 2011 IEEE*, 2011, pp. 1-6.
- [82] A. Muetze and C. R. Sullivan, "Simplified Design of Common-Mode Chokes for Reduction of Motor Ground Currents in Inverter Drives," *IEEE Trans. Industry Applications*, vol. 47, pp. 2570-2577, 2011.
- [83] A. Mariscotti, "Determination of the stray capacitance of single layer solenoids," in *Instrumentation and Measurement Technology Conference (I2MTC), 2011 IEEE*, 2011, pp. 1-5.
- [84] M. L. Heldwein, L. Dalessandro, and J. W. Kolar, "The Three-Phase Common-Mode Inductor: Modeling and Design Issues," *IEEE Trans. Industrial Electronics* vol. 58, pp. 3264-3274, 2011.
- [85] S. E. Zirka, Y. I. Moroz, P. Marketos, and A. J. Moses, "A viscous-type dynamic hysteresis model as a tool for loss separation in conducting ferromagnetic laminations," *IEEE Trans. Magnetics*, vol. 41, pp. 1109-1111, 2005.
- [86] Z. Daming, L. YiTao, and H. Song, "Differential Evolution Based Parameter Identification of Static and Dynamic J-A Models and Its Application to Inrush Current Study in Power Converters," *IEEE Trans. Magnetics*, vol. 48, pp. 3482-3485, 2012.
- [87] P. Nakmahachalasint, K. D. T. Ngo, and V.-Q. Loc, "A behavioral model for frequency-dependent hysteresis in power ferrites," *IEEE Trans. Magnetics*, vol. 40, pp. 1784-1790,

- 2004.
- [88] F. Fausto, "Measurements of magnetic materials," *Metrologia*, vol. 47, p. S114, 2010.
- [89] V. J. Thottuvelil, T. G. Wilson, and H. A. Owen, Jr., "High-frequency measurement techniques for magnetic cores," *IEEE Trans. Power Electron.*, vol. 5, pp. 41-53, 1990.
- [90] J. Deane, "Modeling the dynamics of nonlinear inductor circuits," *IEEE Trans. Magnetics*, vol. 30, pp. 2795-2801, 1994.
- [91] S. Wei, W. Fei, D. Boroyevich, and C. W. Tipton, "Loss Characterization and Calculation of Nanocrystalline Cores for High-Frequency Magnetics Applications," *IEEE Trans. Power Electron.*, vol. 23, pp. 475-484, 2008.
- [92] J. Muhlethaler, J. Biela, J. W. Kolar, and A. Ecklebe, "Improved Core-Loss Calculation for Magnetic Components Employed in Power Electronic Systems," *IEEE Trans. Power Electron.*, vol. 27, pp. 964-973, 2012.
- [93] T. Nakamura, "Snoek's limit in high-frequency permeability of polycrystalline Ni-Zn, Mg-Zn, and Ni-Zn-Cu spinel ferrites," *Journal of Applied Physics*, vol. 88, pp. 348-353, 2000.
- [94] P. Nakmahachalasint, K. D. T. Ngo, and V.-Q. Loc, "Effective parameters for toroidal cores based on nonlinear magnetization," *IEEE Trans. Magnetics*, vol. 41, pp. 2432-2435, 2005.
- [95] E. Etien, D. Halbert, and T. Poinot, "Improved Jiles-Atherton Model for Least Square Identification Using Sensitivity Function Normalization," *IEEE Trans. Magnetics*, vol. 44, pp. 1721-1727, 2008.
- [96] R. Marion, R. Scorretti, N. Siauve, M. A. Raullet, and L. Krahenbühl, "Identification of Jiles-Atherton Model Parameters Using Particle Swarm Optimization," *IEEE Trans. Magnetics*, vol. 44, pp. 894-897, 2008.
- [97] D. Zhang and J. E. Fletcher, "Double-Frequency Method Using Differential Evolution for Identifying Parameters in the Dynamic Jiles-Atherton Model of Mn-Zn Ferrites," *IEEE Trans. Instrum. and Meas.*, vol. 62, pp. 460-466, 2013.
- [98] M. Toman, G. Stumberger, and D. Dolinar, "Parameter Identification of the Jiles-Atherton Hysteresis Model Using Differential Evolution," *IEEE Trans. Magnetics*, vol. 44, pp. 1098-1101, 2008.
- [99] M. Mingkai, S. Yipeng, L. Qiang, and F. C. Lee, "Magnetic characterization of low temperature co-fired ceramic (LTCC) ferrite materials for high frequency power converters," in *Energy Conversion Congress and Exposition (ECCE), 2011 IEEE*, 2011, pp. 2133-2138.
- [100] P. Nakmahachalasint, K. D. T. Ngo, and V.-Q. Loc, "Thermal behavior of a dynamic domain-wall motion model for hysteresis in power ferrites," *IEEE Trans. Magnetics*, vol. 41, pp. 140-143, 2005.
- [101] O. Messal, F. Sixdenier, L. Morel, and N. Burais, "Temperature Dependent Extension of the Jiles-Atherton Model: Study of the Variation of Microstructural Hysteresis Parameters," *IEEE Trans. Magnetics*, vol. 48, pp. 2567-2572, 2012.

-
- [102] M. Kumar and V. Agarwal, "Power line filter design for conducted electromagnetic interference using time-domain measurements," *IEEE Trans. Electromagn. Compat.*, vol. 48, pp. 178-186, 2006.
- [103] W. Shuo, F. C. Lee, and W. G. Odendaal, "Characterization, evaluation, and design of noise Separator for conducted EMI noise diagnosis," *IEEE Trans. Power Electron.*, vol. 20, pp. 974-982, 2005.
- [104] R. A. Southwick and W. C. Dolle, "Line Impedance Measuring Instrumentation Utilizing Current Probe Coupling," *IEEE Trans. Electromagn. Compat.*, vol. EMC-13, pp. 31-36, 1971.
- [105] V. Tarateeraseth, H. Bo, S. Kye Yak, and F. G. Canavero, "Accurate Extraction of Noise Source Impedance of an SMPS Under Operating Conditions," *IEEE Trans. Power Electron.*, vol. 25, pp. 111-117, 2010.
- [106] V. Tarateeraseth, S. Kye Yak, F. G. Canavero, and R. W. Chang, "Systematic Electromagnetic Interference Filter Design Based on Information From In-Circuit Impedance Measurements," *IEEE Trans. Electromagn. Compat.*, vol. 52, pp. 588-598, 2010.
- [107] F. Grassi, F. Marliani, and S. A. Pignari, "Circuit Modeling of Injection Probes for Bulk Current Injection," *IEEE Trans. Electromagn. Compat.*, vol. 49, pp. 563-576, 2007.
- [108] G. Cerri, R. De Leo, V. M. Primiani, S. Pennesi, and P. Russo, "Wide-band characterization of current probes," *IEEE Trans. Electromagn. Compat.*, vol. 45, pp. 616-625, 2003.
- [109] C. Carobbi and L. Millanta, "Circuit Loading in Radio-Frequency Current Measurements: The Insertion Impedance of the Transformer Probes," *IEEE Trans. Instrum. and Meas.*, vol. 59, pp. 200-204, 2010.
- [110] V. Tarateeraseth, "EMI filter design: Part II: Measurement of noise source impedances," *IEEE Electromag. Compat. Magazine*, vol. 1, pp. 42-49, 2012.
- [111] S. Kye Yak and D. Junhong, "Measurement of noise source impedance of SMPS using a two probes approach," *IEEE Trans. Power Electron.*, vol. 19, pp. 862-868, 2004.
- [112] L. Fang, D. Boroyevich, and P. Mattavelli, "Improving EMI filter design with in circuit impedance mismatching," in *Applied Power Electronics Conference and Exposition (APEC), 2012 Twenty-Seventh Annual IEEE*, 2012, pp. 1652-1658.
- [113] D. A. Frickey, "Conversions between S, Z, Y, H, ABCD, and T parameters which are valid for complex source and load impedances," *IEEE Trans. Microwave Theory and Techniques*, vol. 42, pp. 205-211, 1994.